Numerical and Experimental Studies of Shallow Cone Penetration in Clay

Edmund Hazell

Trinity Term, 2008

A thesis submitted for the degree of
Doctor of Philosophy
at the University of Oxford

Abstract

The fall-cone test is widely used in geotechnical practice to obtain rapid estimates of the undrained shear strength of cohesive soil, and as an index test to determine the liquid limit. This thesis is concerned with numerical modelling of the penetration of solids by conical indenters, and with interpretation of the numerical results in the context of the fall-cone test. Experimental studies of shallow cone penetration in clay are also reported, with the aim of verifying the numerical predictions. The practical significance of the results, in terms of the interpretation of fall-cone test results, is assessed.

Results are reported from finite element analyses with the commercial codes ELFEN and Abaqus, in which an explicit dynamic approach was adopted for analysis of continuous cone indentation. Quasi-static analyses using an elastoplastic Tresca material model are used to obtain bearing capacity factors for shallow cone penetration, taking account of the material displaced, for various cone apex angles and adhesion factors. Further analyses are reported in which a simple extension of the Tresca material model, implemented as a user-defined material subroutine for Abaqus, is used to simulate viscous rate effects (known to be important in cohesive soils). Some analyses with the rate-dependent model are displacement-controlled, while others model the effect of rate-dependence on the dynamics of freefall cone indentation tests.

Laboratory measurements of the forces required to indent clay samples in the laboratory are reported. Results from displacement-controlled tests with imposed step-changes in cone speed, and from freefall tests, confirm that the numerical rate-dependent strength model represents the observed behaviour well. Some results from experiments to observe plastic flow around conical indenters are also presented.

Finally, additional numerical analyses are presented in which a critical state model of clay plasticity is used to study the variation of effective stress, strain and pore pressure around cones in indentation tests at various speeds.

Acknowledgements

I would like to thank my supervisor, Chris Martin, for his invaluable assistance in planning and executing this work, and for his patient advice and support through all my research at Oxford. Dr. Martin was generous in providing financial support from his personal budget for the experimental apparatus and computer hardware and software without which this work would not have been possible.

My thanks go to Mr. Tim Carrington and Mr. Tom Aldridge, of Fugro GeoConsulting Ltd., for providing access to the software ELFEN at their Wallingford offices, and to Guangquan Xu (also at Fugro) for his practical advice and support in using the software.

All custom-designed components of the laboratory equipment were produced in the workshops of the Department of Engineering Science, by Clive Baker, Bob Sawala and Chris Waddup, who also offered much helpful advice during the design process.

The friendship, advice and practical assistance offered by my fellow students in the Civil Engineering Research Group are gratefully appreciated. In particular, I thank Mobin, Oliver and Jens.

I wish to acknowledge the funding I have received from the Department of Engineering Science, in the form of a studentship funded by the EPSRC, and the additional support I have received from Jesus College. Their financial assistance has enabled me to travel to conferences and devote time to writing this thesis without the additional pressure of financial difficulties.

Finally, my heartfelt thanks go to my parents, family and friends for their support during the last few years, and to Meleri, whose presence in my life during my time in Oxford has ensured that I will always cherish my memories of my time here.

Contents

List of Figures

List of Tables

Chapter 1

Introduction

It is well known that the undrained shear strength of a soil can vary with the rate of deformation. Commonly, an increase in strength of 5–20 % may be expected for every tenfold increase in rate of strain (Casagrande and Wilson, 1951; Graham et al., 1983). Despite this, many commonly-used tests for soil strength involve mechanisms in which the magnitude and spatial distribution of strain rates is not well understood. Often, this is because it is necessary to balance two factors: a more elaborate test in which the deformation rate is carefully controlled (e.g. the laboratory triaxial test or the in-situ cone penetration test) will require expensive equipment; a simpler test requiring inexpensive equipment may allow only crude rate control, but can be kept available for use whenever and wherever it is needed. The fall-cone is an example of this type of test; others include hand-held "pocket penetrometers" and shear vanes, which are commonly used for estimating the strength of soils exposed in excavations and trial pits. The uncertainty of results from these devices limits their usefulness – for example, the pocket penetrometer is reliable only to within ±20–40 % (OSHA, 1999).

Rate-dependent strength also becomes important when a test involves a dynamic event – strain rates can then vary widely over time. Several tests, including both in-situ and laboratory procedures, involve conical indenters or penetrometers falling into soil under gravity. The most common example is the laboratory fall-cone, which is released from rest from an initial position just touching the surface of a soil sample. Recently developed offshore in-situ tests employ probes that free-fall through the water and embed themselves in the seabed. Examples include the Free Fall Cone Penetration Test (FFCPT, Brooke Ocean Technology Ltd., 2004) and the Seabed Terminal Impact Newton Gradiometer (STING, Poeckert et al., 1997).

Analysis of results from any of these tests would benefit from an improved understanding of the variation of strain rate – and therefore undrained shear strength – in the plastically deforming soil. This thesis focuses on the deformation mechanism produced in a fall-cone test, but will also be applicable to the initial shallow penetration stage of an FFCPT or pocket penetrometer test.

1.1 The fall-cone test

The fall-cone test was developed in Scandinavia as a rapid method for characterizing cohesive soils. The test is carried out by placing a metal cone vertically with its apex just touching the horizontal surface of a sample of clay. The cone is then released and allowed to fall freely, and the depth of the resulting penetration is measured. The test is extremely simple to perform, and takes very little time.

1.1.1 Index properties obtained with the fall-cone

Results from fall-cone tests may be used in either of two distinct ways. Originally, the test was viewed essentially as a means of categorizing materials, and the results were used to derive index properties that allowed comparisons to be made between soils without necessarily being related to any fundamental model of their behaviour.

The original method of interpreting fall-cone test results was proposed by the Geotechnical Commission of the Swedish State Railways (1922). On the basis of fall-cone test results, materials were assigned a "strength number" H, which was defined such that the number 10 corresponded to a 10 mm deep indentation with a 60°, 60 g cone. The ratio of the hardness number H_1 of a remoulded soil to the value H_3 for an undisturbed sample is used as a measure of sensitivity. The Geotechnical Commission also defined the "fineness number" F, equal to the water content for which the remoulded hardness number H_1 was equal to 10 (i.e., the depth of indentation with a 60°, 60 g cone was 10 mm). The fineness number is the approximate equivalent of the liquid limit used in English-speaking countries.

In the UK, the fall-cone test has been widely adopted as a means of determining the liquid limit w_L of a soil. The liquid limit of a cohesive soil is now usually defined as the water content which results in a penetration $h = 20\,\mathrm{mm}$ in a fall-cone test with a 30°, 80 g cone. The method is set down in BS 1377, Part 2 (BSI, 1990), and was based on the earlier Scandinavian practice. BS 1377 suggests that the fall-cone test be used in preference to the earlier Casagrande percussion-cup method, following the recommendation of Karlsson (1961). In comparing the two methods, the British Standard notes that the fall-cone method is "fundamentally more satisfactory", since results obtained with the Casagrande method are susceptible to variation due to differences between operators and to "dynamic effects".

1.1.2 Use of the fall-cone to determine undrained shear strength

Although the British Standard defines the liquid limit arbitrarily in terms of a specific depth of penetration with a fall-cone, the test is equivalent to determining the water content for which a soil has a particular strength. This is because the results of a fall-cone test depend primarily on the undrained strength s_{u} – according to Wood and Wroth (1978), the value of s_{u} at the liquid limit is approximately 1.7 kPa. Hansbo (1957) found that the undrained shear strength s_{u} could be determined from the depth of penetration h by use of the expression

$$s_{\mathrm{u}} = \frac{KW}{h^2}, \tag{1.1}$$

where W is the weight of the fall-cone, and K is a "cone factor". The value of K depends primarily on the angle of the cone, but is also influenced by (amongst other factors) the roughness of the cone, and the effects of strain rate on s_{u}.

Cone factors obtained from experiment

Hansbo (1957) determined values of K by correlating the results of fall-cone tests with values of undrained shear strength s_{u} obtained with a shear vane. Separate correlations were performed for undisturbed and remoulded samples. In tests on (nominally) undisturbed material, Hansbo obtained values of K that varied between 0.8 and 1.0 for the 30° cone and between 0.2 and 0.25 for the 60° cone. He attributed this variation in K to the amount of disturbance caused by the type of sampler used in each case. For remoulded clay, K was given as 0.3 for the 60° cone; no value was obtained for a 30° cone with remoulded material, although Wood (1982) proposed a value of $K \approx 1.2$ based on the result for a 60° cone and analogy with the strength correlations for undisturbed samples.

Several later authors have carried out similar studies to Hansbo's, correlating fall-cone results with values of s_{u} obtained from vane tests and giving their own estimates of K. In general, their results were similar to those reported by Hansbo.

Cone factors from theoretical and numerical analyses

Much research has been devoted to determining values of the cone factor K by theoretical and numerical analyses of fall-cone tests. The problem of quasi-static surface indentation by a cone is usually analysed as a preliminary step in developing a dynamic model of the fall-cone test.

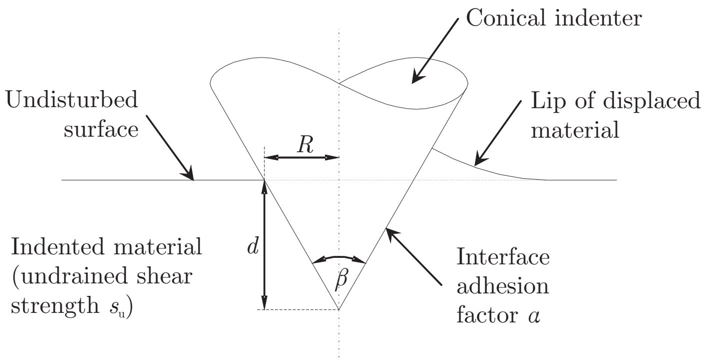

Figure 1.1: Schematic view of cone indentation

Figure 1.1 shows a schematic view of cone indentation. At the instant shown, the cone has penetrated to a depth d (measured relative to the level of the original, undisturbed surface). Since the apex angle of the cone is β, the radius R of the cone at the original surface level is $R = d \tan \frac{\beta}{2}$. The relationship between the force Q that must be applied to the cone to cause further penetration, and the shear strength s_{u} of the indented material, can be expressed in terms of either of these measures of the length scale of the indentation, through the use of a dimensionless bearing capacity factor N_{ch}:

$$Q = N_{\mathrm{ch}} s_{\mathrm{u}} \pi R^2 = N_{\mathrm{ch}} s_{\mathrm{u}} \pi \tan^2(\tfrac{\beta}{2}) d^2. \tag{1.2}$$

The value of N_{ch} will be affected by the build-up of displaced material around the cone. The notation is that of Koumoto and Houlsby (2001); the subscript "h" denotes "heave". Alternatively, Q can be related to the depth of the indentation d through the use of an alternative parameter F (used by Houlsby, 1982).

$$Q = F s_{\mathrm{u}} d^2. \tag{1.3}$$

F is convenient to work with since its calculation (given Q, d and s_{u}) is simpler, however either parameter can easily be determined from the other.

Values of N_{ch} or an equivalent parameter have been determined by several researchers using the method of characteristics (Lockett, 1963; Houlsby, 1982; Koumoto and Houlsby, 2001). However, the form that the free surface should take has been a particular difficulty. Lockett (1963) determined the correct shape of the lip of displaced material, but could only obtain solutions for $\beta \geq 105°$. Later researchers (Houlsby, 1982; Koumoto and Houlsby, 2001) have also been unable to account properly for the displaced material around cones with $\beta < 105°$, and have instead assumed the surface profile to be a straight line.

Given a value of N_{ch}, a dynamic analysis of the fall-cone test can be performed (neglecting rate effects) by solving the equation of motion of the cone

$$\frac{\mathrm{d}^2 z}{\mathrm{d}t^2} = g - \frac{Q}{m} = g - \frac{F s_{\mathrm{u}} z^2}{m} \tag{1.4}$$

where m is the mass of the cone. Houlsby (1982) showed, on the basis of this analysis, that the final indentation depth h would be equal to $h_{\mathrm{s}}\sqrt{3}$, where h_{s} is the static indentation depth at which the resistance Q is equal to the weight W of the cone.

As discussed in Section 2.2.7, Koumoto and Houlsby (2001) extended this dynamic analysis in a simple manner to take account of rate effects. They showed that the final penetration of the cone would be $h = h_{\mathrm{s}}\sqrt{3\zeta}$, where $\zeta = s_{\mathrm{u0}}/s_{\mathrm{ud}}$ is the ratio of the material's static strength s_{u0} to the dynamic strength exhibited in the fall-cone test s_{ud} ($> s_{\mathrm{u0}}$). Values of N_{ch} and ζ can be combined to give a value of the cone factor K:

$$K = \frac{s_{\mathrm{u0}} h^2}{W} = \frac{3\zeta}{F} = \frac{3\zeta}{\pi N_{\mathrm{ch}} \tan^2(\beta/2)}. \tag{1.5}$$

1.2 Research aims

The primary aim of the research presented in this thesis was to perform numerical analyses to determine values of the cone factor K. This has been approached in two stages: first, to determine N_{ch} by quasi-static analyses, then to determine ζ by dynamic analyses with rate-dependent strength. These numerical analyses make use of the finite element (FE) method. Unlike analyses by the method of characteristics, FE analyses do not require prior knowledge of the form the solution should take, allowing the unknown shape of the displaced surface around the cone to be accounted for in a relatively straightforward fashion. It is also possible to perform analyses with various constitutive models, which may include rate-dependent behaviour (whereas the method of characteristics can be used only with Tresca materials). Various contact conditions at the interface between the cone and clay can also be accounted for. All the analyses model the complete cone penetration process, beginning with the tip of the cone level with the undisturbed surface of the material to be indented.

The finite element analyses are described in Chapters 3 to 5. The explicit dynamics approach provided by the commercial FE codes ELFEN (Rockfield Software, 2005) and Abaqus (Simulia, 2007) has been used. The differences between the more common implicit FE method and the approach adopted here (which involves explicit integration of the model in the time domain) are discussed in Chapter 3. The fundamental advantage of the explicit dynamics approach is that the global stiffness matrix need never be assembled; assembling this matrix and solving the corresponding linear system of equations dominates the computational effort required to solve a traditional finite element model. For problems involving large deformations and a high degree of non-linearity due to contact, explicit FE analyses give better efficiency than the traditional implicit FE approach (see e.g. Susila and Hryciw, 2003). The finite element models utilise adaptive meshing to ensure a high quality mesh is maintained throughout the analysis, despite the large strains that occur in the indented material.

In Chapters 3 and 4, quasi-static analyses are performed with a rate-independent Tresca material, with the aim of determining values of the bearing capacity factor N_{ch}. In Chapter 5, a rate-dependent material model is introduced, and dynamic analyses of a freefall cone test are performed to determine values of the parameter ζ that governs the overall influence of rate effects on fall-cone test results. Combining the values of N_{ch} and ζ allows values of the cone factor K to be determined.

Experimental work is also presented. Chapter 7 describes experiments carried out on remoulded samples of kaolin using conical indenters (with angles $\beta = 30°$ and $60°$). The cones were either pushed in slowly by an actuator or released from rest and allowed to act as fall-cones. The rate dependence of the kaolin was assessed by imposing changes in the rate of penetration during the displacement-controlled tests, and by comparing force–displacement curves from freefall tests with results from displacement-controlled tests on similar samples. Experimental values of ζ for the kaolin used in the laboratory were determined from the freefall tests.

A further set of laboratory tests were performed to observe the patterns of deformation around conical indenters in kaolin. The deformation mechanisms are compared with those obtained in finite element analyses. These experiments are described in Chapter 6.

Finally, Chapter 8 describes an additional series of finite element analyses, in which the indented clay was represented by a material obeying the Cam clay model, with constitutive behaviour modelled in terms of effective stress. Since these analyses account for the variation of pore pressure (and flow of pore fluid) within the deforming region, they allow the development of a better understanding of the drainage conditions in some of the tests described in Chapter 7.

Chapter 2

Literature review

2.1 Material tests using surface indentation

2.1.1 History

It has long been common practice in many areas of engineering to test materials by the use of (comparatively) rigid penetrometers or indenters of various standard geometries – spheres, pyramids and cones are all widely used. Indentation or penetration tests may be conducted under displacement control or load control. In the former case the indenter is pushed into the sample at a constant rate; in the latter the indenter is allowed to move into the material under some constant force, usually the self-weight of the indenter assembly itself. The tests are applied to materials as varied as lubricating greases, metals and soils.

Some of the earliest indentation tests were used in measuring the hardness (i.e. resistance to plastic deformation) of metals. In metallurgy, hardness is generally quantified as the mean pressure exerted by an indenter on the tested material, under some predefined conditions. A spherical indenter was used in the Brinell hardness test, developed in 1900 and first described in English by Wahlberg (1901). Not long afterwards, in 1908, a conical diamond indenter was used by Ludwik. Other commonly-used metal hardness tests employ the Vickers and Knoop indenters, which take the form of pyramids.

At first, little was understood about the exact deformation processes undergone by indented materials. Tests were not concerned with the direct determination of fundamental material properties, such as shear strength or elastic modulus, but were instead used to compare various materials (especially different batches of steel). Clearly, some correlation between the measured hardnesses and material properties was to be expected, and various empirical methods were used to relate test results and strength. Tabor (1951) provides a succinct description of the development of indentation tests for metals, and their analysis, in the first half of the 20th century.

Tests using conical indenters are also prevalent in geotechnical engineering. The fall cone test was developed by the Swedish State Railways (1922), and came to be used, as an alternative to the original Casagrande percussion method, to determine the liquid limit of a remoulded sample of cohesive soil. The liquid limit is one of the Atterberg consistency limits by which fine-grained soils are often characterized (the other in common use being the plastic limit). In theory the liquid limit should be defined as the water content at which a clay is practically liquid (i.e. has near-zero shear strength), but since soils do not display a well-defined transition to the liquid state as water content increases, the liquid limit is taken to be the water content for which the clay has some small but measurable undrained shear strength. In practice, the limit is defined by the results of various laboratory tests; in Britain the procedures and apparatus to be used in these tests are defined by the British Standards Institution (BSI). A soil's water content at the liquid limit is given the symbol w_{L}.

The original Geotechnical Commission fall cone apparatus is shown in Figure 2.1. The liquid limit test used today retains most of the key features of the original. A soil sample is prepared and placed in the test cup; a cone of prescribed mass and dimensions is positioned with its tip just touching the sample surface; the cone is released from rest and the distance through which it has fallen after a prescribed period (5 s) is measured. After the prescribed period, the intention is that the cone should be almost at rest – any further movement will be very gradual and due to consolidation and creep effects.

The current British test differs only slightly from that depicted in Figure 2.1. The sample container prescribed by the British Standard is straight-sided, rather than bowl-shaped, with diameter 55 mm and depth 40 mm. The cone used has an apex angle of 30° rather than the 60° originally used in Sweden, and is also heavier at 80 g instead of 60 g. Koumoto and Houlsby (2001) provide a summary of the standards used in various countries. For full details of the British method see BS 1377 (BSI, 1990); a concise description is provided by Whitlow (2001).

The method of determining a soil's plastic limit (w_{P}) given by BS 1377 is quite different from either of those suggested for the liquid limit, and involves rolling and hand-drying a series of small samples to determine the water content at which a thread-like cylindrical

Figure 2.1: The fall cone apparatus of the Swedish State Railways (1922). From geoforum.com (2005)

specimen will just begin to crumble when rolled to a diameter of 3 mm. Several authors have proposed that this limit too could be estimated by the use of the fall cone apparatus, perhaps with some additional measurements being made (see, for example, Wood and Wroth, 1978; Harison, 1988; Stone and Phan, 1995; Fall, 2000). Some of these authors note that the current plastic limit method is highly subjective, and too dependent on the details of the procedure followed. The use of the fall cone for the determination of the plastic limit as well as the liquid limit would give a consistent and reproducible basis for the two measurements, which would be especially desirable when they are combined in calculating the plasticity index $I_\mathrm{P} = w_\mathrm{L} - w_\mathrm{P}$.

Though the fall cone test is widely used to determine liquid limit, it is fundamentally a measure of soil strength – indeed, this was its original purpose. Penetration depths have been converted to shear strengths by empirical correlations with other strength tests. Hansbo (1957) correlated fall-cone test results with values of s_u from field and laboratory vane tests, and his results still form the basis for shear strength measurement using the fall cone apparatus (Geonor, 2005a). Other work has focused on producing theoretical models of the mechanics of cone penetration, from which strength may be determined more rationally. Some of these studies will be reviewed in the following sections.

2.1.2 Analysis by the method of characteristics

The use of the method of characteristics – also known as the slip line method – in soil mechanics has been described by many authors. A useful summary is given by Houlsby and

Wroth (1982).

Essentially, the method involves the integration of a hyperbolic system of partial differential equations, derived from the yield criterion and the equations of equilibrium, by proceeding along directions (known as characteristics) in which the partial differential equations reduce to ordinary ones. In these analyses it is common to adopt the Tresca yield criterion (which is equivalent to the Mohr-Coulomb criterion with angle of friction $\phi = 0$) and to assume an associated plastic flow rule. In carrying out a bearing capacity analysis, only that region of the soil which is deforming plastically is initially included. The solution proceeds from a boundary on which the stresses in the soil are known (e.g. the free surface adjacent to a footing or penetrometer) to the boundary on which the stresses are to be determined (the underside of the footing, say). These stresses can then be integrated to give the failure load on the footing or penetrometer. Formally, the solutions obtained in this way must be regarded as incomplete lower bounds to the exact result, unless and until they can be shown to be exact. Proof of exactness requires that two key steps be taken: it must be shown that the evaluated stress field can be extended into the surrounding soil without violating the equation of yield; and it must be shown that the stress field can be associated with a kinematically admissible velocity field giving a matching upper bound for the bearing capacity. Martin (2005) has recently shown this to be possible for a wide range of materials obeying the Mohr-Coulomb yield criterion and an associated flow rule (optionally with the cohesive strength c varying linearly with depth), in the plane strain problem of strip footing bearing capacity.

An early axisymmetric analysis by the method of characteristics was performed by Shield (1955). The author considered the indentation of the surface of a semi-infinite body by a smooth, flat circular punch. The material was assumed to obey the Tresca yield criterion. The average pressure on the punch at failure was found to be $5.69k$, where k is the shear strength of the material. This result was then shown to be exact by extending the stress field and determining the corresponding velocity field as described above. This analysis can be easily recreated using the program ABC (Martin, 2004), though the publicly available version does not yet perform the additional steps required for proof of exactness – see Martin (2005).

In order to determine the exact maximum load that can be sustained by a conical indenter, as opposed to a flat punch, it is necessary to account for the fact that (assuming

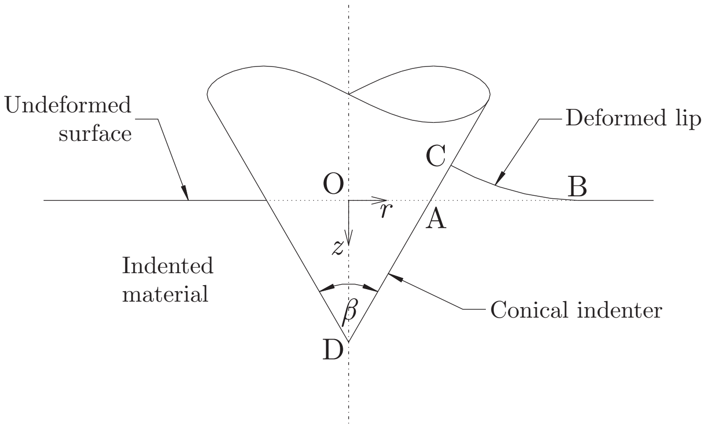

Figure 2.2: Schematic view of the cone indentation problem

the indented material is incompressible) the free surface around the indenter will be forced upwards to form a lip. This situation is shown schematically in the right-hand side of Figure 2.2. The precise form that this lip will take must be regarded as one of the unknown elements in a rigorous solution for continuous indentation, and this has been a major difficulty in previous work on this subject. As was pointed out by Lockett (1963), there is no characteristic length in the problem specification and so geometric similarity must be preserved at every stage. In other words, the shape of the deformed lip and the velocity field at any instant should be related such that the shape of the lip is preserved after a further increment of indentation.

Lockett used an iterative numerical procedure to obtain the maximum load on a smooth conical indenter. He accounted for the lip of material formed by the process of indentation, and his solution allowed self-similarity of the mechanism geometry to be preserved under continued penetration. The calculations began with the case of a flat punch (as considered by Shield, 1955) which can be regarded as a cone of apex angle $\beta = 180°$. For this case, Lockett found his solution agreed closely with that previously obtained by Shield, giving an average pressure on the punch of $5.68k$ (in fact, it is now known that the earlier solution was the more accurate). Lockett went on to consider cones of apex angle β equal to 160°, 140°, 120° and 105°, but found that he was unable to obtain solutions for cones sharper than this. Attempts to do so foundered on the fact that the included angle of the fan zone of the characteristic mesh (originating from point C in Figure 2.2) became equal to zero for $\beta = 105°$, and would thereafter be predicted to be negative if the same procedure was followed.

Since the work of Lockett (1963), investigators in this field have generally assumed a

Figure 2.3: Characteristic meshes for $\beta = 60°$, from Koumoto and Houlsby (2001). In the left half of the figure, heave of the surface has been neglected, while a straight inclined profile has been assumed for the mesh on the right. The example is for a cone of intermediate roughness

shape for the lip of displaced material, rather than allowing this to be determined by the condition of self-similarity. Such an approach was used by Houlsby (1982), who first used the method of characteristics to analyse the case of incipient indentation of an existing conical hole in the surface of a semi-infinite block (as shown in the left-hand portion of Figure 2.2). He then went on to account approximately for the effect of the lip formation, by assuming the deformed surface (line BC in Figure 2.2) to take the form of a straight line. This assumption, together with the fact that the volume of material in the lip ABC should be equal to the volume introduced by the cone OAD, makes it possible to proceed in a relatively straightforward manner: the difficulty of dealing with an initially unknown surface profile is removed, though iteration remains necessary to find the extent of the plastically deforming region such that the outermost characteristic intersects the cone tip. Of course, the solution obtained in this way will not satisfy the condition of self-similarity as further indentation occurs. The use of the true curved surface profile would give a larger area of contact between the cone and clay, and would be expected to give a slightly higher bearing capacity (Houlsby, 1982).

Koumoto and Houlsby (2001) re-present the data of Houlsby (1982), together with the results of additional calculations. Typical examples of the meshes of characteristics used in this work are shown in Figure 2.3, for the case when $\beta = 60°$. The left-hand portion of this figure shows the mesh used when heave of the soil surface is neglected; the right-hand portion shows the mesh when an approximate straight inclined surface has been used.

Figure 2.4 shows the theoretical variation of two bearing capacity factors, designated N_c and N_{ch}, with cone apex angle β as given by Koumoto and Houlsby (2001). N_c relates to the bearing capacity of a "wished-in-place" cone when surface heave is not accounted for, and

Figure 2.4: Bearing capacity factors for smooth and rough cones of varying apex angle β, from Koumoto and Houlsby (2001)

N_{ch} relates to the value obtained when the approximate straight surface profile is assumed. In the first case, the bearing capacity factor is defined such that the load Q on the cone at failure is given by

$$Q = N_{\mathrm{c}} s_{\mathrm{u}} A = N_{\mathrm{c}} s_{\mathrm{u}} \pi R^2 = N_{\mathrm{c}} s_{\mathrm{u}} \pi \tan^2 (\beta/2)\, d^2 \tag{2.1}$$

where R is the radius of the cone at the level of the soil surface, and d is the depth of indentation. In the case of N_{ch} an expression similar to Equation 2.1 must be used, with N_{c} simply being replaced by N_{ch}. The correct value of R to use in this case is the cone radius at the level of the original soil surface, that is the line OA in Figure 2.2.

It is clear from Figure 2.4 that the influence of heave is reduced for both smooth and rough cones as the apex angle β is reduced. For example, consider a smooth cone: when $\beta = 30°$, the effect of accounting (approximately) for heave is to enhance the bearing capacity by only around 8 %; when $\beta = 150°$ the enhancement is almost 49 %.

The solutions of Koumoto and Houlsby (2001) have not been formally established as exact, even for the approximate geometry for which they are valid, though they do agree with the exact result of Shield (1955) for a flat punch. The extensibility of the stress field has not been established, nor have associated upper bounds been calculated. Note, however, that Houlsby (1982) did check the extensibility of the stress field for one case, ignoring heave and assuming a rough, rigid-sided cup around the sample. Houlsby and Wroth (1982) determined the displacement field for an example cone penetration problem, but did not perform the upper bound calculation.

2.1.3 Finite element analysis

As seen in Section 2.1.2, the method of characteristics has allowed various investigators to progress towards theoretical models for the physical process involved in the fall cone test. There are, however, certain limitations on the solutions obtained by this method, the most serious being that they all pertain to a rigid–perfectly plastic Tresca material. Unfortunately solutions obtained by the method of characteristics cannot readily be generalized to account for more complex material behaviour. For example, we might seek to know the effect of introducing a finite elastic shear modulus, strain softening (or hardening), or a dependence of shear strength on the rate of shear strain. In addition, some authors have suggested that the method of characteristics falls short of adequately describing the extent of the plastic zones in indentation or penetration problems (Bhattacharya and Nix, 1991).

Even within the constraints of the assumed rigid–plastic material properties, none of the method of characteristics solutions so far obtained can be regarded as entirely definitive. In particular, the treatment of the lip of displaced material has meant that even the most recent work (Koumoto and Houlsby, 2001) fails to meet the need for self-similarity under continued indentation. Recall that the work of Lockett (1963) achieved this for some cases, but failed to yield results for cones of apex angle $\beta < 105°$. The questions of stress field extensibility and finding identical upper bounds remain as barriers to establishing most of the solutions as exact.

The finite element method is currently the most widely-used of the numerical methods adopted to solve boundary value problems in engineering. An abundance of work has been published on finite element modelling of indentation tests – an extensive bibliography can be found in Mackerle (1999). Much of this literature focuses on issues which are of little relevance to the indentation testing of soils: for instance, the reliability of micro- and nano-scale indentation tests on metals, and the use of indentation to investigate surface coatings and films. Two particularly relevant studies will however be discussed here.

Bhattacharya and Nix (1991) analysed the problem of incipient indentation of a cone in a conical hole, using an elastic–perfectly plastic von Mises model for the indented material. They were particularly concerned to study the development of the plastic zone around a conical indenter for a range of values of Young's modulus E and yield stress σ_{y}. They also sought to compare the shape and extent of this zone with the predictions of the method of characteristics and the hemispherical cavity expansion model used by Marsh (1964) to study

Figure 2.5: Comparison of yielded zones for various E/σ_y ratios, with indenter angle of 136°, from Bhattacharya and Nix (1991)

pyramidal indentation (after Hill, 1950), later adapted to cones by Johnson (1970).

The cavity expansion model involves assuming that the process of indentation can be modelled by the expansion, under an internal hydrostatic pressure, of a hemispherical cavity in the elastic–plastic solid. The model has its limitations, however: according to Bhattacharya and Nix (1991) it cannot reliably be applied to materials with high rigidity index E/σ_y, nor is it well suited to indenters with a small apex angle. A key conclusion of Bhattacharya and Nix was that the shape and extent of the yielded zone for an elastic–plastic (von Mises) solid under a conical indenter is a strong function of the rigidity index. Figure 2.5 shows some typical results. The shapes of the plastic zones were always found to differ from those assumed in the method of characteristics,[1] extending deeper into the material and to greater distances from the indenter; they were not found to be modelled well by the cavity expansion model either.

Larsson (2001) also used an elastic–plastic von Mises material model. In this study, the values for E and σ_y were selected in order to allow the approach to rigid-plastic conditions to be studied. Particular attention was given to the factors affecting the deformation of the free surface around the indenter (line BC in Figure 2.2). This deformation was characterized by the parameter c, given by the equation

$$c = r_\mathrm{C}/r_\mathrm{A} \tag{2.2}$$

[1] Of course, when the stress field is extended in the method of characteristics a bigger plastic zone may obtained, but the stresses outside the deforming zone are not unique.

where r_A and r_C are respectively the radial coordinates of the points A and C, as defined in Figure 2.2. It can be seen that $c > 1$ corresponds to the formation of a lip of displaced material, while $c < 1$ indicates sinking in of the surrounding surface; c^2 gives the ratio of the predicted contact area to that obtained by assuming a horizontal surface profile. Larsson states that his numerical results suggest the variation of c to be solely a function of a rigidity parameter Γ, where

$$\Gamma = \frac{E \tan \frac{\pi - \beta}{2}}{(1 - \nu^2)\, \sigma_y}\,. \tag{2.3}$$

Here E, σ_y and ν are respectively the Young's modulus, axial yield stress and Poisson's ratio of the indented material, and β is the apex angle of the conical indenter. So, for a given geometry of indenter the formation of a lip is governed by the properties of the indented material, as indicated in Figure 2.6, which shows the variation of c^2 with $\log \Gamma$.

If we were to assume the material in Larsson's analyses to be incompressible ($\nu = 0.5$), then Γ would simply be the rigidity index multiplied by a constant factor dependent on the cone angle β. Unfortunately, the values of Poisson's ratio ν used in the analyses are not given – Larsson states only that "many different combinations of yield stress, Young's modulus and Poisson's ratio, were investigated"; only the variation of the results with Γ is shown. It is unlikely that the approach to incompressibility ($\nu \to 0.5$) was investigated, since the Vickers and Berkovich indenters studied are usually used with metals (with μ typically in the range 0.3–0.4) and ceramics (for which ν is smaller still).

Both Larsson (2001) and Bhattacharya and Nix (1991) used the commercial finite element program Abaqus (Simulia, 2007) to implement their models.[2] In each study, a two-dimensional finite element mesh was employed, exploiting the axisymmetric nature of the cone indentation problem to reduce computation time. Four-noded quadrilateral axisymmetric elements were used in both studies, in preference to higher-order elements. Bhattacharya and Nix state that this choice was justified by the resulting substantial reduction in the computational burden, and cite an earlier study (Bhattacharya and Nix, 1988) which showed the low order elements still gave good agreement with experimental results when a sufficiently fine mesh was used. Larsson (2001) used hybrid-type elements (where the pressure stress in each element is interpolated independently of the other solution variables – see Simulia,

[2]Unfortunately neither Larsson (2001) nor Bhattacharya and Nix (1991) state clearly whether the implicit or explicit solver provided by the Abaqus product suite was used. It appears that Bhattacharya and Nix at least must have used the implicit version (Abaqus/Standard), since they refer to the use of contact elements which are not available in Abaqus/Explicit.

Figure 2.6: Influence of rigidity parameter Γ on shape of indentation, as characterized by c. The variables Γ and c are defined in Equations 2.2 and 2.3. From Larsson (2001)

2007) to avoid problems when modelling near-incompressible materials ($\nu \approx 0.5$). Larsson analysed indentation of an initially flat horizontal surface, and presumably there must have been considerable deformation of the mesh as the cone penetrated. However, no mention is made of any adaptive meshing algorithm being used to alleviate this.

2.1.4 Influence of soil self-weight

The expressions for the force on a conical indenter given in Sections 1.1.2 and 2.1.2 assume that the resistance to cone penetration is dominated by the force needed to cause plastic deformation, and neglect any contribution from the self-weight of the indented material. Houlsby (1982) showed that the additional force on the cone due to the weight of displaced material is

$$P = \pi \gamma d^3 \tan^2 \left(\beta/2\right)/3 \tag{2.4}$$

where γ is the unit weight of the indented material. Equation 2.4 slightly underestimates the influence of soil self-weight since it does not include the weight of the lip of displaced material around the cone. The effect of this additional surcharge would be small by comparison, since the lip makes up only a small proportion of the volume of soil in the deforming region.

The total force on the cone is equal to $Q+P$, where Q is the force required to bring about plastic deformation of the indented material and is given by Equation 1.2, and P is the force due to the self-weight of the indented material and is given by Equation 2.4. Houlsby (1982) showed that the contribution of soil self-weight to the cone resistance would be small – for an 80 g, 30 deg cone pushed to a depth $h = 20$mm in a typical soil, it would be around 1.5 % of the weight of the cone. Since 20mm is a relatively large penetration depth (the maximum recommended by Geonor, 2005a) and the value of P depends on h^3 (whereas Q varies with h^2), it is apparent that the overall effect of soil self-weight in a fall-cone test is small.

2.1.5 Dynamic analysis

The analyses discussed so far consider the interaction of an indenter with the indented material under quasi-static conditions. The results allow the reaction on a fall-cone to be predicted for a given depth of penetration into the soil, if the response of the material is assumed to be simply rigid–plastic. For a cone indenting a soil sample, assuming quasi-static conditions, we would expect force equilibrium to be reached once the resisting force Q (obtained from Equation 2.1) became equal to the force on the indenter. Using the notation of Koumoto and Houlsby (2001), this situation will occur when the cone tip has penetrated to $z = h_{\mathrm{s}}$, where z is the vertical coordinate defined in Figure 2.2 and the subscript 's' denotes 'static'. In practice, however, the cone is allowed to fall freely under its own weight, and the dynamics of the falling cone must therefore be considered. Houlsby (1982) performed such an analysis; by integrating the cone's equation of motion with appropriate initial conditions (when $t = 0$, the cone's penetration depth and velocity are also zero), it was found that the cone would come to rest with its tip at $z = h_{\mathrm{s}}\sqrt{3}$, regardless of its apex angle.

A further complication arises in a dynamic analysis if consideration is given to the possibility that soil strength may be a function of strain rate; this will be discussed in Section 2.2.7.

2.2 Influence of strain rate on undrained shear strength of clays

It is well known that the undrained shear strength of many clays increases with faster rates of deformation. Even a relatively modest variation in shear strength can have practical significance given the large range of strain rates encountered in laboratory and in-situ tests, and under typical operating conditions for offshore foundations. It is easy to conceive of circumstances in which rates of loading could vary over eight orders of magnitude or more (Randolph, 2004). Various authors have attempted to provide equations to model this effect, and to justify their models by theory and experiment. Their work is reviewed in this section.

2.2.1 Rate process theory: activation energy and frequency

The flow model of Eyring provides a physical basis for the analysis of the rate-dependent nature of many processes. Early development of the theory may be found in literature on physical chemistry (e.g. Eyring, 1936; Glasstone et al., 1941). The theory has been applied to many processes involving the time-dependent rearrangement of matter, and has been used in studies of the mechanics of ceramics, polymers, textiles, asphalt and concrete. It has also been applied to, for example, chemical reaction rates and the viscous flow of fluids. Early work on the application of the theory to problems in soil mechanics includes that of Murayama and Shibata (1958) and Mitchell (1964). An extensive review of the application of rate process theory to soil behaviour is given by Mitchell (1993).

The basic concept underlying rate theory is that *flow units*, which may be e.g. clay particles, must possess a certain minimum energy if relative motion is to occur. This quantity of energy, generally termed the activation energy ΔF, is required in order that the energy barriers between adjacent equilibrium positions may be overcome. The situation is shown schematically in Figure 2.7a.

The required activation energy (ΔF) depends on the type of process and the material involved. The range of reported values for applications involving clays is approximately 96–393 kJ/mole of flow units (Mitchell, 1993), with these extreme values corresponding to remoulded high water-content samples and frozen soils respectively. For comparison, values in the range 12–17 kJ/mole have been suggested for water.

The energy for displacement of a flow unit may derive either from its thermal energy or from the action of some external agent. In our problem of the strength of a clay sample, this will be a shear stress. The mean thermal energy of a flow unit is kT, where k is Boltzmann's constant ($1.38 \times 10^{-23}\,\mathrm{J\,K^{-1}}$), and T is the absolute temperature. The actual energies of flow units will be distributed about this value according to a Boltzmann distribution (see

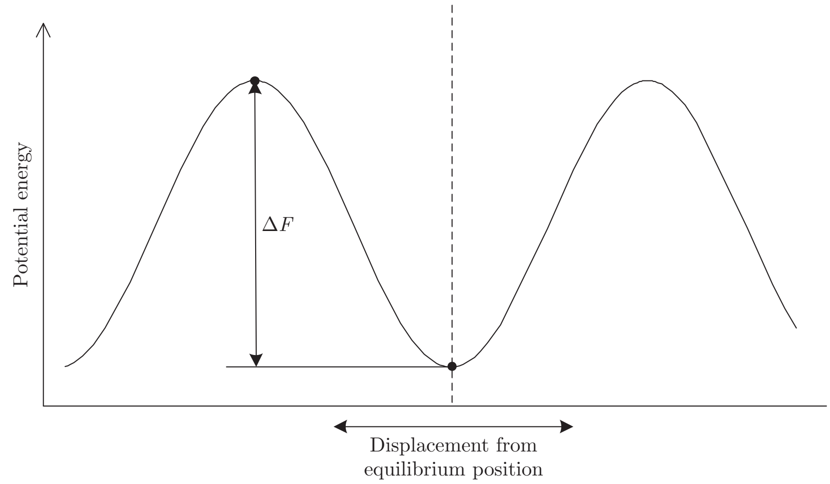

(a) Energy barriers in absence of shear force

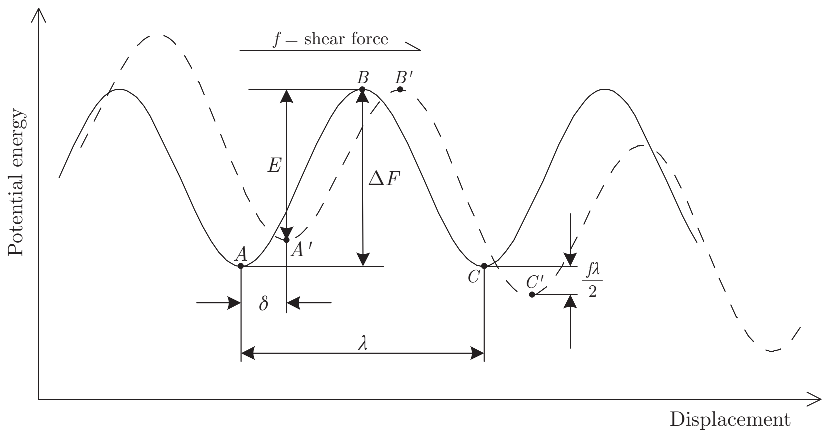

(b) Energy barriers with shear force present (dashed line), and without (solid line)

Figure 2.7: Some notation used in rate process theory, after Mitchell (1993)

e.g. Blatt, 1992). It can be shown that the frequency of activation will then be

$$v = \frac{kT}{h} \exp\left(\frac{-\Delta F}{NkT}\right) \tag{2.5}$$

With no shear stress applied, the height of the potential barrier – and therefore the frequency with which barrier crossings occur – is equal in all directions. Activations then have no observable effect so long as the temperature is low enough for the material to remain in the solid state. This is the situation depicted in Figure 2.7a.

If a shear stress is applied, the barrier heights will be affected (as shown schematically in Figure 2.7b), so that barrier crossings do not occur at the same frequency in all directions. Equation 2.5 can then be used to find the frequency of activations in each direction, and the shear strain rate will be proportional to the net activation frequency in the direction of interest. This is shown in Equation 2.6:

$$\dot{\varepsilon} = X\left(\vec{v} - \overleftarrow{v}\right) = 2X\frac{kT}{h}\exp\left(-\frac{\Delta F}{NkT}\right)\sinh\left(\frac{\tau\lambda}{2SkT}\right). \tag{2.6}$$

where the parameter X may be time and structure dependent. The force f on a flow unit has here been expressed as τ/S, where τ is the shear stress and S the number of flow units per unit area. A derivation is provided by Mitchell (1993).

Equation 2.6 can be used to derive an expression for shearing resistance, indicating that (all other factors being equal) shearing resistance will be proportional to the inverse hyperbolic sine of the strain rate. Mitchell suggests replacing the $\sinh(\cdots)$ term in Equation 2.6 by an exponential function, stating this to be a good approximation in most solid deformation problems (specifically, for $\dfrac{\tau\lambda}{2SkT} > 1$). He therefore concludes that shearing resistance should increase linearly with the logarithm of strain rate.

Note that Equation 2.6 also predicts that strength should depend on temperature (decreased strength is predicted at higher temperature, Mitchell, 1964), and there is some experimental evidence to support this conclusion. The temperature effect is not expected to be significant here, though the possible influence of localized heating due to frictional dissipation should not be discounted and has been suggested as a factor in some landslides, for example (Vardoulakis, 2000).

2.2.2 Empirical flow laws

Various expressions have been used to propose empirical relationships between strength and strain rate. Probably the most widely used expression for the strain rate dependence of undrained shear strength s_u is

$$\frac{s_\mathrm{u}}{s_\mathrm{u0}} = 1 + \mu\log_{10}\left(\frac{\dot{\gamma}}{\dot{\gamma}_0}\right) \tag{2.7}$$

which is essentially the Johnson–Cook formula (Johnson and Cook, 1983) in the notation of soil mechanics. Here μ is the rate of increase of shear strength per decade, and s_u0 is a reference shear strength measured at a shear strain rate of $\dot{\gamma}_0$ (which might be, for instance, the strain rate used in a typical triaxial test). This is the form of expression used by, for instance, Koumoto and Houlsby (2001). If Equation 2.7 is used with $\mu = 0.1$, the relationship obtained corresponds to the common rule of thumb that s_u increases by roughly one tenth for every tenfold increase in strain rate. This form of rate dependence was observed by Ladd and Foott (1974) and Kulhawy and Mayne (1990), among others. The expression is also consistent with the simplified logarithmic form of the expression proposed by Mitchell (1993), as described in the previous section.

Equation 2.7 gives rise to certain difficulties in practice. As the strain rate decreases, the predicted values of s_u become very small and eventually negative. This problem can be avoided by applying a minimum strength of s_u0 at strain rates below the reference rate $\dot\gamma_0$. Equation 2.7 then becomes

$$\frac{s_\mathrm{u}}{s_\mathrm{u0}} = 1 + \mu \log_{10}\left(\frac{\max\left(\dot\gamma, \dot\gamma_0\right)}{\dot\gamma_0}\right). \tag{2.8}$$

An alternative expression involving the inverse hyperbolic sine function may also be used:

$$\frac{s_\mathrm{u}}{s_\mathrm{u0}} = 1 + \mu' \sinh^{-1}\left(\frac{\dot\gamma}{\dot\gamma_0}\right). \tag{2.9}$$

As noted by Randolph (2004), if $\mu' = \mu/\ln(10)$ then this expression closely approximates the behaviour given by Equation 2.8 at high strain rate. When $\dot\gamma < \dot\gamma_0$ and $\mu \approx 0.1$, the strain rate effect decays rapidly to give a minimum strength roughly 4% lower than the reference value when $\dot\gamma$ is less than about $0.1\dot\gamma_0$.

Figure 2.8 shows the variation of strength with strain rate that is obtained with each of Equations 2.7, 2.8 and 2.9 when $\mu = 0.1$. Parameters have been chosen such that the strengths given by Equations 2.9 and 2.8 agree at the reference strain rate $\dot\gamma$. Alternatively, agreement could have been obtained at low strain rate ($\dot\gamma \to 0$).

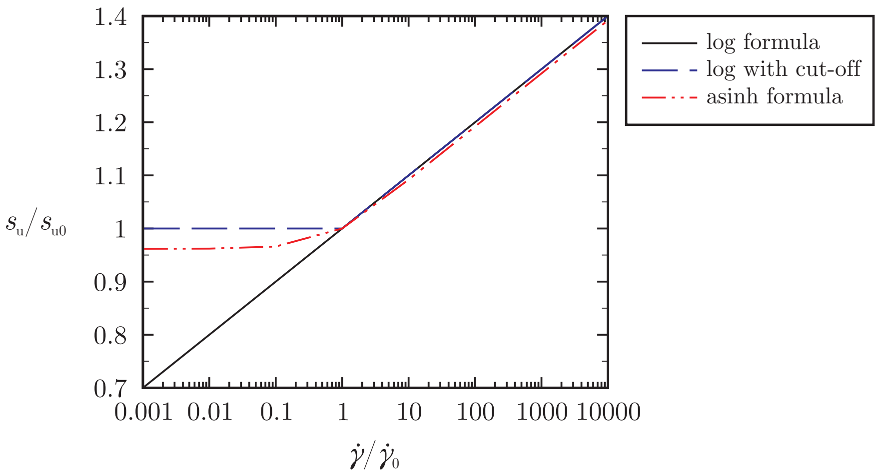

Figure 2.8: Variation of strength with strain rate given by Equations 2.7, 2.8 and 2.9

The Cowper-Symonds power law formula (Cowper and Symonds, 1957) is in common use for metals at high strain rates (but not for soils). In terms of axial stresses and strain rates the expression is

$$\frac{\sigma_0'}{\sigma_0} = 1 + \left(\frac{\dot{\varepsilon}}{D}\right)^{1/q} \tag{2.10}$$

where σ_0' is the dynamic axial yield stress at a plastic strain rate $\dot{\varepsilon}$ and σ_0 is the yield stress under quasi-static conditions; D and q are experimentally determined material constants. Alternatively, this may be expressed in the notation used above:

$$\frac{s_{\mathrm{u}}}{s_{\mathrm{u0}}} = 1 + \left(\frac{\dot{\gamma}}{D'}\right)^{1/q'} . \tag{2.11}$$

2.2.3 Constitutive laws with inherent rate dependence

Expressions like those described in Section 2.2.2 are widely used in modelling rate-dependent strength in soils. For examples, see the recent work by Einav and Randolph (2005) and by Randolph (2004). They model rate effects by scaling yield stress with strain rate, while still using this varying yield stress in a simple, originally rate-independent yield criterion. An alternative approach is to adopt a constitutive law in which strain rate is more fully integrated into the relevant equations. Such a constitutive law is often termed *viscoplastic*, since the rate dependence may be thought of as similar to that of viscous flow in liquids.

In viscoplasticity, the key change is that load points outside the yield surface are admissible. This is why some formulations are referred to as *overstress* models. The overstress concept was introduced by Perzyna (1963), and involves the assumption that the yield stress may be enhanced at nonzero strain rates by an additional component linked to viscous effects in the material. Figure 2.9 (Dunne and Petrinic, 2005) shows strain–time and stress–strain curves for a rigid–viscoplastic material with no strain hardening, at a range of strain rates. While a time-independent perfectly plastic material would deform at the yield stress σ_{y}, this value can be exceeded in viscoplasticity. The difference between σ_{y} and the stress that is actually achieved is the viscous overstress σ_{v}. The overstress is sometimes represented as a simple power law function of the plastic strain rate (if strains are sufficiently large the elastic strain component may be neglected, and plastic strain rate is essentially equal to total strain rate). In the multidimensional case an effective strain rate, $\dot{\bar{\varepsilon}}$, is adopted, therefore

$$\sigma = \sigma_{\mathrm{y}} + K\dot{\bar{\varepsilon}}^{m} \tag{2.12}$$

(a) Applied strain (b) Rate-dependent stress response

Figure 2.9: Rate-dependent yield strength in a viscoplastic material, from Dunne and Petrinic (2005)

where m is the strain rate sensitivity factor. Equation 2.12 is of similar form to Equation 2.11; expressions similar to Equations 2.7 and 2.9 could be obtained by adopting alternative expressions for the variation of the viscous overstress with the strain rate.

When the overstress is a linear function of strain rate (i.e. when the strain rate sensitivity factor m is unity), Equation 2.12 reduces to the Bingham plasticity model (Bingham, 1922). A Bingham plastic is essentially equivalent to a Newtonian fluid that requires some minimum shear stress to initiate flow. This model is widely used for materials such as drilling muds (used for lubrication in borehole drilling) and wet concrete.

An alternative approach in viscoplasticity involves the derivation of constitutive relations based on thermodynamic considerations (see e.g. Jirásek and Bažant, 2001; Houlsby and Puzrin, 2006). Such an approach was taken, for example, by Houlsby and Puzrin (2002), who built on earlier work on rate-independent materials to show that the entire constitutive response of a viscoplastic material can be derived from two scalar potential functions: an energy potential and a force or flow potential. The approach was applied to both linear (Bingham) and nonlinear viscoplasticity, and was also shown to be consistent with the idea that rate-dependent processes may be thermally activated, as discussed in Section 2.2.1.

2.2.4 Experimental evidence of rate-dependent behaviour

Several studies have attempted to quantify the strain rate dependence of the undrained shear strength of clays by laboratory testing. Kulhawy and Mayne (1990) compiled a large dataset from CIUC triaxial tests on 26 clays. Their results were reproduced by Chen and Mayne (1994) and also by Mitchell (1993). Figure 2.10 shows their experimental data, together with the relationship of Equation 2.7 with $\mu = 0.1$ (note that the strain rate shown is the axial strain rate $\dot{\varepsilon}_\mathrm{a}$; in an undrained triaxial test $\dot{\varepsilon}_\mathrm{a}$ is equal to two thirds of the maximum shear

Figure 2.10: Effect of strain rate on undrained strength; data from CIUC triaxial tests on 26 clays by Kulhawy and Mayne (1990). Reproduced from Mitchell (1993)

strain rate $\dot{\gamma}$). It is clear that, for the soil samples tested, across the range of strain rates considered, the proposed relationship generally gives a good fit to the available experimental data.

Koumoto and Houlsby (2001) reproduced triaxial test data from three earlier studies (Berre and Bjerrum, 1973; Lefebvre and LeBoeuf, 1987; Vaid and Campanella, 1977), which gave a total of 15 data points spanning a range of shear strain rates from approximately 1×10^{-2} %/hour to 6×10^{4} %/hour. Koumoto and Houlsby showed that Equation 2.7 gave a good fit to this data.

Sheahan et al. (1996) studied the rate dependence of the shear strength of a particular saturated clay at various overconsolidation ratios (OCRs; values used were 1, 2, 4, and 8). The results, reproduced in Figure 2.11, do not support the idea of a linear relationship between strength and the logarithm of strain rate. The parenthetical values given in the figure ($\rho_{0.5}$) are equivalent to the coefficients (μ) to be used in Equation 2.7 for a reference axial strain rate $\dot{\varepsilon}_{\mathrm{a}} = 0.5$ %/hour. Note, however, that percentage values are given in the figure. Though the data presented are limited, it appears that the parameter μ in Equation 2.7 is itself a function of strain rate. This type of behaviour could perhaps be better modelled by a power law expression similar to Equation 2.11.

The results of Figure 2.11 also suggest the existence of a threshold strain rate below

Figure 2.11: Normalized undrained shear strength versus strain rate, from CK_0UC triaxial tests on clay at various OCRs, from Sheahan et al. (1996)

which the rate effect disappears, at least for heavily overconsolidated clays. Even for clays with low OCR the authors note that "a threshold strain rate. . . may well exist at strain rates lower than those used in the test program."

Koumoto and Houlsby (2001) estimated the shear strain rate in a fall-cone test to be approximately 1×10^6 %/hour with a 30° cone or 2.5×10^6 %/hour with a 60° cone (their method is discussed in Section 2.2.7). Since the results presented so far in this section are from triaxial tests performed at no more than 10^4 %/hour, applying them to fall cone tests would involve substantial extrapolation (over at least two orders of magnitude). Other researchers have attempted to investigate the strength of clays and other soils at higher rates than can be achieved in a standard triaxial test.

Cheng (1976) performed tests on hollow cylindrical specimens of Mississippi Buckshot clay, which were held in a modified triaxial cell. High rates of deformation were achieved by first accelerating a large flywheel above the specimen, then using a clutch to engage the flywheel with a shaft attached to the top of the specimen. The water content w of the specimens was between 30 and 34 % (compare the material's liquid and plastic limits of 61 % and 28 %, respectively).

The results published by Cheng are shown in Figure 2.12. The strain rates are shown in terms of the angular velocity of the platen. Consideration of the geometry of the samples shows 1 radian/second to be equivalent to $\dot{\gamma} = 6.7 \times 10^6$ %/hour. The author fitted expo-

Figure 2.12: Relationship between undrained strength and strain rate, from Cheng (1981)

nential functions to the data, and suggested that the results show undrained strength to be bounded by an upper limit that he calls the ultimate dynamic strength. It would be more conventional to show these results with a logarithmic scale for the strain rate, which might well have revealed an underlying trend of a similar form to that shown in Figure 2.10.

Carroll (1988) used a piston driven by compressed nitrogen to apply rapid loading to soil samples. The equipment used (dubbed the fast triaxial shear device or FTRXD) proved to be capable of loading small specimens (1.9 cm in diameter by 3.8 cm high) to nominal axial strains of 15 % in tests lasting as little as 2 ms. The maximum strain rates were therefore of the order of 2.7×10^7 %/hour. The work confirmed the existence of a link between strength and strain rate for the clayey sand studied. However, interpretation of FTRXD results was complicated by dynamic effects. The author noted that load cell readings were affected, and that "system dynamics may overwhelm a weak specimen in some circumstances." A further study by the same author (Carroll, 1989) went on to consider the possibility that results were also significantly influenced by longitudinal inertia in the specimen.

Further evidence of the rate dependence of undrained strength is presented by Graham et al. (1983). Results from tests of various types (triaxial extension and compression, direct simple shear) performed on four different clays are shown to follow trends of the form given by Equation 2.7. The authors also review several studies showing an influence of strain rate on the results of oedometer tests, leading to the conclusion that the changes in undrained strength at different strain rates are a consequence of a more general rate-dependent expansion of the yield envelope as strain rates increase. Figure 2.13 shows the influence of time effects on the behaviour of a particular clay, from undrained and drained triaxial extension

Figure 2.13: Effect of strain rate on yield envelope, Belfast clay. From Graham et al. (1983)

and compression tests and oedometer results.

Finally, Graham et al. (1983) re-analyse results (originally from Lew, 1981) of various triaxial tests on Winnipeg clay. These are shown in Figure 2.14. They conclude that "strain rate effects observed in undrained triaxial tests and oedometer tests are specific examples of a more general time-dependent yielding of the clay fabric," going on to suggest that the data, though limited, support the hypothesis that yield envelopes associated with different strain rates are homothetic (of similar shape, but scaled).

2.2.5 Discontinuities and shear bands in rate-dependent media

Many of the proposed solutions to problems of plastic collapse in geotechnical engineering involve localized failure surfaces across which step changes in velocity occur. For example, the well-known classical mechanisms proposed by Prandtl and by Hill for surface indentation in plane strain both predict the presence of a discontinuity surface as the outer boundary of the deforming region. The idealisation of regions of high strain rate as failure surfaces of zero thickness may be reasonable for soils whose strength remains constant with strain rate, and is certainly valid for soils exhibiting significant strain-softening (Vardoulakis and

Figure 2.14: Effect of strain rate on yield envelope, Winnipeg clay. From Graham et al. (1983)

Graf, 1985). However, as discussed here it is often the case that real geomaterials increase in strength at elevated strain rates. In such materials, the work rate involved in deformation will be minimized if a velocity discontinuity is spread over a diffuse region of some finite thickness.

Randolph (2004) discusses this issue, and shows that (for strain rate-dependent strengths represented by equations 2.7 and 2.9) it is possible to derive an expression for the optimum thickness of a curved (but not a straight) shear band. Reducing the shear band thickness below this optimum value will increase dissipation because the higher strain rate increases soil strength, while increasing shear band thickness from the optimum increases the volume of deforming soil.

2.2.6 Rate effects in non-geomaterials

Though the materials encountered in geotechnical engineering present certain unique combinations of challenges, they are not alone in displaying varying yield strength with strain rate. In fact, much literature is available on such effects in a wide range of materials, particularly metals and polymers. Given the very high strain rates involved in some of the manufacturing processes to which such materials are subjected, this is only to be expected.

Processes involving the forging or cutting of metals involve very rapid deformation, and given the ubiquity of these processes it is unsurprising that any variation in strength with strain rate should have become the focus of much attention. A review of rate effects, focusing on metals, can be found in Jones (1997). Mild steel is one of the most widely-used metals,

Figure 2.15: Experimental variation of dynamic uniaxial lower yield stress of mild steel with axial strain-rate, with the curve of Equation 2.10 ($D = 40.4\,\mathrm{s}^{-1}$ and $q = 5$). From Symonds (1967) as reproduced by Jones (1997)

and Figure 2.15 summarizes its yield behaviour as strain rate varies. As is usual outside soil mechanics, the uniaxial yield stress is used. Also shown in the figure is the curve given by the empirical Cowper-Symonds constitutive law (Equation 2.10). The expression fits the given data fairly well, though there is a large degree of scatter. Jones suggests that the scatter relates to the range of steels tested and the varying details of the test procedures.

Other metals also display variations in yield strength with strain rate. Jones (1997) also presents data showing such phenomena for various alloys of titanium and aluminium. He suggests that, although some authors report no variation in the strength of aluminium with strain rate, this may simply be because they failed to vary the strain rate across a sufficiently wide range – the variation is not nearly so marked for aluminium and its alloys as is the case for most steels. Low and Fields (1991) investigated the mechanical behaviour of solder at various strain rates and found it could be modelled well by an expression having the form of Equation 2.7.

Polymers also show a strong dependence of yield stress on strain rate. The flow model of Eyring (1936), as described in Section 2.2.1, provides a basis for successful analyses (McCrum et al., 1997). As noted earlier, the Eyring model predicts a reduction in strength with increased temperature. Though this is not generally taken into account in soil mechanics it is of great importance in polymer engineering, as many common manufacturing processes take place at elevated temperatures. Given the very different structures of clays and polymers it might be surprising that the same model can be applied to materials of both types. However, Figure 2.16 shows some experimental results, from which it can be seen that this material

Figure 2.16: Experimental variation of axial yield stress with axial strain rate for polycarbonate at various temperatures. From McCrum et al. (1997), after Bauwens-Crowet et al. (1969)

obeys the central predictions of the Eyring model well: at constant temperature there is a linear increase in strength with the logarithm of strain rate, and an increase in temperature gives reduced strength. McCrum et al. (1997) point out that the log-linear relationship between strength and strain rate will hold only if the flow process is controlled by a unique mechanism. In some materials (at least in some polymers) one mechanism may dominate up to a certain temperature, before another takes over.

2.2.7 Rate effects in soil tests

Koumoto and Houlsby (2001) gave an approximate treatment of the influence of rate-dependent strength in the fall cone test. They estimated the overall shear strain undergone by the soil from the change of an angle, originally equal to $\frac{\pi}{4}$, to $\left(\frac{\pi}{4}+\delta\right)$ as the cone penetrates the soil (δ is the angle ABC in Figure 2.2 – recall that Koumoto and Houlsby assumed the deformed surface BC to be straight). Therefore, the average strain in the deforming soil during cone penetration is assumed to be $\gamma \approx 2\delta$. As the authors acknowledge, this is "…no better than an approximate estimate of the order of magnitude…" of the strain undergone by the soil; in reality there will be a complex variation in strain across the deformed region. The authors then estimate the rate of shear strain as $\dot{\gamma} \approx (2\delta/t)$, where t is the total time taken for the cone to penetrate to full depth. If a relationship between strain rate and shear strength is available (as in e.g. Equations 2.7 and 2.9) then the cone penetration depth can be predicted by using a dynamic analysis similar to that of Houlsby (1982), discussed in Section 2.1.5, but taking s_{ud} ($> s_{\mathrm{u}}$) as the undrained strength under dynamic conditions.

By an extension of the dynamic analysis of a fall-cone in rate-independent material, Koumoto and Houlsby (2001) predicted that a fall-cone in material with rate-dependent strength would come to rest at $z = h$ where $h = h_{\mathrm{s}}\sqrt{3\zeta}$, where $\zeta = s_{\mathrm{u0}}/s_{\mathrm{ud}}$ is the ratio of a clay's undrained strength s_{u0} at a reference strain rate to the strength s_{ud} in the fall-cone test (the subscript "d" denotes dynamic); h_{s} is the quasi-static penetration depth defined in Section 2.1.5. A similar rate-independent analysis by the same authors gave the final cone penetration depth as $h = h_{\mathrm{s}}\sqrt{3}$, so the influence of strain rate dependence on penetration depth may be approximately quantified by $\sqrt{\zeta}$. Koumoto and Houlsby's estimated strain rate and the assumed rate dependence equation gave a value of $\zeta \approx 0.74$ for the 30° cone and 0.73 for 60° or 90° cones.

As an alternative to regarding s_{ud} as the "average" dynamic strength exhibited by the rate-dependent material, it can also be thought of as the undrained strength of a rate-independent material which would result in the same fall-cone penetration h. It might appear that it would be more natural to define a ratio $s_{\mathrm{ud}}/s_{\mathrm{u0}}$ ($= \zeta^{-1}$), which would in general be greater than unity. However the notation $\zeta = s_{\mathrm{u0}}/s_{\mathrm{ud}}$ of Koumoto and Houlsby (2001), which will be adopted in this thesis, has the advantage that ζ is the correction factor that must be applied to the dynamic strength exhibited in a fall-cone test in order to give the "static" strength that is most often of interest to the engineer.

The value assigned to the parameter ζ is of great importance if theoretical or numerical analyses of cone indentation are to be used as the basis for interpreting fall-cone test results and obtaining values of undrained shear strength s_{u}. Since a quasi-static analysis shows the weight of the cone W to be related to h_{s} by $W = F s_{\mathrm{u0}} h_{\mathrm{s}}^2$, and the final dynamic penetration with a rate-dependent material is $h = h_{\mathrm{s}}\sqrt{3\zeta}$, values of ζ and N_{ch} or F can be combined to give the cone factor K defined in Section 1.1.2:

$$K = \frac{s_{\mathrm{u0}} h^2}{W} = \frac{3\zeta}{F} = \frac{3\zeta}{\pi N_{\mathrm{ch}} \tan^2(\beta/2)}. \tag{2.13}$$

If a value of K obtained in this way is used to determine a value of s_{u0} from a fall-cone test result (by the use of Equation 1.1), the resulting value of s_{u0} will be affected directly by the value of ζ that is used. Since K is directly proportional to ζ, an error of (for example) 10% in ζ will result in s_{u0} being incorrect by the same margin.

A brief attempt to assess the significance of rate-dependent strength in another practical test was made by Kulhawy and Mayne (1990). They considered the piezocone test and suggested that, for a 10 cm^2 cone (diameter 35.7 mm) penetrating at 20 mm/s, a strain rate of approximately 2×10^5 %/hour was appropriate.[3] By adopting the logarithmic rate dependence formula of Equation 2.7 with $\mu = 0.1$, the s_u value from the piezocone test was predicted to be 53 % higher than that which would be measured at a reference strain rate of 1 %/hour.

Less relevant to the cone indentation problem, but still of interest, is the recent work on rate effects in shear vane testing reported by Randolph (2004). The usual approach to analysis of this test is to assume the soil shears on a cylindrical surface surrounding the rotating vane. This surface is generally assumed to be of zero thickness. Randolph assumed the soil strength to be rate-dependent, obeying Equation 2.7 with $\mu = 0.1$. In such a soil, it was calculated that the torque required for rotation of a 65 mm diameter vane at 0.1°/s would be $T = 1.44T_0$, where T_0 is the torque if rate dependent strength is ignored. It was predicted that a finite shear band of thickness 2 mm would form, rather than a zero-thickness discontinuity. A more rigorous analysis, maintaining torsional equilibrium and using Equation 2.9 to represent rate dependence, gave similar results.

Einav and Randolph (2005) included the effect of rate-dependent strength in their analysis of the T-bar and ball penetrometers. Assuming the soil to obey Equation 2.7 with $\mu = 0.1$, the rate-dependent analysis of the smooth T-bar gave a penetration resistance 70 % greater than in an analysis ignoring rate effects. For the ball penetrometer, resistance when rate effects were accounted for was 51 % greater than when they were ignored.

The results of the previous studies reviewed here suggest that rate effects have a very significant influence on the results of tests to measure the undrained strengths of clays. In the specific case of the fall cone test, Koumoto and Houlsby (2001) predict that the assumed rate dependence will change cone penetration depths by approximately 15 %, but acknowledge this to be only an initial, approximate estimate.

[3] Unfortunately, the methodology used to derive this figure is not given.

Chapter 3

ELFEN analysis with rate-independent material

As described in Section 2.1.2, several attempts have been made to analyse the process of quasi-static cone indentation by the method of characteristics, with the aim of determining the value of the parameter

$$N_{\mathrm{ch}} = \frac{Q}{s_{\mathrm{u}} \pi R^2} \tag{3.1}$$

where Q is the force that must be applied to the cone for further indentation, R is its radius at the level of the undisturbed clay surface, s_{u} is the undrained strength of the clay, and the subscript "h" denotes "heave" and indicates that the value of N_{ch} takes account of the build-up of displaced material around the cone. Equivalently, the problem may be cast in terms of the parameter

$$F = \frac{Q}{s_{\mathrm{u}} d^2} = N_{\mathrm{ch}} \pi \tan^2\left(\frac{\beta}{2}\right) \tag{3.2}$$

where β is the angle of the cone and d the depth of the indentation. See also Chapter 1. Values of F or N_{ch} depend primarily on the cone angle β and adhesion factor α.

This chapter describes a series of analyses conducted using the finite element (FE) software ELFEN (Rockfield Software, 2005), with the primary aim of determining values of N_{ch}. The analyses cover a broad range of values of β and α. The entire indentation process is analysed, with the surface of the clay material initially undisturbed. The form of the displaced surface therefore emerges naturally from the analysis, rather than needing to be assumed *a priori* (as in Koumoto and Houlsby, 2001) or obtained by *ad hoc* trial-and-error iteration (as in Lockett, 1963). This is one of the primary advantages of tackling this problem using the finite element method rather than the method of characteristics.

It will be possible to compare the finite element solutions directly with those of Lockett (for large β). Since Lockett's results are likely to be exact (subject to the stress field being extensible outside the deforming region and to a matching upper bound being obtained), strong similarity between his solutions and those of the present analyses (in terms of the deformed geometry and the value of N_{ch}) will lend support to the validity of the FE analyses. Analyses for sharper cones may then be compared with the results of Koumoto and Houlsby, allowing the impact of their key assumption (that the surface profile is a straight line) to be assessed.

The analyses described in later chapters made use of the Abaqus/Explicit FE program (Simulia, 2007), together with a VUMAT material behaviour subroutine which provides the option of simulating rate-dependent strength. A subset of the ELFEN analyses presented in this chapter were repeated with Abaqus (without rate dependence) to verify the correct operation of the VUMAT. Comparisons of these results will be presented in Chapter 4.

3.1 Implicit and Explicit FE methods

Most of the solutions presented in this thesis were generated using the explicit FE method. In this chapter, the specific software used was ELFEN. There are important differences between explicit solvers and those using the more common implicit method.

Generally, any numerical method for the solution of time-varying differential equations may be either implicit or explicit. The goal in either case is to determine the state of a (finite element or other) model at time $t + \Delta t$ from that at time t. If the state at time t is denoted by $Y(t)$, an explicit method determines $Y(t + \Delta t)$ from the current state

$$Y(t + \Delta t) = F(Y(t)) \tag{3.3}$$

while an implicit method involves the solution of an equation

$$G(Y(t), Y(t + \Delta t)) = 0. \tag{3.4}$$

In general, a single step with an implicit method is more computationally expensive. However, for many problems (called *stiff*) the explicit method suffers from the fact that exceedingly small time steps Δt are required to guarantee stability. An implicit solution with fewer steps may therefore be faster overall. The optimum choice of solution strategy will depend on the particular problem.

3.1.1 Implicit solution method

Implicit FE solvers may adopt any of a number of solution strategies, but most commonly the Newton–Raphson method is used; this is the default in the implicit versions of both ELFEN and Abaqus. To solve a quasi-static problem, a set of non-linear equations $\mathbf{F}$ is constructed in terms of the nodal displacements $\mathbf{u}$, which may be represented as:

$$\mathbf{F}(\mathbf{u}) = \mathbf{P} - \mathbf{I} = 0 \tag{3.5}$$

Here $\mathbf{P}$ is the vector of applied loads and $\mathbf{I}$ the vector of internal forces.

Non-linear models are solved incrementally, applying loads or displacements in time steps Δt. To update the model from time t to time $t + \Delta t$, an iterative strategy is adopted to obtain the solution to Equation 3.5. If the approximation to the solution at time $t + \Delta t$ after i iterations is denoted by $\mathbf{u}_i$ and the difference between this estimate and the exact result is $\delta\mathbf{u}_{i+1}$, then from Equation 3.5 we have

$$\mathbf{F}(\mathbf{u}_i + \delta\mathbf{u}_{i+1}) = 0. \tag{3.6}$$

Expanding the left-hand side as a Taylor series and taking the first two terms only (on the understanding that $\delta\mathbf{u}_{i+1}$ is small) gives

$$\left[\frac{\partial \mathbf{F}}{\partial \mathbf{u}}(\mathbf{u}_i)\right]\delta\mathbf{u}_{i+1} = -\mathbf{F}(\mathbf{u}_i)\,. \tag{3.7}$$

This linear system in Equation 3.7 must be solved for $\delta\mathbf{u}_{i+1}$. The value of $\delta\mathbf{u}_{i+1}$ is then used to give $\mathbf{u}_{i+1}$ as $\mathbf{u}_i + \delta\mathbf{u}_{i+1}$, and the next iteration begins.

When the model is highly non-linear, the iterative process may require a great many steps. Non-linearity may result from, for example, material behaviours or contact interactions. In practice, if the number of iterations exceeds a certain value an FE program will usually restore the model state to the start of the increment (time t) and proceed to try a smaller increment Δt.

Solving the system in Equation 3.7 is the most computationally expensive aspect of the Newton–Raphson solution method. Abaqus/Standard offers as an alternative the modified Newton method, in which the Jacobian (global stiffness) matrix is recalculated only occasionally. This is suitable for some mildly non-linear problems, but not for severe non-linearity. In other cases, approximations to the Jacobian may be used, either to reduce computation time or because the exact value cannot be calculated easily. In addition, there are a wide variety of quasi-Newton methods (Simulia, 2007).

3.1.2 Explicit solution method

The explicit solution method was primarily developed for dynamic problems, though it may be applied to solve quasi-static problems provided that inertial effects are negligible. As a result, masses and accelerations are important.

Both ELFEN and Abaqus adopt an explicit central difference integration rule to advance the solution from increment i (time t) to increment $i+1$ (time $t+\Delta t$):

$$\dot{\mathbf{u}}^{\left(i+\frac{1}{2}\right)} = \dot{\mathbf{u}}^{\left(i-\frac{1}{2}\right)} + \frac{\Delta t^{(i+1)} + \Delta t^{(i)}}{2}\ddot{\mathbf{u}}^{(i)} \tag{3.8}$$

$$\mathbf{u}^{(i+1)} = \mathbf{u}^{(i)} + \Delta t^{(i+1)}\dot{\mathbf{u}}^{\left(i+\frac{1}{2}\right)}. \tag{3.9}$$

Here $\dot{\mathbf{u}}$ is velocity and $\ddot{\mathbf{u}}$ acceleration. The superscript (i) refers to an increment number, and $\left(i \pm \frac{1}{2}\right)$ indicates the value of a variable midway between increments. It can be seen that the integration operator is explicit in the sense described previously: the state can be advanced using known values from the previous increment.

The computational efficiency of the explicit solution procedure lies in the use of diagonal ("lumped") element mass matrices. For a dynamic problem, Equation 3.5 becomes:

$$\ddot{\mathbf{u}}^{(i)} = \mathbf{M}^{-1} \cdot \left(\mathbf{P}^{(i)} - \mathbf{I}^{(i)}\right), \tag{3.10}$$

where $\mathbf{M}$ is the mass matrix and $\mathbf{P}$ and $\mathbf{I}$ have the same meaning as in Section 3.1.1. With lumped mass matrices $\mathbf{M}$ is diagonal so its inverse is trivial to find and Equation 3.10 can easily be used to determine the accelerations at the beginning of an increment. Each time increment in the explicit method is therefore computationally inexpensive: the only matrix to be inverted is diagonal and this need only be done once per increment (as there is no iteration). The tangent stiffness matrix need never be assembled, let alone inverted.

The maximum allowable size of the time increment Δt is determined by the Courant–Friedrichs–Lewy (CFL) condition (Courant et al., 1967), a stability condition that essentially states the time step must be sufficiently small that information has time to propagate through the spatial discretization. Specifically, it is necessary to use

$$\Delta t \leq \Delta t_{\mathrm{cr}} = \min\left(\frac{L_{\mathrm{e}}}{c_{\mathrm{d}}}\right) \tag{3.11}$$

where the minimum is to be found, over all elements in the model, of the ratio of L_{e} (a characteristic element length) to c_{d} (the speed of a dilational wave in the material), given by

$$c_{\mathrm{d}} = \sqrt{\frac{(\lambda + 2\mu)}{\rho}} \tag{3.12}$$

where λ and μ are the first and second Lamé constants for the material and ρ is the density. The relationship between stable time increment Δt_{cr} and element size L_{e} means refining the mesh will influence solution time more strongly than would otherwise be the case. In a 2D analysis where c_{d} is constant, repeating the analysis with double the mesh density in all directions will increase the solution time by a factor of eight: there will be four times as many elements, and the time increment will be halved. In a 3D analysis the solution time would rise sixteen-fold.

The existence of a maximum stable time increment results in the explicit finite element method requiring a large number of increments to solve many practical problems. It is common for an analysis to require between 10^5 and 10^6 increments, but this must be considered in the light of the low computational cost of each increment.

3.1.3 Comparison of implicit and explicit methods

In considering whether to use an implicit or an explicit solution strategy for a particular problem, a balance must be struck between the high computational cost of an increment in the implicit approach and the much larger number of steps needed in the explicit method. There are other factors to consider, however, some of which are discussed here.

It would appear that the explicit method is particularly disadvantageous for simulating quasi-static processes that take place over long periods of time, as the absolute value of the stable time increment is fixed (for a given material and element size) rather than depending on the time period modelled. For a given size of problem, computation time will depend on the number of increments needed, $T/\Delta t$, where Δt is the increment size and T the total time. Since the natural time scale is not generally important in quasi-static analyses, one strategy to reduce computation time is to artificially increase the loading rate (decreasing T). For models involving rate-dependent material behaviour (which may nevertheless be quasi-static in the sense that inertial effects are negligible), this approach will not be appropriate. Inspection of Equations 3.11 and 3.12 suggests an alternative strategy: decreasing the elastic wave-speed c_{d}. This is most commonly done by mass scaling, artificially increasing the density of the materials in the model (Simulia, 2007).

When using mass-scaling to speed up a quasi-static analysis, it is important to ensure that inertial forces do not become large enough to affect the mechanical response. 5% (Chung et al., 1998; Kim et al., 2002) and 10% (Simulia, 2007) have been suggested as maximum recommended values for the ratio of kinetic energy to strain energy.

Another area in which implicit and explicit methods differ is in dealing with non-linearity. Implicit methods can become very inefficient if the iterative methods employed fail to converge rapidly. Besides the increased computational expense of resorting to smaller increment sizes, the effort already expended on attempting the increment is wasted. In cases where a model is highly non-linear, the required increment may be impractically short, or the iteration may fail to converge entirely (Jung and Yang, 1998; Harewood and McHugh, 2007). Explicit methods do not suffer from convergence problems, as there is no iteration.

Several considerations that are important in implicit FE can be ignored when an explicit method is used. For instance, bandwidth optimization or equation reordering (to minimize the time needed to solve Equation 3.7, see e.g. Astley, 1992) can be dispensed with. In addition, the small time steps simplify the simulation of contact.

Although the explicit finite element method was developed for use in dynamic problems with deformable bodies, it has come to be used very extensively in modelling non-linear quasi-static problems, especially in the simulation of metal-forming processes (see e.g. Harewood and McHugh, 2007; Kim et al., 2002; Kugener, 1995; Jung and Yang, 1998; Taylor et al., 1995). Since the problem to be analysed here shares many of the features of such an analysis, it seems reasonable to expect that the explicit method will provide a robust and efficient approach.

3.2 Description of ELFEN model

The explicit solver provided by ELFEN was used to analyse the quasi-static penetration of a rigid conical indenter into a clay sample contained in a rigid hemispherical cup of diameter 55 mm (as specified by Standard Norge, 1988). The parameters α (the adhesion factor of the cone–clay interface) and β (the apex angle of the cone) were varied. The geometry of the cone and cup allowed a two-dimensional axisymmetric model to be used. The model takes proper account of large material deformations by using consistent finite strain plasticity algorithms (Rockfield Software, 1998). To maintain solution accuracy under large deformations, ELFEN's automatic adaptive remeshing routines were used to generate a new mesh whenever element distortions or local error estimates exceeded specified thresholds.

The geometry of the model is shown in Figure 3.1. The cone tip is initially at $(r, z) = (0, 0)$. During the analysis, the cone was moved 10 mm downwards at constant velocity, over a time period of 1 s. Further details of the model are presented in the following sections.

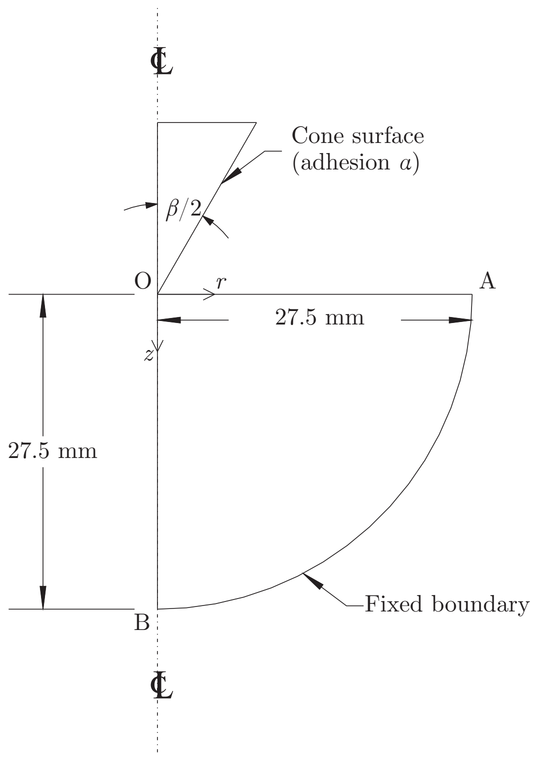

Figure 3.1: Basic features of ELFEN finite element model

3.2.1 Choice of element type

ELFEN provides first order isoparametric elements with reduced integration for use with the explicit solver. Four-noded quadrilateral elements were selected for use in this analysis.

Reduced integration implies that the integration used to determine internal forces and stiffnesses is one order less than the full scheme. This might seem a poor approximation, but the method has several advantages. Fully integrated first-order elements can exhibit a phenomenon known as "volumetric locking" when used to represent near-incompressible material behaviour, as in this case. Non-physical stresses develop, causing the elements to exhibit behaviour that may be orders of magnitude too stiff, giving unusable results. Fully integrated second order elements can also suffer from this problem, though only after significant deformation (Simulia, 2007). The use of reduced integration, with a single integration point for each element, reduces the number of constraints imposed on the solution by the choice of element and eliminates the locking problem.

Another advantage is that, for first-order elements, the use of reduced integration means that the strains used are the exact average strains over the element volume. This is useful for output and also beneficial when non-linear constitutive models are used, since the strains passed to the constitutive routines are representative of the actual strains (Simulia, 2007). Finally, reduced integration decreases the computational cost of formulating the element.

The disadvantage of reduced integration is that certain deformation modes remain stress-free. If a mesh deforms in one of these modes, the deformation will not be resisted as no stresses occur at the integration points and the deformation will quickly dominate the solution (Flanagan and Belytschko, 1981). These spurious modes have been called variously zero-energy, hourglass and kinematic modes; the term "keystoning" has also been used. Hourglassing can be eliminated by introducing a small artificial viscosity or stiffness to resist the spurious deformations if they are detected. The former approach is adopted in ELFEN. Rockfield Software (2005) note that problems will arise if the non-physical hourglass-resisting forces absorb too large a proportion of the energy in the system. However, the advised remedy in the event of problems arising is to use a finer mesh, so the usual process of ensuring adequate mesh refinement should prevent any problems.

3.2.2 Material behaviour

The indented material was modelled as elastoplastic, obeying Tresca's yield criterion with associated flow. ELFEN does not provide a simple Tresca model directly, but a Mohr–Coulomb model with Rankine tension cutoff is available (Figure 3.2). The tension cutoff introduces an additional yield criterion $\sigma_i - \sigma_\mathrm{t} = 0$ $(i = 1, 2, 3)$ where σ_i refers to each principal stress and σ_t is the tensile strength. The desired Tresca behaviour was obtained by setting the friction and dilation angles ϕ and ψ to zero. The shear strength c $(= s_\mathrm{u})$ was set to an arbitrary value of 1 kPa. The tension cut-off σ_t was set to an arbitrarily large value (10^{99} MPa), though identical results would have been obtained with any value of σ_t that was not exceeded in the analysis.

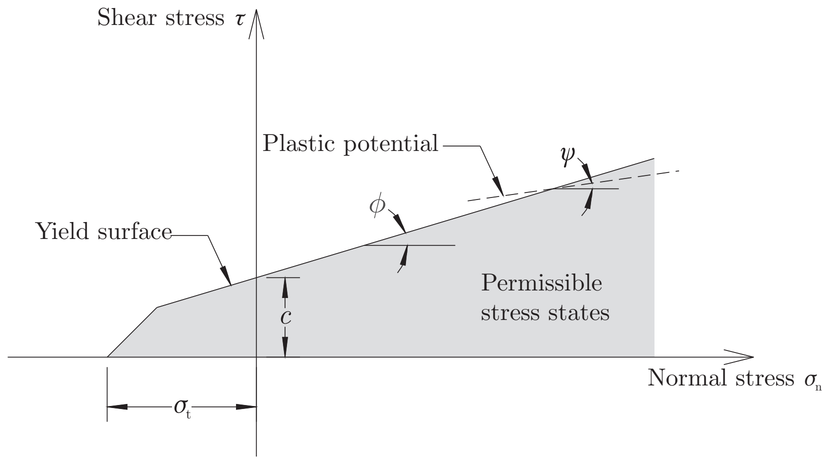

Figure 3.2: Yield surface (in τ–σ_n space) of Mohr–Coulomb model provided by ELFEN (Rockfield Software, 2005)

The elastic behaviour was defined by a Poisson's ratio of 0.49 (making the material approximately incompressible). In order to compare the results with those of Lockett (1963) and Koumoto and Houlsby (2001), an approximately rigid–plastic response is required. Rigidity can be quantified by means of the rigidity index

$$I_\mathrm{R} = \frac{G}{s_\mathrm{u}} = \frac{E}{2\,(1+\nu)\,s_\mathrm{u}}. \tag{3.13}$$

The value of I_R in these analyses was 1500, which is larger than the maximum values commonly adopted by researchers investigating the influence of rigidity index on clay plasticity (Walker and Yu, 2006; Zhou and Randolph, 2007). Together with the restraint provided by the boundary conditions on the sample, it was felt that this value would be sufficiently large. The validity of this assumption can be assessed by comparing the results with those of other authors. The selection of rigidity index led to the Young's modulus being specified as 4.47 MPa.

3.2.3 Cone–clay interface

In the ELFEN model, contact at the cone–clay interface was modelled as follows.

To determine the force normal to the surface, ELFEN's penalty algorithm was used. In each increment, the model was first advanced into a predicted configuration without taking contact into account. Some nodes of the indented material would have penetrated the surface of the cone, and the program then determined the force to apply at each node to resist the penetration. These forces were applied to the nodes of the indented material, causing them to lie at the interface. Equal and opposite forces were applied to the corresponding nodes of the indenter. The penalty coefficient (that determines the sizes of the forces to apply) has a default value equal to the Young's modulus of the underlying material. In purely elastic models this could give rise to excessive interpenetration of the two surfaces (Simulia, 2007), but since plastic deformations dominated in this analysis the default option was found to work well. Because the detection of contact in ELFEN is based on the penetration of surfaces consisting of sets of nodes, large relative motions of the two bodies were allowed; interactions did not always have to be between the same node pairs.

Contact was modelled variously as fully smooth, fully rough, or intermediate. In the smooth case, no tangential forces were applied, so that the surfaces were free to slide relative to one another. In cases with non-zero adhesion factor, relative motion was allowed if and only if the stress tangential on the surface exceeded a threshold value equal to αs_{u}, where α is the interface adhesion factor. The values $\alpha = 0$ and $\alpha = 1$ recover the fully smooth and fully rough cases respectively. This behaviour was implemented via the model shown in Figure 3.3, with μ set to a large value (10^{24}) and τ_{cr} equal to αs_{u}.

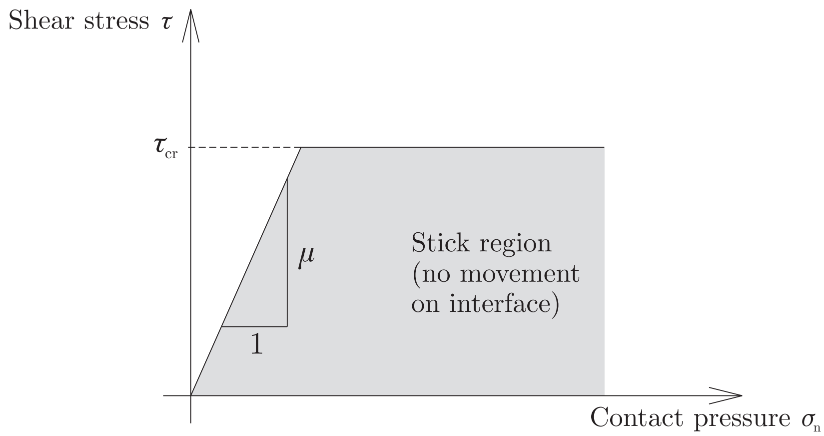

Figure 3.3: Tangential contact interaction relationship used in FE models for fully or partially rough cones

3.2.4 Mesh generation and automatic adaptive remeshing

The clay sample was initially discretized into a graded mesh of quadrilateral elements, using an advancing front algorithm. The maximum target element size (measured as the mean side length) was 2.5 mm, and this value was used for most of the material. At the point where the cone would first contact the material, the element size was decreased to 0.25 mm. The transition was controlled by specifying that the maximum relative change in length between two adjacent elements should be 0.35. The cone was meshed with elements having mean side length 0.5 mm. During the analysis, the clay region was periodically remeshed; the same mesh was used on the cone throughout. The initial mesh for a clay sample and 60° cone is shown in Figure 3.4a.

Element distortion in the clay sample was checked every 100 increments. The method used in ELFEN is to subdivide each element into four triangles along its diagonals and determine the change in area of each triangle. If the change exceeded 2.5% in any element, a new mesh was created.

Once the element distortion measure exceeded 2.5%, ELFEN generated a new mesh in which the element size was determined by the accumulated effective plastic strain $\bar{\varepsilon}_{\mathrm{pl}}$, ranging from 2.5 mm in unstrained material to 0.25 mm in regions of high strain (greater than a specified threshold). The threshold value of $\bar{\varepsilon}_{\mathrm{pl}}$ was chosen so that the minimum element size was used throughout the deforming region. Values for the threshold were chosen after some trial-and-error and depended on β as shown in Table 3.1.

Table 3.1: Values of effective plastic strain below which the minimum element size was used

β (°)	30	60	90	105	120	140	150	160
Threshold value of $\bar{\varepsilon}_{\mathrm{pl}}$	0.25	0.25	0.25	0.25	0.25	0.15	0.1	0.05

After remeshing, the state of the model was transferred to the new mesh using the default method of mapping within the background elements (of the original mesh) for both nodal and integration-point variables.

Figure 3.4 shows meshes at selected time increments for a typical analysis (a smooth 60° cone), together with a graph showing the variation in the number of elements in the model over time. Clearly, the mesh used at the beginning of the analysis will give an exceedingly poor discretization of the deforming material. In fact, the cone will initially be in contact with only *one* element, and as the analysis progresses more and more elements will come to be included in the deforming region. Part of the analysis of the results will be to look for attainment of a steady, self-similar state in which the load on the cone is proportional to the square of the cone displacement – equivalently, the value of F (Equation 3.2) should reach a constant value once there are sufficient elements in the mesh. This provides an inherent check that the mesh is sufficiently refined.

3.2.5 Boundary conditions

The curved outer surface of the sample (arc AB in Figure 3.1) was fixed in both r and z directions, representing the restraint provided by a rigid, rough-sided cup. The size of the sample, and the shape of the boundary, were selected to represent the fall cone test recommended by Standard Norge (1988) and Geonor (2005a). Analyses with other boundary conditions were conducted in Abaqus, and showed choice of cup shape and roughness to have little or no impact on the results (see Section 4.4).

If the cone displacement was too large relative to the radius of the cup, the deformation mechanism would be influenced by the presence of the boundary. This would be apparent from the extent of the mechanism and also as a change in the value of N_{ch} or F, which would fail to converge to a constant value.

At first, the sample edge lying on the axis (line OB in Figure 3.1) was fixed in the r direction, but special treatment of this part of the model was later adopted. More information is given in Section 3.2.8.

3.2.6 Soil self-weight

As discussed in Section 2.1.4, the self-weight of the indented material makes a small contribution to the force resisting indentation – around 1 to 2% of the weight of the cone at large (20 mm) penetration, and much less for smaller penetrations.

As well as making only a comparatively minor contribution to the cone resistance, the effect of self-weight is independent of the rate of penetration (rate dependence will be the focus of analyses in later chapters). For these reasons, the buoyancy and surcharge effects associated with self-weight were neglected in the finite element model. This simplifies the analyses as an additional body force would otherwise need to be applied to each element. The effect of this simplification is not expected to be large. It would be relatively simple to introduce a correction for this effect, but this has not been done here.

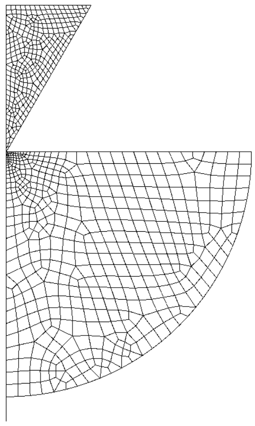

(a) $t = 0\,\mathrm{ms}$

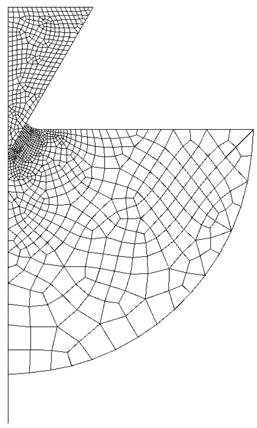

(b) $t = 250\,\mathrm{ms}$

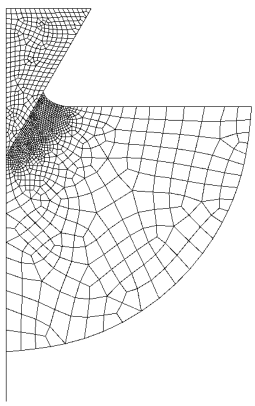

(c) $t = 500\,\mathrm{ms}$

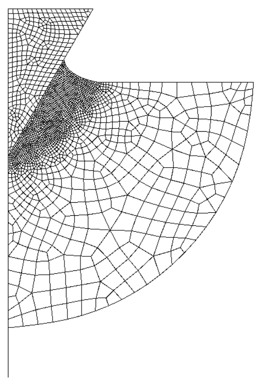

(d) $t = 750\,\mathrm{ms}$

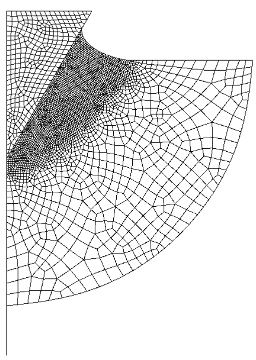

(e) $t = 1000\,\mathrm{ms}$

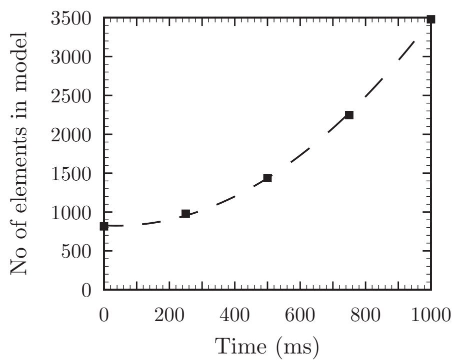

(f) Variation of number of elements during analysis

Figure 3.4: Evolution of finite element mesh during analysis of the case $\alpha = 0$, $\beta = 60°$. Cone displacement was increased linearly to a maximum of $10\,\mathrm{mm}$ at $t = 1000\,\mathrm{ms}$.

Although the weight of the indented material has been neglected, it has been assigned a density. This is required (even in the quasi-static analyses performed with ELFEN) because the explicit formulation of the finite element method is fundamentally a dynamic analysis method as described in Section 3.1.2.

3.2.7 Cases considered

Table 3.2 shows the combinations of α and β that were analysed by either Koumoto and Houlsby (2001) or Lockett (1963). All the cases considered by either Koumoto and Houlsby or Lockett were re-analysed using ELFEN. Note that previous authors also considered the limiting case $\beta = 180°$, but this was not included in the present work.

Table 3.2: Combinations of cone angle β and adhesion factor α considered in ELFEN analyses

	α						
β (°)	0.0	0.2	0.4	0.5	0.6	0.8	1.0
30	$*$	$*$	$*$	$*$	$*$	$*$	$*$
60	$*$	$*$	$*$	$*$	$*$	$*$	$*$
90	$*$	$*$	$*$	$*$	$*$	$*$	$*$
105	$\bigcirc$						
120	$\circledast$	$*$	$*$	$*$	$*$	$*$	$*$
140	$\bigcirc$						
150	$*$	$*$	$*$	$*$	$*$	$*$	$*$
160	$\bigcirc$						

LEGEND:
$*$ case previously analysed by Koumoto and Houlsby (2001)
$\bigcirc$ case previously analysed by Lockett (1963)

3.2.8 Treatment of material close to axis

After preliminary trial analyses using a smooth 60° cone, it became apparent that the results were not as expected. In the ELFEN model, the force Q on the cone was found to be larger than expected such that the value of N_{ch} was 9.91. For comparison, Koumoto and Houlsby (2001) found $N_{\mathrm{ch}} = 5.266$. While some differences were expected due to the inherently approximate nature of finite element analysis, and to the assumptions made by the previous authors, a disparity of almost 90% was suprising.

Adaptive remeshing made it difficult to see at a glance whether the deformation of the sample appeared reasonable, but the analysis was rerun with ELFEN's material grid option enabled. This option superimposes a square grid on the sample, and tracks displacements of the grid nodes to allow visualization of the underlying material motion. Figure 3.5a shows the results. Rather than flowing towards the surface along the smooth face of the cone, material that was initially close to the axis deformed substantially and unrealistically. Removing the boundary condition on the left side of the sample caused the analysis to terminate with errors as material tried to cross into the $r < 0$ region.

In Susila and Hryciw (2003), a one-sided boundary condition was applied to prevent material from displacing across the centre line of the model, while allowing outward and vertical movement. It is not clear how this was achieved, but an approach based on ELFEN's contact modelling capability is adopted here to give a similar effect.

To allow material to flow away from the axis without being able to cross it, the geometry of the cone and sample were modified as follows. The left edge of the clay sample was moved from $r = 0$ to $r = R_{\text{excluded}}$, and the tip of the cone was modified by attaching a needle-like protrusion of radius R_{excluded}. This protrusion is visible at the base of the samples in Figures 3.4a to 3.4e. Contact between the needle and the clay material was treated as described in Section 3.2.3, with the exception that the interface was always smooth. It was hoped that, by excluding a small part of the model in this way, the problems described above could be avoided without significantly influencing the results.

A series of analyses was conducted to investigate the influence of R_{excluded} on the force needed for indentation. The results are shown in Figure 3.6, together with those of the original analysis and of Koumoto and Houlsby (2001) for reference. R_{sample} is the radius of the cup, 27.5 mm. As the excluded radius was reduced, N_{c} approached a value close to the result of Koumoto and Houlsby. Note that when $R_{\text{sample}}/R_{\text{excluded}}$ was equal to 1000, the ratio of the *areas*, which might be expected to be more significant in determining the force on the cone, was 10^6.

Figure 3.5b shows the distorted grid for $R_{\text{sample}}/R_{\text{excluded}} = 1000$. Note that the profile of the free surface is substantially lower than in Figure 3.5a, suggesting the numerical difficulties in the first analysis meant the results failed to satisfy the condition of volumetric conservation (the material should be near-incompressible since $\nu \approx 0.5$ and $\psi = 0$).

The technique described here, with $R_{\text{sample}}/R_{\text{excluded}} = 1000$, was applied in all subsequent analyses.

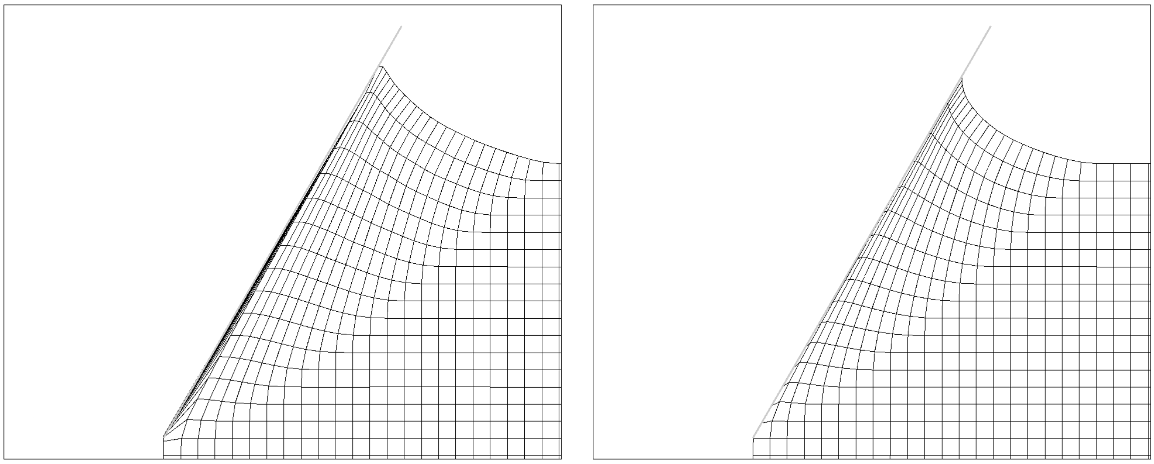

(a) Original boundary conditions (b) Modified boundary conditions

Figure 3.5: Distortion of initially square grid in ELFEN analysis of material indentation by a smooth 60° cone. Grid spacing 0.625 mm, final cone penetration 10 mm

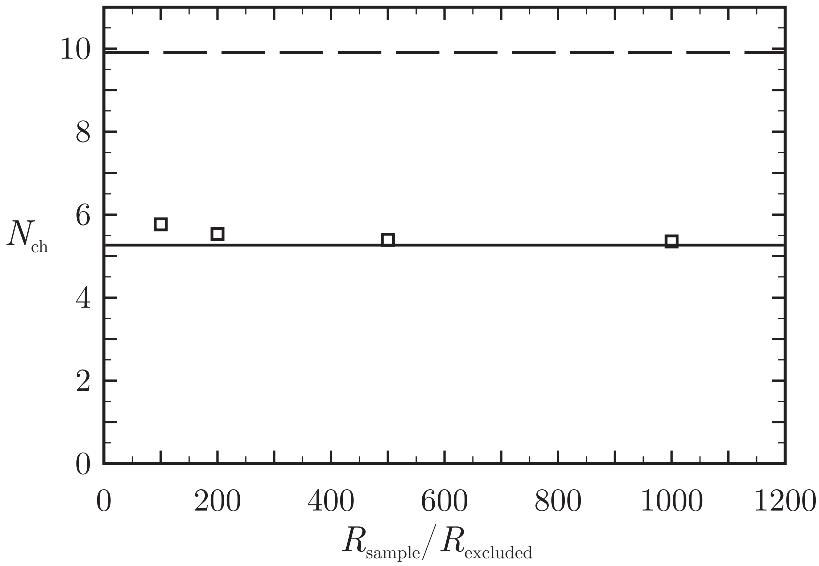

Figure 3.6: Convergence of N_{ch} with reduction in radius of excluded region $R_{excluded}$, for smooth 60° cone. Solid line shows value given by Koumoto and Houlsby (2001); dashed line is ELFEN result with original boundary condition

3.3 Results of ELFEN analyses

3.3.1 Smooth cones: force–displacement data

Smooth cones with a range of angles were analysed first. In each case, the analysis was carried out under displacement control. The contact force Q and displacement d were recorded at 1 ms intervals, giving 1000 data points per analysis. Plotting the data revealed a certain amount of high-frequency noise, a side-effect of the adaptivity process remeshing the model and interpolating variables onto the new mesh. To remove this, a 49-point moving average of the results was calculated. Figure 3.7 shows the data before and after smoothing for an example analysis. Anecdotal reports from experienced users of ELFEN suggest that the noise in results obtained with adaptive meshing is often much more severe than in Figure 3.7a, particularly when remeshing is performed less frequently than here (Xu, 2008).

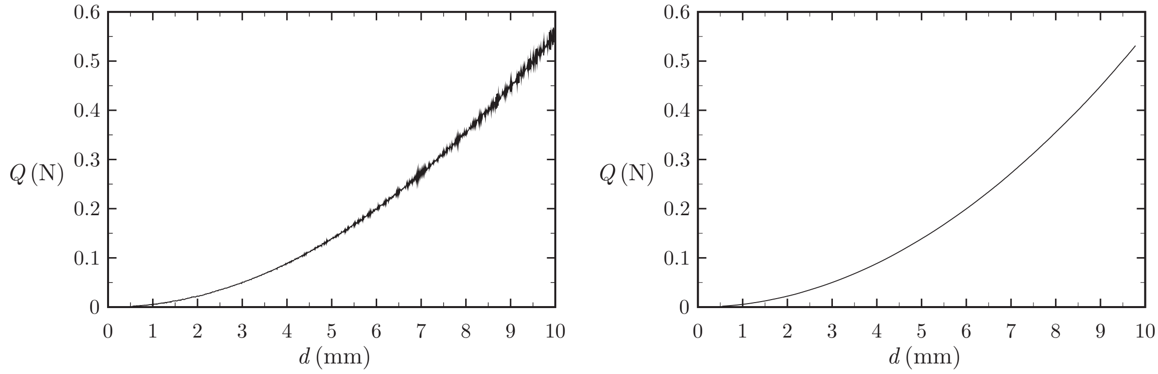

(a) Noisy data

(b) Smoothed data

Figure 3.7: Removal of high-frequency noise from force–displacement data for smooth 60° cone

For each load–displacement curve, the final averaged force and corresponding displacement were used to determine the value of the parameter N_{ch} (defined in Equation 3.1). Values of N_{ch} (and the alternative parameter F) are shown in Table 3.3.

Table 3.3: Values of N_{ch} and F for smooth cone indentation, from ELFEN

β (°)	N_{ch}	F
30	5.056	1.140
60	5.302	5.552
90	6.216	19.53
105	6.809	36.33
120	7.357	69.34
140	8.183	194.1
150	8.499	371.9
160	8.843	893.5

Figure 3.8 shows N_{ch} as a function of β; the results of the present analysis are shown along with the results of Koumoto and Houlsby (2001) and Lockett (1963). Note that Lockett did not give values of N_{ch} directly, but reported the force required to give an indentation of a certain size (as a multiple of πs_{u}); these forces, together with given data on the geometry of the mechanism, allowed N_{ch} to be determined.

It can be seen that there is close agreement between the present analysis and the results of Lockett over the range of β where he was able to obtain a solution. The new results differ from Lockett's by a maximum of 1.07% (for $\beta = 105°$); in all other cases the discrepancy is

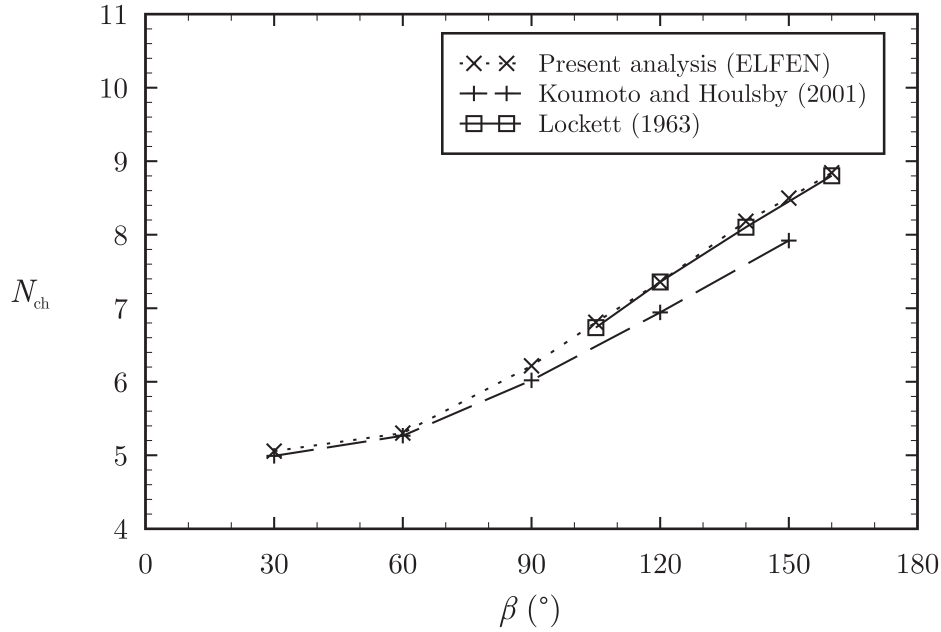

Figure 3.8: Variation of N_{ch} with β for smooth cones

less than 1%, and when $\beta = 120°$ it is only 0.002%. The close agreement obtained suggests that the ELFEN model represents the idealised rigid–plastic behaviour well.

In comparing the ELFEN results with those of Koumoto and Houlsby, it is important to remember that their analysis involved approximating the profile of the deformed surface with a straight line. Close agreement is therefore not expected in general. It can be seen that the straight surface approximation seems to work well for the small cone angles used in the fall cone test. For $\beta = 60°$, the ELFEN result differs from that of Koumoto and Houlsby by less than 0.8%. As β increases, the discrepancy between the analyses becomes increasingly large, until at $\beta = 150°$ the results differ by 7.3%.

3.3.2 Smooth cones: geometry of mechanism

Figure 3.9 shows the variation with angle β of the contact area A in the ELFEN analyses with smooth cones. A is the area of the curved surface of the cone that is in contact with the indented material. To make the results more generally applicable, the area in each case has been normalised by R^2, where R is the radius of the cone at the original sample surface level. 3.8.

The results of Lockett (1963) and Koumoto and Houlsby (2001) are also shown in Figure 3.9. These authors presented their results in different forms, from which values of A/R^2 had to be calculated. Lockett gave values of the length OA in Figure 3.10a such that the

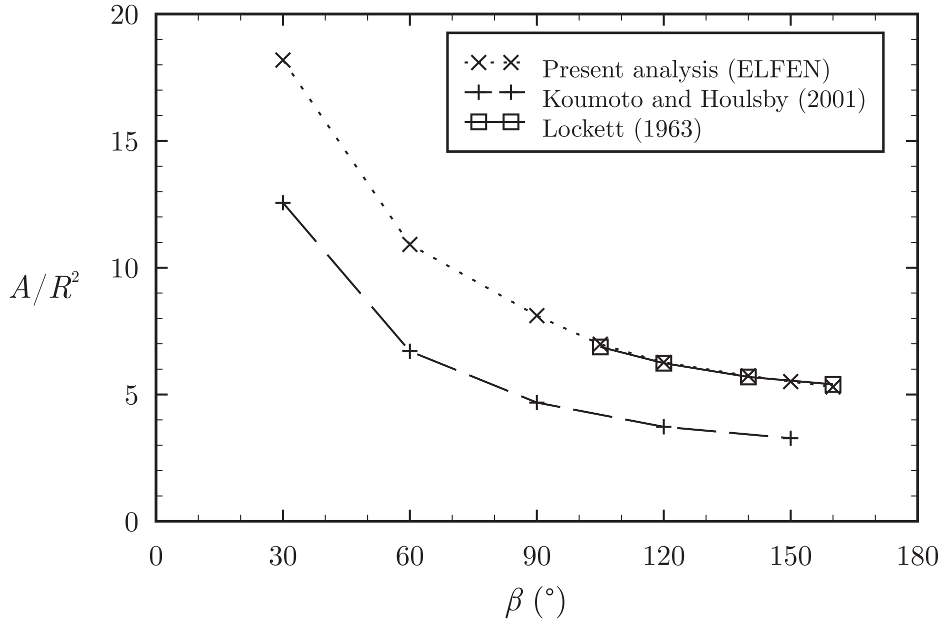

Figure 3.9: Variation of normalised contact area A/R^2 with β for smooth cones

radius AB would be unity. Given the cone angle β, the perpendicular height AC of the conical contact area could easily be found. The area of contact A could then be found and normalised by R^2 to allow comparison with the new results. Koumoto and Houlsby gave values of the angle δ between their assumed straight surface profile and the horizontal axis, as shown in Figure 3.10b. Since the material is incompressible, the inserted volume of the cone (shaded) must be equal to that of the displaced material (also shaded). Together with the angle δ this defined the geometry of the mechanism for given R and allowed A/R^2 to be calculated.

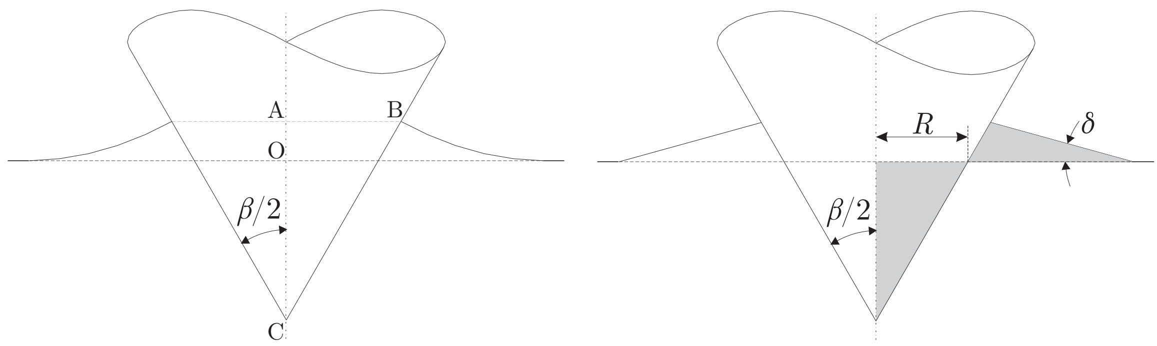

(a) Lockett (1963) (b) Koumoto and Houlsby (2001)

Figure 3.10: Values used to define mechanism geometry in work of previous researchers

Figure 3.9 shows that the ELFEN results agree closely with those obtained by Lockett (1963). The results of Koumoto and Houlsby (2001) lie substantially below the others, differing most strongly for large values of the angle β. For small β the difference is proportionally less, but is still larger than might be expected given the close agreement in N_{ch} for these cones seen in Figure

The close agreement between the contact areas obtained from the present analysis and that of Lockett (1963) is confirmed if the outline of the deforming region given by Lockett is superimposed on the pattern of deformation given by Elfen's material grid option. Figure 3.11 shows examples of this for $\beta = 105°$ and $120°$. There is strong agreement between the two solutions in terms of free surface geometry and the extent of deformation.

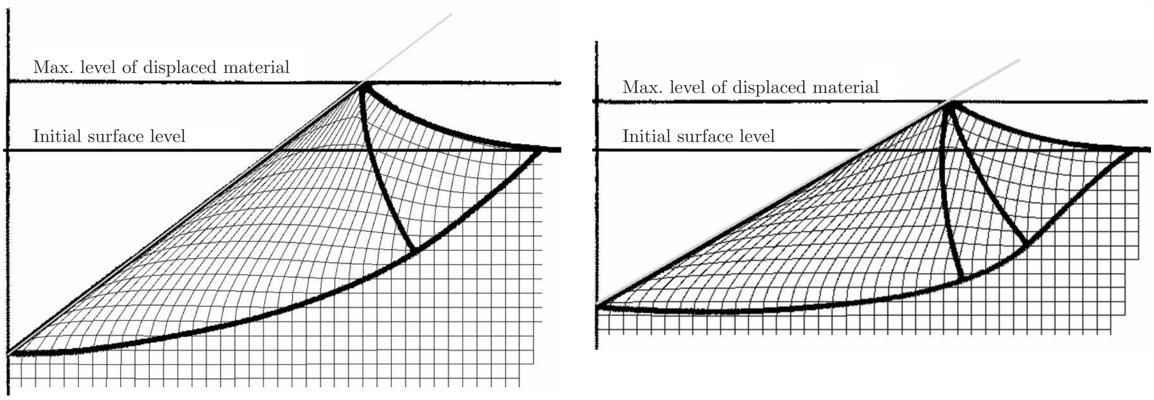

(a) $\beta = 105°$ (b) $\beta = 120°$

Figure 3.11: Comparison of the zones of plastic deformation given by the present analysis (thin gridlines) and Lockett (1963, thick outline)

3.3.3 Smooth cones: stresses in displaced lip

For cones with small angles ($\beta = 30°$ or $60°$), the straight surface profile approximation used by Koumoto and Houlsby gave results that were quite close to the N_{ch} values obtained here, despite large differences in the contact areas. A better understanding of the reasons for this was obtained when the stresses in the displaced lip were investigated. Throughout most of the yielded material around the cone, the stress state (taking compression positive) can be represented by

$$\sigma_1 = \sigma_2 + 2s_{\mathrm{u}}, \quad \sigma_2 = \sigma_3, \tag{3.14}$$

where σ_1 and σ_2 are the maximum and minimum principal stresses in the meridional plane and σ_3 is the out-of-plane or hoop stress (which is the third principal stress). Because the hoop stress is equal to one of the in-plane principal stresses, the shear stress that causes yield can be determined by considering only the in-plane stresses. This is invariably assumed to be the case throughout the deforming material when an indentation problem is analysed by the method of characteristics (see Section 2.1.2); the assumption is known as the Haar–von Kármán hypothesis (Haar and von Kármán, 1909).

A different stress regime was found to exist in the upper part of the displaced lip. Here, the principal stresses were related by

$$\sigma_1 = \sigma_2 = \sigma_3 + 2s_\mathrm{u}, \tag{3.15}$$

so that the hoop stress was no longer equal to one of the in-plane principal stresses, and indeed was no longer intermediate. In this regime the hoop stress plays a vital role in determining whether the material yields. Specifically, it was found that the in-plane principal stresses σ_1 and σ_2 were close to zero, while σ_3 was approximately equal to $-2s_\mathrm{u}$. The stress state is analogous to that in a thin hoop being stretched, or indeed a rod being pulled along its axis. This helps to explain the close agreement between the present results and those obtained by Koumoto and Houlsby (2001): although the curved surface profile gives a larger contact area than their assumed straight profile, the stresses normal to the cone face are close to zero in this lip region. The fact that, for cones with angle $\beta < 105°$, the Haar–von Kármán hypothesis is not applicable in all of the deforming material may perhaps explain why Lockett (1963) was only able to find solutions for large β.

Figure 3.12 shows how the stress state at a particular point close to the free surface changed during indentation with a smooth, 30° cone. The location studied is shown in Figures 3.12a to 3.12b. Figures 3.12c and 3.12d are two views of principal stress space, showing how the the stress regime changed from $t = 0$ (blue) to $t = 1\,\mathrm{s}$ (red). Immediately after yield the Haar–von Kármán hypothesis applies, but the stress regime changes to the hoop-stretching mode as the material moves up into the lip. Figure 3.12e plots the variation of the principal stresses σ_1 to σ_3, the deviatoric stress invariant q and the Tresca effective stress σ_tresca equal to twice the maximum shear stress. During the transition between regimes, the point in principal stress space moves across one of the planes of the yield surface and q temporarily decreases. The data for Figure 3.12 came from the Abaqus analyses to be presented in Chapter 4, because the Abaqus postprocessor, CAE, offered a more convenient method of obtaining stresses at a specific location. Similar results could have been obtained from ELFEN.

The extent of the hoop-stretching region can be most easily visualised by plotting contours of the deviatoric stress q, as shown in Figure 3.13. The boundary marking the transition

(a) Location of point at $t = 0$

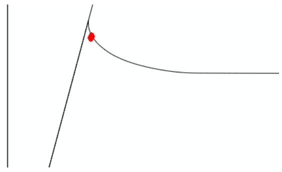

(b) Location of point at $t = 1\,\mathrm{s}$

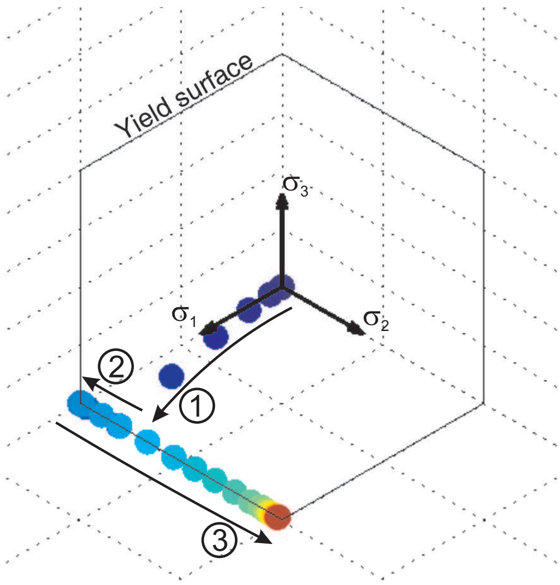

(c) Principal stresses at marked point during indentation, view along $\sigma_1 = \sigma_2 = \sigma_3$

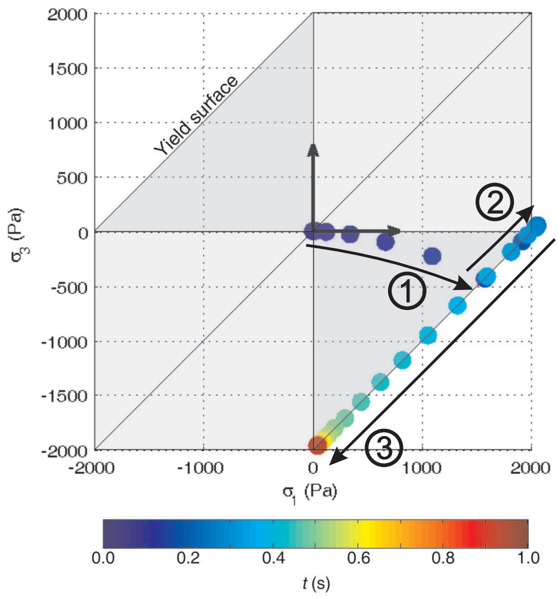

(d) Principal stresses at marked point during indentation, view of (σ_1, σ_3) plane

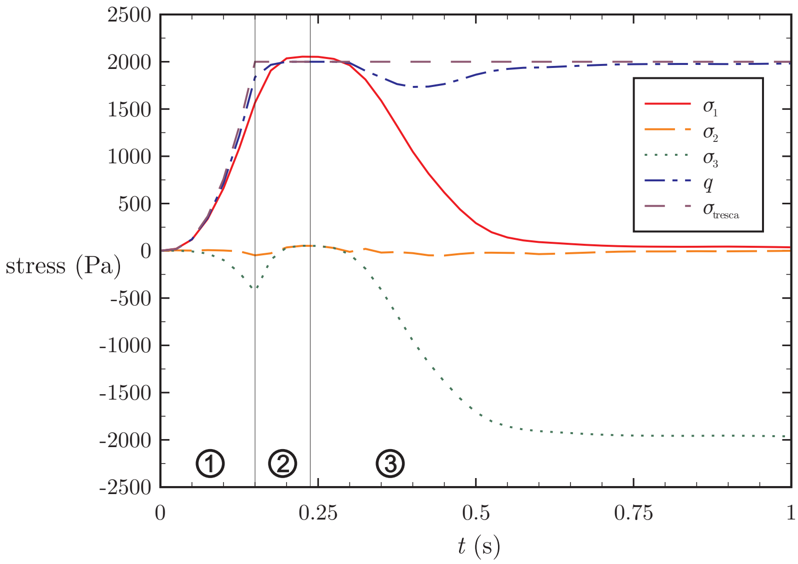

(e) Variation of various stress quantities at marked point during indentation

Figure 3.12: Evolution of stress state at a specific material point during indentation. By $t = 0.15\,\mathrm{s}$, the material has yielded (stage 1). After yielding σ_1 continues to increase and the stress state moves along the yield surface (stage 2) until $\sigma_1 = \sigma_2 + 2s_\mathrm{u}$ and $\sigma_2 = \sigma_3$. Subsequently there is a transition (stage 3) to the $\sigma_1 = \sigma_2 = \sigma_3 + 2s_\mathrm{u}$ regime that applies in the displaced lip

between stress regimes is visible as a narrow band in the vicinity of the lip where the deviatoric stress q drops from its maximum value of 0.002 MPa as the stress state passes across the face of the yield surface. This is equivalent to the dip on the q–t curve in Figure 3.12e, which corresponds to the same transition. For $\beta = 30°$, $60°$ and $90°$, the transition boundary is a straight line perpendicular to the face of the cone, meeting the free surface approximately tangentially. When $\beta \geq 105°$, the transition disappears and the Haar–von Kármán hypothesis applies everywhere. In the limiting 105° case, the free surface meets the face of the cone at right angles allowing a smooth transition between the cases with and without the hoop-stretching region. This is in agreement with the results of Lockett (see Figure 3.11a of this thesis and Table 1 of Lockett, 1963).

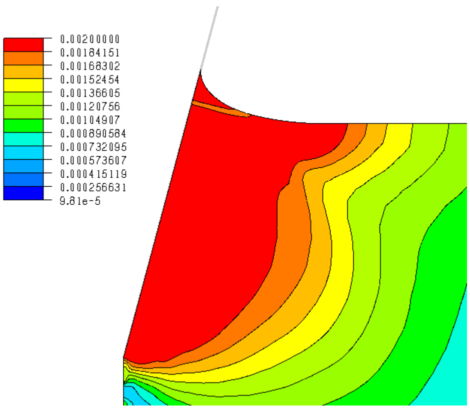

(a) $\beta = 30°$

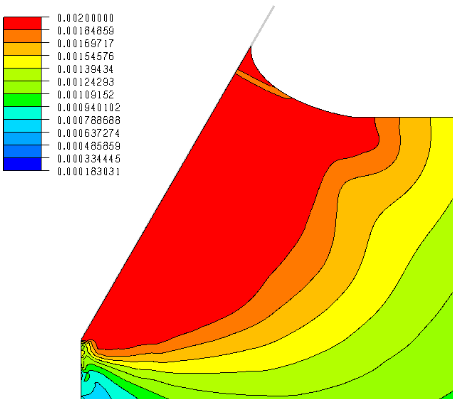

(b) $\beta = 60°$

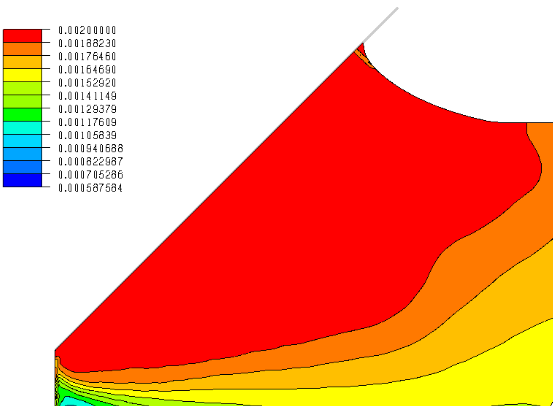

(c) $\beta = 90°$

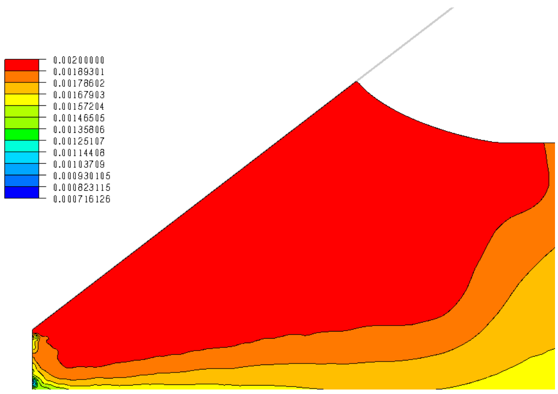

(d) $\beta = 105°$

Figure 3.13: Contours of deviatoric stress q (in MPa) around indentations made by smooth cones of various angles β in material of strength $s_u = 1$ kPa.

3.3.4 Rough cones: force–displacement data

The force–displacement curves for rough and semi-rough cones were smoothed using a moving average as described in Section 3.3.1. For certain combinations of angle and adhesion factor, particularly when α was close to 1 and β was small, the variation in force Q as cone displacement d increased was such that N_{ch} (see Equation 3.1) did not converge to a limiting value as in the case of smooth cones, but seemed to alternate between periods of gradual decrease and shorter periods of more rapid increase. An example, for $\alpha = 0.8$, $\beta = 30°$ is shown in Figure 3.14. In this case two increases in N_{ch} followed one another in close succession, giving an overall rise in N_{ch} of almost 4%. In most cases imperfections were more separated, resulting in variations that were smaller than those seen here.

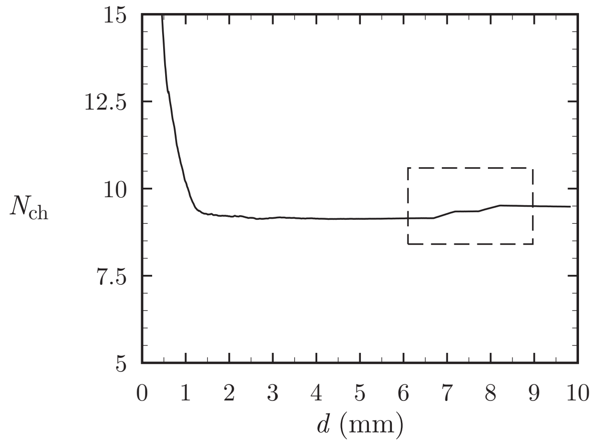

Figure 3.14: Imperfections (boxed) in converged value of N_{ch} for partly rough 30° cone ($\alpha = 0.8$). Data has been smoothed by taking a 49-point moving average

Examination of the meshes in these cases revealed that the sudden increases in cone resistance occurred when an element that had been part of the free surface "turned the corner" and became part of the contact region, giving a sudden increase in the area of contact. For the smooth cones already discussed, this would have made little difference to Q since the stress normal to the cone was so small in the lip (see Section 3.3.3). For rough cones, every part of the cone–clay contact contributed to the tangential force on the cone, making these changes in contact area more significant. No special steps were taken to mitigate this imperfect convergence of N_{ch}; the final values from the smoothed data sets were used as before. Note that remeshing did not prevent this problem as new meshes always preserved the material boundary from the previous step.

Table 3.4 shows values of N_{ch} and F derived from the final points of the smoothed force–displacement curves for available combinations of cone angle β and adhesion factor α. The same data are presented graphically in Figure 3.15. For smooth ($\alpha = 0$) cones, larger β always gave larger N_{ch}, but this was not the case with more general contact conditions. In all other cases, N_{ch} has a minimum value for a certain cone angle. When $\alpha = 1$ this angle is between 60 and 90°, but as α is reduced minimum N_{ch} is obtained with smaller angles. The values of N_{ch} for cones with larger included angles are less sensitive to the adhesion factor, as shown by the increasingly close spacing of the curves as β increases.

Table 3.4: Values of N_{ch} and F for (partially-) rough cone indentation, from ELFEN

	$\beta = 30°$		$\beta = 60°$		$\beta = 90°$		$\beta = 120°$		$\beta = 150°$	
α	N_{ch}	F	N_{ch}	F	N_{ch}	F	N_{ch}	F	N_{ch}	F
0.0	5.056	1.140	5.302	5.552	6.216	19.53	7.357	69.34	8.499	371.9
0.2	6.290	1.419	6.178	6.470	6.868	21.58	7.708	72.65	8.759	383.3
0.4	7.420	1.674	6.914	7.241	7.395	23.23	8.103	76.37	8.990	393.4
0.5	7.952	1.794	7.249	7.591	7.605	23.89	8.234	77.60	9.042	395.6
0.6	8.441	1.904	7.571	7.929	7.755	24.36	8.344	78.64	9.123	399.2
0.8	9.481	2.139	8.018	8.396	8.185	25.71	8.608	81.13	9.216	403.3
1.0	10.241	2.310	8.543	8.946	8.439	26.51	8.694	81.94	9.148	400.3

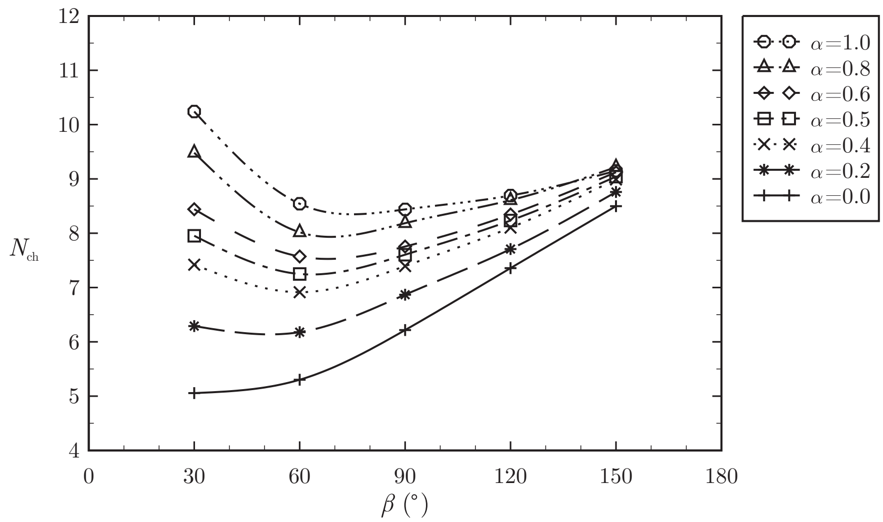

Figure 3.15: Variation of N_{ch} with cone angle β and adhesion factor α

The N_{ch} results obtained for smooth cones were found to agree quite closely with those of Koumoto and Houlsby for cone angles of 30° and especially 60°. The variation of N_{ch} with adhesion factor α for these two cone angles is shown in Figure 3.16. For both cone angles, there is an increasingly large discrepancy between the results of the two sets of analyses as α is increased. The reason for this has already been touched on: underestimating the area of contact makes a substantial difference to the results in terms of Q and N_{ch} even though stresses normal to the cone are close to zero in the lip region, because the interface model still requires the same minimum shear stress tangential to the cone before allowing movement to occur.

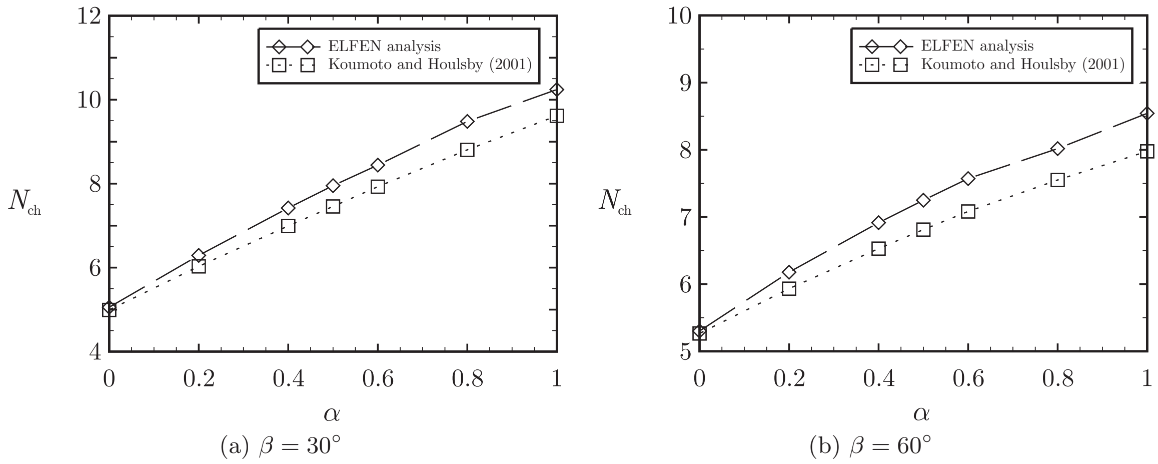

Figure 3.16: Variation of N_{ch} with α for 30° and 60° cones, together with the results of Koumoto and Houlsby (2001)

3.3.5 Rough cones: geometry of mechanism

For a given cone angle, the normalised contact area A/R^2 decreases as the adhesion factor α increases. This is because the size of the lip of displaced material is diminished by material adjacent to the cone being dragged downwards by the frictional force tangential to the cone face. Figure 3.17 shows the deformation of a square grid tracking material deformation around 30° and 60° cones. The left-hand grids were obtained with smooth cones ($\alpha = 0$), while rough ($\alpha = 1$) cones were used for the grids on the right. Note in each case the final position of the point that initially lay on the free surface adjacent to the tip of the cone, which has been marked in red. In the smooth cases it has remained at the surface and forms the highest part of the displaced lip, while in the rough cases it has been dragged to a position some distance down the cone face.

Distorted grids obtained with larger cone angles are shown in Figure 3.18. Note that when the cone angle is sufficiently large, material immediately adjacent to the point where the cone penetrates does does not remain at the surface even with zero adhesion, but comes to rest some distance along the face. The limiting value of β is close to 90°, but the precise value has not been established.

For a given cone angle β, the contact area decreases as adhesion factor α increases,

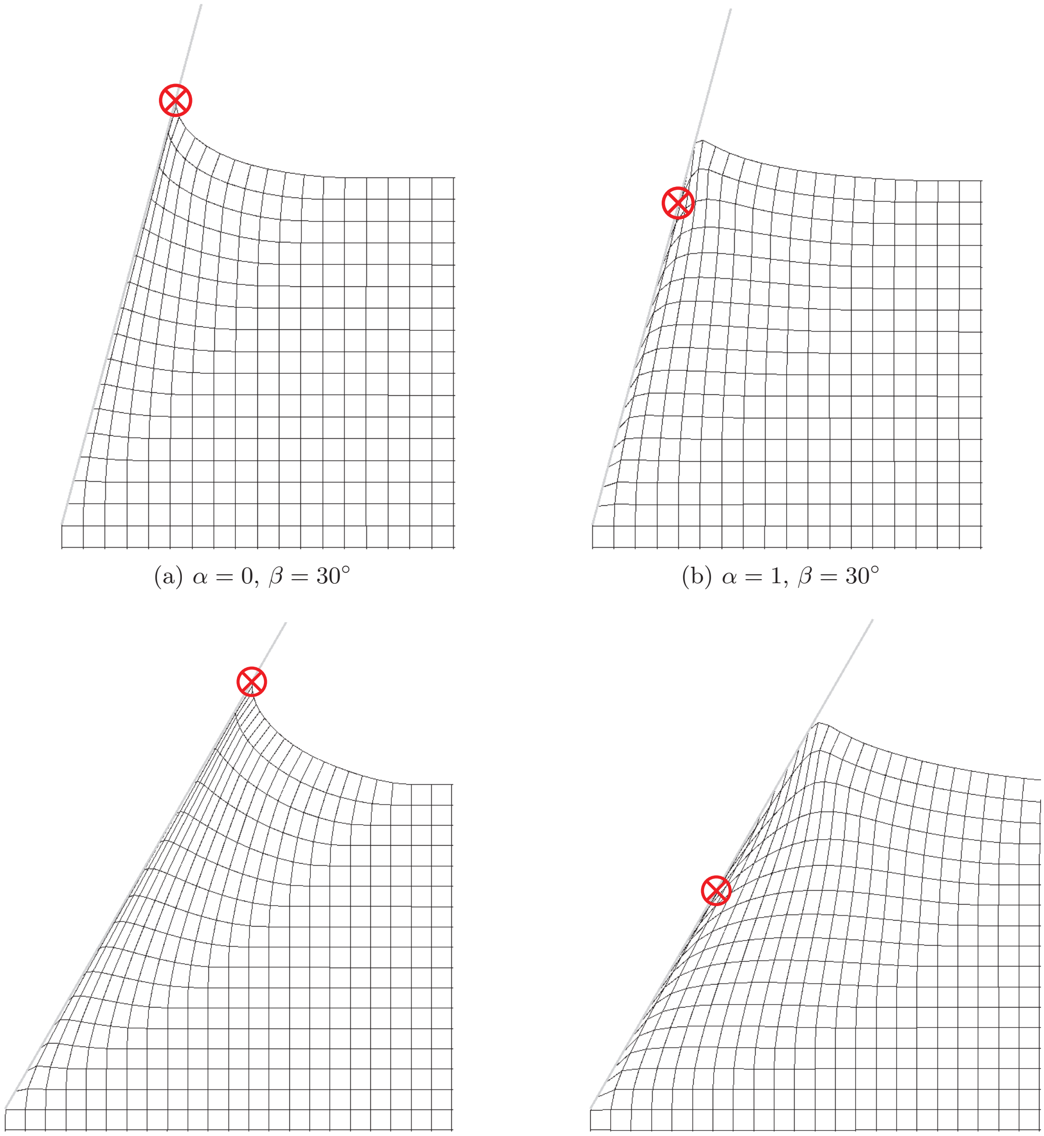

(a) $\alpha = 0$, $\beta = 30°$ (b) $\alpha = 1$, $\beta = 30°$

(c) $\alpha = 0$, $\beta = 60°$ (d) $\alpha = 1$, $\beta = 60°$

Figure 3.17: Deformation of an initially square grid after indentation by 30° and 60° cones with smooth ($\alpha = 0$) and rough ($\alpha = 1$) faces. Red markers indicate final position of the point initially at $(r, z) = (0, 0)$

because the displaced material does not build up to as great a height. The variation in normalized contact area with adhesion factor is shown in Figure 3.19 for 30° and 60° cones. Data derived from Koumoto and Houlsby (2001) is also shown (although contact area was not provided directly, it could be found from the inclination of the (straight) surface and the condition of volumetric incompressibility). Contact area did not vary much with adhesion factor in the work of Koumoto and Houlsby, so the difference between the contact areas from the two sets of analyses decreases for rougher cones. Had this not been the case, it is likely that the discrepancies between the values of N_{ch} for rough cones in Figure 3.16 would have been larger.

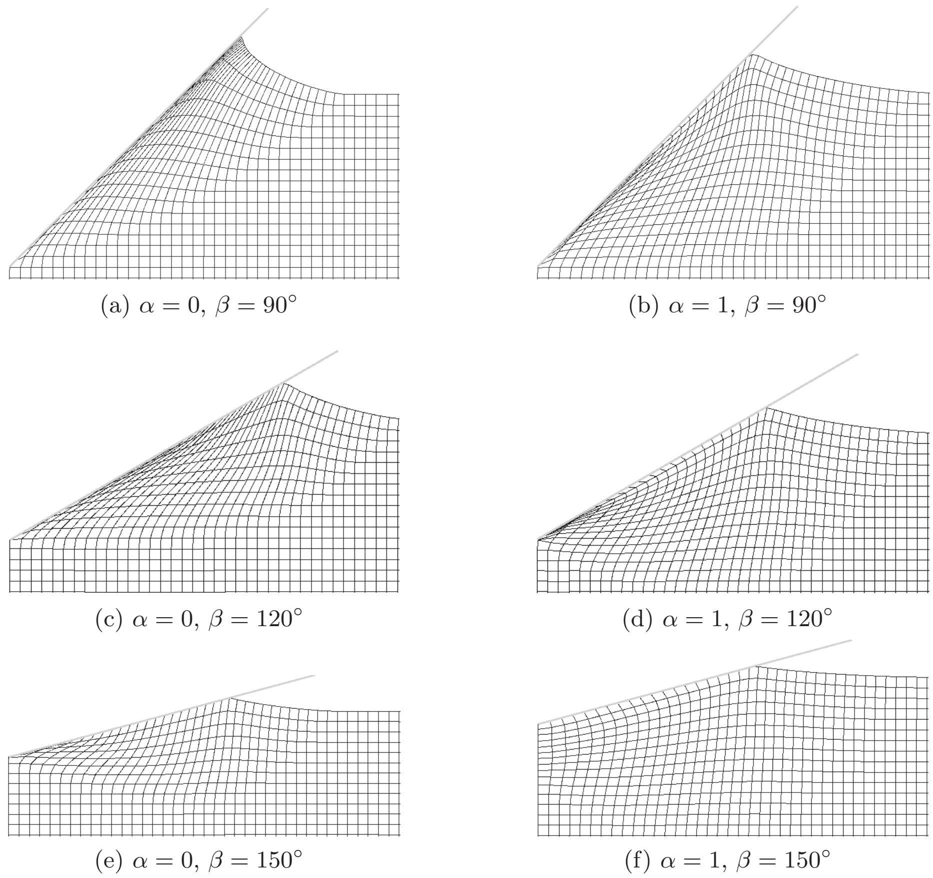

Figure 3.18: Deformation of an initially square grid after indentation by 90°, 120° and 150° cones with smooth ($\alpha = 0$) and rough ($\alpha = 1$) faces

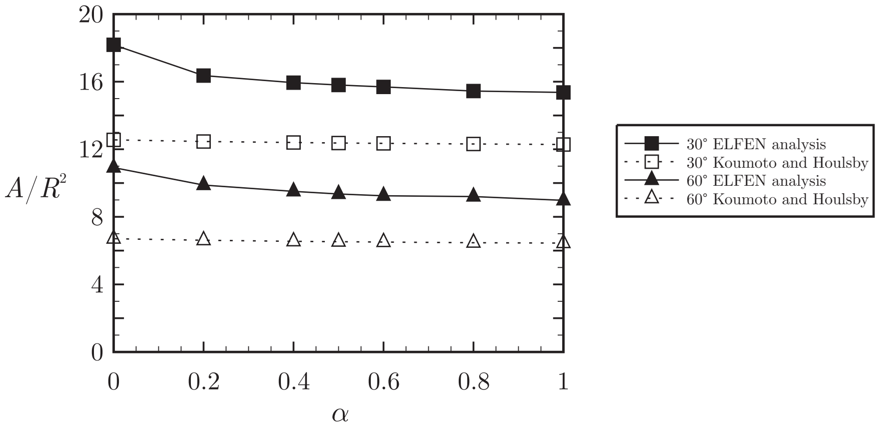

Figure 3.19: Change in normalized contact area with increasing adhesion factor α for 30° and 60° cones. Dotted lines indicate results derived from the work of Koumoto and Houlsby (2001)

3.3.6 Rough cones: frictional force contribution

Once the values of N_{ch} and A/R^2 are known for a particular combination of α and β, it is simple to determine the contribution of the frictional shear force Q_{s} to the total force Q from

$$\frac{Q_{\mathrm{s}}}{Q} = \frac{\alpha s_{\mathrm{u}} A \cos(\beta/2)}{\pi R^2 N_{\mathrm{ch}} s_{\mathrm{u}}} = \frac{\alpha \left(A/R^2\right) \cos(\beta/2)}{\pi N_{\mathrm{ch}}}. \tag{3.16}$$

The results of this calculation are shown in Figure 3.20. Q_{s}/Q is largest when $\alpha = 1$ and $\beta = 30°$. This is confirmed by inspection of Equation 3.16: maximising the left-hand side requires that α be large and β small. In this case the shear stress on the cone contributes almost half of the total force. Performing the same calculation using only the contact area above the original sample surface level revealed that, for the case with $\alpha = 1$ and $\beta = 30°$, almost 10% of the cone resistance came from the shear stress between the cone and the displaced lip.

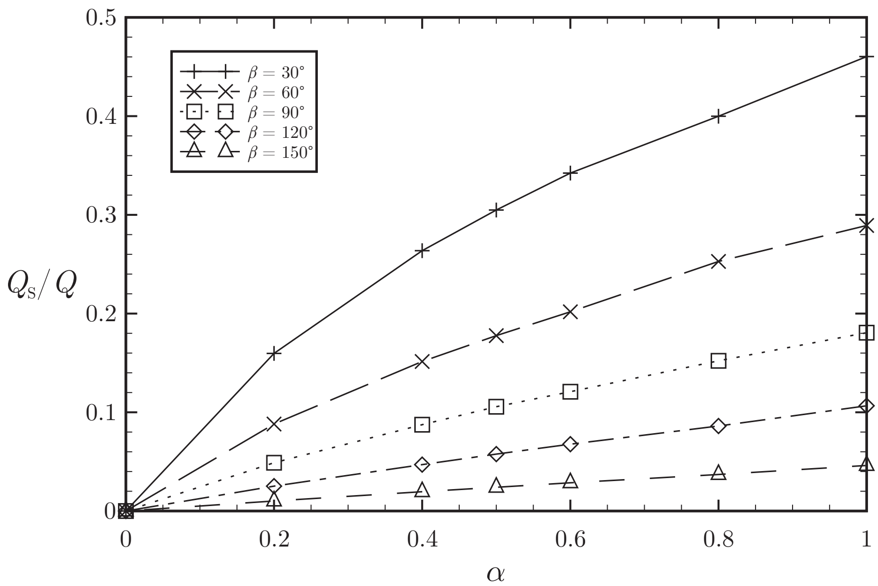

Figure 3.20: Ratio of shear force Q_{s} to total force Q for various combinations of α and β

3.3.7 Influence of displaced material

The present analysis takes account of the presence of a lip of material displaced by the cone, which contributes significantly to the resistance Q in certain cases. As an alternative means of assessing this contribution, the ratio $\lambda = N_{\mathrm{ch}}/N_{\mathrm{c}}$ is plotted in Figure 3.21a. N_{ch} is the cone bearing capacity factor taking account of displaced material and N_{c} is the factor for a "dug-in" conical footing with a flat surface around it. The variation of λ with cone angle β is shown, for fully smooth ($\alpha = 0$) and fully rough ($\alpha = 1$) cones. The values of N_c were taken from Koumoto and Houlsby (2001). The variation of λ given by Koumoto and Houlsby is shown in Figure 3.21b.

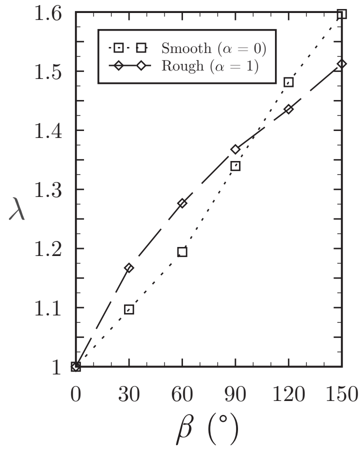

(a) ELFEN

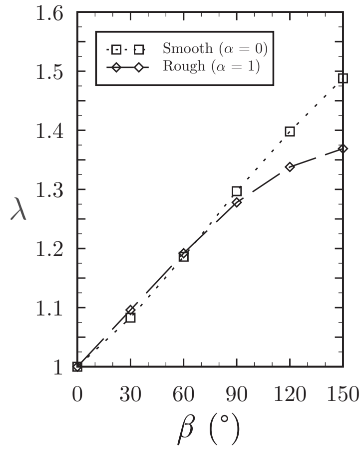

(b) Koumoto and Houlsby (2001)

Figure 3.21: Variation of ratio $\lambda = N_{ch}/N_c$ with cone angle

Chapter 4

Abaqus analysis with rate-independent material

The remainder of the analyses presented in this thesis were performed using Abaqus/Explicit (Simulia, 2007), as this software was more readily available to the author. Implementing a material obeying the Tresca yield criterion was not as straightforward as it had been in ELFEN. In that program, the Tresca criterion may be obtained as a limiting case of the Mohr–Coulomb model, by setting the friction angle ϕ to 0. In Abaqus/Standard (which uses an implicit solver), the Tresca model is also available as a special case of Mohr–Coulomb, though with questionable treatment of the flow rule – a piecewise-elliptic plastic potential is used. The Mohr–Coulomb model is not available in Abaqus/Explicit, however. Since the explicit method was felt to be advantageous for use in these analyses (as discussed in Section 3.1.3), a VUMAT user subroutine was written to implement the required model. The subroutine, written in Fortran, is called by the main Abaqus/Explicit executable to implement the constitutive model. It takes the stresses at a point at the start of an increment, together with the strains to be applied during the increment, and returns the new stress at the end of the increment. The implementation is valid for two-dimensional plane strain and axisymmetric stress states.

4.1 Integration of material model

4.1.1 Introduction to return mapping methods

The integration of the equations describing material behaviour is one of the key parts in any analysis by the finite element (FE) method. One of the most widely-used approaches is based on the radial return mapping method proposed by Wilkins (1964) and Maenchen and Sack (1964) for use with the von Mises yield criterion. The idea is quite simple in concept: the stress is first updated assuming the material remains elastic. If the elastic trial stress obtained in this way lies outside the yield surface, the stress is projected onto the closest point on the yield surface. This projection or stress return ensures that the stress at the end of the increment does not violate the yield condition. The return is radial for a Von Mises material as the yield surface is circular in section. The method has been generalised for use with other convex yield surfaces, though the return is not radial in general.

Figure 4.1 shows a schematic view of the stress return scheme. At the start of an increment the stress at the point under consideration is $\boldsymbol{\sigma}^{\mathrm{A}}$, which is shown in the elastic region ($f < 0$, where f is the yield function), but could equally well lie on the yield surface ($f = 0$). The elastic predictor increment is shown as $\Delta\boldsymbol{\sigma}^{\mathrm{e}}$, and leads to the trial stress $\boldsymbol{\sigma}^{\mathrm{B}}$. The addition of the plastic corrector increment $-\Delta\boldsymbol{\sigma}^{\mathrm{p}}$ returns the stress to the final point $\boldsymbol{\sigma}^{\mathrm{C}}$, on the yield surface.

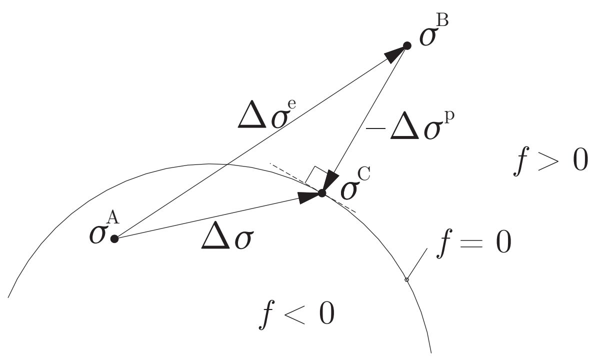

Figure 4.1: Schematic view of stress return

The radial return method is inexpensive due to its simplicity, but still gives good accuracy. Many algorithms developed subsequently have been shown to be inferior in terms of simplicity and accuracy (see e.g. Krieg and Krieg, 1977; Ortiz and Popov, 1985).

Radial return methods belong to the class of implicit integration schemes, so are unconditionally stable. Explicit integration of the constitutive model is also possible, for example by a forward Euler method. Explicit methods have the advantage of simplicity (though implicit methods can also result in very straightforward implementations as we shall see), but it is possible for the solution to drift gradually away from the yield surface over many time steps as the process does not ensure that the yield condition is satisfied at the end of an increment (Dunne and Petrinic, 2005).

Note that the choice of an implicit or explicit method for integration of the constitutive model is independent of whether the code itself is implicit or explicit, as described in Section 3.1. Both Abaqus and ELFEN use backward Euler (implicit) stress return schemes within their explicit FE solvers by default.

4.1.2 Yield surfaces with singularities

The Mohr–Coulomb yield criterion commonly used in soil mechanics, and the Tresca model adopted here (which is a special case of Mohr–Coulomb), are formulated as linear functions of the principal stresses. The yield surfaces are composed of a series of planes in principal stress space, and where these planes intersect the derivatives of the yield function become singular. This happens where two planes meet along a line or where three or more planes meet at a point. Careful treatment is required when stresses are to be returned to these discontinuities, since implicit stress return schemes generally require the derivatives of the yield function, and the first and second derivatives of the plastic potential (which may be the same as the yield function for associated flow).

Koiter (1953) provided a generalisation of plasticity theory to accommodate singularities, but nevertheless the most common way to deal with the problem has been to replace the true, multi-planar yield surface with a curved approximation, at least in the vicinity of a discontinuity. Early examples (such as Nayak and Zienkiewicz, 1972) effectively replaced the singular yield surface by one of the existing differentiable yield functions in the neighbourhood of the corner (for example, replacing the Tresca criterion by that of Von Mises). This had the disadvantage of introducing new corners where the two functions intersected. Later examples of the approach ensured a smooth transition between the regular plane surface and the curved approximation at the corner. Examples include Sloan and Booker (1986), Abbo and Sloan (1995), and Smith and Griffiths (1998). However, the large curvature close to the corner of such a yield surface is itself problematic, since Ortiz and Popov (1985) showed that strongly curved parts of the yield surface were associated with poor accuracy and stability.

The stress return method employed here involves carrying out the return mapping in three-dimensional principal stress space, where the ease of visualising stress states facilitates a geometric approach. Simple formulae for the stress update are obtained using basic matrix notation, and the resulting algorithm is substantially simpler than many based on more general tensor algebra. Clausen et al. (2006) give a useful description of this approach, which they apply to a Mohr–Coulomb material. Significant further simplifications are possible when, as here, the method is used with a Tresca material.

The simplicity of the algorithm does not come at the cost of accuracy or speed, however. The method requires no iteration, and the procedure is exact within the framework of the return mapping scheme. Despite the overhead associated with transforming the stresses to principal stress space, Clausen et al. (2006) showed their method to be faster than a conventional implementation of the Mohr–Coulomb criterion, where stresses were expressed in terms of invariants (the method used for comparison was that of Crisfield, 1997). For a return to a line (the intersection of two planes of the yield surface), the method of Clausen et al. was faster by 48%.

4.1.3 Details of general return mapping scheme

The following derivations follow the notation of Clausen et al. (2006). Bold symbols denote vectors or matrices, and a superscript 'T' denotes a vector transpose.

A material yields when the value of the yield function $f(\boldsymbol{\sigma})$ becomes zero. Here $\boldsymbol{\sigma}$ is the stress tensor in Voigt notation (that is, represented as a column matrix). Under the assumption of an associated flow rule, the infinitesimal plastic strain increment is

$$\mathrm{d}\boldsymbol{\varepsilon}^{\mathrm{p}} = \mathrm{d}\lambda \frac{\partial f}{\partial \boldsymbol{\sigma}} = \mathrm{d}\lambda \mathbf{a}, \tag{4.1}$$

where $\frac{\partial f}{\partial \boldsymbol{\sigma}} = \nabla f = \mathbf{a}$ is the gradient of the yield function and $\mathrm{d}\lambda$ is a non-negative plastic multiplier.

If a strain increment $\Delta\boldsymbol{\varepsilon}$ is imposed between increments j and $j+1$ of the analysis, the stresses are updated according to

$$\Delta\boldsymbol{\sigma} = \int_{\boldsymbol{\varepsilon}_j}^{\boldsymbol{\varepsilon}_j + \Delta\boldsymbol{\varepsilon}} \mathbf{D}^{\mathrm{ep}}(\boldsymbol{\sigma})\ \mathrm{d}\boldsymbol{\varepsilon} \tag{4.2}$$

where $\boldsymbol{\varepsilon}_j$ is the total strain after increment j and $\mathbf{D}^{\mathrm{ep}}$ the infinitesimal elasto-plastic constitutive matrix.

Since $\mathbf{D}^{\mathrm{ep}}$ is highly dependent on $\boldsymbol{\sigma}$, approximate solutions to Equation 4.2 are usually used. As seen in Section 4.1.1, the basic assumption of the return mapping scheme is that the strain increment $\mathrm{d}\boldsymbol{\varepsilon}$ is made up of an elastic contribution $\mathrm{d}\boldsymbol{\varepsilon}^{\mathrm{e}}$ and a plastic contribution $\mathrm{d}\boldsymbol{\varepsilon}^{\mathrm{p}}$ so that

$$\mathrm{d}\boldsymbol{\varepsilon} = \mathrm{d}\boldsymbol{\varepsilon}^{\mathrm{e}} + \mathrm{d}\boldsymbol{\varepsilon}^{\mathrm{p}}. \tag{4.3}$$

The elastic stress increment is found by applying Hooke's law

$$\mathrm{d}\boldsymbol{\sigma} = \mathbf{D}\mathrm{d}\boldsymbol{\varepsilon}^{\mathrm{e}} = \mathbf{D}\left(\mathrm{d}\boldsymbol{\varepsilon} - \mathrm{d}\boldsymbol{\varepsilon}^{\mathrm{p}}\right) \tag{4.4}$$

where $\mathbf{D}$ is the elastic constitutive matrix.

Equations 4.1 and 4.4 lead to

$$\mathrm{d}\boldsymbol{\sigma} = \mathbf{D}\mathrm{d}\boldsymbol{\varepsilon} - \mathrm{d}\lambda\mathbf{D}\mathbf{a}. \tag{4.5}$$

Integration of the above leads to the return mapping scheme of Figure 4.1:

$$\Delta\boldsymbol{\sigma} = \Delta\boldsymbol{\sigma}^{\mathrm{e}} - \Delta\boldsymbol{\sigma}^{\mathrm{p}} \quad \text{or} \quad \boldsymbol{\sigma}^{\mathrm{C}} = \boldsymbol{\sigma}^{\mathrm{B}} - \Delta\boldsymbol{\sigma}^{\mathrm{p}} \tag{4.6}$$

where $\Delta\boldsymbol{\sigma}^{\mathrm{e}} = \mathbf{D}\mathrm{d}\boldsymbol{\varepsilon}$ is the elastic predictor increment and $-\Delta\boldsymbol{\sigma}^{\mathrm{p}}$ the plastic corrector. The final stress $\boldsymbol{\sigma}^{\mathrm{C}}$ is obtained from the trial stress by subtracting $\Delta\boldsymbol{\sigma}^{\mathrm{p}}$, which is given by

$$\Delta\boldsymbol{\sigma}^{\mathrm{p}} = \int_{\lambda}^{\lambda+\Delta\lambda} \mathbf{D}\mathbf{a}\,\mathrm{d}\lambda. \tag{4.7}$$

In general, this is evaluated numerically as

$$\Delta\boldsymbol{\sigma}^{\mathrm{p}} = \Delta\lambda\mathbf{D}\,\mathbf{a}|_{\mathrm{P}} \tag{4.8}$$

where the subscript P denotes the point on the integration path at which $\mathbf{a}$ is to be evaluated. In the backward Euler scheme, iteration is required since P corresponds to $\boldsymbol{\sigma}^{\mathrm{C}}$, the unknown final stress state. However, in the case of a yield criterion that is linear in the principal stresses (such as Tresca's), $\mathbf{a}$ is constant along the integration path; it can therefore be evaluated at $\boldsymbol{\sigma}^{\mathrm{B}}$ with no loss of accuracy.

4.1.4 Return mappings with linear yield functions

After determining the elastic predictor stress from Equation 4.4, the next step is to transform the stresses into principal stress space. The stress is then returned to the yield surface in principal stress space, then transformed back to the original coordinate system. The transformation can be easily reversed since the principal stress directions are unchanged during the return to the yield surface (the shear stresses remain zero). In this section, all manipulations are performed in principal stress space, so that the shear components of the stress and strain tensors are zero. They will be omitted for convenience.

Three distinct possibilities for the stress return are considered by Clausen et al. (2006). First, a return to a point lying on a single yield plane. Second, a return to a point on the line formed by the intersection of two planes. The final possibility is a return to a point, the intersection of three or more yield planes. Stress returns for the three cases will be discussed here in general terms. Examples will then be given of how the general formulae reduce to particularly simple forms for the Tresca material of interest here. The third case (return to a point) will not be required for a Tresca material, but will be discussed in any case; it is trivial.

The general form of the stress return equations is derived here, together with examples of the simplifications that result when the general forms are applied to Tresca materials. Full details of the VUMAT are given in Appendix A, and the Fortran source code is in Appendix B.

The Tresca yield criterion

Before considering the stress return in detail, the representation of the Tresca yield criterion in principal stress space will be introduced. The yield surface takes the form of a hexagonal prism aligned with the line $\sigma_1 = \sigma_2 = \sigma_3$, and can be defined by the six yield functions

$$
\begin{aligned}
f_1(\boldsymbol{\sigma}, s_\mathrm{u}) &= \sigma_1 - \sigma_2 - 2s_\mathrm{u} & \qquad f_2(\boldsymbol{\sigma}, s_\mathrm{u}) &= \sigma_2 - \sigma_1 - 2s_\mathrm{u} \\
f_3(\boldsymbol{\sigma}, s_\mathrm{u}) &= \sigma_2 - \sigma_3 - 2s_\mathrm{u} & \qquad f_4(\boldsymbol{\sigma}, s_\mathrm{u}) &= \sigma_3 - \sigma_2 - 2s_\mathrm{u} \\
f_5(\boldsymbol{\sigma}, s_\mathrm{u}) &= \sigma_3 - \sigma_1 - 2s_\mathrm{u} & \qquad f_6(\boldsymbol{\sigma}, s_\mathrm{u}) &= \sigma_1 - \sigma_3 - 2s_\mathrm{u}.
\end{aligned}
\tag{4.9}
$$

For $i = 1, \ldots, 6$, the equation $f_i(\boldsymbol{\sigma}, s_\mathrm{u}) = 0$ corresponds to a plane S_i in principal stress space. These six yield planes are shown in Figure 4.2. Since the implementation described here is for plane strain and axisymmetric stress states, the out-of-plane stress is known to be one of the principal stresses (σ_3, say). Of the two in-plane principal stresses, if the ordering of σ_1 and σ_2 is such that $\sigma_1 > \sigma_2$ then we may consider only stress returns to one half-space as shown in Figure 4.2. The relative size of the third stress σ_3 is unknown (in axial symmetry, σ_3 is not necessarily intermediate as seen in Section 3.3.3). Stresses may need to be returned to any of the planes S_1, S_4 or S_6, or the lines at the edges of these planes (L_{45}, L_{14}, L_{61} or L_{36}).

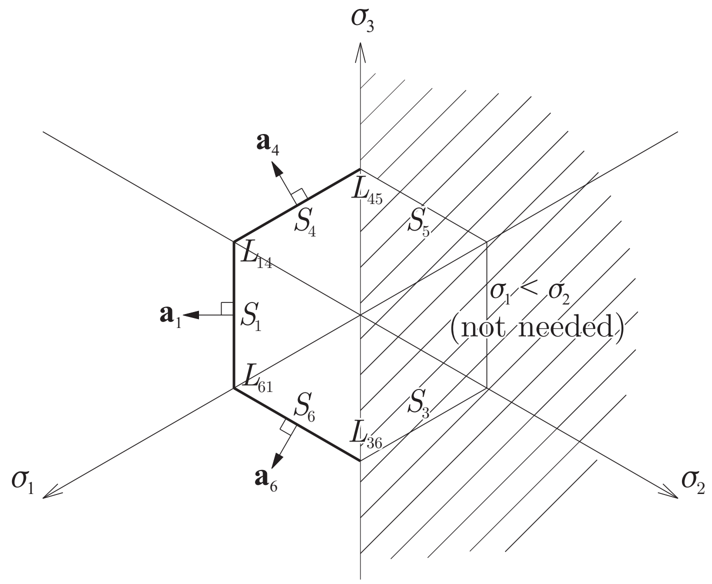

Figure 4.2: Plane surfaces S_i which form the Tresca yield surface. Only the $\sigma_1 > \sigma_2$ half-space is shown in detail. Also shown are the directions of the gradients $\mathbf{a}_i$ of the yield functions and the lines L_{ij} on which planes S_i and S_j intersect.

Return to a plane

In general, a yield criterion that involves only linear functions of the principal stresses can be expressed as

$$f(\boldsymbol{\sigma}) = \mathbf{a}^{\mathrm{T}}\left(\boldsymbol{\sigma} - \boldsymbol{\sigma}^f\right) = 0 \tag{4.10}$$

where $\mathbf{a} = [a_1\ a_2\ a_3]^{\mathrm{T}}$ is the gradient of the yield plane in principal stress space and $\boldsymbol{\sigma}^f$ is a point on the plane.

When returning the stress state to a plane, the well-known solution for the incremental plastic multiplier $\Delta\lambda$ (see e.g. Crisfield, 1997) can be used:

$$\Delta\lambda = \frac{f}{\mathbf{a}^{\mathrm{T}}\mathbf{D}\mathbf{a}}\,. \tag{4.11}$$

$\Delta\lambda$ is the scalar quantity that determines the magnitude of the plastic corrector stress increment $-\Delta\boldsymbol{\sigma}^{\mathrm{p}}$ (Equation 4.8). For principal stresses, the elastic constitutive matrix $\mathbf{D}$ is given by

$$\mathbf{D} = \frac{E}{(1+\nu)(1-2\nu)} \begin{bmatrix} 1-\nu & \nu & \nu \\ \nu & 1-\nu & \nu \\ \nu & \nu & 1-\nu \end{bmatrix}. \tag{4.12}$$

Taking the solution for $\Delta\lambda$ together with Equation 4.8 gives the plastic corrector as

$$\Delta\boldsymbol{\sigma}^{\mathrm{p}} = \frac{f\left(\boldsymbol{\sigma}^{\mathrm{B}}\right)}{\mathbf{a}^{\mathrm{T}}\mathbf{D}\mathbf{a}}\mathbf{D}\mathbf{a} = f\left(\boldsymbol{\sigma}^{\mathrm{B}}\right)\mathbf{r}^{\mathrm{p}}, \quad \text{where} \quad \mathbf{r}^{\mathrm{p}} = \frac{\mathbf{D}\mathbf{a}}{\mathbf{a}^{\mathrm{T}}\mathbf{D}\mathbf{a}}. \tag{4.13}$$

In general, the plastic corrector will be at an angle to $\mathbf{a}$ that depends on Poisson's ratio ν.

When Tresca's yield criterion is used, further simplifications result. Taking plane S_1 (shown in Figure 4.2) as an example, $\mathbf{a} = [1, -1, 0]^{\mathrm{T}}$. Substituting for $\mathbf{a}$ and $\mathbf{D}$ in Equation 4.13 gives $\mathbf{r}^{\mathrm{p}} = [1/2, -1/2, 0]^{\mathrm{T}}$, so that the stress at the end of the increment, $\boldsymbol{\sigma}^{\mathrm{C}} = \boldsymbol{\sigma}^{\mathrm{B}} - \Delta\boldsymbol{\sigma}^{\mathrm{p}}$, is given simply by

$$\boldsymbol{\sigma}^{\mathrm{C}} = \begin{bmatrix} \sigma_1^{\mathrm{B}} \\ \sigma_2^{\mathrm{B}} \\ \sigma_3^{\mathrm{B}} \end{bmatrix} - \begin{bmatrix} 1/2 \\ -1/2 \\ 0 \end{bmatrix} f_1 \tag{4.14}$$

where the yield function f_1 is evaluated at the trial stress $\boldsymbol{\sigma}^{\mathrm{B}}$.

Similar expressions can be obtained for the other planes that make up the Tresca yield surface. The values of $\Delta\boldsymbol{\sigma}^{\mathrm{p}}$ are given in Appendix A.

Return to a line

A line in principal stress space can be represented parametrically as

$$\boldsymbol{\sigma} = t\mathbf{r}^{l} + \boldsymbol{\sigma}^{l} \tag{4.15}$$

where t is a parameter with the dimensions of stress, $\mathbf{r}^{l}$ is a vector in the direction of the line and $\boldsymbol{\sigma}^{l}$ is a point in principal stress space that lies on the line.

With an associated flow rule, the direction $\mathbf{a}$ of the plastic strain increment must be perpendicular to $\mathbf{r}^{l}$. From this orthogonality condition and Equation 4.6 (substituting for

$\boldsymbol{\sigma}^{\mathrm{C}}$ from 4.15 and $\Delta\boldsymbol{\sigma}^{\mathrm{p}}$ from 4.8), a system of equations can be obtained:

$$\begin{aligned} &\Delta\lambda\mathbf{a} = \mathbf{D}^{-1}\left(\boldsymbol{\sigma}^{\mathrm{B}} - \left(t\mathbf{r}^{l} + \boldsymbol{\sigma}^{l}\right)\right) \\ &\mathbf{a}^{\mathrm{T}}\mathbf{r}^{l} = 0 \end{aligned} \tag{4.16}$$

Solving for t gives

$$t = \frac{\left(\mathbf{r}^{l}\right)^{\mathrm{T}}\mathbf{D}^{-1}\left(\boldsymbol{\sigma}^{\mathrm{B}} - \boldsymbol{\sigma}^{l}\right)}{\left(\mathbf{r}^{l}\right)^{\mathrm{T}}\mathbf{D}^{-1}\mathbf{r}^{l}} \tag{4.17}$$

and the final stress $\boldsymbol{\sigma}^{\mathrm{C}}$ is obtained by inserting this value of t into Equation 4.15.

As an example for the Tresca model, consider a stress return to line L_{14} (the intersection of planes S_1 and S_4). With $\mathbf{r}^{l} = [1,1,1]^{\mathrm{T}}$ and $\boldsymbol{\sigma}^{l} = [0, -2s_{\mathrm{u}}, 0]^{\mathrm{T}}$, Equation 4.17 gives

$$t = \tfrac{1}{3}\left(\sigma_1^{\mathrm{B}} + \sigma_2^{\mathrm{B}} + \sigma_3^{\mathrm{B}}\right) + \tfrac{2}{3}\left(s_{\mathrm{u}}\right). \tag{4.18}$$

Hence, from Equation 4.15,

$$\boldsymbol{\sigma}^{\mathrm{C}} = t\mathbf{r}^{l} + \boldsymbol{\sigma}^{l} = \begin{bmatrix} \frac{1}{3}\left(\sigma_1^{\mathrm{B}} + \sigma_2^{\mathrm{B}} + \sigma_3^{\mathrm{B}}\right) + \frac{2}{3}\left(s_{\mathrm{u}}\right) \\ \frac{1}{3}\left(\sigma_1^{\mathrm{B}} + \sigma_2^{\mathrm{B}} + \sigma_3^{\mathrm{B}}\right) + \frac{2}{3}\left(s_{\mathrm{u}}\right) \\ \frac{1}{3}\left(\sigma_1^{\mathrm{B}} + \sigma_2^{\mathrm{B}} + \sigma_3^{\mathrm{B}}\right) + \frac{2}{3}\left(s_{\mathrm{u}}\right) \end{bmatrix} + \begin{bmatrix} 0 \\ -2s_{\mathrm{u}} \\ 0 \end{bmatrix}. \tag{4.19}$$

For ease of implementation, this can be manipulated into a similar form to Equation 4.14, as $\boldsymbol{\sigma}^{\mathrm{C}} = \boldsymbol{\sigma}^{\mathrm{B}} - \Delta\boldsymbol{\sigma}^{\mathrm{p}}$:

$$\boldsymbol{\sigma}^{\mathrm{C}} = \begin{bmatrix} \sigma_1^{\mathrm{B}} \\ \sigma_2^{\mathrm{B}} \\ \sigma_3^{\mathrm{B}} \end{bmatrix} - \begin{bmatrix} \frac{2}{3} & -\frac{1}{3} \\ -\frac{1}{3} & -\frac{1}{3} \\ -\frac{1}{3} & \frac{2}{3} \end{bmatrix} \begin{bmatrix} f_1 \\ f_4 \end{bmatrix} \tag{4.20}$$

Appendix A gives the stress returns for the other corners of the Tresca yield surface.

Return to a point

If the stress is to be returned to a point, no calculations are necessary. If the point is $\boldsymbol{\sigma}^{a}$ then $\boldsymbol{\sigma}^{\mathrm{C}} = \boldsymbol{\sigma}^{a}$. This case does not arise for a Tresca material.

4.1.5 Determining the type of stress return required

Clausen et al. (2006) introduced the concept of *stress regions* to determine the type of stress return required for a given elastic trial stress $\boldsymbol{\sigma}^{\mathrm{B}}$. Each plane, line or point on the yield surface has a region of principal stress space associated with it, and when $\boldsymbol{\sigma}^{\mathrm{B}}$ lies in a particular region the stress should be returned to the associated plane, line or point.

When the yield functions are planes, the region boundaries will themselves be planes. The orientation of the boundary between the regions for the plane S_i and its edge L_{ij} is defined by the direction $\mathbf{r}_i^{\mathrm{p}}$ of the plastic corrector for the plane, and the direction of the line $\mathbf{r}_{ij}^{l}$. The normal $\mathbf{n}_{i-ij}^{\mathrm{T}}$ to the boundary plane is given by the cross product $\mathbf{r}_i^{\mathrm{p}} \times \mathbf{r}_{ij}^{l}$, so the equation of the boundary plane is

$$p_{i-ij}\left(\boldsymbol{\sigma}\right) = \mathbf{n}_{i-ij}^{\mathrm{T}}\left(\boldsymbol{\sigma} - \boldsymbol{\sigma}^{l}\right) = \left(\mathbf{r}_i^{\mathrm{p}} \times \mathbf{r}_{ij}^{l}\right)^{\mathrm{T}}\left(\boldsymbol{\sigma} - \boldsymbol{\sigma}^{l}\right) = 0. \tag{4.21}$$

The stress region boundaries planes for Tresca's yield criterion with associated flow are shown as dotted lines in Figure 4.3. The boundaries of the stress region associated with each face of the yield surface are a pair of planes perpendicular to the relevant face, passing through the lines at the edges of that face. The stress regions associated with lines are bounded by planes passing through that line, perpendicular to the two faces that meet at that line.

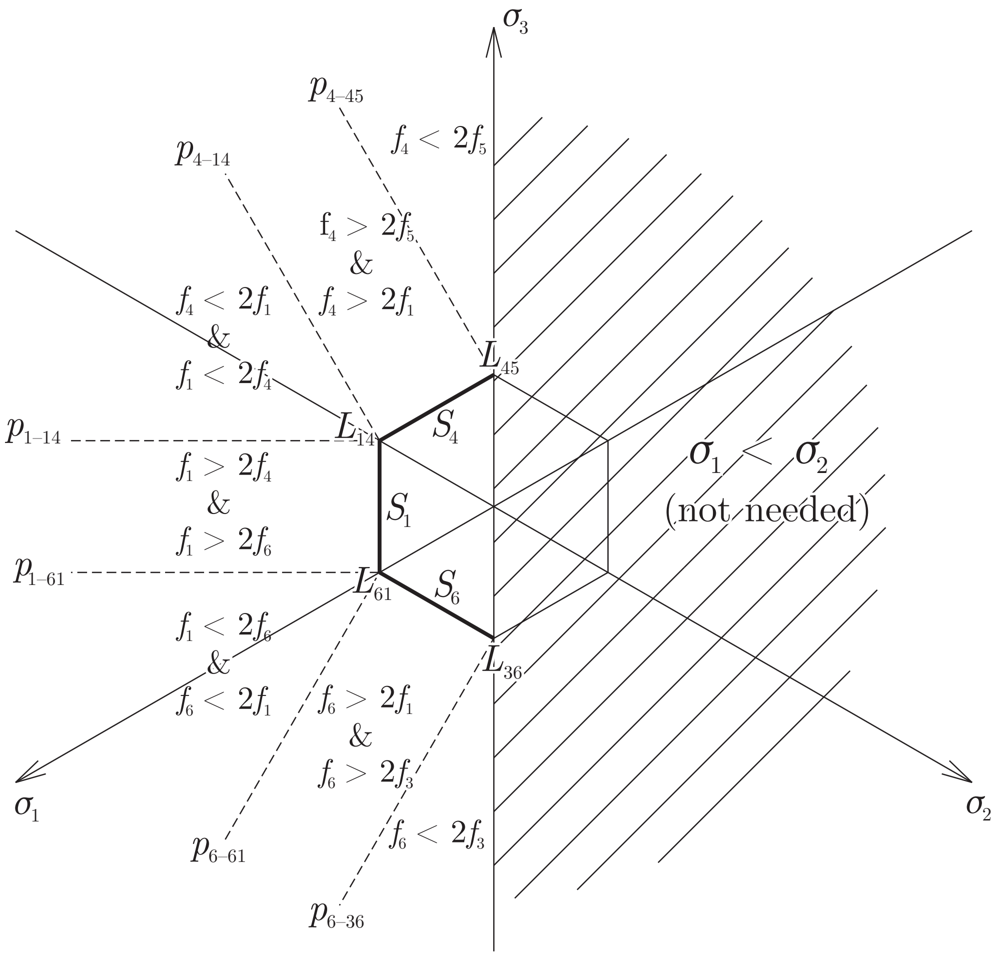

Figure 4.3: Boundaries of stress regions associated with returns to the planes S_i and lines L_{ij} of the Tresca yield surface. Region boundaries (p_{i-ij}) are shown as dotted lines. Expressions relating values of yield functions f_i in each region are also shown.

The specific geometry of the Tresca yield surface means that simple relationships exist between the values of the yield functions on the stress region boundaries. For example, Figure 4.4 shows a point $\boldsymbol{\sigma}_{4-14}$ in principal stress space that lies on the boundary plane p_{4-14}. At any point on this plane, $f_4 = 2f_1$. The plane therefore separates principal stress space into two half-spaces: one in which $f_4 > 2f_1$ and one in which $f_4 < 2f_1$. Similar relationships can be derived for the other boundary planes. The resulting inequalities are shown in Figure 4.3.

By reference to these inequalities, the stress region in which a particular elastic trial stress $\boldsymbol{\sigma}^{\mathrm{B}}$ lies can easily be determined from the values of the yield functions at that stress, $f_i\left(\boldsymbol{\sigma}^{\mathrm{B}}\right)$. For example, if $f_1 > 2f_4$ and $f_1 > 2f_6$, the final stress $\boldsymbol{\sigma}^{\mathrm{C}}$ lies on plane S_1 of the yield surface and the correct stress return is given by Equation 4.14.

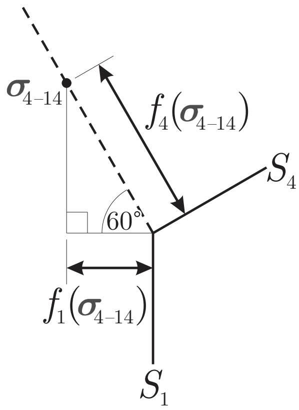

Figure 4.4: Relationship between yield function values on a stress region boundary

4.2 Validation of model: wedge indentation

In order to check the correct functioning of the VUMAT material model, various example problems were analysed. The first of these (other than simple single-element tests) was an analysis of the indentation of a rigid–plastic block (representing e.g. clay) by a rigid wedge, a problem that may be regarded as the plane strain analogue of the cone indentation problem that is the focus of this thesis.

4.2.1 Previous solutions

Wedge indentation was chosen as a validation problem for the Abaqus model because it shares many features with the cone problem, but high quality existing solutions are available. Continuous indentation with a smooth wedge was investigated by Hill et al. (1947) using the method of characteristics. The analysis was repeated by Grunzweig et al. (1954), who also gave results for rough wedges.

The mechanism given by Hill et al. is shown in Figure 4.5. Rigid–plastic material is indented by a smooth wedge, of which AB is one face. The surface of the indented material was initially horizintal and lay on OC. In the deformed configuration the free surface is a straight line AC, of length l_{AC}. The speed is the same throughout the deforming region, and is equal to $V\sqrt{2}\sin\frac{\beta}{2}$ where V is the downward velocity of the wedge. At any instant region ABD moves as a rigid block parallel to BD (at 45° to the face of the wedge). ADE is a region of diffuse shear, with material moving on curved paths parallel to arc DE centred at A. AEC moves as a rigid block parallel to EC (at 45° to AC).

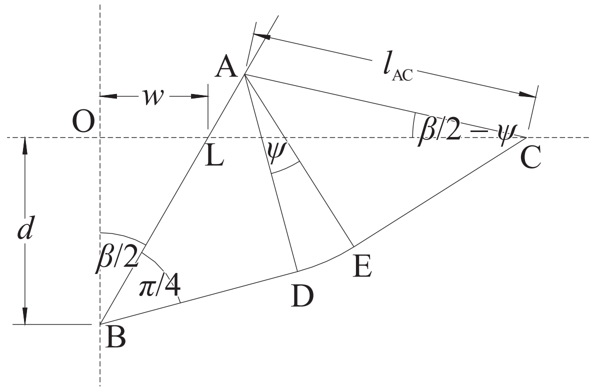

Figure 4.5: Indentation of a plane surface by a smooth wedge, mechanism from Hill et al. (1947)

Hill et al. derived the relationship between the angles β and ψ as

$$\cos(\beta-\psi)=\frac{\cos\psi}{1+\sin\psi}. \tag{4.22}$$

The pressure p normal to the face of the wedge was found to be $2s_{\mathrm{u}}(1+\psi)$. For given β, Equation 4.22 can be solved for ψ, allowing the load on the wedge per unit width to be found as

$$Q=2pl_{\mathrm{AC}}\sin\tfrac{\beta}{2}=4s_{\mathrm{u}}l_{\mathrm{AC}}(1+\psi)\sin\tfrac{\beta}{2}. \tag{4.23}$$

4.2.2 Abaqus analysis

An Abaqus/Explicit model was created to analyse the wedge indentation problem with the VUMAT subroutine described in Appendix A. Some features of the analysis are described below.

Geometry of model

The dimensions of the model were as given in Figure 3.1, with the important difference that the diagram now represents a section through a plane strain model of a wedge (of angle β) indenting a sample of material held in a rigid semicylindrical vessel of radius 27.5 mm. The symmetry of the model was exploited by considering only the right-hand half of the model.

The final depth of the indentation varied with the wedge angle (to ensure the boundary of the sample did not affect the results). The 30° wedge was pushed in by 12 mm, the 60° wedge by 8 mm, and the 60° wedge by 7 mm.

Material properties

The indented material had the same undrained strength as in Section 3.1 ($s_\mathrm{u} = 1\,\mathrm{kPa}$), and the Poisson's ratio was also unchanged ($\nu = 0.49$, approximately incompressible) but the Young's modulus was lower ($E = 0.447\,\mathrm{MPa}$), meaning that the rigidity index I_R was 150. It was considered that this would still be sufficient to approximate rigid–plastic behaviour while giving shorter run-times for the analyses (recall that the stable time increment in an explicit analysis depends on the elastic wavespeed, see Equation 3.11). The density of the material was $1800\,\mathrm{kg/m^3}$.

Choice of element type

As in the ELFEN FE model described in Section 3.2, first order quadrilateral elements with reduced (single-point) integration were used. Some of the advantages of such elements were described previously. In addition, these elements have the advantage of being compatible with Abaqus/Explicit's Arbitrary Langrangian Eulerian (ALE) adaptive meshing (which can only be used with reduced-integration first order elements). ALE adaptivity was not used for these plane strain analyses, but will be introduced in some of the work presented later in the thesis.

In Abaqus, various methods of preventing zero-energy or hourglass modes are provided for use with reduced-integration elements. The default "integral viscoelastic" approach was used here, and involves applying a force Q to resist the excitation of an hourglass mode. Q is given by

$$Q = \int_0^t K(t-t')\frac{\mathrm{d}q}{\mathrm{d}t}\mathrm{d}t' \qquad (4.24)$$

where K is an hourglass stiffness (which is chosen automatically), and q is the magnitude of the hourglass mode deformation (Simulia, 2007).

Wedge–clay interface

To avoid unnecessarily increasing the number of degrees of freedom in the model, the wedge was modelled as an unmeshed analytical rigid body. The motion of the wedge could then be defined by considering only the motion of a single reference point, whereas in ELFEN the motions of all the nodes of the elements making up the wedge were tracked individually.

In order to enforce a "one-way" boundary condition on the axis of symmetry, the indented material was prevented from crossing the axis of symmetry by a smooth rigid "knife-edge" added to the front of the wedge. Unlike in the axisymmetric case the width of this knife-edge was of no significance, since all dimensions could be measured from its outer face.

The contact formulation used in Abaqus also differed from that used in ELFEN, as the kinematic contact enforcement method was used in place of the penalty algorithm. In each increment, Abaqus first finds a predicted configuration without considering contact. Based on the resulting penetration of nodes into the analytical rigid wedge surface, forces are found which would have caused the nodes to contact the surface exactly. By applying the resisting forces from all the nodes to the analytical body representing the wedge, and adding the masses of the contacting nodes to the rigid body, a corrected acceleration is found for the wedge. Acceleration corrections for the contacting nodes are obtained based on the analytical surface's acceleration.

The kinematic contact algorithm enforces contact constraints more strictly than a penalty method and conserves momentum, but some energy may be lost on impact. The energy involved is usually insignificant unless very high-speed impacts occur. Unlike the penalty method, the kinematic algorithm does not alter the stable time increment (Simulia, 2007).

Finite element mesh

The same mesh was used for the whole analysis, so the initial mesh refinement needed to be sufficient throughout. Although Abaqus/Explicit has an adaptive meshing capability, the method does not involve generating *new* meshes during the analysis but merely *smoothes* the existing mesh, maintaining element quality by shifting the nodal positions. It cannot be used to improve mesh density around the indenter, as in the analyses with ELFEN (Chapter

3). Since element distortions were not generally excessive, Abaqus's ALE adaptivity was not used in these plane strain analyses.

A rectangular area of the model, extending beyond the region to be deformed, was given a uniform structured mesh; away from the deforming region an unstructured mesh was used with decreasing mesh density as shown in Figure 4.6. The mesh illustrated, which was used for the 30° wedge, has the finer mesh covering a rectangular region 20 mm wide and 14 mm deep. For the 60° wedge the region was 20 mm wide and 10 mm deep, and for the 90° wedge it was 24 mm wide by 12 mm deep.

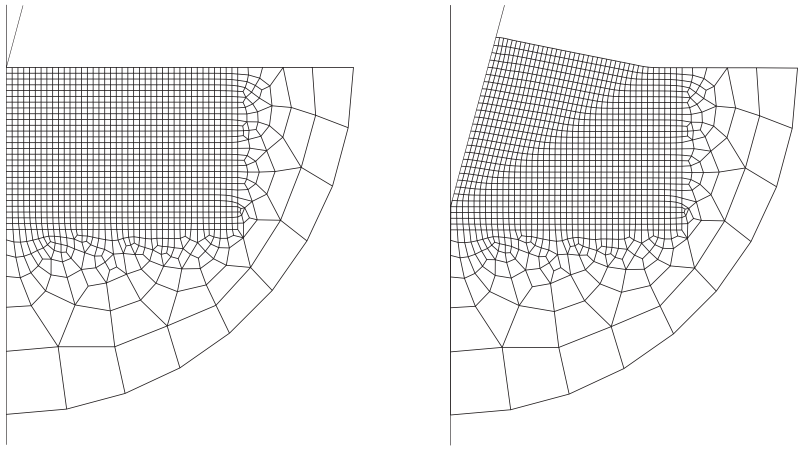

(a) Initial configuration, $t = 0$ s (b) Final configuration, $t = 1$ s

Figure 4.6: Mesh used in Abaqus analysis of indentation with a smooth wedge, $\beta = 30°$

The Abaqus analysis was repeated with three separate meshes: in the coarsest mesh the elements in the region closest to the wedge were squares of side 1 mm. In the medium and fine meshes this dimension was halved (to 0.5 mm) and halved again (to 0.25 mm). Figure 4.6 shows a medium mesh. The maximum element size on the periphery of the sample was not changed.

Soil self-weight

As in the earlier analyses of cone indentation using ELFEN, the self-weight of the indented material was not taken into account here. For similar reasons to those discussed in Section 3.2.6, it is believed that the self-weight has a relatively minor influence on the results that will be obtained. In addition, the intention is to verify the correct functioning of the VUMAT material model by comparing results with those obtained by Hill et al. (1947) using the method of characteristics – and neglecting the influence of self-weight.

4.2.3 Results

Figure 4.7 shows the load–displacement curves obtained using the finest of the three meshes, for smooth wedges with angles of 30°, 60° and 90°. The lines obtained from the results of Hill et al. (1947) are also plotted. In general, agreement is very good. A "saw-tooth" oscillation is visible in the Abaqus results shown, and was much more pronounced for the results with coarser meshes. The oscillation was caused by the repeated growth and disappearance of a small void between the wedge tip and the indented material, as shown in Figure 4.8. The effect would be less serious in an axisymmetric analysis because the same change in the *length* of contact at this point would correspond to a much smaller proportional change in *area*.

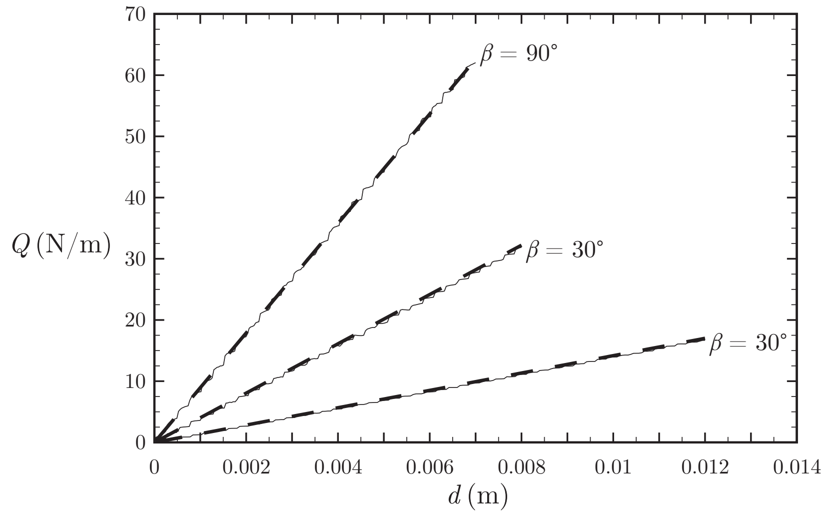

Figure 4.7: Load Q against depth of indentation d for smooth wedges. Solid lines show results of Abaqus analyses, heavy dashed lines show results of Hill et al. (1947)

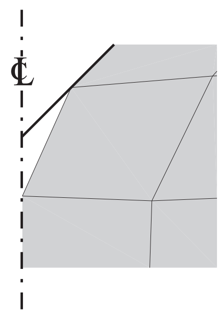

Figure 4.8: Magnified view of void between tip of 90° wedge and indented material

The wedge indentation loads may be presented in dimensionless form similarly to those for cones, by defining a bearing capacity factor $N_{\rm ch}$ that takes account of heave adjacent to the wedge:

$$N_{\mathrm{ch}} = \frac{Q}{s_{\mathrm{u}} w} \tag{4.25}$$

where Q is the force per unit length of wedge and w is the half-width of the wedge at the original soil surface level (Figure 4.5). Values of N_{ch} were obtained from the Abaqus results corresponding to the last peaks of the load-displacement curves, since at these points there was no error in the size of the contact area. Figure 4.9 compares the Abaqus results with the curve obtained from Equations 4.23 and 4.25. There is good agreement between the sets of results; the largest relative error is with $\beta = 30°$ when the Abaqus result lies 0.88% below that of Hill et al.

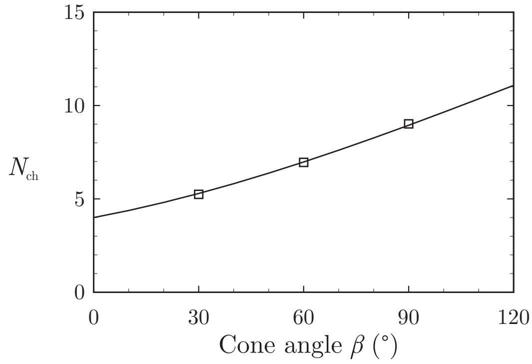

Figure 4.9: Bearing capacity factor N_{ch} against wedge angle β, for smooth wedges. Solid line (——) shows results of Hill et al. (1947) while squares (□) show Abaqus results

In order to make more detailed comparisons between the Abaqus results and those of Hill et al. (1947), a computer program was written to calculate displacements during continuous indentation, based on the velocities given by the analytical solution in Figure 4.5. The program was implemented in Matlab (MathWorks, 2007). The code took as input a grid of points within the material to be indented, coincident with the initial nodal locations of the Abaqus finite element mesh. The indentation was broken down into n increments, in each of which the wedge was displaced downwards by a distance $\Delta d = h/n$ where h is the final depth of the indentation. For each increment, the program determined the current position of the wedge and therefore in which region of the mechanism each point lay (based on the known values of β and ψ, and the current wedge displacement d). The velocity of the point could then be found, and simple numerical integration gave the displacement and the updated location of the point.

By taking the displaced grid points as the nodes of triangular constant strain triangles, rotations and strains could be calculated as described in Appendix C. Displacement data from Abaqus were also processed using the same Matlab script to enable direct comparison of the graphical output. Note that, while quadrilateral elements were used in the Abaqus analysis, the Matlab script calculated strains etc. using triangles, and these are the elements shown in the output. Figures 4.10, 4.11 and 4.12 show marker locations, rigid body rotations, and shear and volumetric strains for material indented by smooth 30°, 60° and 90° wedges. In the plots of marker locations, the point that was originally at the origin is shaded. Strains were re-calculated at each increment from the new marker positions, rather than being derived from the incremental strains in all previous increments.

In general, the graphical output shows good agreement between the Abaqus results (left column) and those obtained from the work of Hill et al.. The Abaqus results correctly show a mechanism with a rigid block adjacent to the wedge, another at the surface, and a fan region of diffuse shear between the two. Volumetric strain was close to zero everywhere, showing that the incompressibility condition was modelled well.[1] There are some differences between the sets of results, however. In general the Abaqus analyses show the extent of the deformation to be slightly less than in the reference results, which may be partly because the edge of the deforming region was less well-defined in Abaqus (an expected consequence of spatial discretization). The Abaqus shear strain plots also show bands of higher strain adjacent to the wedges that are not present in the analytical solution given by Hill et al..

[1] Some of the plotted values of ε_{v} are far from zero, but these occur as pairs of adjacent triangles with tensile and compressive values. Similar patterns can be seen in the Hill et al. results and reflect a limitation of the Matlab postprocessing rather than a problem with the Abaqus analysis.

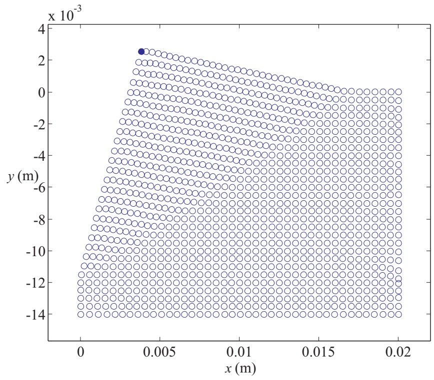

(a) Final marker locations, Abaqus analysis

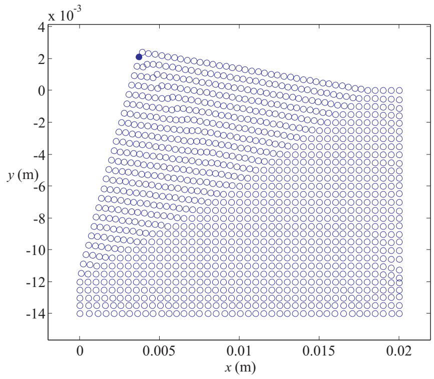

(b) Final marker locations, Hill et al.

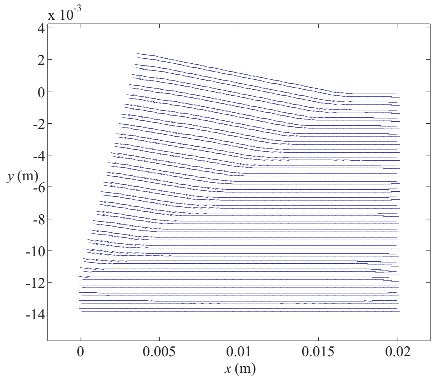

(c) Rotations, Abaqus analysis

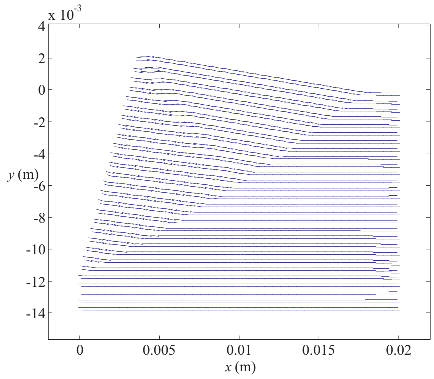

(d) Rotations, Hill et al.

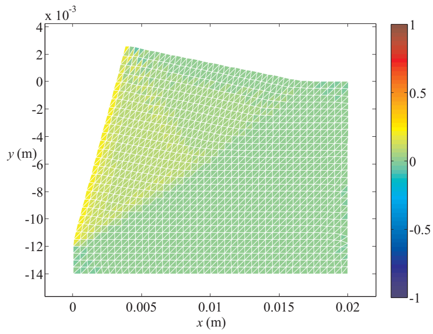

(e) Total shear strain γ_{xy}, Abaqus analysis

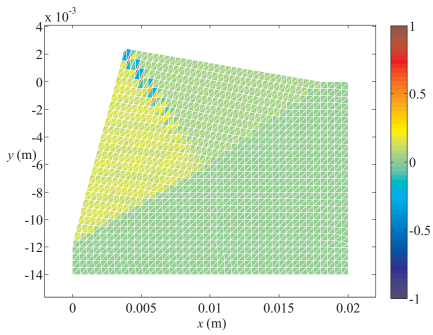

(f) Total shear strain γ_{xy}, Hill et al.

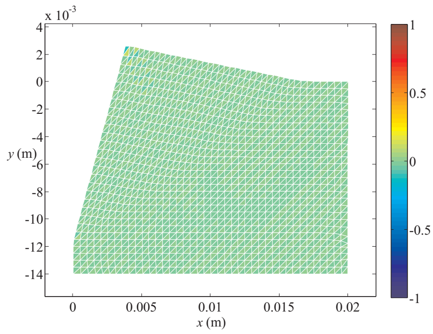

(g) Total volumetric strain ε_{v}, Abaqus analysis

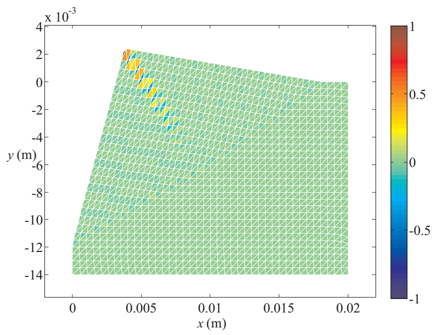

(h) Total volumetric strain ε_{v}, Hill et al.

Figure 4.10: Indentations made with smooth 30° wedge in material with original surface $y = 0$. In each case only the material to the right of the centreline $x = 0$ is shown; the final position of the wedge tip is $(x, y) = (0, -12\,\mathrm{mm})$

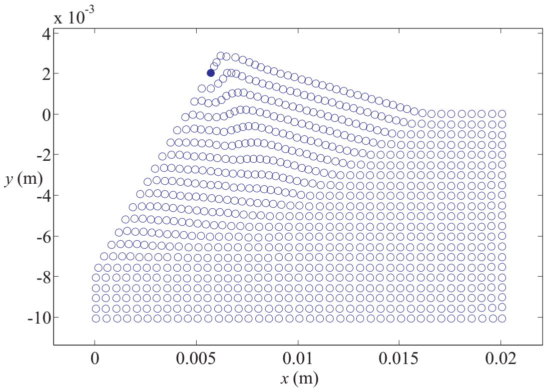

(a) Final marker locations, Abaqus analysis

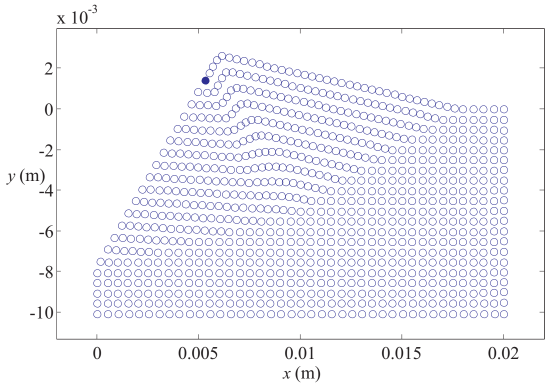

(b) Final marker locations, Hill et al.

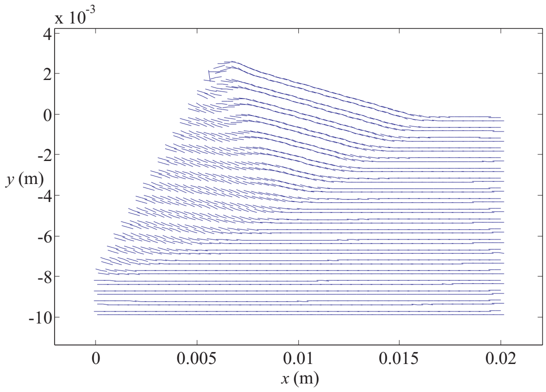

(c) Rotations, Abaqus analysis

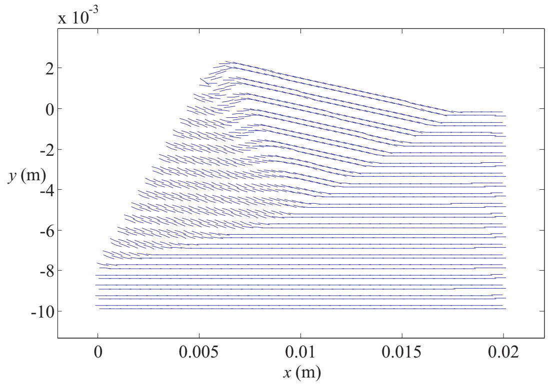

(d) Rotations, Hill et al.

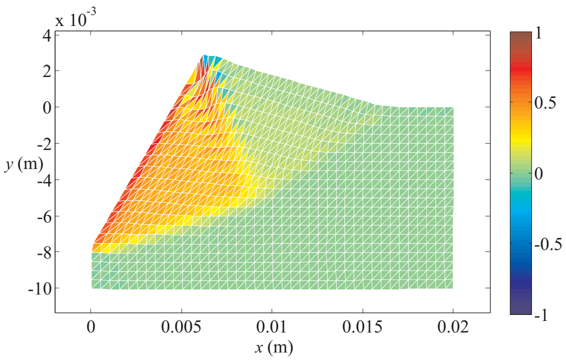

(e) Total shear strain γ_{xy}, Abaqus analysis

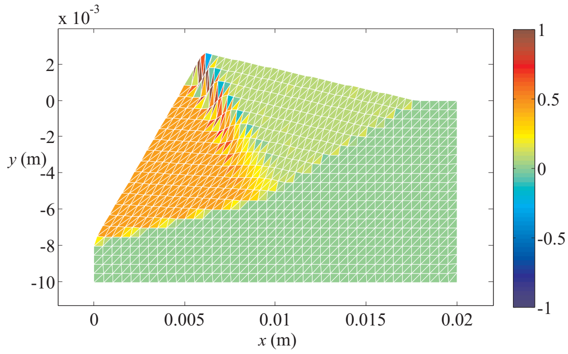

(f) Total shear strain γ_{xy}, Hill et al.

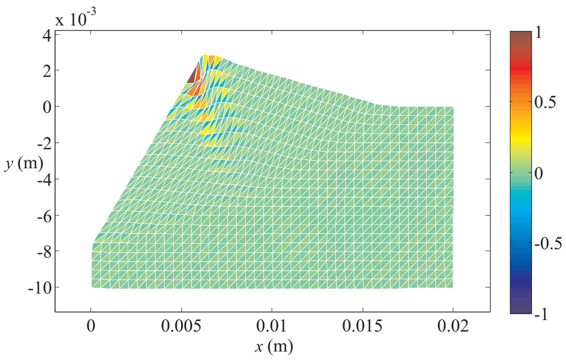

(g) Total volumetric strain ε_{v}, Abaqus analysis

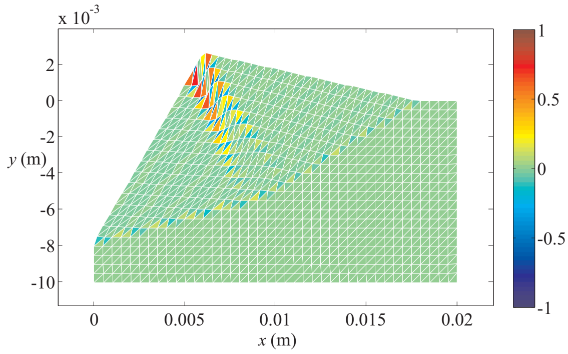

(h) Total volumetric strain ε_{v}, Hill et al.

Figure 4.11: Indentations made with smooth 60° wedge in material with original surface $y = 0$. In each case only the material to the right of the centreline $x = 0$ is shown; the final position of the wedge tip is $(x, y) = (0, -8\,\mathrm{mm})$

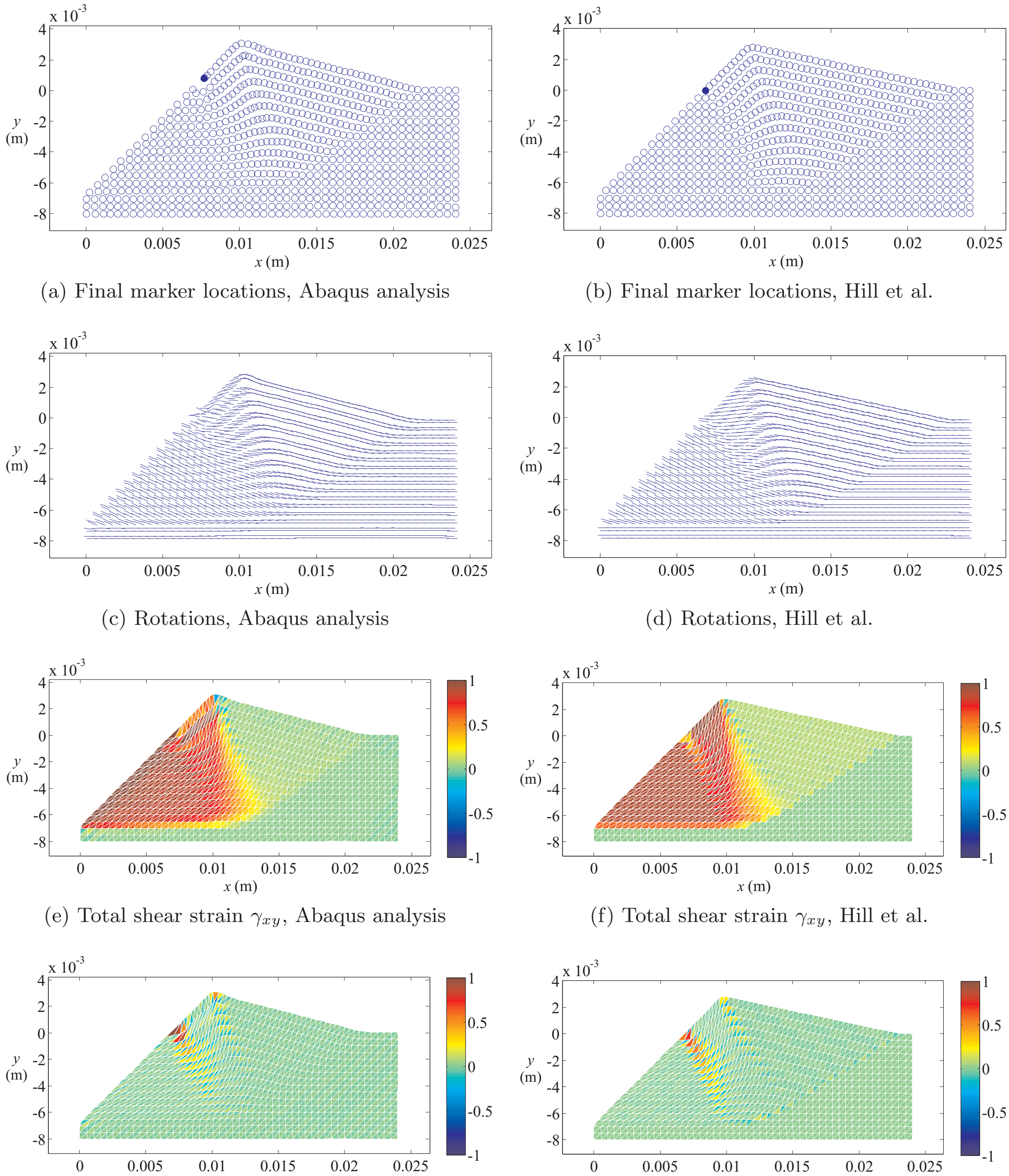

(a) Final marker locations, Abaqus analysis

(b) Final marker locations, Hill et al.

(c) Rotations, Abaqus analysis

(d) Rotations, Hill et al.

(e) Total shear strain γ_{xy}, Abaqus analysis

(f) Total shear strain γ_{xy}, Hill et al.

(g) Total volumetric strain ε_{v}, Abaqus analysis

(h) Total volumetric strain ε_{v}, Hill et al.

Figure 4.12: Indentations made with smooth 90° wedge in material with original surface $y = 0$. In each case only the material to the right of the centreline $x = 0$ is shown; the final position of the wedge tip is $(x, y) = (0, -7\,\mathrm{mm})$

4.3 Quasi-static cone indentation

In the previous section it was established that the Abaqus analysis (including the VUMAT material behaviour model) worked as expected for plane strain conditions. The next step was to use Abaqus to cross-verify the ELFEN results for cone indentation, which were presented in Chapter 3.

The Abaqus model used for the cone indentation analyses was somewhat similar to that used in the wedge analyses described in the previous section. The obvious difference was that, though the geometry of the two-dimensional model was identical, it now represented an axisymmetric situation out of the plane. There were other changes, as described below.

4.3.1 Element distortion and adaptive meshing

In the wedge indentation analyses, satisfactory results were obtained by using the same fixed mesh throughout. However, there were reasons to suspect that the cone analyses would present extra difficulties. The indented material is stretched considerably in the hoop direction as it moves away from the axis $r = 0$. Since the indented material is modelled as approximately incompressible, volume must be conserved during the analysis. An element that is fixed to the deforming material must therefore decrease in area as it moves outwards, away from the axis.

Figures 3.17 and 3.18 showed the distortions predicted with ELFEN analyses for initially square grids moving with material indented by cones. The ELFEN analyses used a fine mesh and automatic remeshing, so the actual elements were not substantially distorted. If a fixed mesh of initially square elements was used throughout an analysis, the elements might be expected to undergo distortions similar to those shown by the ELFEN material grids. These distortions would be much greater than would usually be tolerated in an FE analysis.

ALE adaptivity in Abaqus

To alleviate potential problems caused by element distortion, Abaqus' ALE (Arbitrary Lagrangian Eulerian) adaptive meshing was used to reduce element distortions during the analysis, ensuring that a higher quality mesh was used than would otherwise have been the case. The ALE method is so called because it combines features of Lagrangian and Eulerian analysis. Element formulations, boundary conditions, loads, contact conditions etc. are first handled in a manner consistent with a standard Lagrangian analysis (in which the mesh is fixed, and deforms with the underlying material). After the Lagrangian analysis step, mesh sweeps are performed to smooth the mesh; the mesh then moves relative to the material (Eulerian analysis). Finally an advection sweep is performed to remap solution variables to the new mesh.

In an increment when adaptive meshing has been requested, a replacement mesh is generated not by building a new mesh from scratch (as in the ELFEN analyses of Chapter 3) but by sweeping iteratively over the existing mesh and relocating nodes based on the positions of adjacent nodes and elements. The default volume smoothing method used here relocates a node by determining a volume-weighted average of the centres of the elements surrounding it. In Figure 4.13a, if the node to be relocated is M, its new position is determined by a volume-weighted average of the positions of element centres C_1 to C_4. This will tend to push M away from C_1 and toward C_3, reducing the distortion of all four elements.

(a) Relocation of a node during a mesh sweep

(b) Second-order advection

Figure 4.13: Abaqus ALE adaptive meshing (Simulia, 2007)

After the mesh sweeps, an advection sweep is performed to transfer element and material variables to the new mesh. The default second-order method is based on the work of van Leer (1977). An element variable θ is remapped to the new mesh by first fitting a linear distribution to the variable within the old mesh. The process is illustrated in Figure 4.13b – first a quadratic interpolation $\theta_{\text{quadratic}}$ is found from the values of θ at the integration points of the middle element and those adjacent to it. A trial linear distribution θ_{trial} is found using the slope of $\theta_{\text{quadratic}}$ at the middle element's integration point. If necessary, the slope of θ_{trial} is limited so that its maximum and minimum are in the range of the original adjacent values, a process called flux-limiting that is required to ensure monotonicity (see below). The linear distribution θ_{limited} in the *old* elements are integrated over the *new* elements, and the results are divided by the volumes of the new elements to give the new values of the variables.

The method described above meets certain fundamental conditions for an advection scheme: it is monotonic (i.e., if a quantity has a monotonic increasing value over part of the old mesh, that property will be preserved on the new mesh); it is consistent (if the new and old meshes are identical, all quantities remain unchanged); and it conserves element variables in an integral sense (the integral of any variable over the domain is unchanged after adaptive meshing).

In the quasi-static cone indentation analyses that follow, ALE adaptive meshing (with volume smoothing and second-order advection) were used in all cases. One mesh smoothing sweep after every ten Lagrangian analysis increments proved sufficient to maintain a good quality mesh with well-shaped elements. For comparison, the analyses were also performed without adaptivity.

4.3.2 Initial meshes

The initial meshes were similar to those used for the wedge indentation analyses (Figure 4.6a), having a uniform more finely-meshed region around the cone and progressively larger elements outside this. The extent of the uniform mesh region was chosen by trial-and-error for each cone angle to cover the deforming region. Each analysis was performed with two meshes. The first (referred to as the coarse mesh) had square elements of side 0.625 mm in the region around the cone. The second (referred to as the medium mesh) had elements whose linear dimensions were half this (0.3125 mm). Examples of initial meshes are shown in Figure 4.14. A few cases were also analysed with a fine mesh in which the elements were of length 0.15625 mm.

4.3.3 Contact on cone–clay interface

Contact forces normal to the surface of the cone were determined as for the wedge indentation analyses. Forces tangential to the contact surface were either zero (in the case of smooth cones) or were treated similarly to the ELFEN analyses (see Section 3.2.3). That is, relative motion of the cone and clay was allowed only if the shear stress on the surface exceeded a value of αs_u where $0 < \alpha < 1$. The friction coefficient μ on the interface (see Figure 3.3) was again given a value of 10^{24} so that the force required for movement on the interface was independent of contact pressure.

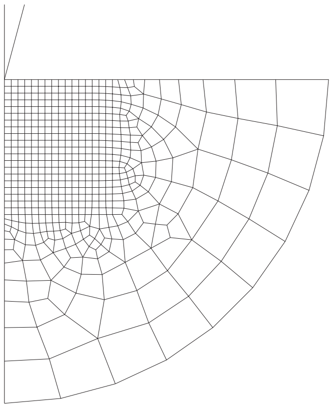

(a) Coarse mesh for 30° cone (512 elements)

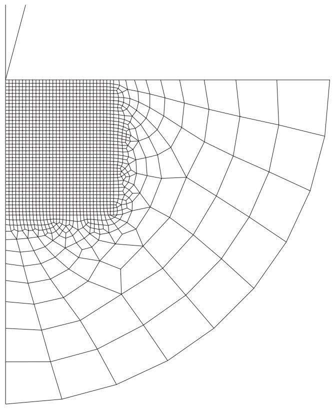

(b) Medium mesh for 30° cone (1616 elements)

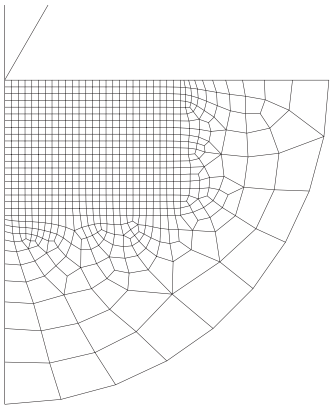

(c) Coarse mesh for 60° cone (1056 elements)

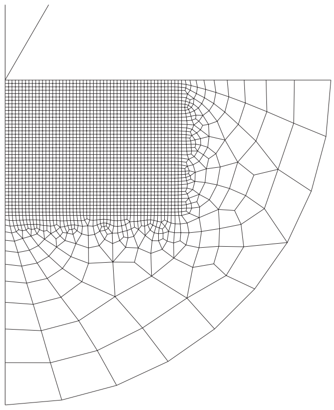

(d) Medium mesh for 60° cone (2994 elements)

Figure 4.14: Initial meshes for some Abaqus cone indentation analyses

In addition to the αs_{u} limiting shear stress method, an additional approach to rough cone analyses was trialled. In this, once the cone and clay came into contact, no slip was allowed between the two surfaces. All the deformation was therefore forced to take place within the sample. This boundary condition type will be used in Chapter 5, when indentations in material with rate-dependent strength are analysed. If the original αs_{u} contact condition was used in such cases, the strength of the material itself would be enhanced by increased strain rates while the stress on the interface would be unaffected, leading the mechanism to adapt to favour interface slip. Even if the contact condition could be adapted to become rate dependent, it is unclear what form the relationship should take as the strain rate on the interface is very large (effectively infinite) when slip occurs. Forcing all deformation to occur within the indented material would allow a pattern of strain rates to arise naturally from the analysis. In these rate-independent analyses, the no-slip results were expected to be similar to those with $\alpha = 1.0$.

4.3.4 Cases considered

The first batch of analyses replicated the smooth cases analysed with ELFEN in Chapter 3. Cone roughness was varied only for cone angles of direct interest in the fall cone test, namely 30°and 60°. The full selection of cases considered is shown in Table 4.1. In most of the analyses, cones were displaced 10 mm, but for larger β the increased radius of the mechanism meant that only shallower indentations could be accommodated by the model. The displacement applied to the cone in each case is shown in the table.

Table 4.1: Combinations of cone angle β and roughness α considered in Abaqus analyses. "N/A" indicates a combination that was not analysed here.

	Final indentation depth (mm)						
β (°)	$\alpha = 0.0$	$\alpha = 0.2$	$\alpha = 0.4$	$\alpha = 0.6$	$\alpha = 0.8$	$\alpha = 1.0$	no-slip
30	10.00	10.00	10.00	10.00	10.00	10.00	10.00
60	10.00	10.00	10.00	10.00	10.00	10.00	10.00
90	10.00	N/A	N/A	N/A	N/A	N/A	N/A
105	10.00	N/A	N/A	N/A	N/A	N/A	N/A
120	7.500	N/A	N/A	N/A	N/A	N/A	N/A
140	5.000	N/A	N/A	N/A	N/A	N/A	N/A
150	3.250	N/A	N/A	N/A	N/A	N/A	N/A
160	1.625	N/A	N/A	N/A	N/A	N/A	N/A

4.3.5 Results: smooth cones

As expected, elements became very distorted when analyses were run without adaptive meshing. The coarse mesh after analysis of indentation with a smooth 30° cone without adaptive meshing is shown in Figure 4.15b. Some elements are very distorted. Those adjacent to the face of the cone have essentially zero length in the direction normal to the cone face, implying that their aspect ratios are extremely large. Figure 4.15c shows the final mesh when ALE adaptivity was used: the elements remained comparatively undistorted throughout the analysis. Despite the severe distortion of some elements when no adaptivity was used, the predicted shapes of the displaced lip of material were similar whether or not adaptivity was used.

Output of the total vertical force needed to move the cone was obtained at 1000 equal intervals during each analysis. Figure 4.16 shows the load–displacement curves for $\alpha = 0$, $\beta = 30°$. Surprisingly, the overall curves obtained with and without adaptive meshing are near-identical. In the case with no adaptivity (Figure 4.16a) the curve has small steps which

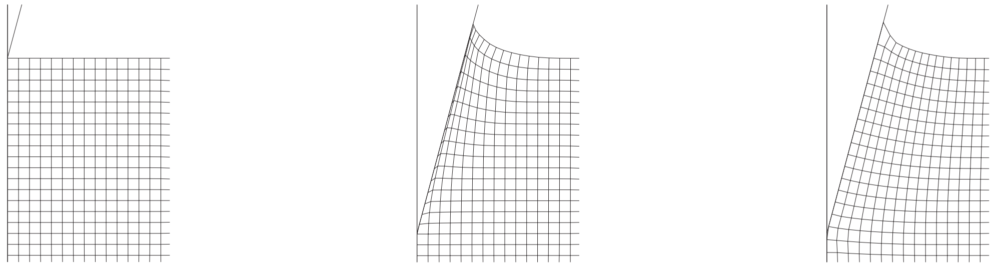

(a) $d = 0$ (b) $d = 10\,\mathrm{mm}$, no adaptivity (c) $d = 10\,\mathrm{mm}$, ALE adaptivity

Figure 4.15: Detail of coarse mesh with 30° cone, adhesion factor $\alpha = 0$

can be seen most clearly in a close-up view of the first part of the curve (Figure 4.16b). The cause of these steps is that a small void repeatedly opens and closes at the cone tip as it passes each element on the axis. The same phenomenon was observed in the wedge indentation analyses, as illustrated in Figure 4.8. For a given element size, the effect is less severe in cone indentation than with a wedge because the void is so close to the centreline and represents a smaller fraction of the contact area.

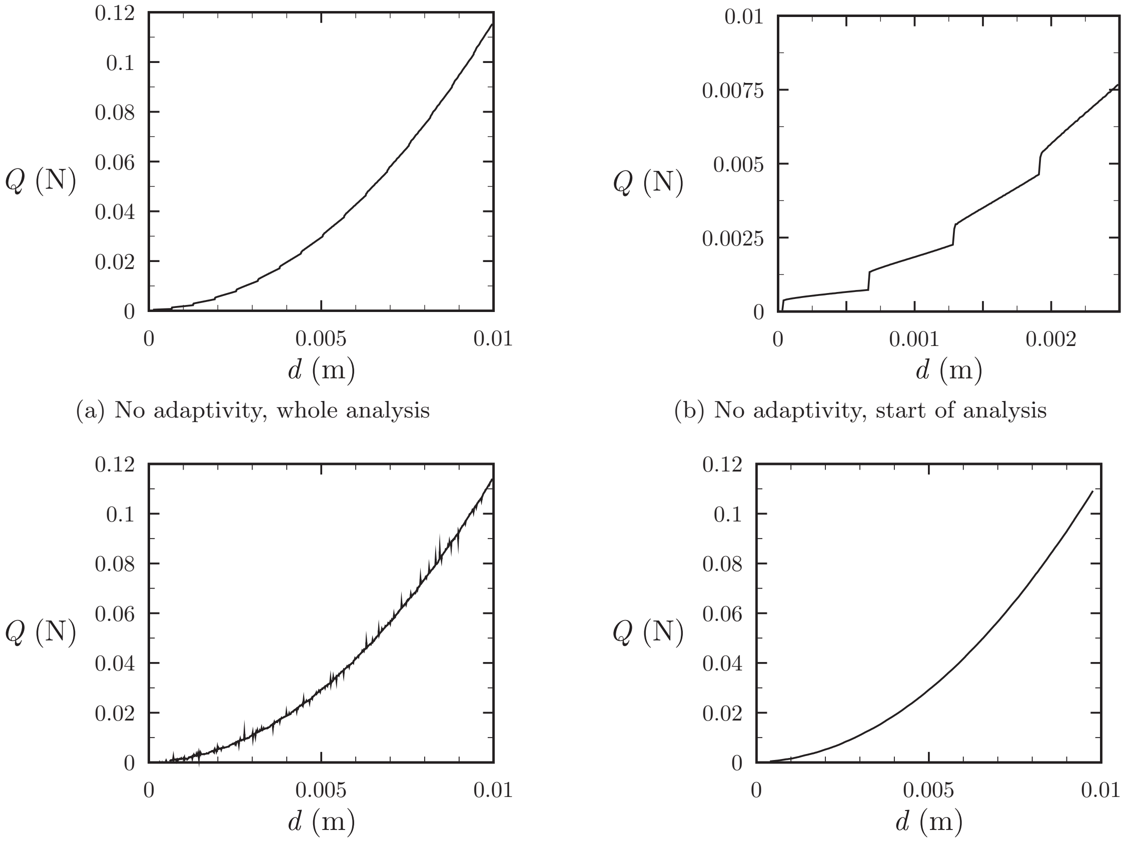

(a) No adaptivity, whole analysis (b) No adaptivity, start of analysis

(c) ALE adaptivity, unfiltered data (d) ALE adaptivity, filtered data

Figure 4.16: $Q - d$ curves for indentation with smooth 30° cone, obtained with coarse mesh

With ALE adaptivity switched on, the Q–d curve shows some spikes of random noise

(Figure 4.16c). A similar effect was observed with ELFEN (see Figure 3.7a). The data were filtered by taking a centred 49-point moving average. As shown in Figure 4.16d, this alleviated the problem satisfactorily.

The final point of each filtered force–displacement curve was used to obtain a value of N_{ch} (defined in Equation 1.2). The values of N_{ch} obtained from Abaqus analyses of indentations with smooth cones of varying angle β are shown in Figure 4.17. The results shown were obtained using medium meshes (with elements of length 0.3125 mm). Curves from analyses with no adaptivity and with ALE adaptivity are shown, together with the ELFEN results from Chapter 3. The three curves lie very close together, particularly for small β. When $\beta = 30°$, N_{ch} from the Abaqus analysis *with* adaptivity is 0.30% less than that from ELFEN; the Abaqus result *without* adaptivity is 0.36% less than that from ELFEN. The discrepancies between the results were even smaller for $\beta = 60°$. It is remarkable that the analyses with no adaptivity still gave results closely comparable with the others. The elements seem to have been highly tolerant of aspect ratio distortion.

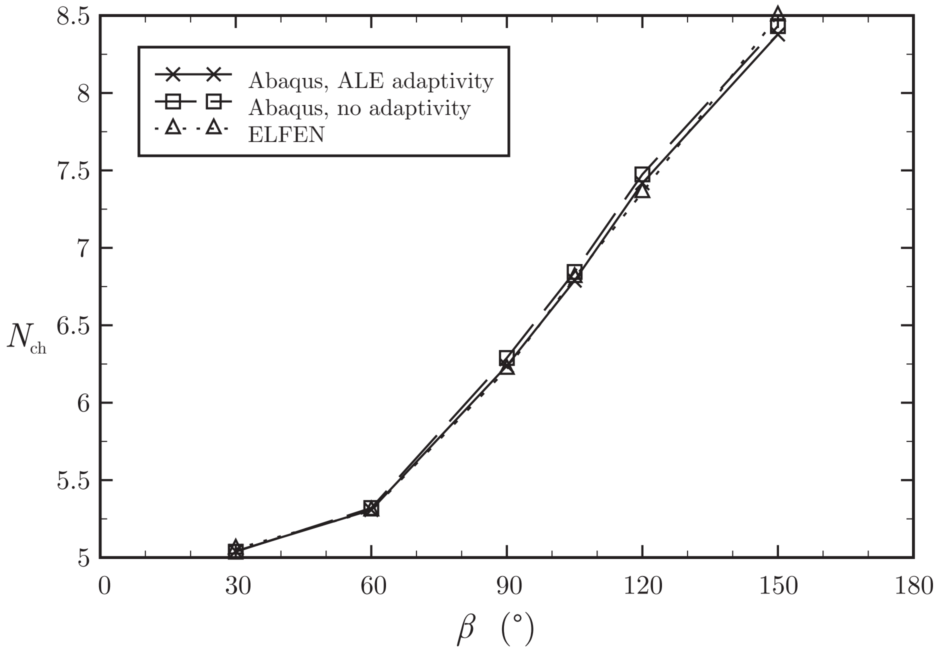

Figure 4.17: Variation of N_{ch} with β for smooth cones

The observations made in Section 3.3.3, about the stress state in the displaced lip for cones sharper than the 105° limit of Lockett, were supported by the results of the Abaqus analyses. Above a line tangential to the clay surface and perpendicular to the cone face, the in-plane principal stresses σ_1 and σ_2 were close to zero and σ_3 was approximately $-2s_{\mathrm{u}}$. The stress history at a point passing into the lip region during the Abaqus analysis of a smooth

30° cone, with no adaptivity, is shown in Figure 3.12e. The non-adaptive analysis was used for this purpose because obtaining history output for a particular material point was difficult in the analyses with ALE adaptivity – with adaptivity, a given element did not correspond to a fixed region of the clay material.[2]

4.3.6 Results: rough cones

Force–displacement results from the analyses of rough and partially rough 30° and 60° cones were analysed to obtain values of N_{ch} as for the smooth cones. The results of the analyses that used the limiting shear stress (αs_{u}) roughness model are shown in Figure 4.18. These curves were obtained from the analyses with medium mesh refinement. Results are shown for Abaqus results without adaptive meshing and with ALE adaptivity enabled, and the ELFEN results have been re-plotted for comparison. For the most part, all three curves are indistinguishable. The greatest discrepancy occurs for 60° cones with $\alpha = 0.8$. Here the Abaqus curve with adaptivity lies 0.82% above the ELFEN result and the no-adaptivity Abaqus result exceeds the ELFEN value by 1.59%. Possibly the ELFEN curve at this point is slightly anomalous, as its slope increases again in the interval 0.8–1.0. The close agreement between the Abaqus and ELFEN results confirms that the VUMAT is working correctly and that the performance of the first-order reduced integration elements is satisfactorily tolerant of the element distortions seen in these analyses.

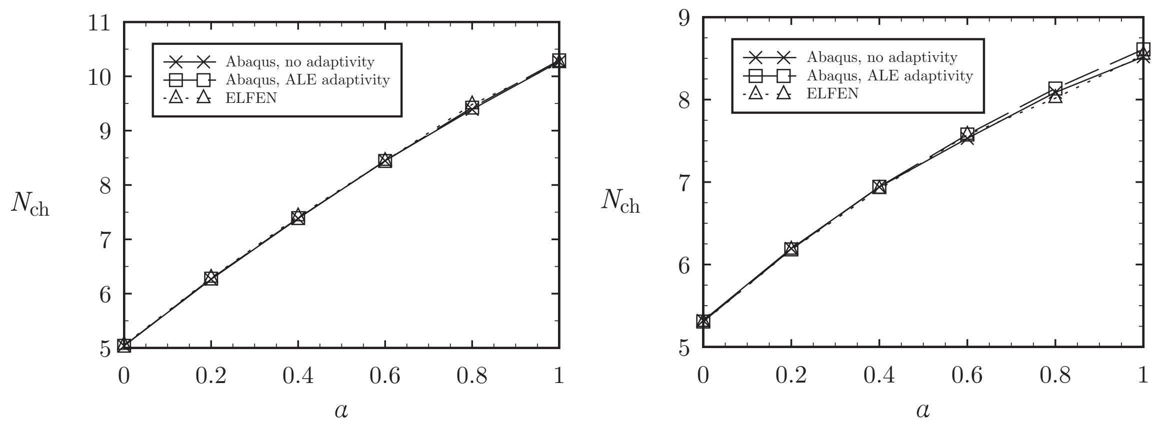

(a) $\beta = 30°$ (b) $\beta = 60°$

Figure 4.18: Variation of N_{ch} with roughness α

Figure 4.19 shows the region of the coarse mesh closest to the tip of the rough cone

[2]In Abaqus/Explicit, "Tracer particles" can be placed in the deforming material to track the history of displacements (but not other quantities) at specific material points. Their behaviour, at least in this application, was found to be unreliable: apparently random displacements were frequently observed in material that was expected to remain undisturbed.

(adhesion factor $\alpha = 1.0$). The mesh is shown at the beginning of the analysis and after the cone had been pushed in by $d = 10\,\text{mm}$. Figure 4.19b shows the deformed mesh when no adaptive meshing was used, and Figure 4.19c shows the mesh with ALE adaptivity. As in the analysis with a smooth cone, running the analysis with no adaptivity meant that some elements close to the cone became very distorted. In the case with ALE adaptivity, element distortions have been kept to a low level. The use of adaptive meshing also had the effect of slightly increasing the mesh density at the surface adjacent to the cone by "pulling in" nodes from further away in the model.

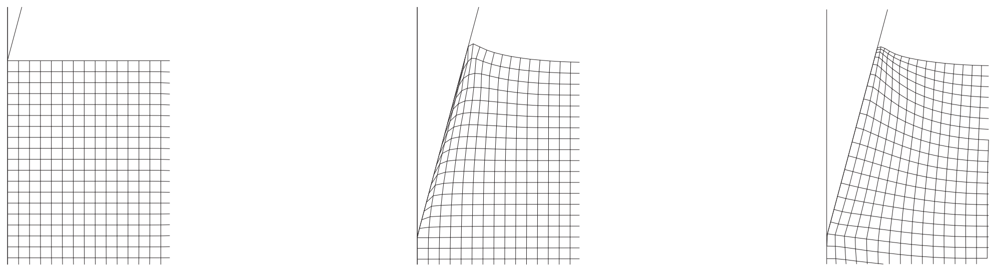

(a) $d = 0$ (b) $d = 10\,\text{mm}$, no adaptivity (c) $d = 10\,\text{mm}$, ALE adaptivity

Figure 4.19: Detail of coarse mesh with 30° cone, adhesion factor $\alpha = 1$

In addition to the rough cone analyses with a limiting shear stress contact condition, analyses were performed for 30° and 60° cones with a no-slip contact condition. As discussed above, this approach will be required for analysis of rough cones indenting rate–dependent material. Results were obtained only with ALE adaptive meshing enabled, as element distortions were otherwise too great for Abaqus to complete the analyses. Even with ALE adaptivity, the settings used in the previous analyses were not sufficient to prevent excessive distortion of the elements adjacent to the cone face: an adaptive mesh sweep was needed every five increments of the analysis, rather than every ten.

The more aggressive remeshing strategy was required because the elements adjacent to the cone face would otherwise become distorted very rapidly. These elements had to accommodate the deformation that would otherwise have occurred on the interface if the contact model allowed it. Figure 4.20 shows the effective strain rate $\dot{\bar{\varepsilon}}$ in elements close to the cone face in the analysis with a fine mesh (elements of length 0.15625 mm). Strains are concentrated in the layer of elements immediately adjacent to the cone, raising the possibility that the result may be strongly dependent on the mesh density.

Force–displacement curves (averaged as before) for the 60° cone are shown in Figure

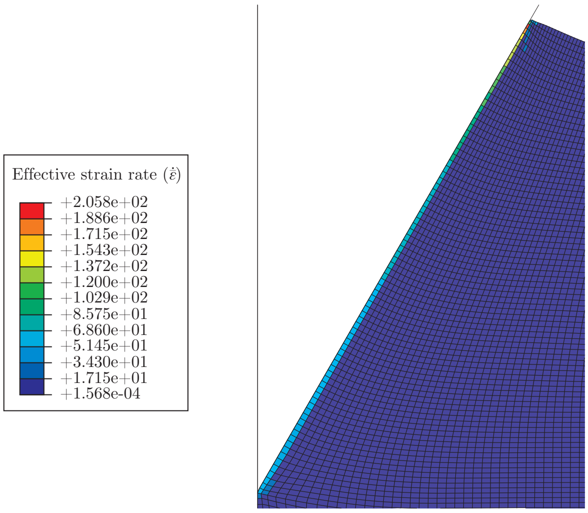

Figure 4.20: Effective strain rate $\dot{\bar{\varepsilon}}$ during indentation analysis with no-slip contact condition; refined mesh

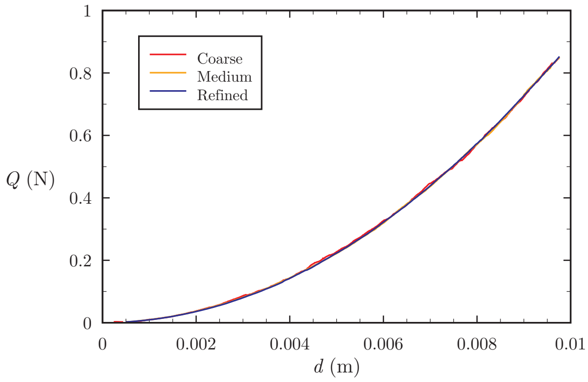

Figure 4.21: Force–displacement curves for 60° cone indentation with no-slip contact condition

4.21. There is strong agreement between the three analyses, indicating the results are not excessively mesh-dependent. The final points on these curves, together with those for the 30° cones, were used to obtain N_{ch} bearing capacity factor values. Medium mesh results are shown in Table 4.2. The no-slip contact condition gave N_{ch} values that were very similar to the original $\alpha = 1$ limited shear stress interface condition. Results from Abaqus (with the medium mesh and no-slip contact model) differed from those obtained with ELFEN (using the $\alpha = 1$ contact condition) by no more than 0.5%. With the refined mesh, the difference decreased to -0.47% for the 30° cone and just $+0.06\%$ for the 60° cone. The similarity of these results suggests that the two rough interface contact models are equivalent, at least for a rate-independent material.

Table 4.2: Values of N_{ch} for fully rough cones. Results of analyses with $\alpha = 1.0$ were obtained either from ELFEN or Abaqus (with or without ALE adaptivity); results with the no-slip interface condition are also shown. All Abaqus analyses used the medium mesh

		Abaqus N_{ch}			Change from ELFEN result		
β	ELFEN N_{ch}	$\alpha = 1$ no adap.	$\alpha = 1$ ALE	no slip ALE	$\alpha = 1$ no adap.	$\alpha = 1$ ALE	no slip ALE
30°	10.24	10.27	10.30	10.19	+0.29%	+0.54%	−0.50%
60°	8.54	8.52	8.61	8.52	−0.28%	+0.78%	−0.29%

4.4 Influence of sample container shape

All the FE analyses so far (whether in this or the preceding chapter) have been performed with boundary conditions representing the 27.5 mm radius hemispherical cup prescribed by Standard Norge (1988), and supplied by Geonor for use with their fall cone apparatus (Geonor, 2005b). However, fall cone tests are frequently carried out on samples in cylindrical cups, as is the case for the British fall-cone liquid limit test, performed in a cylindrical vessel of radius 22.5 mm (BSI, 1990). Although no slip was allowed on the boundary of the cup in the previous analyses (representing a rough interface), there will inevitably be variation in roughness, even between two cups of the same shape. In addition, fall cone tests may sometimes be performed on samples without lateral restraint, for example when testing sections cut from borehole samples.

4.4.1 Cases considered

Ten displacement-controlled analyses were performed to investigate the influence of boundary conditions on fall cone test results. The model used for the quasi-static cone analyses already presented was re-used, with appropriate changes to the shape of the soil region boundary and the restraints applied to the material there. The cases considered were: rough and smooth hemispherical cups, rough and smooth cylindrical cups, and a cylindrical sample free to expand in the radial direction. The hemispherical samples had radius 27.5 mm and the cylindrical samples had radius 22.5 mm. In the rough cup cases, material on the boundary was restrained from moving in any direction. Material in the smooth cups could move freely along the direction of the boundary, but was restrained from moving perpendicular to it. The boundary of the unconstrained sample was free to move radially or vertically, while the base could move freely in the radial direction only (so that the model represented a cylindrical specimen resting on a smooth rigid support).

Two sets of analyses were performed (each covering the five boundary conditions). For one set, a smooth 30° cone was used and for the other a smooth 60° cone. The 30° cones were pushed to a final depth of $d = 25$ mm, while the 60° cones were pushed to $d = 21$ mm. These values were selected as being equal to or exceeding the maximum penetrations typically used in actual laboratory fall cone tests. BS 1377 recommends that tests with the 30° cone cover a range of penetration values of approximately 15 mm to 25 mm (BSI, 1990). Geonor (2005a) suggest that the maximum depths of penetration for the 30° and 60° cones should generally be 15 mm; for particularly soft soils ($s_\mathrm{u} < 1$ kPa), they suggest that the 60°, 10 g cone may be used with a penetration of up to 20 mm.

4.4.2 Results

In general, results did not appear to be influenced by boundary effects in the analyses with smooth or rough cylindrical cups, or with rough hemispherical cups. However, unconfined cylindrical samples and (to a lesser extent) samples constrained in smooth hemispherical cups showed some influence of the boundary conditions.

Figure 4.22 shows velocity vectors at the nodes of the finite element mesh under indentation by smooth 60° cones. Results obtained with the rough hemispherical cup (Figure 4.22a), the smooth cylindrical cup (Figure 4.22c) and the rough cylindrical cup (not shown) were found to be indistinguishable from one another. Samples with other boundary conditions (unrestrained cylindrical samples and those in smooth hemispherical cups) were also found to behave similarly when d was very much less than the sample radius. As the depth of indentation increased, the patterns of deformation changed. Figure 4.22b shows how the material in the smooth hemispherical cup began to slide along the boundary of the cup. In the case of an unconstrained cylindrical sample, material at the sample boundary began to move radially outward when the depth of indentation became sufficiently large. The sample expanded significantly on the upper part of the outer vertical face, as can be seen in Figure 4.22d. The directions of the velocities close to the face of the cone are also different: in the confined samples, velocities in this region generally had significant upward components, which is not the case in Figure 4.22d. The analyses with 30° cones showed qualitatively similar behaviour.

The results (in terms the variation of force with displacement) also differed very little

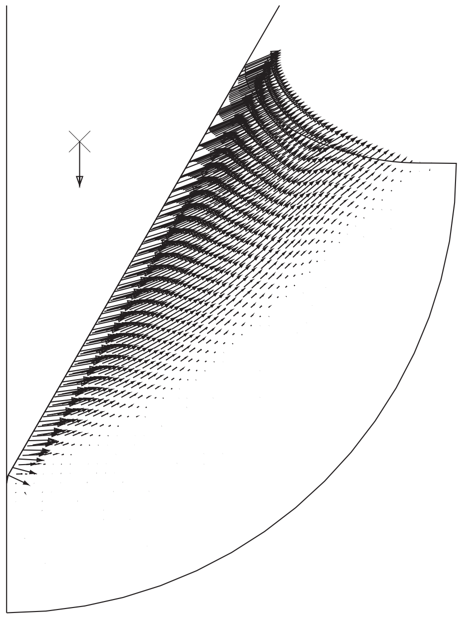

(a) Velocities in rough hemispherical cup

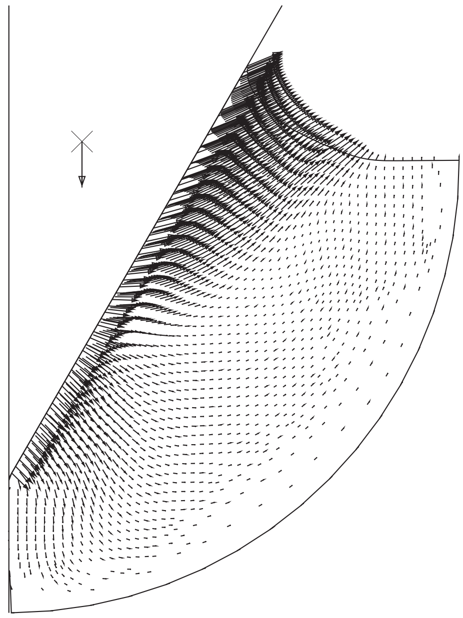

(b) Velocities in smooth hemispherical cup

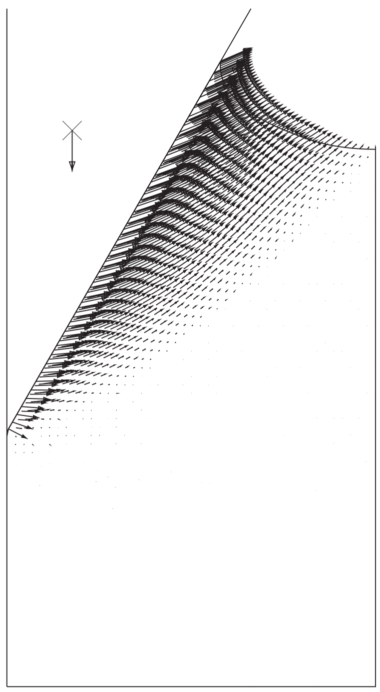

(c) Velocities in smooth cylindrical cup

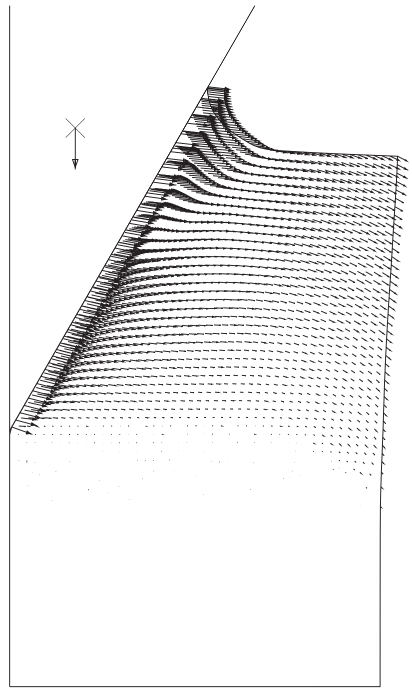

(d) Velocities in unconfined sample

Figure 4.22: Velocities around a smooth 60° cone at penetration $d = 21\,\mathrm{mm}$

between the rough, smooth, cylindrical and hemispherical cups. In each of the ten analyses, values of Q and d were obtained at 1000 equal intervals. The curves were smoothed using a moving average as before, and values of $F = Q/(s_u d^2)$ were calculated (equivalently, values of N_{ch} could have been plotted). The variation of F with d for each analysis is shown in Figure 4.23 for both 30° and 60° cones. Lines are also plotted to indicate the values of F previously obtained using ELFEN (see Table 3.4). In all cases, the FE analyses overpredicted F (and therefore Q) at the start of the analysis. This was expected, since initially the discretization is poor (at first the deforming region consists of only a single element). As an analysis proceeds, the number of elements in the deforming region increases. In all the analysis cases involving a confined sample, F converged to approximately the value predicted by ELFEN, indicating that the shapes and roughnesses of the sample containers were not significant. Of course, boundary effects would be expected to become important if the cones were displaced further.

In the analyses with unconfined cylindrical samples, represented in Figure 4.23 by gold-coloured curves, the results initially followed the same relationship as in the other (confined) cases. The F values began to converge to the same values as the other analyses, even with the outer face of the sample unconfined. The results for both 30° and 60° cones were similar to those for confined samples until at least $d = 10\,\mathrm{mm}$. In the 30° case, the error due to boundary effects first exceeded 1% when d was 16.6 mm; in the 60° case, this happened earlier, when $d = 12.8\,\mathrm{mm}$. Eventually, the Q–d curves deviated quite substantially from the usual behaviour. By the end of the relevant analyses, the forces on the 30° and 60° cones differed by 8.9% and 29% respectively from predictions based on values of F given by ELFEN.

In the analyses with boundary conditions representing smooth, hemispherical cups, the problems were not so severe. However, the curves of F against d (shown by red lines in Figure 4.23) began to deviate noticeably from the value obtained from ELFEN towards the end of each test. In the case of a 30° cone, the difference in the resistance Q did not exceed 1% until the depth of indentation was almost 22 mm, which is greater than the maximum penetration recommended by Geonor (2005a) for use with a 30° cone. In the case of a 60° cone, a 1% difference in Q was observed when d was approximately 19 mm. Since a 60° cone is recommended for use with particularly soft soils with d up to 20 mm, it is possible that slip along the cup wall may have a minor influence on results in a few cases. To be certain of avoiding problems, a larger cup could be used.

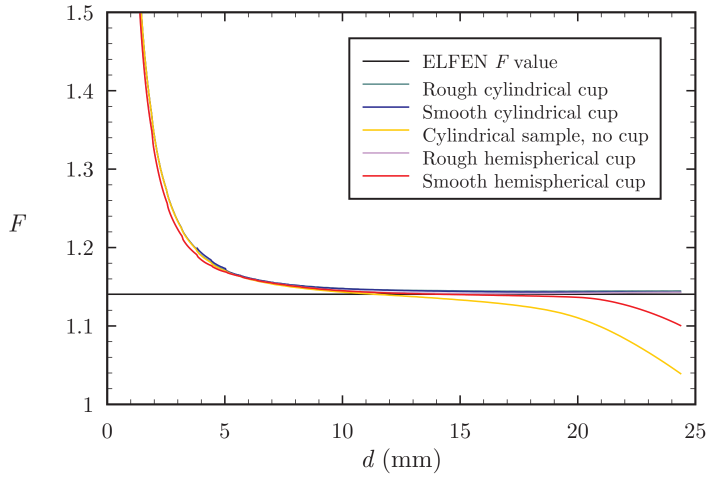

(a) $\beta = 30°$

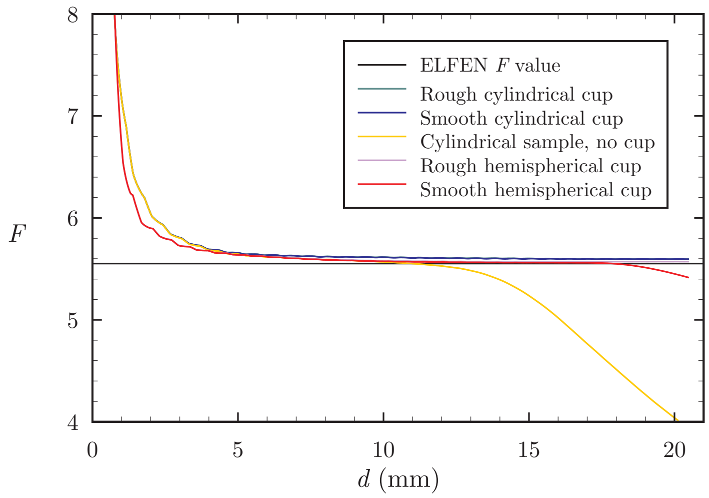

(b) $\beta = 60°$

Figure 4.23: Variation of F with d during FE analysis of smooth cone indentation

4.5 Dynamic cone indentation

The dynamic analysis of the fall cone test performed by Hansbo (1957) – in which it was assumed that the resisting force Q during a test depended only on the square of the indentation depth – indicated that cone should comes to rest at

$$h = h_{\mathrm{s}}\sqrt{3} \tag{4.26}$$

where h_{s} is the quasi-static penetration depth at which the indentation force Q is equal to the cone weight W. The dynamic analysis was discussed in Chapter 1. To cross-validate this result with the Abaqus finite element model, a series of dynamic analyses was performed using fully smooth (no interface shear stress) and fully rough (no interface slip) 30° and 60° cones.

The cones used in the dynamic analyses were assigned masses corresponding to two of the cones supplied with the Geonor fall cone apparatus (Geonor, 2005a): 100 g for the 30° cone and 60 g for the 60° cone. Unlike the previous displacement-controlled analyses, these tests were conducted under load control. The cones were free to move vertically under the action of two forces: the weight W (determined by multiplying the mass by an assumed value of g, 9.81 m/s^2), and the resisting force Q (found from the cone–clay contact condition).

The time-span of each analysis had to be correctly chosen to ensure the cone had time to reach its maximum indentation. This required some trial-and-error. In practice, analyses were allowed to proceed for 20–30% longer than necessary to ensure the cone reached full penetration. This allowed observation of any rebound that occurred after the maximum penetration was reached.

4.5.1 Cases considered

To ensure the analyses covered a range of indentation depths, the material strength s_{u} was selected to give a particular predicted depth of indentation h, based on Hansbo's dynamic analysis and the N_{ch} results from ELFEN (Chapter 3). For each of the four cone types (all combinations of 30° and 60° with smooth and rough contact), analyses were performed with three different values of s_{u}, chosen to give h of approximately 5, 10 and 15 mm for each cone. After choosing the desired value of h, h_{s} was obtained from Equation 4.26 and s_{u} was selected using

$$s_u = \frac{W}{\pi N_{ch} \tan^2\left(\frac{\beta}{2}\right) h_s^2}. \tag{4.27}$$

4.5.2 Meshing

Meshes similar to Figure 4.14 were used, with the region close to the cone sized appropriately for the extent of the deformation in each case. Two mesh densities were used: a coarse mesh with elements such that the indentation depth $h \approx 16l_e$ (where l_e is the length of an element in the undeformed mesh), and a fine mesh with $h \approx 32l_e$.

ALE adaptivity was used here, as for the quasi-static analyses. One mesh sweep was requested after every ten increments for smooth cones, and after every five analysis increments for rough cones.

4.5.3 Results

The key result from each dynamic FE analysis with Abaqus was the final depth of indentation h. Values of cone displacement d, velocity v and acceleration a, as well as resisting force Q were output at 1000 equal intervals during each analysis, and the curves for a and Q were smoothed using a centred moving average as previously described (no smoothing of velocities or displacements was found to be necessary). Values of final penetration depth h were obtained by finding the maximum value of d in the results, while h_s was determined by first finding the time at which $Q = W$ (using linear interpolation between the available values), then finding the corresponding value of d (again using linear interpolation).

Before the Abaqus analyses were run, the depth of indentation was first predicted theoretically, for each combination of cone angle, roughness and material strength s_u. From Equation 4.27,

$$h_s = \sqrt{\frac{Q}{\pi N_{ch} s_u \tan^2 \frac{\beta}{2}}}, \tag{4.28}$$

where the values of N_{ch} were obtained from ELFEN (see Chapter 3). Values of h were obtained simply by multiplying h_s by $\sqrt{3}$.

Values of h and h_s from Abaqus analyses with the finer mesh are shown in Table 4.3 for each of the cases analysed here, along with the predictions obtained with Equation 4.28. There is generally good agreement between the theoretical values and the Abaqus results, a fact underlined in Figure 4.24a, where the Abaqus h values are plotted against the predicted values. In Figure 4.24b, the relationship between the Abaqus h and h_s results is shown. The relationship in Equation 4.26 fits the data well.

Table 4.3: Theoretical and numerical predictions of cone penetration depth

	m	N_{ch}	s_u	Theoretical		FE (Abaqus)	
Cone type	(g)	(ELFEN)	(kPa)	h_s (mm)	h (mm)	h_s (mm)	h (mm)
30°, smooth	100	5.056	103	2.890	5.005	2.886	5.007
30°, smooth	100	5.056	25.0	5.866	10.160	5.861	10.155
30°, smooth	100	5.056	11.4	8.687	15.046	8.659	15.019
30°, rough	100	10.241	50.9	2.889	5.003	2.867	4.971
30°, rough	100	10.241	12.7	5.783	10.016	5.719	9.952
30°, rough	100	10.241	5.65	8.670	15.017	8.637	14.876
60°, smooth	60	5.302	12.7	2.889	5.004	2.890	5.007
60°, smooth	60	5.302	3.20	5.756	9.969	5.742	10.155
60°, smooth	60	5.302	1.41	8.671	15.019	8.535	15.019
60°, rough	60	8.543	7.90	2.886	4.999	2.886	4.971
60°, rough	60	8.543	2.00	5.736	9.934	5.711	9.952
60°, rough	60	8.543	0.876	8.666	15.011	8.566	14.864

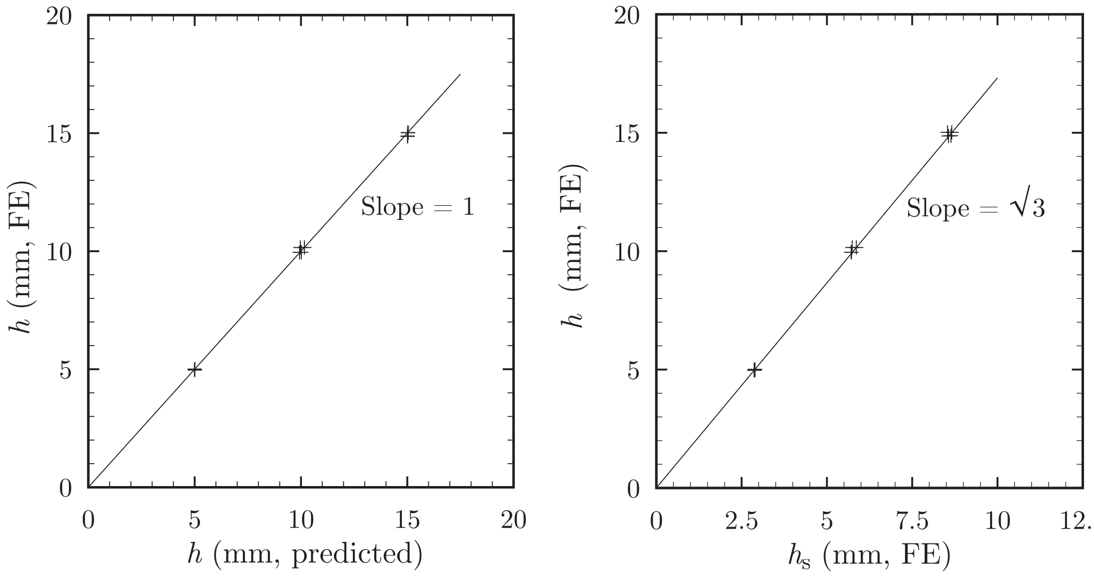

(a) Values of h from theory and Abaqus analysis (b) Relationship between Abaqus h and h_s results

Figure 4.24: Values of h and h_s from Abaqus analyses and theory. Crosses show Abaqus results, solid lines show predicted relationships

The close agreement observed in the values of h and h_s given by Abaqus and by Hansbo's dynamic analysis was also apparent in the shapes of the displacement–time, velocity–time and acceleration–time curves. Hansbo derived the acceleration a of the cone as

$$a = g\left(1 - 3\left(\tfrac{d}{h}\right)^2\right) \tag{4.29}$$

and the velocity v as

$$v = \left(2gd\left(1 - \left(\tfrac{d}{h}\right)^2\right)\right)^{\frac{1}{2}}. \tag{4.30}$$

The displacement–time relationship was found from

$$t = \int_0^d \left(2gd\left(1 - \left(\tfrac{d}{h}\right)^2\right)\right)^{-\frac{1}{2}} \mathrm{d}z \tag{4.31}$$

by numerical integration.

Figure 4.25 shows how displacement, velocity and acceleration varied during the analyses. All quantities are taken to be positive if they act *downwards*. The values of d, v and a have been normalised by dividing them by the final penetration h, the peak velocity $v_{\max}$ and the gravitational acceleration g, respectively. Since the time for cones to reach $d = h$ varied, the time t has been divided by t_{h}, the time at which peak displacement h was reached. Curves for each of the twelve Abaqus analyses using the finer meshes have been plotted, along with the theoretical curves (in black).

The normalized plots of the cones' motion all show very similar behaviour. Indeed the displacement–time curves from Abaqus are indistinguishable from one another. In each analysis the cone initially accelerates downwards with an acceleration $a = g$, because the only force acting is the weight W. The acceleration immediately begins to decrease as the resisting force Q increases. Since Q is proportional to d^2, Q increases rapidly as d increases, until (when $t/t_{\mathrm{h}} \approx 0.602$) the net force begins to act upwards and the cone begins to decelerate.

The most noticeable difference between the theoretical curve and the FE results is that the latter show the cones rebounding slightly after reaching maximum penetration. The theoretical curve shows no rebound, because it is based on an assumption of rigid–plastic material behaviour. The FE model used a finite rigidity index ($G/s_{\mathrm{u}} = 150$), so a certain amount of elastic deformation occurred. When released, the stored elastic strain energy allowed the cone to be pushed up slightly.

4.6 Accuracy of calculated forces at start of analysis

Because the finite element analyses presented here model the entire cone penetration event from the beginning (when the penetration is zero), the first part of each analysis effectively involves representing the deforming region of clay by a very coarse mesh. At the very

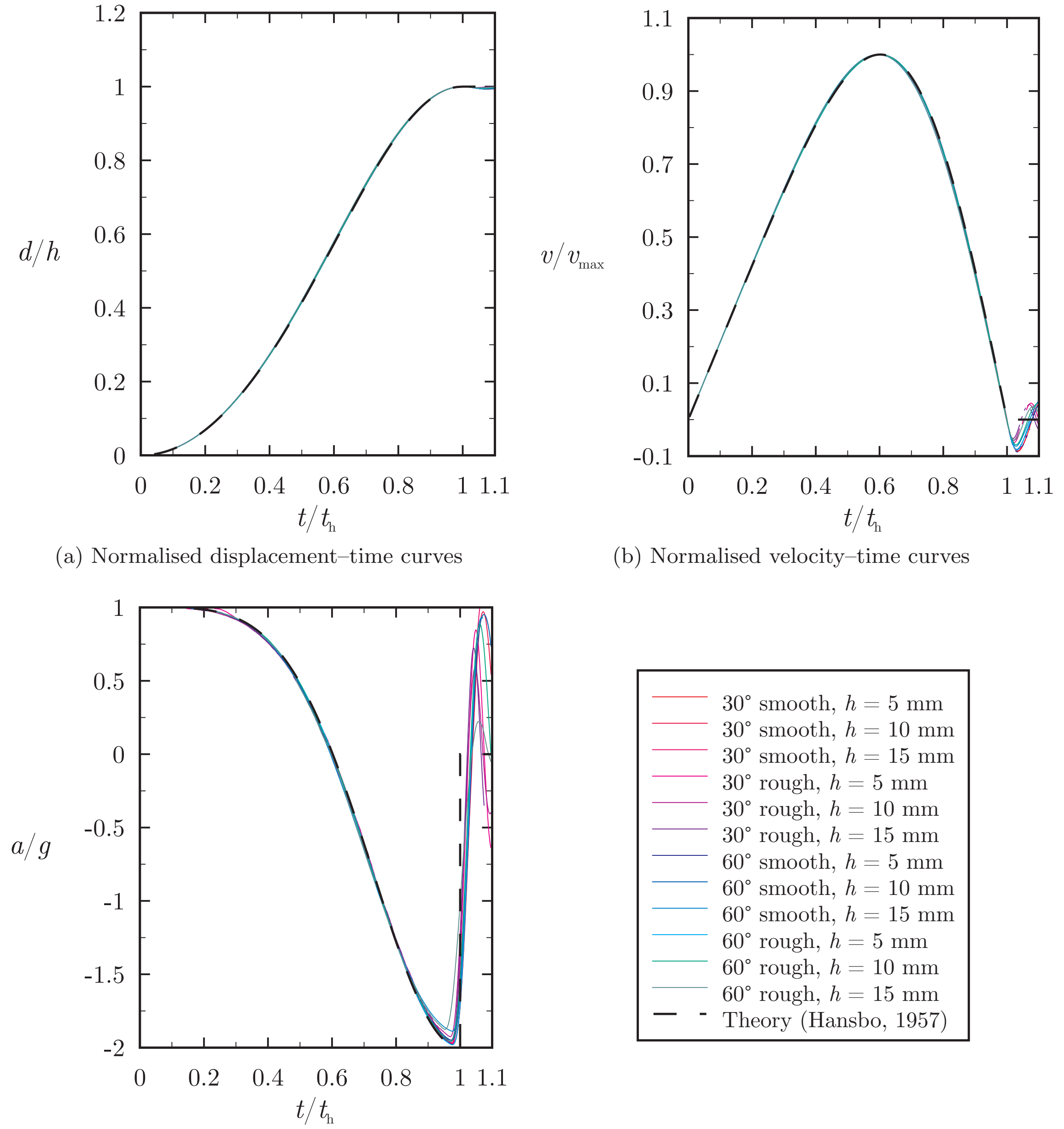

(a) Normalised displacement–time curves

(b) Normalised velocity–time curves

(c) Normalised acceleration–time curves

(d) Legend

Figure 4.25: Motion of cone in dynamic Abaqus FE analyses

beginning, the deforming region is composed of only one element. This means that the force Q that resists the cone's downward movement into the clay will be determined very inaccurately in the early part of the analysis. As displacement d increases, the number of elements in the deforming region increases, improving the spatial discretization. Eventually the mesh in the deforming region provides an adequate representation of the continuous problem and the cone resistance per unit area converges to a constant value (as shown in Figure 4.23).

In the quasi-static analyses, the result of interest has generally been the cone resistance near the end of the analysis, when the value of N_{ch} (or F) has converged. The inaccurate resistance early in the analysis is not a problem in such a case. The situation at the end of the analysis does depend on the earlier stages, in that the deformed geometry has developed throughout the analysis, but once the shape of the lip has reached a steady state accuracy will not be impaired.

In the dynamic analyses of Section 4.5, the force on the cone in the early stages of the analysis is important in determining its acceleration, and therefore the accuracy of the soil resistance is more important. Taking as an example the dynamic analysis of a smooth 30° cone in material with $s_{\mathrm{u}} = 25\,\mathrm{kPa}$, Figure 4.26a shows the relative error in the values of resistance Q obtained from this Abaqus dynamic analysis compared to those obtained using the formula $Q = Fs_{\mathrm{u}}d^2$, with F values from Table 3.4. Similar results could have been obtained from the other analyses. The relative error in Q is large at the start of the Abaqus analyses – in the example the first value of Q was over sixty-eight times larger than the theoretical value. The relative error decreased over the course of the analysis, dropping below 100% when $d \approx 0.3\,\mathrm{mm}$, 10% when $d \approx 1.5\,\mathrm{mm}$ and 1% when $d \approx 4.75\,\mathrm{mm}$. The relative error in Q is therefore quite large for a considerable part of each analysis.

However, the motion of the cone early in the analysis is governed not by the small resistance Q but by the net downward force on the cone $P = W - Q$, where W is the weight of the cone. The relative error in the value of P from FE compared with theory is plotted in Figure 4.26b for the example case. For small d, Q is small and P is roughly equal to W: despite the large relative error in Q, the absolute value is still very small. The largest relative error in P occurs at $d = h/\sqrt{3}$, when P is near-zero as $Q \approx W$. Although the relative error in P is large here, the effect on the final cone displacement h is not significant since P (and hence also the cone's acceleration) is small.

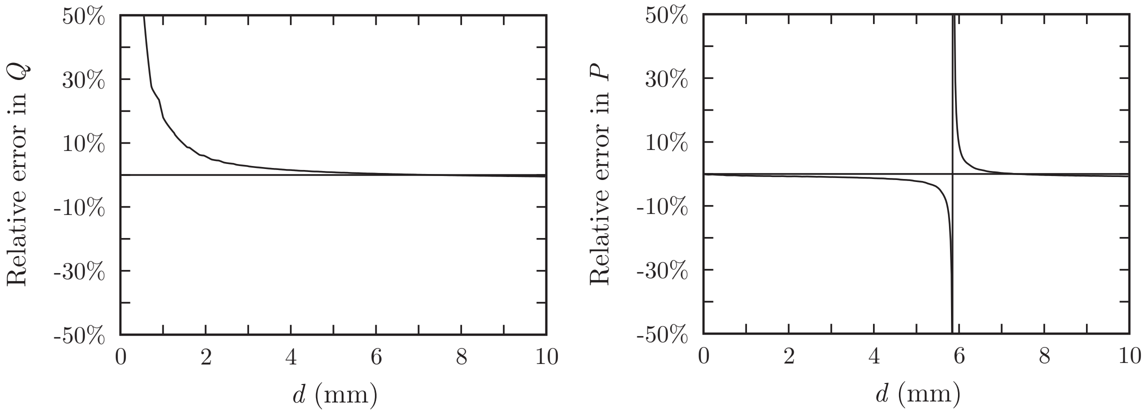

(a) Relative error in cone resistance Q

(b) Relative error in net force P on cone

Figure 4.26: Relative error in force obtained from Abaqus dynamic analysis of smooth 30° cone, compared to theoretical analysis with ELFEN F value

Chapter 5

Abaqus analysis with rate-dependent material

In Chapter 4 it was established that an Abaqus/Explicit finite element model, using a VUMAT user material subroutine to implement Tresca's yield criterion, was able to reproduce theoretical solutions for the fall cone test with a high degree of accuracy. In this chapter, the same VUMAT model is adapted to allow a simple rate-dependence rule to be included, such that the undrained strength s_u is a function of strain rate. This model is then used to investigate the influence of strain rate on the fall cone problem, through various displacement-controlled and freefall analyses.

5.1 Implementation of rate-dependence in Abaqus VUMAT

Various models for the rate-dependence of undrained strength have been proposed, as described in Section 2.2.2. The simplest of these models is adopted here: the elastoplastic Tresca material used in the previous chapter has been extended in a simple fashion by making s_u depend on the effective strain rate $\dot{\bar{\varepsilon}}$. The particular measure of effective strain rate adopted here is the maximum incremental shear strain rate, so that

$$\dot{\bar{\varepsilon}} = \dot{\gamma}_\mathrm{max} = |\dot{\varepsilon}_1 - \dot{\varepsilon}_3|_\mathrm{max} \tag{5.1}$$

where $\dot{\varepsilon}_1$ and $\dot{\varepsilon}_3$ are the major and minor principal strain rates. For brevity the subscript "max" will be omitted henceforth.

The relationship between strength and strain rate implemented in the VUMAT is

$$s_{\mathrm{u}} = s_{\mathrm{u0}} \left[1 + \mu \log_{10} \left(\frac{\max\left(\dot{\gamma}, \dot{\gamma}_{\mathrm{ref}}\right)}{\dot{\gamma}_{\mathrm{ref}}} \right) \right] \tag{5.2}$$

where μ is the proportional increase in strength per decade and s_{u0} is a reference strength, used when $\dot{\gamma} \leq \dot{\gamma}_{\mathrm{ref}}$. The variation of strength with strain rate for the case $\mu = 0.1$ is shown in Figure 5.1.

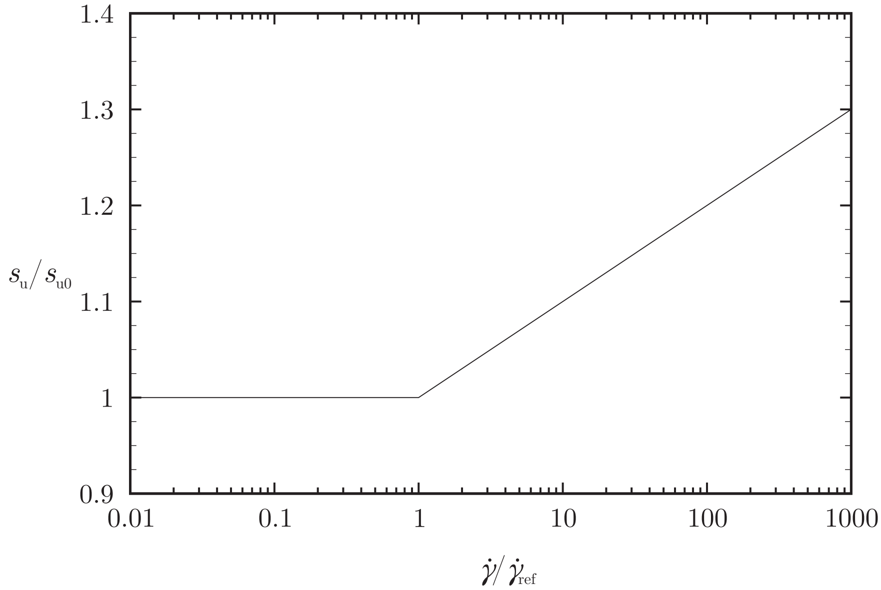

Figure 5.1: Variation of strength with strain rate (as defined by Equation 5.2)

The same strain measure $\dot{\bar{\varepsilon}} = \dot{\gamma}$ was used by Zhou and Randolph (2007), who adopted a similar extension to the Tresca model to describe rate-dependent strength in their analyses of full-flow penetrometers in soft sediments. Zhou and Randolph used an implicit formulation, and found that their model gave spurious oscillations in strength. When the shear strength was augmented due to high strain rate, the stress in the following increment would lie inside the newly enlarged Tresca yield surface. The strain rate in the newly strengthened material would be lower, and in the following increment the lower strain rate would give lower strength, and so on. To mitigate this oscillation problem, Zhou and Randolph damped abrupt changes in strength by taking the strength at each increment to be the mean of the old and new values.

No problems of the sort reported by Zhou and Randolph (2007) were encountered in the present work. The choice of an explicit dynamic FE formulation meant that rate dependence could be implemented in a particularly convenient manner: to advance the solution over a time increment, the explicit solver first obtains the strain increment (based on the displacements, velocities and accelerations in the previous increment); updated stresses are then obtained from the strains, in this case by the VUMAT subroutine. The displacements for the present increment, and hence the strain rate and the corresponding s_u, are known before the stresses are calculated, ensuring that combinations of strain rate, strength and stress are always consistent. Any oscillations would be insignificant because of the very small step sizes used in explicit dynamic FE analysis, and would be damped because dynamic effects in the analysis mean abrupt changes in strain rate are not possible.

Full details of how the modifications were incorporated in the VUMAT stress return algorithm can be found in Appendix A; the source code is in Appendix B.

5.2 Displacement-controlled FE analysis with rate-dependent soil

Finite element analyses were performed to simulate cones being pushed into blocks of clay under displacement control at a wide range of rates, covering several orders of magnitude. The samples were modelled as elastoplastic Tresca materials exhibiting rate dependence of the form defined in Equation 5.2. As in the work of Zhou and Randolph (2007), the reference strain rate $\dot{\gamma}_{ref}$ was taken as $3 \times 10^{-6}\,s^{-1}$, approximately 1 %/hour, and the reference strength s_{u0} as 10 kPa. Initially the rate parameter μ was given the value 0.1.

The samples were subject to boundary conditions equivalent to a rough-sided cylindrical cup of radius 27.5 mm, with the clay in contact with the cup fixed in both radial and vertical directions. Recall from Section 4.4 that the shape and roughness of the sample container were not found to have any significant influence on the force required for cone penetration (as long as the depth of penetration did not exceed certain limits).

5.2.1 Analysis procedure

Analyses in this section were performed with two cone angles (30° and 60°) and two contact conditions: fully smooth (no shear stress) and fully rough (no slip). For each of the four combinations of cone properties, analyses were performed under displacement control so as to create an indentation of depth 20 mm with respect to the undisturbed soil surface. In the first analysis, the material was modelled as having strength that was independent of strain rate. The results of this first analysis were used to give the variation with penetration depth of a reference resistance denoted Q_{ref}. This was used to determine the significance of the rate effect in each of the subsequent rate-dependent analysis.

In the first rate-dependent analysis with each cone, the cone velocity v was taken as 100 mm/s so that reaching 20 mm penetration took time $T = 0.2$ s. The analysis was then rerun several times, each time decreasing v by a factor of 10, until the normalised cone resistance Q/Q_{ref} was approximately unity. At this point, it could be inferred that the strain rate in the plastically deforming soil was nowhere significantly greater than $\dot{\gamma}_{\text{ref}}$.

5.2.2 Mass scaling

The analyses for this section covered a very broad range of time periods. The fastest indentation events took 0.2 s and the slowest 2×10^7 s. Because the stable time increment in an explicit FE analysis depends on the elastic wave speed, the model used for the fastest analysis would take an excessively long time to complete in the slowest case. To avoid this problem, the mass-scaling technique mentioned in Section 3.1.3 was employed.

In the fastest analyses (with $T = 0.2$ s), a density of 2×10^3 kg/m^3 was used. This was increased in the slower analyses to maintain the same kinetic energy in the deforming material (i.e. the mass of the material was inversely proportional to v^2). For example, in an analysis with $T = 2$ s the density was 2×10^5 kg/m^3. To ensure this mass scaling was not excessive, two rate-independent analyses were performed with each combination of cone angle and roughness, using the speeds and densities from the fastest and slowest rate-dependent analyses. The two curves of Q_{ref} against d were checked for consistency with one another and with the rate-independent analyses reported in Chapters 3 and 4 (the results of this check are given in Section 5.2.4).

5.2.3 Meshing

Each analysis was conducted with two different meshes. The first (coarse) had elements of length 1.25 mm in the deforming region, while the second (fine) mesh had four times as many elements, of length 0.625 mm. Abaqus/Explicit's ALE adaptive mesh smoothing option was used in these analyses, with all settings taking their default values.

Throughout this section, the results presented were obtained with the finer mesh. In Section 5.2.8, some key results obtained with the coarse mesh are presented to give an indication of the degree to which the quantities derived from the analyses are mesh-dependent.

5.2.4 Results: Smooth 30° cones

The results of the fast and slow rate-independent analyses indicated that the mass scaling technique discussed in Section 5.2.2 was not influencing the results significantly. Comparing cone forces at the same depth between the pairs of analyses revealed only very small, apparently random differences of order 0.01%.

The first set of analyses were those for the smooth 30° cone with $\mu = 0.1$. The curves of resistance Q against displacement d for the fastest and slowest analyses are shown in Figure 5.2a. The curves shown were obtained with the finer mesh, but very similar results were seen when the coarse mesh was used, suggesting no further mesh refinement was necessary. The graph shows the curves obtained from the fastest and slowest rate-dependent analyses (with $v = 1 \times 10^{-1}$ m/s and $v = 1 \times 10^{-8}$ m/s respectively) as well as the rate-independent results. The slowest rate-dependent analysis gave results that were essentially identical with the rate-independent test, so no change in resistance would be expected if the analysis was repeated with lower speed. In Figure 5.2b, the same Q–d results are shown, but the cone

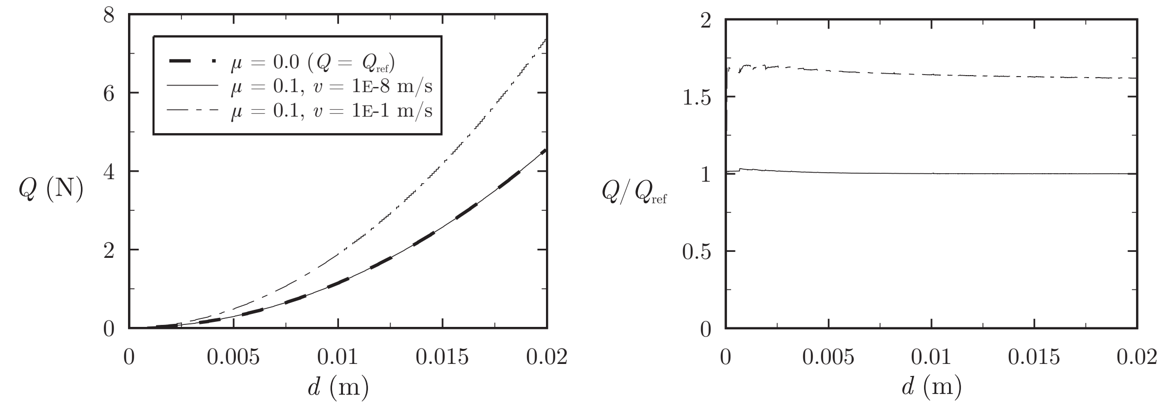

(a) Cone resistance against displacement, with rate-independent result

(b) Normalised cone resistance against displacement

Figure 5.2: Resistance during fast and slow rate-dependent FE analyses of smooth 30° cone indentation

resistance Q has been normalised by dividing every value by the rate-independent result Q_{ref}, from the results reported in Chapter 4. The ratio Q/Q_{ref} is a measure of the increase in cone resistance due to the rate effect, and is related to some measure of the operative average strain rate in the deforming material, which will be denoted by $\dot{\gamma}_{\text{ave}}$. The form this averaging process should take is unclear, as a simple volume average will not suffice: the correct method would need to be weighted in favour of the parts of the deforming region in which most plastic work was being done. With $v = 1 \times 10^{-8}$ m/s, Q/Q_{ref} was found to be close to unity throughout, showing a very slight (maximum 3.3%) rate effect at the beginning of the analysis. With $v = 1 \times 10^{-1}$ m/s, Q/Q_{ref} is generally between 1.6 and 1.7, again decreasing slightly during the analysis.

It should not be surprising that Q/Q_{ref} decreases during each analysis, as dimensional considerations dictate that the average strain rate in the deforming region depends on the ratio v/d. As v is constant throughout each of these analyses, the average strain rate constantly decreases as d increases. The results shown are not entirely consistent with this prediction, however, as v/d will be very large for small d – initially, the average strain rate should be infinite. This behaviour is not captured because the spatial discretisation of the deforming region in the early part of the analysis is insufficient. Deformations are not concentrated in one part of the mechanism as they would be in a continuum analysis, but are "smeared out" over a few elements (initially only a single element). Analysis with a finer mesh would be expected to show increased rate effects at the start. This is consistent with the observed results, as shown in Figure 5.3 for the case $v = 1 \times 10^{-8}$ m/s. The finer mesh gives a higher value of Q early in the analysis, though only by 3.3%. The mesh would need to be very refined indeed to accurately take account of strain rate effects at the very beginning of the indentation when $d \approx 0$. Instead, conclusions will be drawn based on forces from later in the analysis, after the cone had penetrated to at least $d = 10$ mm. By this stage, the curves in Figure 5.3 differ by only 0.10%.

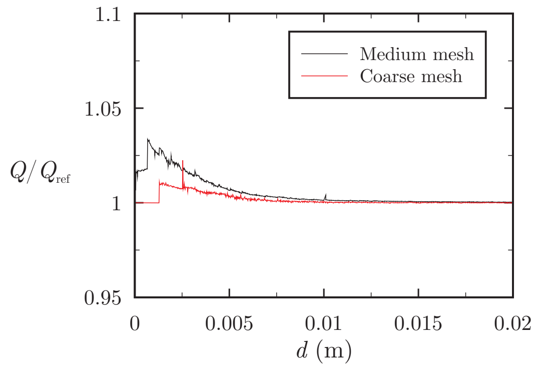

Figure 5.3: Normalised resistance Q/Q_{ref} in analyses with differing mesh refinement

The normalised load-displacement curves shown in Figure 5.2b, together with those obtained from similar analyses with different speeds, were processed in the following way: three data points were taken from each curve, consisting of the values of Q/Q_{ref} when d was equal to 10, 15 and 20 mm. The points obtained from all the analyses were combined to give the curves in Figure 5.4a, which shows the variation of Q/Q_{ref} with v for each of the three depths. Each of the three curves clearly shows that, in the slowest rate-dependent cases analysed, the force required to increase cone penetration was roughly equal to the reference values obtained with no strength enhancement due to rate effects. As the cones were pushed in more rapidly, the force necessary began to increase. After an initial transitional phase (the existence of which was confirmed by performing an additional analysis with v midway between 1×10^{-5} and 1×10^{-4} mm/s), the force needed began to increase with increasing velocity, with the slope of the line being determined by the rate parameter μ.

To present the results in a more general form, the three curves from Figure 5.4a are shown again in 5.4b, but with Q/Q_{ref} plotted against v/d. The choice of the depth of penetration d is convenient, but any characteristic length would have done just as well (for instance, the radius at the free surface). This causes the three curves to collapse onto a single line. The fact that this unique relationship exists in the results confirms that the strain rate that determines the material strength at any instant around a fall cone in rate-dependent material depends on the ratio v/d. It also provides confirmation that the meshes used in the analyses were adequately refined, since an approximately self-similar state was evidently achieved before the indentation depth reached 10 mm.

The fact that the relationship between Q and $\log_{10}(v)$ is linear and has the same slope μ as the defined relationship between stress and strain rate may at first appear unremarkable, or even trivial. However, it was possible that changes in the deformation mechanism could have partially offset the effect of increasing material strength, leading to the slope of the curve in Figure 5.4b being less than μ. The slope is found to be equal to μ in this case, suggesting that the deformation mechanism remains similar as cone speed is increased. In this respect, the case of fall-cone indentation differs from others in which deformations are concentrated in narrow shear bands. This type of behaviour was described by Einav and Randolph (2006), who analysed the case of a shear vane in rate-dependent material. They found that when the angular velocity of the vane was increased, the thickness of the shear band increased to an optimum value that minimized the rate of plastic work. Einav and Randolph found that the slope of a plot of normalized torque against angular velocity for a shear vane (analogous to Figure 5.4a) had a slope less than that which might be expected based on the assumed strength–strain rate relationship.

As stated above, although the force needed to push a cone into rate-dependent material

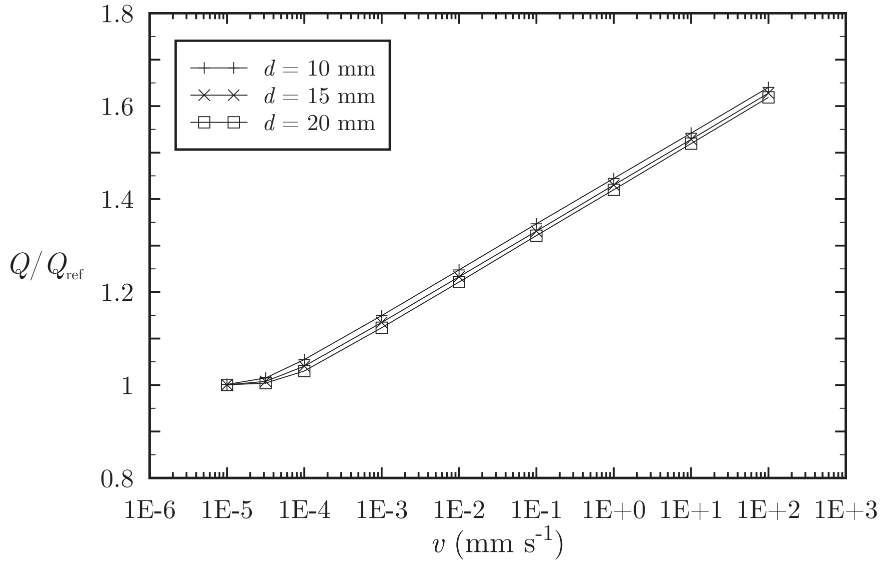

(a) Variation of normalised cone resistance Q/Q_{ref} with speed v at various indentation depths

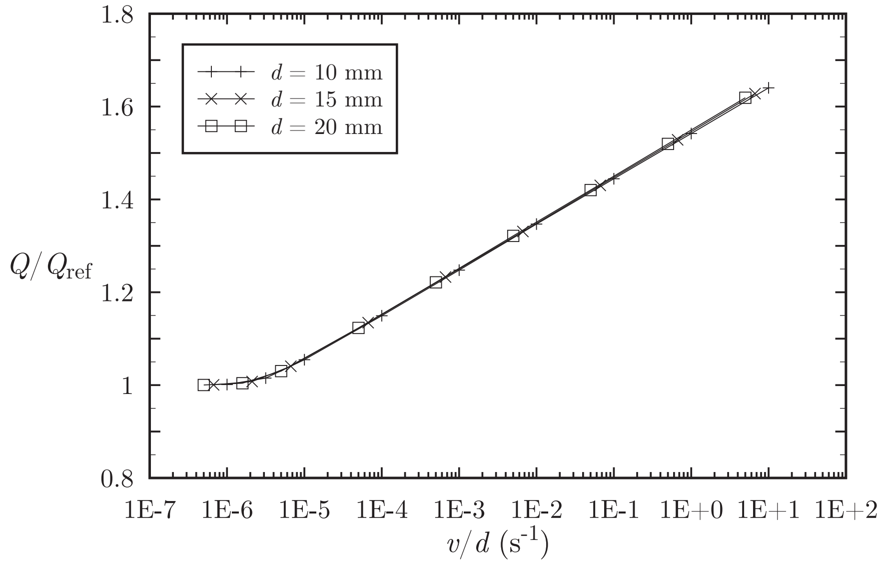

(b) Variation of normalised cone resistance Q/Q_{ref} with speed ratio v/d

Figure 5.4: Influence of rate effect in indentation analyses at various speeds

is clearly dependent on $\dot{\gamma}_{\text{ave}}$ (a measure of the operative average strain rate in the deforming material) it is unclear exactly how this average value can be determined from the spatial distribution of strain rates within the plastically deforming region. However, the results already presented, together with knowledge of the rate dependence relationship in the indented material (from Equation 5.2), provide an indirect and approximate means of determining $\dot{\gamma}_{\text{ave}}$. If we assume that the cone resistance Q is equal to $Fs_{\text{u,ave}}d^2$ in the rate-dependent analyses, where the value of F is unchanged from the rate-independent analyses and $s_{\text{u,ave}}$ represents the typical strength mobilised in the deforming material, it follows that

$$\frac{Q}{Q_{\mathrm{ref}}} = \frac{s_{\mathrm{u,ave}}}{s_{\mathrm{u0}}}. \tag{5.3}$$

Combining this assumption with the rate dependence relation of Equation 5.2 gives

$$\frac{\max\left(\dot{\gamma}_{\mathrm{ave}}, \dot{\gamma}_{\mathrm{ref}}\right)}{\dot{\gamma}_{\mathrm{ref}}} = 10^{\frac{1}{\mu}\left(\frac{Q}{Q_{\mathrm{ref}}}-1\right)}. \tag{5.4}$$

When $\dot{\gamma}_{\mathrm{ave}} > \dot{\gamma}_{\mathrm{ref}}$, the right-hand side of this expression can be multiplied by $\dot{\gamma}_{\mathrm{ref}}$ to obtain the strain rate that would have to be applied to the material in order to give it the correct strength to account for the observed cone resistance. With a smooth 30° cone, the condition $\dot{\gamma}_{\mathrm{ave}} > \dot{\gamma}_{\mathrm{ref}}$ appears to have applied in analyses with $v > 1 \times 10^{-4}$ mm/s, since (in Figure 5.4b) the results for cases with higher values of v lie on a straight line with slope μ.

Using Equation 5.4, approximate values of average strain rate $\dot{\gamma}_{\mathrm{ave}}$ were determined from the values of Q/Q_{ref} shown in Figure 5.4b. Results from the slowest analyses (those with $v < 1 \times 10^{-4}$ mm/s) were not used, for the reason given in the previous paragraph. Dividing $\dot{\gamma}_{\mathrm{ave}}$ by the cone speed ratio v/d gave a value that remained near-constant as v/d varied over several orders of magnitude, as shown in Figure 5.5. The observed values of $\dot{\gamma}_{\mathrm{ave}}/(v/d)$ were generally in the range 0.8 to 1.0, or slightly higher at the lowest rates of penetration.

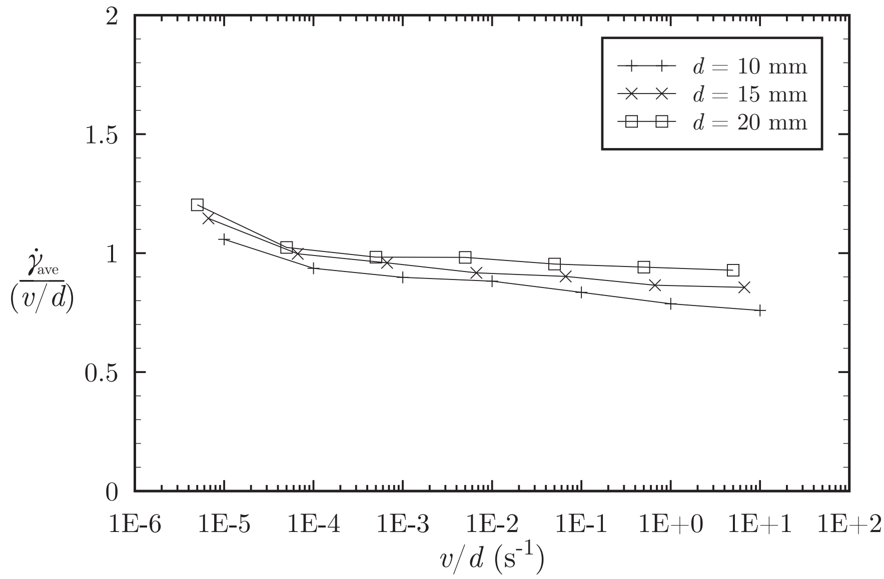

Figure 5.5: Average effective strain rate $\dot{\gamma}_{\mathrm{ave}}$ under smooth 30° cone indentation when $\mu = 0.1$

The analyses described so far (using material with $\mu = 0.1$) were one of three sets with smooth 30° cones. In the other two sets, the value of μ was either halved or doubled, taking the values 0.05 and 0.2. The three sets of results were initially plotted as Q/Q_{ref} against v/d, giving graphs similar in appearance to Figure 5.4b. All three sets of analyses showed identical results for velocities below a certain threshold which will be referred to as $(v/d)_{\mathrm{ref}}$, which was to be expected since the only change between them was in the value of μ, which became relevant only above the threshold strain rate. Above $(v/d)_{\mathrm{ref}}$ the three sets of analyses gave three diverging lines, each with a different slope μ. These lines can be approximated by the equation

$$\frac{Q}{Q_{\mathrm{ref}}} = 1 + \mu \log_{10}\left(\frac{v/d}{(v/d)_{\mathrm{ref}}}\right). \tag{5.5}$$

The value of $(v/d)_{\mathrm{ref}}$ was selected by choosing the value that gave the best fit to the numerical data in a least-squares sense, using the Solver plug-in in Microsoft Excel. Figure 5.6 shows the results. Since the fitted curves were intended to represent the data on the sloping part of each graph, the unshaded points were excluded from the fit. The value of $(v/d)_{\mathrm{ref}}$ obtained from this analysis was $3.63 \times 10^{-6}\,\mathrm{s}^{-1}$. Since $(v/d)_{\mathrm{ref}}$ corresponds to an average effective strain rate of $\dot{\gamma}_{\mathrm{ref}}$ (taken as $3 \times 10^{-6}\,\mathrm{s}^{-1}$), this suggests that $\dot{\gamma}_{\mathrm{ave}}$ and (v/d) are related by

$$\dot{\gamma}_{\mathrm{ave}} = 0.83(v/d), \tag{5.6}$$

which is consistent with, though towards the lower end of, the range of values shown in Figure 5.5. It seems likely that Equation 5.6 represents a reliable estimate of strain rate under indentation by a smooth 30° cone, since it is based on the combined results of many analyses.

The velocity vectors in Figure 5.7 show the deformation mechanism when $d = 20\,\mathrm{mm}$ in the fastest and slowest analyses (those with $v = 100\,\mathrm{mm/s}$ and $1 \times 10^{-5}\,\mathrm{mm/s}$ respectively). There is very little difference between the two plots, supporting the conclusion that the pattern of deformation within the indented material does not change significantly to compensate for the effects of rate-dependent strength when the speed of the cone is increased. In the analysis with high cone speed, material far from the cone exhibits small, apparently random movements that are not present in the low-speed analysis, suggesting that the significant rate-dependence may cause minor numerical instabilities in the analysis. However these effects do not significantly affect the deformation mechanism or the overall response of the model.

Figure 5.8 shows the extent of the region in which the strain rate $\dot{\gamma}$ is greater than the

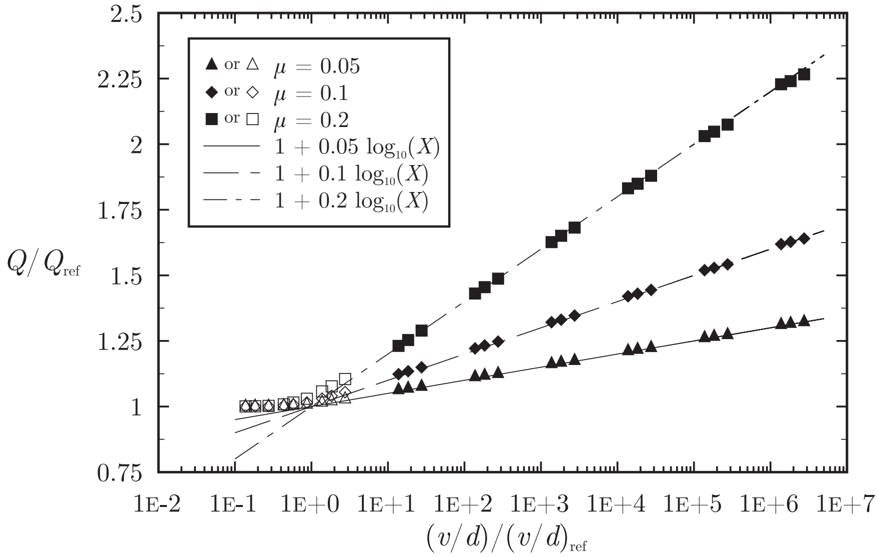

Figure 5.6: Increase in cone resistance due to rate effect, smooth 30° cone. By fitting lines to the shaded data points, $(v/d)_{\mathrm{ref}}$ was found to be $3.63 \times 10^{-6}\,\mathrm{s}^{-1}$

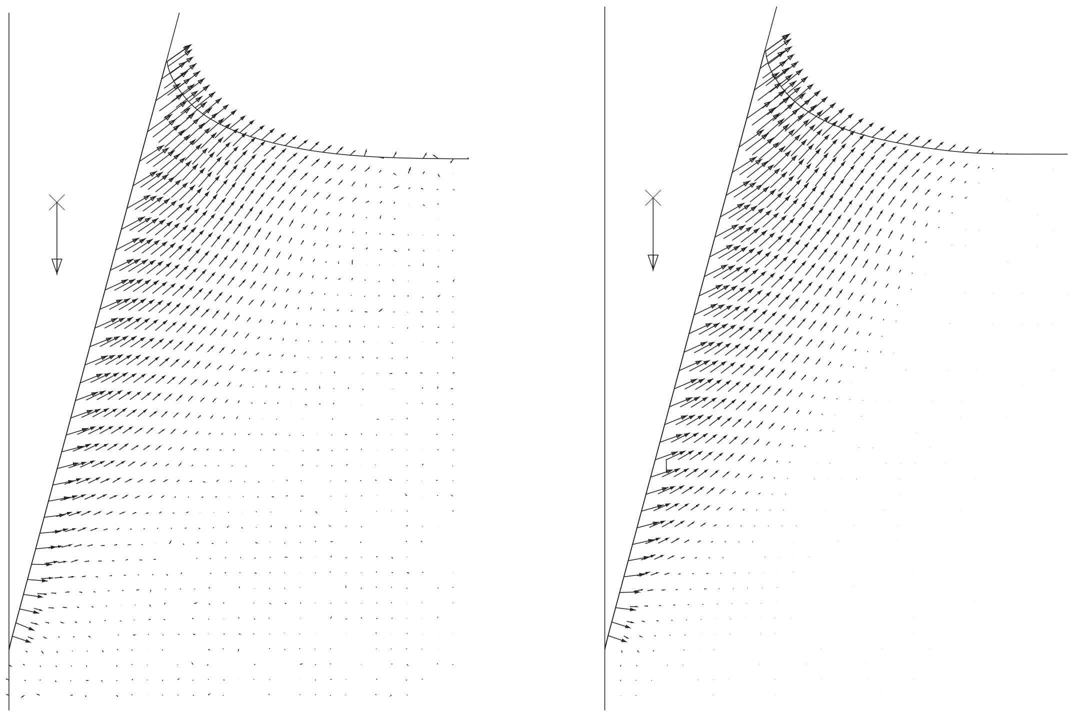

(a) $v/d = 5\,\mathrm{s}^{-1}$

(b) $v/d = 5 \times 10^{-7}\,\mathrm{s}^{-1}$

Figure 5.7: Velocity field around a smooth 30° cone at high and low speed ($\mu = 0.1$)

average value $\dot{\gamma}_{\text{ave}}$, and the variation of $\dot{\gamma}$ within that region. Note that the strain rate in some elements close to the tip of the cone is very much greater than the average value determining the indentation resistance. The extent of the $\dot{\gamma} > \dot{\gamma}_{\text{ave}}$ region did not vary significantly with cone speed.

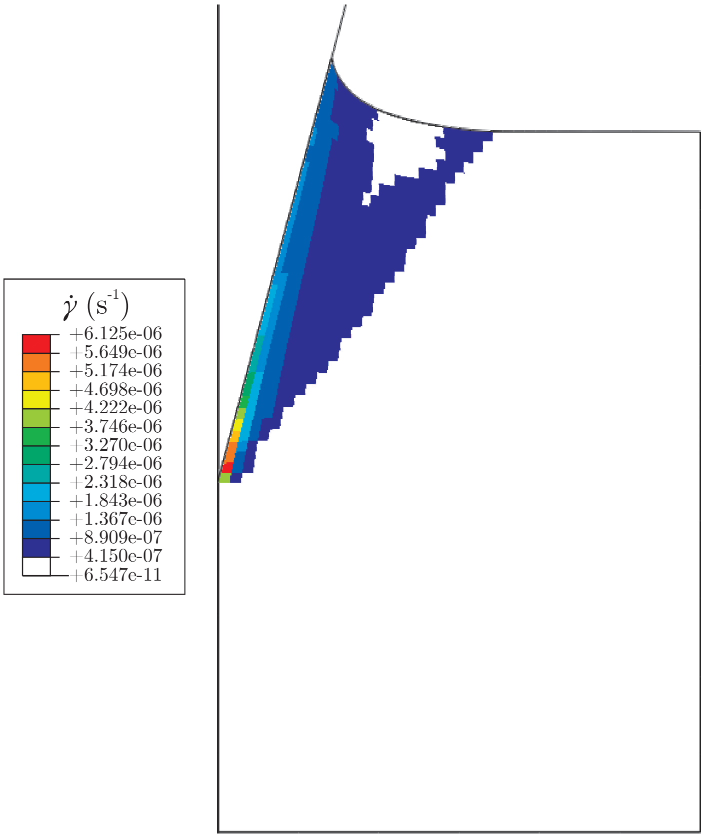

Figure 5.8: Strain rate in elements with $\dot{\gamma} > \dot{\gamma}_{\text{ave}}$ during indentation with a smooth 30° cone ($v/d = 5 \times 10^{-7}\,\text{s}^{-1}$)

5.2.5 Results: Smooth 60° cones

Analyses of indentation with a smooth 60° were performed next. These were similar in most respects to the smooth 30° cone analyses for which results have already been presented.

As before, effective strain rates were deduced from the values of Q/Q_{ref} at $d = 10\,\text{mm}$, 15 mm and 20 mm in each of the analyses. Values of $\dot{\gamma}_{\text{ave}}$ were converted to dimensionless form by dividing by (v/d), and the results are shown in Figure 5.9. Comparison with Figure 5.5) reveals that strain rates in analyses with a smooth 60° cone were higher than those around the smooth 30° cone by a factor of approximately 2.

Results for three different values of μ were again combined, and a value of $(v/d)_{\text{ref}}$ estimated so as to give a best fit to the data on the sloping portion of the graphs in Figure

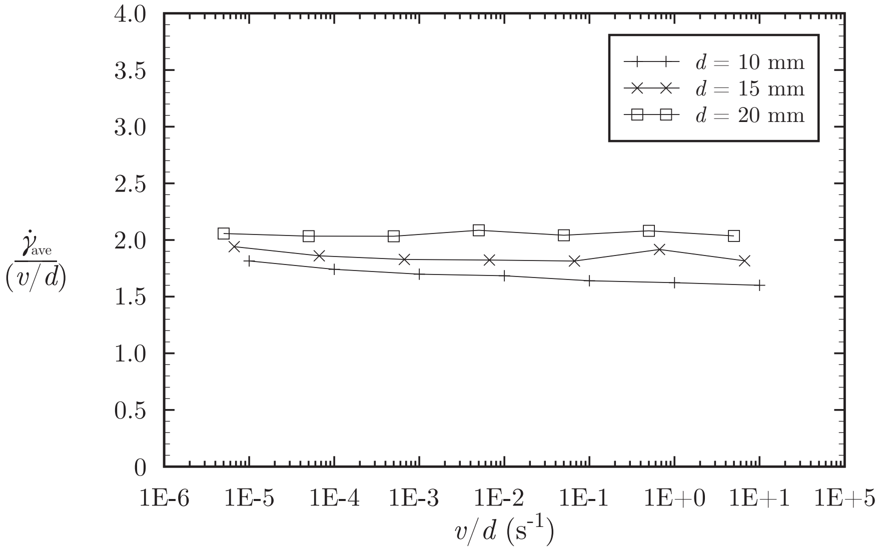

Figure 5.9: Average effective strain rate $\dot{\gamma}_{\text{ave}}$ under smooth 60° cone indentation when $\mu = 0.1$

5.10. The optimum value was found to be $(v/d)_{\text{ref}} = 1.75 \times 10^{-6}\,\text{s}^{-1}$, implying the following relationship between average strain rate and (v/d):

$$\dot{\gamma}_{\text{ave}} = 1.7(v/d). \tag{5.7}$$

The constant relating (v/d) to $\dot{\gamma}_{\text{ave}}$ is approximately twice that for the smooth 30° cone, given in Equation 5.6.

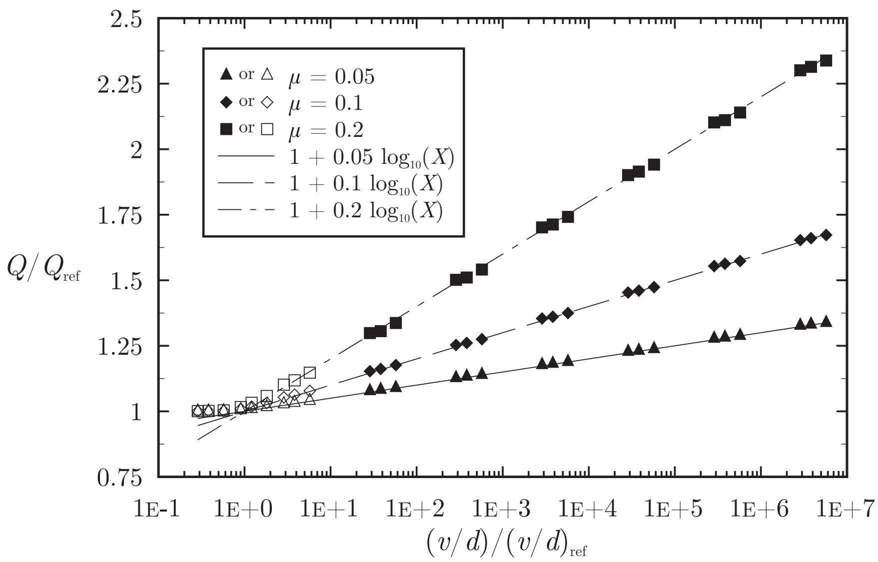

Figure 5.10: Increase in cone resistance due to rate effect, smooth 60° cone. By fitting lines to the shaded data points, $(v/d)_{\text{ref}}$ was found to be $1.75 \times 10^{-6}\,\text{s}^{-1}$

5.2.6 Results: Rough 30° cones

The force-displacement curves for analyses with rough cones (with no slip allowed between the face of the cone and the adjacent material) were more noisy than those obtained with smooth cones. This was in accordance with the observed behaviour in rate-independent analyses, reported in Section 4.3.6, and can probably be attributed to the larger adjustments to node locations made by the ALE adaptive mesh smoothing algorithm in the rough cone analyses, and the associated interpolation errors when mapping variables to the new meshes.

Figure 5.11a shows the variation of force Q with displacement d in three of the rough 30° cone analyses: the fastest and slowest rate-dependent analyses (with $\mu = 0.1$) and the reference rate-independent ($\mu = 0$) analysis from Chapter 4. Although the results have been smoothed using a 49-point centred moving average as before, all three curves exhibit apparently random, small but noticeable deviations from the expected parabolic shape. When the values of Q and Q_{ref} were used to obtain the normalized curves in Figure 5.11b, the noisiness of the curves became more apparent.

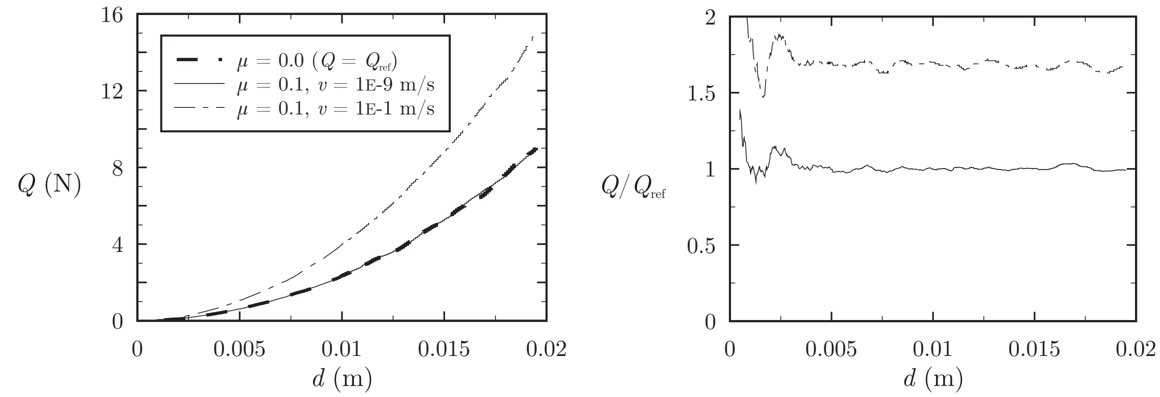

(a) Cone resistance against displacement, with rate-independent result

(b) Normalised cone resistance against displacement

Figure 5.11: Resistance during fast and slow rate-dependent FE analyses of rough 30° cone indentation

Despite the poorer quality of the results obtained with rough cones, the overall trend of the analyses followed the expected pattern. For each value of μ, cone resistance Q was close to Q_{ref} for low-speed indentation, then began to increase by a factor of μ with every tenfold increase in cone speed. Initially, the same values of v were used as in the smooth cone analyses. However, additional low-speed analyses had to be performed before values of Q/Q_{ref} close to unity were obtained.

As before, the ratio of cone speed to indentation depth at which rate effects became significant was determined by choosing $(v/d)_{\text{ref}}$ to minimize the mean square error when comparing the theoretical curves and selected numerical results, as shown in Figure 5.12. The value of $(v/d)_{\mathrm{ref}}$ was found to be $1.33 \times 10^{-6}\,\mathrm{s}^{-1}$, implying that the relationship between strain rate and v/d for a rough 30° cone is

$$\dot{\gamma}_{\mathrm{ave}} = 2.3(v/d). \tag{5.8}$$

The FE analysis therefore suggests that a rough 30° cone induces higher average strain rates in the indented material than a smooth cone with $\beta = 30°$ or 60°, for equal values of cone speed and indentation depth.

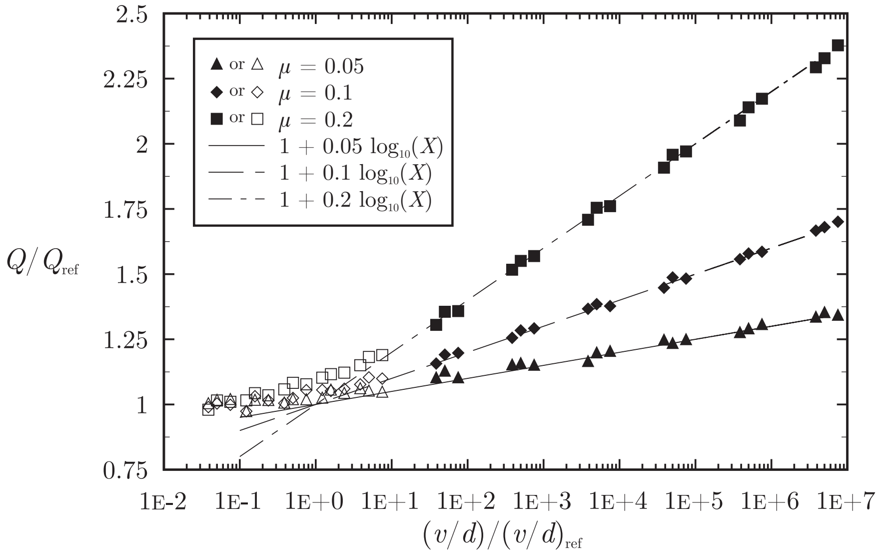

Figure 5.12: Increase in cone resistance due to rate effect, rough 30° cone. By fitting lines to the shaded data points, $(v/d)_{\mathrm{ref}}$ was found to be $1.33 \times 10^{-6}\,\mathrm{s}^{-1}$

Figure 5.13 shows the strain rate in the mesh region with $\dot{\gamma} > \dot{\gamma}_{\mathrm{ave}}$ under indentation with a rough 30° cone. The cone speed and depth of indentation are the same as in the similar plot for a smooth cone (Figure 5.13), so that $v/d = 5 \times 10^{-7}\,\mathrm{s}^{-1}$. The region with strain rate larger than $\dot{\gamma}_{\mathrm{ave}}$ is concentrated in a narrow band adjacent to the cone. The largest strain rates occur on the upper part of the cone face, rather than close to the tip as in the case of a smooth cone. Much of the deformation is concentrated in a single layer of elements adjacent to the face of the cone, and the strain rate here will be highly dependent on the mesh density as discussed in Section 4.3.6 for rate-independent Abaqus analyses. In the rate-independent analyses, the overall force on the cone Q was not found to be excessively dependent on mesh refinement despite this potential problem. The influence of mesh density on the results of these rate-dependent analyses is discussed further in Section 5.2.8.

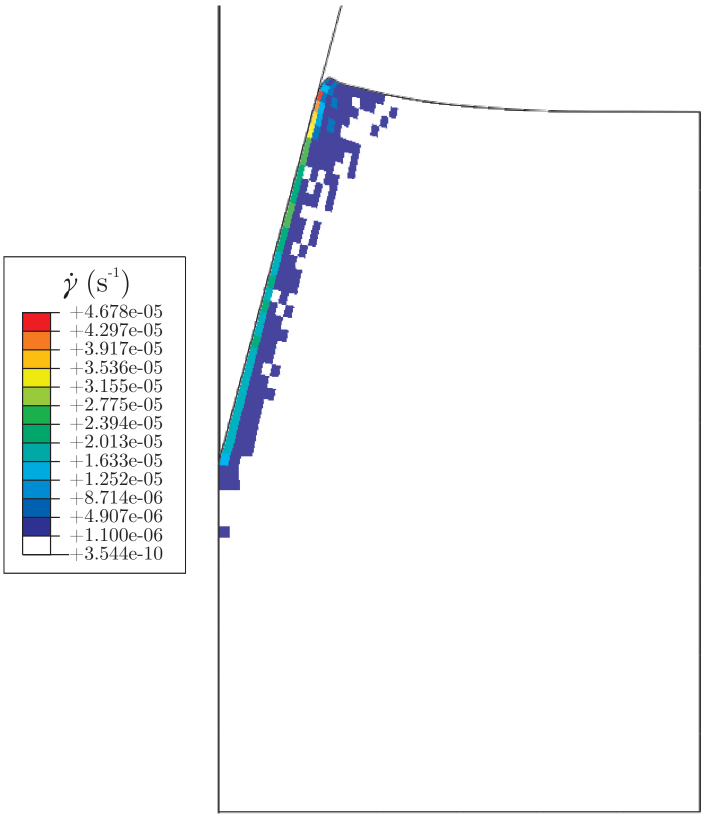

Figure 5.13: Strain rate in elements with $\dot{\gamma} > \dot{\gamma}_{\mathrm{ave}}$ during indentation with a rough 30° cone ($v/d = 5 \times 10^{-7}\,\mathrm{s}^{-1}$)

5.2.7 Results: Rough 60° cones

Finally, analyses were performed with rough 60° cones. The results were processed as before, giving Figure 5.14. The best-fit value of $(v/d)_{\mathrm{ref}}$ was found to be $2.11 \times 10^{-6}\,\mathrm{s}^{-1}$, implying that

$$\dot{\gamma}_{\mathrm{ave}} = 1.4(v/d). \tag{5.9}$$

So, for a given value of (v/d) a rough 60° cone seems to give *lower* strain rates than a smooth 60° cone (the opposite trend to that seen with 30° cones).

5.2.8 Summary of key results

Table 5.1 summarises the values of $(v/d)_{\mathrm{ref}}$ and $\dot{\gamma}_{\mathrm{ave}}/(v/d)$ deduced from FE analyses of displacement-controlled cone penetration in rate-dependent Tresca materials as described in Sections 5.2.4 to 5.2.7. Values obtained from results of analyses with a coarser mesh (in which the spacing of nodes was twice that in the fine mesh) are also shown. In the case of smooth 30° and 60° cones and rough 30° cones, there is good agreement between the

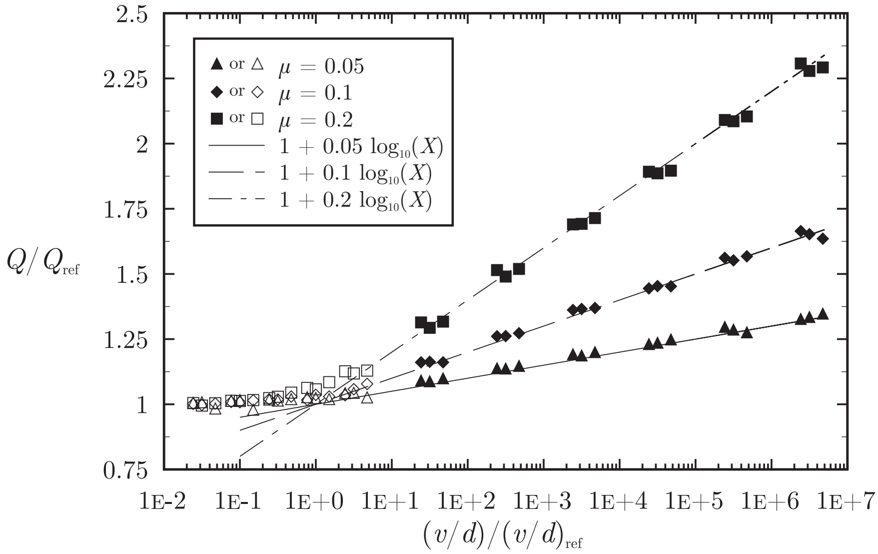

Figure 5.14: Increase in cone resistance due to rate effect, rough 60° cone. By fitting lines to the shaded data points, $(v/d)_{\mathrm{ref}}$ was found to be $2.11 \times 10^{-6}\,\mathrm{s}^{-1}$

dimensionless strain rates deduced from the results – the second significant figures differ by no more than one. The discrepancy between the values is a little greater for the rough 60° cone (the value obtained with the coarse mesh is approximately 14% greater than that with the fine mesh), but they are still believed to give a reasonable guide to the strain rates that could be expected to pertain.

One conclusion that may be drawn from the results shown here is that the strain rate induced in the indented material is strongly dependent on the roughness of the cone when a 30° cone is used. The values of $\dot{\gamma}_{\mathrm{ave}}$ for a particular cone speed ratio (v/d) differ almost by a factor of three depending on the interface condition. If a 60° cone is used, the same values differ by a factor of only around 1.2. It is therefore particularly important to control the roughness of the cone carefully when a 30° cone is used to test material that may exhibit strongly rate-dependent undrained strength.

Table 5.1: Summary of results from displacement-controlled rate-dependent FE analyses, including values obtained with coarse and fine meshes

		Coarse mesh		Fine mesh	
β (°)	Interface condition	$(v/d)_{\mathrm{ref}}$ ($\mathrm{s}^{-1} \times 10^{-6}$)	$\dot{\gamma}_{\mathrm{ave}}/(v/d)$	$(v/d)_{\mathrm{ref}}$ ($\mathrm{s}^{-1} \times 10^{-6}$)	$\dot{\gamma}_{\mathrm{ave}}/(v/d)$
30	smooth	3.55	0.84	3.63	0.83
60	smooth	1.81	1.7	1.75	1.7
30	rough	1.35	2.2	1.33	2.3
60	rough	1.83	1.6	2.11	1.4

5.3 Freefall FE analysis with rate-dependent soil

An extensive series of finite element analyses was performed to assess the influence of rate-dependence (as represented by the modified Tresca VUMAT) in dynamic fall cone tests. These tests were closely based on those described in Section 4.5, with the introduction of rate-dependent strength (as described earlier in this chapter) being the only new feature.

5.3.1 Cases considered

The analyses performed for Section 4.5 formed the basis of the work described here. Recall that rate-independent dynamic analyses were performed for two cone angles (30° and 60°) and two interface conditions (smooth, or zero shear stress, and rough, or zero slip). For each of the four combinations of angle and roughness, three analyses were performed with s_{u} chosen so as to give final cone penetrations of approximately 5, 10 and 15 mm. The twelve cases are shown in Table 4.3. The table also shows the results of the analyses in terms of the maximum freefall cone penetration h and h_{s}, the penetration at which the weight of the cone would be equal to the resistance Q in a slow displacement-controlled test (with $(v/d) < (v/d)_{\mathrm{ref}}$ at all times, where $(v/d)_{\mathrm{ref}}$ is the value below which rate effects cease to be significant as determined in Section 5.2).

Each of the twelve freefall analyses with rate-independent material (described in Section 4.5 and listed in Table 4.3) was repeated four times with rate-dependent material, each time with a different value of the rate parameter μ. The values used were 0.05, 0.10, 0.15 and 0.20, covering the range of values typically encountered in real materials (Randolph, 2004).

5.3.2 Review of rate-dependent fall cone tests

The dynamic analysis of a fall cone in rate-independent material performed by Hansbo (1957) showed the ratio h/h_{s} to be equal to $\sqrt{3}$, and the rate-independent FE analyses fitted this relationship closely (see Figure 4.24b). Koumoto and Houlsby (2001) performed a similar dynamic analysis to Hansbo's, but accounted for the possibility that the apparent strength exhibited by material during a dynamic fall cone test (which they called s_{ud}) might not be the same as its strength at very low strain rates (s_{u}). A description of their analysis was given in Section 2.2.7. They postulated that the final penetration in a fall cone test on rate-dependent material would be h, where

$$h = h_{\mathrm{s}}\sqrt{3s_{\mathrm{u}}/s_{\mathrm{ud}}} = h_{\mathrm{s}}\sqrt{3\zeta}. \tag{5.10}$$

When $s_{\mathrm{ud}} > s_{\mathrm{u}}$, $\zeta = s_{\mathrm{u}}/s_{\mathrm{ud}}$ will be a factor less than one. For a particular relationship between strength and strain rate (for example, Equation 5.2), the value of ζ will be related to the average strain rate undergone by the deforming material over the course of the entire fall cone test. Note that this is more complicated than the situation in the analyses of displacement-controlled penetration of rate-dependent material (Section 5.2). Approximate values of $\dot{\gamma}_{\mathrm{ave}}$ were obtained from those analyses, but $\dot{\gamma}_{\mathrm{ave}}$ is merely the *instantaneous* average strain rate. To determine ζ would require consideration of the variation of $\dot{\gamma}_{\mathrm{ave}}$ over the duration of the indentation, within which both d and v vary continuously.

Rather than attempt to determine ζ by calculating some form of time-averaged strain rate, Equation 5.10 was rearranged to give

$$\zeta = h^2/(3h_{\mathrm{s}}^2). \tag{5.11}$$

To allow ζ to be determined indirectly, values of h from the dynamic FE analyses of freely-falling cones were combined with the h_{s} results given in Section 4.5, Table 4.3.

5.3.3 Results

Values of the cone's displacement d, velocity v and acceleration a, and the resisting force Q, were calculated and saved to the Abaqus output database at 1000 equally-spaced time intervals during each analysis. As in Section 4.5.3, a moving average was computed to smooth the results for Q and a.

The curves in Figure 5.15 indicate how the displacements, velocities and accelerations of the cones varied over the course of the analyses in the case where μ was equal to 0.2 (which is at the extreme of the range of values expected in real soils). The curves are all shown in normalised form, as they were for rate-independent material in Figure 4.25. Values of d have been divided by the maximum cone displacement h, v has been normalised by its maximum value v_{max} and a by the gravitational acceleration g. Times have been normalised by the time t_{h} at which the cone reaches its maximum penetration h. The heavy black dashed lines show the curves given by the theoretical analysis of Hansbo (1957) for a rigid–plastic, rate-independent material.

The plot of d/h against t/t_h (Figure 5.15a) still fits the theoretical curve closely, even with the large value assigned to the rate parameter here. Some slight differences can be seen in the plot of v/v_max against t/t_h (Figure 5.15b), in particular the peak of the curve is shifted very slightly to the left, because the maximum cone velocity occurred earlier. This means a larger proportion of the total fall time was spent in the deceleration phase, which is consistent with the fact that, when a/g is plotted against t/t_h (Figure 5.15c), the maximum deceleration of the cone is around $1.75g$. In Hansbo's analysis, the maximum magnitude of the cones' deceleration is $2g$, and the rate-independent FE analyses followed this quite closely.

Equation 5.11 was used with h from each rate-dependent freefall analysis and h_s from the appropriate rate-independent analysis to give values of ζ. The first series of results were obtained for a smooth 30° cone. The rate-independent case from Section 4.5 in which s_u0 had been selected to give $h \approx 10\,\mathrm{mm}$ was re-analysed with rate-dependent material, keeping the same value of s_u0 but changing the value of μ in each analysis. The variation of ζ with μ from these analyses is shown in Figure 5.16a.

Similar sequences of analyses were performed for each of the other eleven combinations of cone angle, roughness and s_u0. Values of ζ for a particular value of μ were found to vary very little across all the analyses. Figure 5.16b shows the envelope of the maxima and minima across the twelve sets of analyses. The width of the envelope is roughly constant for all the values of μ used. Since the analyses with $\mu = 0$ should all, in principle, have given $\zeta = 1.0$, it seems reasonable to conclude that on the basis of these results ζ cannot be said to depend on the angle or roughness of the cones used, or on the value of the reference strength s_u0, but only on μ. If other factors have any influence, the present analyses were insufficiently sensitive to detect it reliably.

The numerical values of ζ obtained from the present work are shown in Table 5.2. The minimum, mean and maximum values shown come from the twelve sets of analyses which were performed, each set covering the five values of μ shown (from 0.00 to 0.20). The mean values shown are identical (to two decimal places) to the smooth, 30° cone results shown in Figure 5.16a.

Koumoto and Houlsby (2001) gave approximate values of ζ for the case $\mu = 0.1$ (see Section 2.2.7). The results of their (highly approximate) analysis suggested values of $\zeta = 0.74$

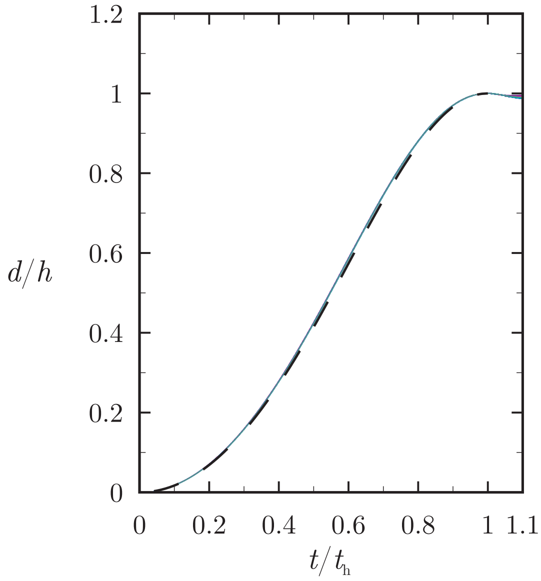

(a) Normalised displacement–time curves

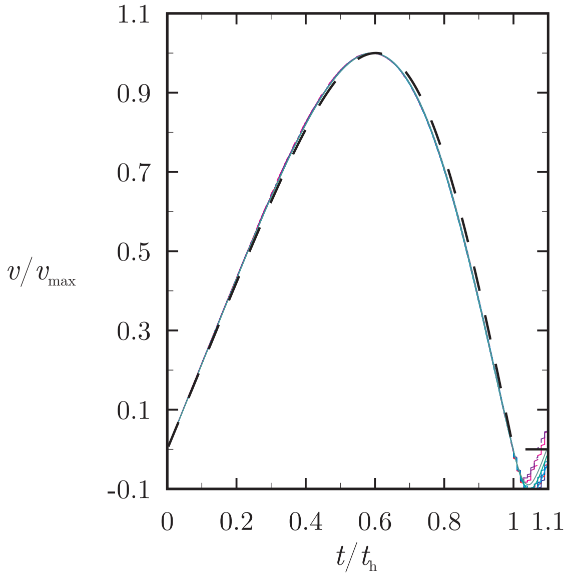

(b) Normalised velocity–time curves

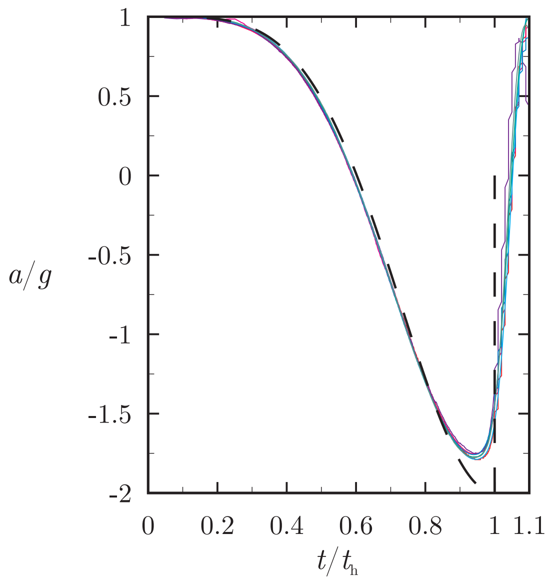

(c) Normalised acceleration–time curves

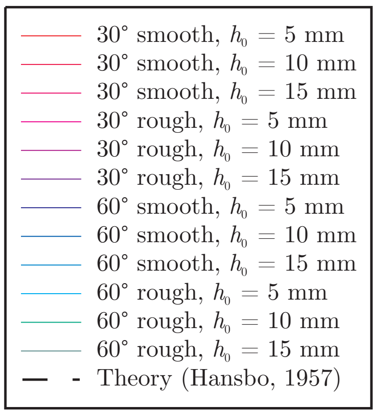

(d) Legend

Figure 5.15: Motion of cone in rate-dependent dynamic Abaqus FE analyses with $\mu = 0.2$. h_0 is the maximum penetration in the corresponding rate-independent freefall analysis

Table 5.2: Values of ζ from 12 sets of analyses

	ζ		
μ	Minimum	Maximum	Mean
0.00	0.99	1.02	1.00
0.05	0.72	0.75	0.74
0.10	0.57	0.60	0.59
0.15	0.47	0.50	0.49
0.20	0.40	0.43	0.42

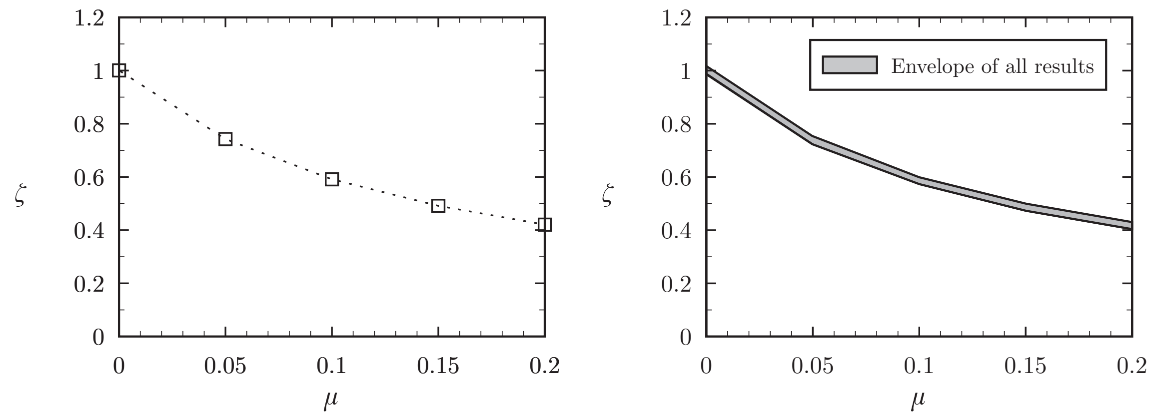

(a) Smooth 30° cone, analyses with $h \approx 10\,\mathrm{mm}$ in rate-independent case

(b) Envelope of all results

Figure 5.16: Variation of ζ with μ

for 30° cones and $\zeta = 0.73$ for 60° and 90° cones. The corresponding value of ζ from Table 5.2 is 0.59, suggesting that the approximate analysis performed by Koumoto and Houlsby (2001) may not have captured the full significance of rate effects in the fall-cone test.

In the analyses presented previously, the strength ratio $\zeta = s_\mathrm{u}/s_\mathrm{ud}$ has been used. However, it is also instructive to consider the variation of $\zeta^{-1} = s_\mathrm{ud}/s_\mathrm{u}$ with μ. The results shown in Figure 5.16b are re-plotted in this form in Figure 5.17. The linear relationship plotted on the same axes,

$$s_\mathrm{ud}/s_\mathrm{u} = 1 + 7.0\mu, \tag{5.12}$$

was obtained by varying the slope to obtain a best fit to the numerical data in a least-squares sense. Taking into account the relationship between strength and the strain rate implemented in the VUMAT for these analyses (Equation 5.2), it is apparent that the observed relationship between ζ and μ is related to the average strain rate $\dot{\gamma}_\mathrm{ave}$ during indentation, and implies that the average strain rate during a fall-cone test, $\dot{\gamma}_\mathrm{ave}$, is 7 orders of magnitude higher than the threshold value $\dot{\gamma}_\mathrm{ref}$. Since the value of $\dot{\gamma}_\mathrm{ref}$ in the VUMAT was taken as $3 \times 10^{-6}\,\mathrm{s}^{-1}$, it follows that $\dot{\gamma}_\mathrm{ave}$ during dynamic indentation is approximately $30\,\mathrm{s}^{-1}$ or $10^7\,\%$/hour. Zhou and Randolph (2009) performed finite element analyses of flow around T-bar and ball penetrometers (at the standard field penetration rate of 20 mm/s) and found that the slope of a similar plot was 4.8, indicating that the average strain rate was 4.8 orders of magnitude above the reference rate (which was, as here, 1 %/hour). So, the data indicate that the fall-cone test involves strain rates approximately 100 times larger than those around a T-bar or ball penetrometer.

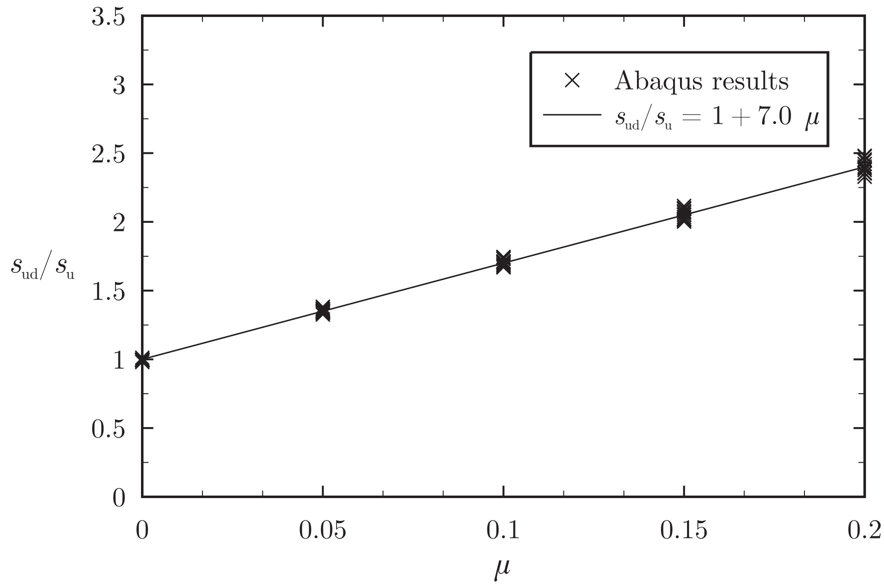

Figure 5.17: Variation of $\zeta^{-1} = s_{\mathrm{ud}}/s_{\mathrm{u}}$ with μ

Chapter 6

Experimental observations of cone indentation mechanisms

The technique of Particle Image Velocimetry (PIV) was originally developed for use in experimental fluid mechanics. The work of White et al. (2003) has led to increasing use of PIV for the visualization of flow in geomaterials (e.g. Hossain et al., 2005; Cheuk et al., 2008).

The PIV technique involves the measurement of flow by analysing photographs of a plane within the deforming region. The method for determining velocities from the images makes use of patterns of randomly varying brightness (or *texture*) within the deforming material. In fluid mechanics, the flowing liquid or gas must be seeded with visible particles or perhaps gas bubbles to make it visible. In geotechnical applications, many materials have sufficient natural texture. Others, such as the clay used here, must be given texture by scattering contrasting material on the surface.

When a full three-dimensional model of a foundation or a penetrometer is tested in the laboratory, the desired images cannot generally be obtained as the plane of deformation is hidden. The technique usually employed has been to model only half of the real-world problem under investigation, splitting the problem on a plane of symmetry and placing a window there through which a camera can record images for later analysis. For example, Hossain et al. (2005) modelled half of a spudcan foundation, moving behind a transparent window through which pictures were taken. A similar approach will be used here.

An alternative technique that allows a full model to be tested (rather than only half) is described by Sadek et al. (2003). Rather than modify the model to position a window at the plane of interest, they carries out tests in the centre of a transparent-sided box, and used transparent material in place of the actual sand or clay. The transparent material used by Sadek et al. consisted of transparent silica with a pore fluid chosen to have a matching refractive index, and represented sand. Iskander et al. (2002) used transparent amorphous silica as a substitute for clay. In order to capture images of the plane under investigation, a laser-generated light-sheet is used to illuminate the model, which is seeded with reflective particles.

Though the use of transparent soil is an interesting approach, particularly for problems that cannot be reduced to two dimensions (e.g. the failure of a rectangular footing), it has several drawbacks. The transparent materials do not behave in precisely the same way as the real geomaterials they represent, and the method requires more elaborate (and expensive) equipment. The more conventional approach used by White (2002) and by Hossain et al. (2005) is adopted here.

6.1 Laboratory equipment and procedure

6.1.1 Preparation of clay samples

Choice of material

Samples of clay were prepared from "Speswhite", a highly refined kaolin produced from deposits in the South West of England by IMERYS Minerals Ltd. and delivered in powder form. This material has been used by a great many previous researchers. Examples include work on piles (Randolph et al., 1979; Martins, 1983; Gue, 1984), the piezocone (May, 1987), the dilatometer (Smith, 1993) and combined loading of offshore foundations (Martin, 1994).

Because of Speswhite's popularity in research, many aspects of its behaviour are well understood and values of key properties are available in the literature: the plastic limit w_{p} and liquid limit w_{l} are approximately 34% and 65% respectively; the specific gravity of the solids G_{s} is approximately 2.6; the coefficient of permeability is relatively high, of order 10^{-9} m/s, allowing rapid consolidation of samples from slurry (the precise permeability varies with void ratio; see Al-Tabbaa and Wood, 1987).

Consolidation apparatus and method

It was vital that the clay samples filled the sample container as completely as possible, with no voids in the corners of the box and no gaps between the clay and the window through which images for PIV were recorded. If any gaps had been present, the clay might have accommodated the insertion of the cone by flowing into unfilled corners of the container rather than by the failure mechanism the test was designed to observe. To ensure there were no gaps around the sample, kaolin samples were prepared by consolidating them in the same box that would be used for the tests. The front and back of the box were then removed and replaced with glass windows for the tests.

The dimensions of the strongbox can be seen in Figure 6.1. The walls of the box were constructed from plates of aluminium alloy (dural). The sides were permanently bolted to the base plate and the joints sealed with silicone sealant. The removable front and back plates were held in place by more bolts, and sealed by a 2 mm-thick hard rubber gasket (not shown in the figure). The base plate was provided with a hole for drainage.

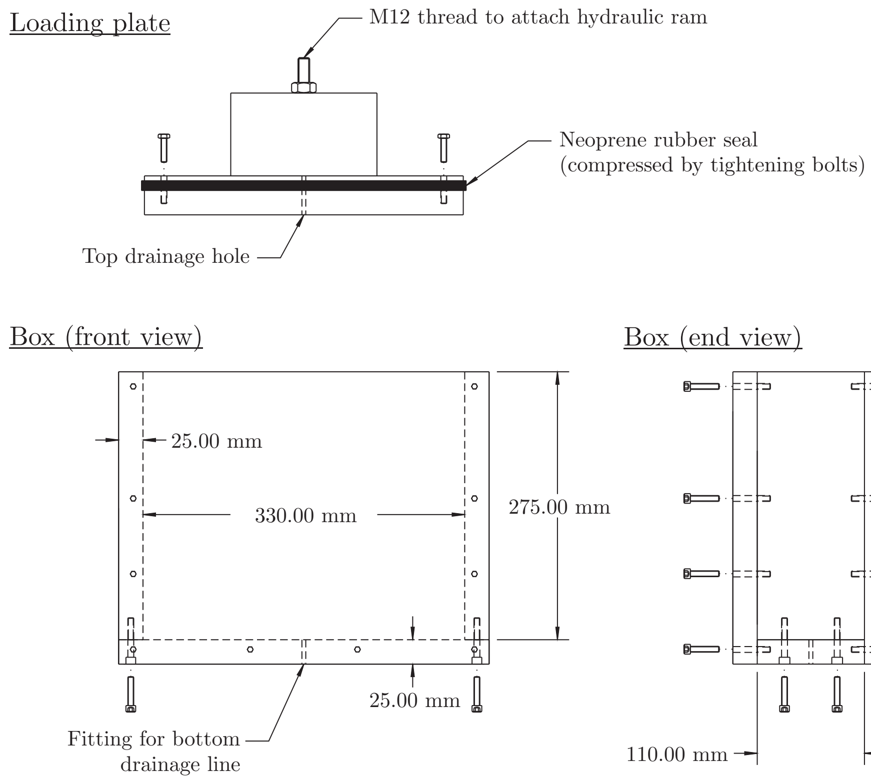

Figure 6.1: Strongbox and loading plate used for sample preparation

Sample preparation followed the method established by Gue (1984) and subsequent researchers. First, the powder (with initial water content $w \approx 1\%$) was mixed with water to produce a slurry with $w \approx 120\%$. This was done in large batches in a 110-litre ribbon-bladed mixer (details are given by Gue, 1984). To minimise the air content of the slurry, a partial vacuum (approximately 0.8 bar) was applied during mixing, which went on for 2 hours. The prepared slurry was then pumped into a storage container and kept under a layer of water.

Blocks were prepared from slurry as required. First, a filter made from 1 mm-thick "Vyon" porous plastic sheet was placed into the base of the strongbox. Slurry was then added, under a layer of water to avoid entraining air. A further Vyon filter was placed on top of the slurry, and a rectangular loading plate inserted in the top of the box. The loading plate was manufactured from 25 mm dural plate and sized to fit the box with 1.5 mm clearance on all sides. This gap was filled by a seal made from a layer of neoprene rubber foam included in the loading plate assembly, which could be compressed to completely fill the space available by tightening a series of bolts. The sample was then consolidated by loading the plate with the hydraulic system described by Gue (1984). During consolidation, water was able to drain away through holes provided in the base and the loading plate (after passing through the filters). A tube led from the drain on the base to a fitting attached to the loading plate, ensuring there was no head difference between the top and bottom of the sample during consolidation. The inside faces of the box were given a thin coating of petroleum jelly before consolidation to reduce friction and aid the creation of a watertight seal around the loading plate.

During consolidation, load was applied in a series of increments (25 kPa, 50 kPa, 100 kPa). This was necessary as the seal around the loading plate was not sufficient to contain the slurry if the final pressure was applied immediately. Partially consolidating the sample before increasing the load solved this problem. The force on the loading plate (measured by a load cell), and its displacement (from an LVDT attached to the reaction frame), were logged to a computer throughout consolidation to ensure that the final pressure was correct and the final increment reached the end of primary consolidation. The variation of applied pressure and sample height during a typical sample preparation are shown in Figure 6.2. It was found that the second (50 kPa) load increment only needed to be maintained for a short period (around two hours) before the final pressure was applied.

Variations in the pressure on the sample can be seen in Figure 6.2a following the final load increment. They are the result of the operation of the pressure regulator that forms part of the hydraulic system used to load the sample during consolidation. This problem was not reported by previous users of the system, but may have been more noticeable on this occasion because the system was used to provide smaller forces than those required by previous researchers (due to the smaller plan area of the samples prepared). The entire consolidation process took approximately 30 hours to complete, but the samples remained loaded until required (in Figure 6.2, unloading took place after approximately 45 hours). The depth of a sample after consolidation was approximately 90 to 95 mm.

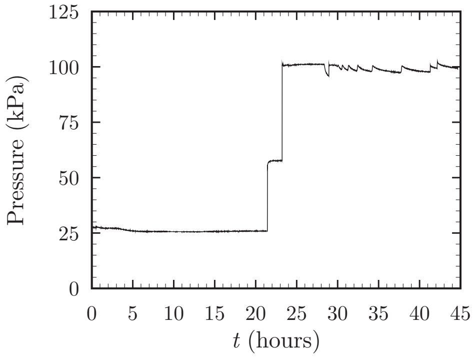

(a) Variation of pressure on sample

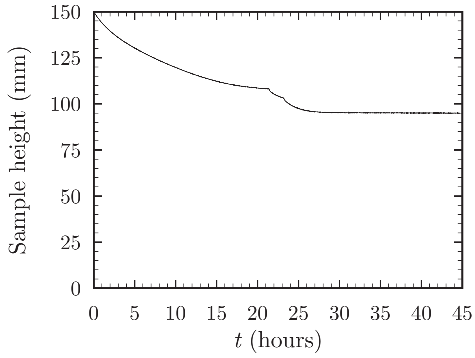

(b) Variation of sample height

Figure 6.2: Preparation of a kaolin sample by consolidation

Final preparation of consolidated samples

Immediately before each sample was tested, the consolidation load was removed by raising the loading plate. The front plate was removed from the strongbox, and the box was placed with the front uppermost. A small sieve was then used to scatter black material over the face of the sample to give texture for the PIV analysis. The material used for this was black-dyed sawdust, purchased as "modelling flock". The back plate was also removed from the box, which was placed on one end while the top of the sample was cut away using a piece of piano wire held in a bow saw frame and guided by straight-edged metal plates clamped onto the front and back of the box. This ensured that the top surface of the sample was level, and that the final height of a prepared sample could be kept constant at 80 mm. The front and back of the sample were then covered by attaching glass plates of thickness 15 mm that had previously been lubricated with petroleum jelly to minimise friction during the tests.

When the glass viewing windows were attached to the sample box, the rubber gaskets used during consolidation were omitted. This meant that the surface of the clay stood slightly proud of the box when the window was applied. Tightening the screws holding the window and frame in place then compressed the clay sample slightly. This procedure was found to help in minimising gaps between the window and the clay sample.

To minimise variation of strength s_u over the depth of the sample, the kaolin was not allowed to swell after unloading but was tested immediately. Clingfilm was used to prevent dessication of the sample, and was removed from a given area of the surface only immediately before testing. Final preparation and all tests on each sample were completed within a period of 1 hour after removal of the consolidation load.

Measurement of sample strength

To check that the method described here gave samples with consistent properties, a small shear vane was used to measure the strength of each block after the completion of all cone tests. The equipment used is described by (Bowden, 1988), and consists of a standard Wykeham Farrance laboratory vane that has been modified to include an electronic torque transducer and is driven by a stepper motor to ensure constant rotation speed. The miniature vane used had diameter 14 mm and height 30 mm, and was rotated at one degree per second.

Shear strengths were deduced from the vane tests in the usual way (see Bowden, 1988) and were always found to lie in the range 8.8 to 9.0 kPa.

6.1.2 Cones and mounting system

The half cones used for this investigation were machined from aluminium alloy. The angles of the cones were 30° and 60°. To prevent kaolin passing between the cone and the window, the flat face of each cone was covered with black rubber. The rubber layer was compressed against the inside of the glass window during testing. Part of the rubber was cut away, and the exposed material covered with white plastic. A black spot at the centre of this white disc allowed the cone to be tracked in the PIV analysis.

The surfaces of the cones received no special attention (e.g. polishing or lubrication) as part of the intention of the tests was to assess the behaviour of a cone as used in the fall cone test where no such measures are used (BSI, 1990).

The cones were attached to the end of a 15 mm-diameter steel shaft that passed through a rolling-element linear bearing. The bearing used had a flange perpendicular to the axis of the shaft, and this was bolted to a dural plate. This was attached to a second plate mounted across the top of the sample container, as shown in Figure 6.3. The upper plate was attached by bolts passing through slots in the lower one, allowing the cone to be positioned against the window before being clamped in place. The lower plate was provided with a set of four screws for levelling, and was attached to rails made from extruded aluminium section, running along the front and back of the sample box.

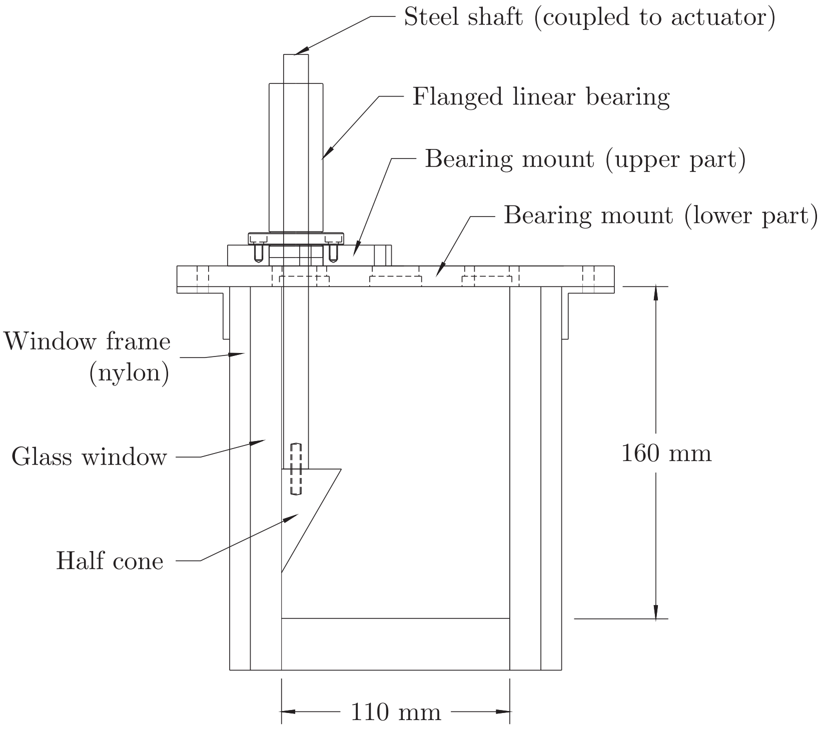

Figure 6.3: Attachment of cone to sample box with linear bearing (fixings not shown)

6.1.3 Actuator

The actuator used for these tests is described in detail in Section 7.1.3. In brief, it comprises a high-precision linear slide driven by a stepper motor via a ball screw. In combination with a microstepping stepper motor drive, the system allows precise positioning and a wide range of speeds. For the tests described here, the cones were pushed into the samples at a constant speed of 20 mm/s.

While the linear bearing for the cone shaft was mounted locally on the sample box for precise positioning, the actuator was mounted independently on a steel frame. For ease of use, the nut block of the actuator was attached to the head of the cone shaft by means of a magnetic coupling using a pair of 25 mm-diameter NIB (Neodymium Iron Boron) permanent magnets. This arrangement allowed the actuator to drive the cone without the need for precise positioning of the strongbox beneath the actuator. The magnetic coupling was quite powerful enough to transfer the forces required during the test (one of the magnets was able to lift a piece of steel weighing around 9 kg); in fact a piece of PVC approximately 10 mm thick was placed between the magnets as they were too difficult to separate if allowed to come into direct contact.

Figure 6.4 shows the sample container (with windows attached) and the cone mounting assembly. The coupling between the cone shaft and the actuator is visible at the top of the picture.

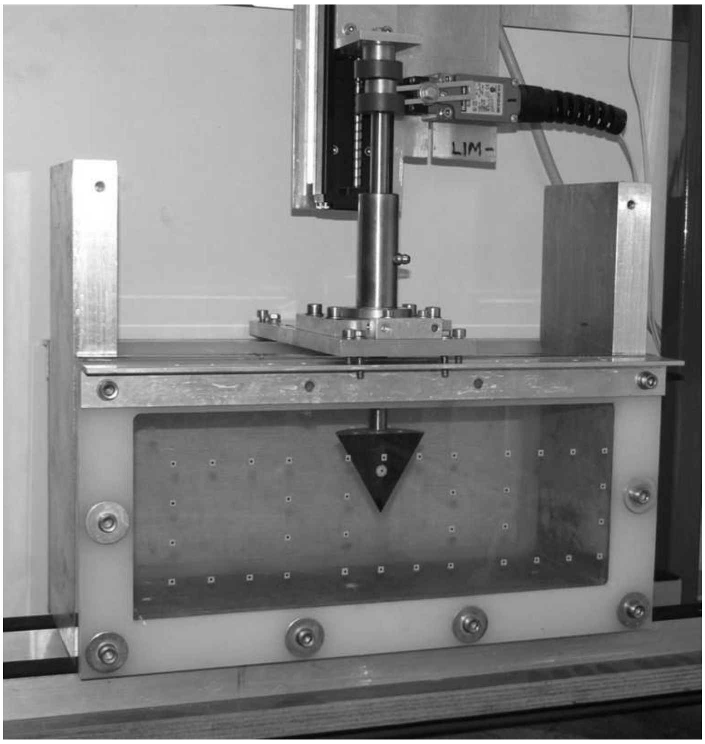

Figure 6.4: Sample container and 60° half cone for PIV work

6.1.4 Camera

For the purposes of this investigation, a FASTCAM 1024 PCI high-speed camera supplied by Photron (Europe) Ltd. was used, with a Sigma 105 mm f/2.8 EX DG macro lens. The camera is capable of recording 10-bit grey-scale images with a maximum resolution of 1024×1024 pixels at a 1 kHz frame rate. The full resolution was always used for the work described here, but higher frame rates are possible if a lower resolution is acceptable (as is the case in Chapter 7).

Figure 6.5: Photron FASTCAM 1024 PCI camera and controller board (`http:\\www.photron.com`)

The camera has a CMOS sensor with large (17×10^{-6} m square) pixels, giving high light-sensitivity. It was nevertheless necessary to provide additional lighting in the form of a 1000 W floodlight. The lighting gave off considerable heat, so care was taken to activate it only when absolutely necessary to avoid drying out the clay samples.

6.1.5 Test procedure

The dimensions of the test container (plan area 110×330 mm) meant that three tests could be performed along each of the front and back faces of the box, with the sites of the tests separated from the ends of the box by 55 mm or from one another by 110 mm. This meant that the space available for each test was double that provided by the standard 55 mm-diameter cups used for the British Standard fall cone test (BSI, 1990).

During testing, the sample was kept covered with clingfilm, with only the part of the surface required for the current test being exposed. Each test was performed by driving the cone in at constant speed controlled by the actuator. The high-speed camera was configured to record images continuously at constant frame-rate, constantly re-filling the available buffer. The controller was then triggered manually immediately after the completion of each test, permanently saving the most recent batch of images.

After each test, the cone was retracted and removed from the box for cleaning. The cone was cleaned, dried and re-attached to the guide shaft in preparation for the next test.

6.2 PIV analysis of results

Analysis of the test images was performed using the software GeoPIV, an implementation of the PIV technique as a set of functions for Matlab (MathWorks, 2007). Full details of GeoPIV are given by White and Take (2002) and White et al. (2003), but a brief description of the software and its use will be given here.

GeoPIV is designed to track a deforming continuum from a sequence of still images by making use of the texture (variation of brightness) within the images. It operates by defining a series of sub-regions or patches within the first of a series of images, and finding the best match for each of these test patches in each subsequent image by finding the peak of the normalised cross correlation or the test patch with the new image.

Figure 6.6 shows how the PIV process might be applied to a typical pair of images from a test involving deforming white kaolin with artificial texture added. Figure 6.6a shows an image captured by the high-speed camera at some time t during the test. From this image, a 20×20 pixel search patch was selected, which forms the basis of the search in subsequent images. In the final tests, the entire deforming region was covered by a grid of such search patches. At some later stage in the test, time $t + \Delta t$, the camera captured the image shown in Figure 6.6b. It is easy to see the new location of the tracking marker by eye, but to automate the process the normalised cross-correlation of the search patch (from Image 1) with Image 2 is calculated. The position (boxed) of the maximum value of the correlation gives the new position of the cone, and its displacement (in this case) is approximately $z_2 - z_1 = -3$ pixels.

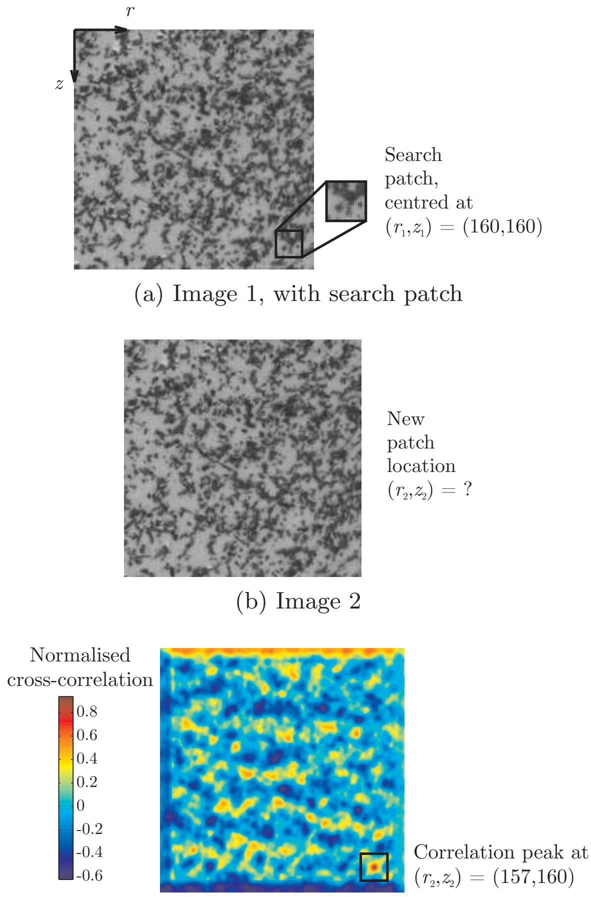

(a) Image 1, with search patch

(b) Image 2

(c) Normalised cross correlation of search patch with Image 2

Figure 6.6: Particle Image Velocimetry used to determine displacement of material patch

The example calculation shown in Figure 6.6 used the Matlab function `normxcorr2`. The use of a normalized cross-correlation (which accounts only for the variation of brightness across a patch, not the absolute values) means that gradual variations in brightness across the image such as would be found with uneven lighting conditions do not cause problems.

The actual GeoPIV software works in a similar fashion, with some additional refinements. Computation time is reduced by performing correlations in the frequency domain after taking the Fast Fourier Transform (FFT) of each patch, and sub-pixel interpolation is performed after the best (integer) pixel match has been found. The interpolation is performed by fitting a bicubic interpolation function over the region closest to the integer peak, giving a result with resolution 0.005 pixels (White et al., 2003).

White et al. (2003) suggest that an upper bound on their software's precision error ρ_{pixel} is given by the empirically-derived expression

$$\rho_{\text{pixel}} = \frac{0.6}{L} + \frac{150\,000}{L^8}, \tag{6.1}$$

where L is the size of the search patch in pixels. With $L = 20$ pixels, $\rho_{\text{pixel}} \approx 0.03$. Dividing this by the dimension of the image (also in pixels) gives the precision as a fraction of the field of view, approximately 3×10^{-5}. Since the height of the image might typically be 80 mm, this theoretical precision is equivalent to 2.4×10^{-6} m. However, the accuracy of the technique is limited by other factors, primarily the accuracy with which displacements in pixels can be converted to real-world measurements.

Conversion from image to object coordinates

In addition to errors due to the PIV technique itself, White et al. (2003) identify imperfections in the conversion between image-space and object-space coordinates (the process of photogrammetry) as an additional source of error. Reasons for this include possible misalignment of the camera relative to the object plane, barrelling/pincushion distortion caused by limitations of the camera optics, refraction through a viewing window and non-squareness of camera sensor pixels.

Several of the problems mentioned by White et al. are unlikely to cause such large errors in the present work. This is because several aspects of their system were constrained by the limited space available in the geotechnical centrifuge where the experiments were performed. For instance, they used an inexpensive compact camera with a small optical system that will inevitably have introduced more distortion than the high-quality 11-element lens used here. Space constraints (and the curvature of the drum centrifuge) also required that the camera be placed comparatively close to the object, which will have further increased distortion by requiring the use of a wide-angle lens and increasing the angle at which rays of light passed through the viewing window. White et al. also report that the increased self-weight of camera and support in the centrifuge could cause physical distortion of the lens system and deflection of the entire camera, introducing further error.

Despite these reasons for optimism regarding the optical performance of the present equipment, care was taken to correct errors caused by distortions when coordinates were converted from image- to object-space. GeoPIV includes a function that corrects for distortion based on parameters derived by modelling the sources of distortion described above. To do this, reference markers with known position (relative to one another) had to be placed within the camera's field of view. Twelve markers were positioned within the frame of each image, and can be seen on the viewing window in Figure 6.4. To ensure the markers were accurately positioned, they were drawn with CAD software and printed onto a self-adhesive sheet of acetate film, which was then carefully attached to the inside face of the viewing window. A 5 mm square area around each marker was then covered with a thin layer of white spray paint, and this was covered with a further layer of acetate film to ensure the marker areas were not scratched or otherwise removed during the tests. A hard rubber printers' roller was used to push down the acetate film to minimize trapped air pockets.

6.3 Results

A typical image recorded during the penetration of the 30° half-cone is shown in Figure 6.7. The lighter-coloured area of the image close to the surface adjacent to the cone corresponds to a region in which the clay had pulled away very slightly from the glass window as the cone was pushed in. This suggests the existence of a region with tensile hoop stresses close to the point where the separation initiated: on the surface adjacent to the cone. This would be in keeping with the findings of the finite element analyses – see Section 3.3.3. The problem of clay pulling away from the viewing window was not reported by previous authors (e.g. White, 2002; Hossain et al., 2005; Cheuk et al., 2008). These previous investigations are unlikely to have induced tensile hoop stresses in material adjacent to the window, however, particularly as they were largely conducted in geotechnical centrifuges where the large self-weight of the material would tend to ensure relatively large compressive stresses prior to a test beginning.

Figure 6.7 also shows the displaced surface profile obtained from the Abaqus finite element analyses with 30° cones (for $\alpha = 0$ and $\alpha = 1$). Although the rough cone FE surface profile is closer to the actual result, the amount of heave around the cone in the experiment was much lower. The volume of material in the displaced lip observed in the laboratory was evidently less than that seen in the FE analysis. Since the total volume of clay must be conserved in an undrained test on clay, the inserted volume of the cone must have been accommodated by movement of material further away from the cone. Alternatively, the kaolin could have contained compressible air pockets (despite the precautions to remove air from the slurry before consolidation), or voids at the edge of the sample container. Since the sample was consolidated in the box, the most likely place for air gaps to exist would have been adjacent to the window. However, to account for an apparent loss of material would require that clay was forced towards the window into pre-existing gaps; observations suggested the opposite was true, as material was pulled away from the glass.

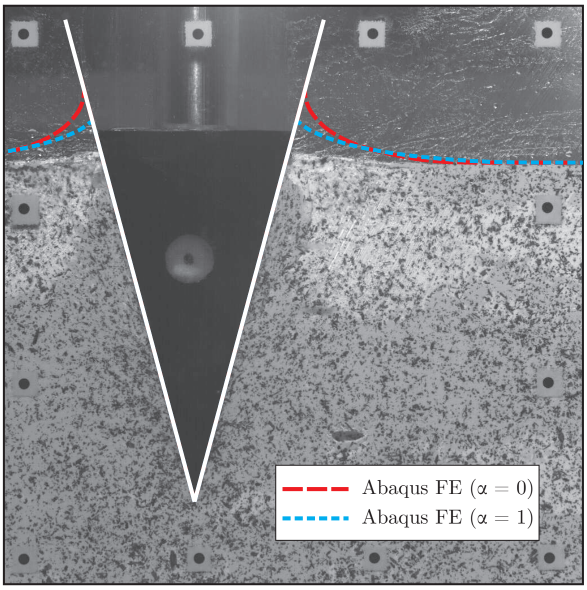

Figure 6.7: Kaolin sample indented by 30° cone, showing surface profiles obtained from Abaqus FEA with smooth ($\alpha = 0$) and rough ($\alpha = 1$) cones

6.3.1 Indentation mechanism

Experimental displacement vectors around the cone were obtained using GeoPIV. Results with the 30° cone are shown in Figure 6.8a, and were obtained by comparing the image shown in Figure 6.7 with one taken 0.03 s later (during which time the displacement of the cone was 0.6 mm). Velocities adjacent to the face of the cone can be seen to be approximately perpendicular to the interface. Comparing Figure 6.8a with similar vector plots from the Abaqus finite element analyses indicated that the experimental results most closely resembled those obtained with a rough cone (adhesion factor $\alpha = 1$). An increase in adhesion between the clay and the cone immediately adjacent to the viewing window may have resulted from the presence of a layer of rubber here. Figure 6.8b shows the velocity vectors obtained in the Abaqus finite element analysis with adhesion factor $\alpha = 1$. Sketched streamlines indicating the general instantaneous direction of flow within the deformation mechanism are also shown. Although the two diagrams are by no means identical, there are some notable similarities. For instance, in both cases the streamlines generally curve upwards towards the surface but their curvature changes before the free surface is reached and they begin to curve outwards away from the cone.

A typical test with a 60° cone is shown in Figure 6.9. Again, the displaced surface profiles obtained in the Abaqus finite element analyses are shown as dotted lines. In this case, the surface profile obtained in the laboratory test showed no build-up of displaced material adjacent to the cone at all. In fact, the surface immediately adjacent to the cone appears to have been dragged downwards during the test. The clay adjacent to the cone was not observed to become separated from the glass in this case.

Displacement vectors and streamlines obtained with the 60° cone are shown in Figure 6.10a, with corresponding Abaqus FEA results (with $\alpha = 1$) in Figure 6.10b. The finite element and experimental results appear less similar than the equivalent plots for the 30° cone. In Figure 6.10a, significant vertical displacements can be seen below the tip of the cone, whereas the Abaqus results in Figure 6.10b show the material here to be essentially at rest. The shapes of the sketched streamlines also differ substantially between the two cases. The PIV result shows little sign of the flow direction turning outwards as the free surface is approached, although this continues to be the case in the plot obtained from Abaqus.

6.3.2 Deformation during indentation

As an alternative to plotting material velocity vectors at a particular stage suring a test, the motion of a patch can be tracked throughout the analysis. The grids shown in Figures 6.11a and 6.11b were obtained by PIV tracking of entire sequences of images from the undeformed state. Because the appearance of a patch could change substantially over the course of the indentation, GeoPIV was set to regenerate the search patches at each step. So, each image was searched for the region giving the best match to a set of pixels from the one before, then a new search patch was chosen for the next step. Note that the squares in the grids of Figure 6.11 do not correspond to the patches used in the PIV analysis. Rather, each node in the

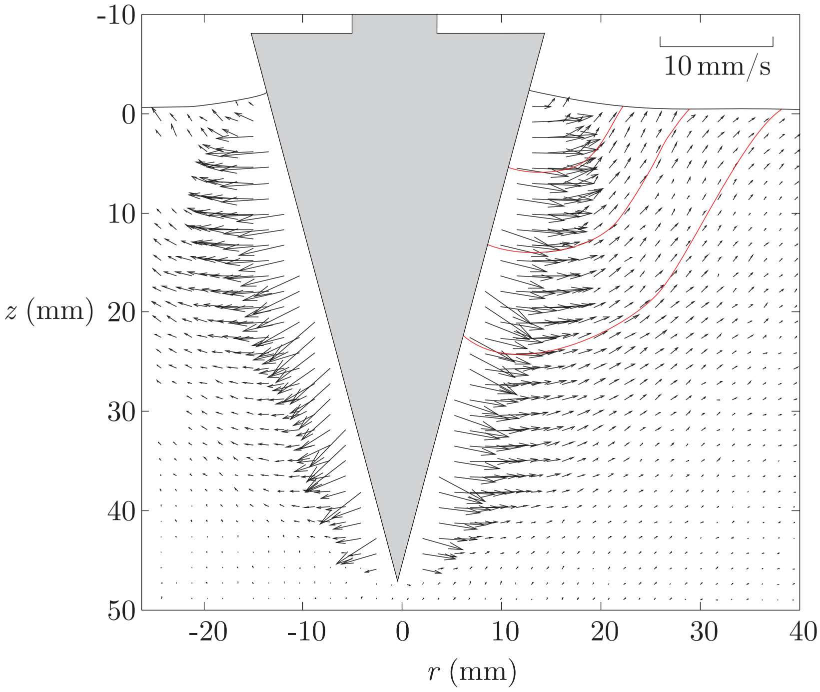

(a) PIV

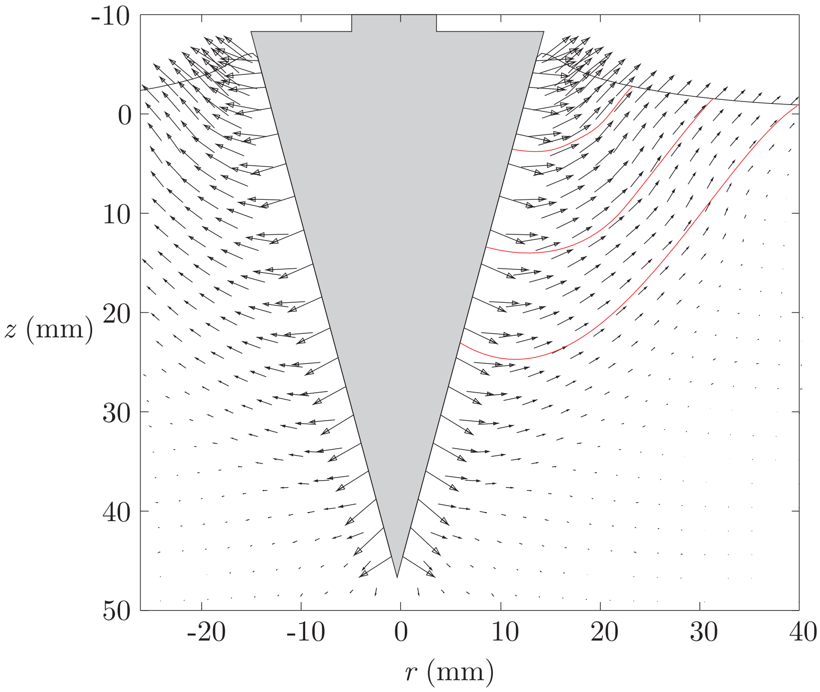

(b) Abaqus FEA with adhesion factor $\alpha = 1$

Figure 6.8: Displacement vector field around a 30° cone, with sketched streamlines (red)

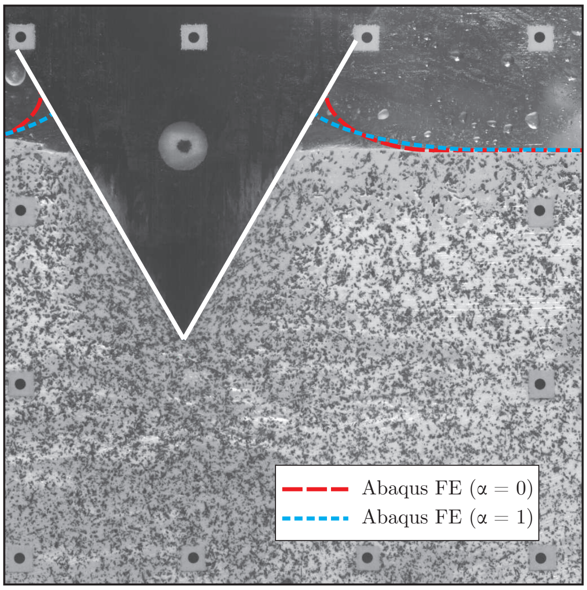

Figure 6.9: Kaolin sample indented by 60° cone, showing surface profiles obtained from Abaqus FEA with smooth ($\alpha = 0$) and rough ($\alpha = 1$) cones

grid shown was obtained from a patch in the original PIV mesh.

It is not clear what level of accuracy can be expected from the tracking of patches immediately adjacent to the faces of the cones, because the search patches included parts of the cones themselves (which were moving vertically downwards) as well as the material being tracked. It was not possible to detect when this happened automatically, and manual intervention was impractical as each sequence consisted of perhaps 2000 images. However, since the cones were relatively featureless, it is hoped that the grids in Figure 6.11 reflect the material displacements fairly well. The grids are believed to give an accurate impression of the overall mode of deformation of the clay.

There are clear differences between the PIV deformation grids (Figure 6.11) and those obtained by the finite element method (see Figure 3.17 for results obtained with ELFEN). Most importantly, PIV results give no indication of material around the cones being displaced upwards. The observed deformations generally involved material “sinking in” rather than “piling up” around the cones, although a small lip of displaced material did eventually form around the 30° (as shown in Figure 6.7). The pattern of deformation around the cone in Figure 6.11 is qualitatively similar to the pattern observed by Hansbo (1957) when he carried out a similar experiment involving indentation of clay by a half-cone against a viewing window.

An alternative method of tracking deformations was to track parts of the material by eye

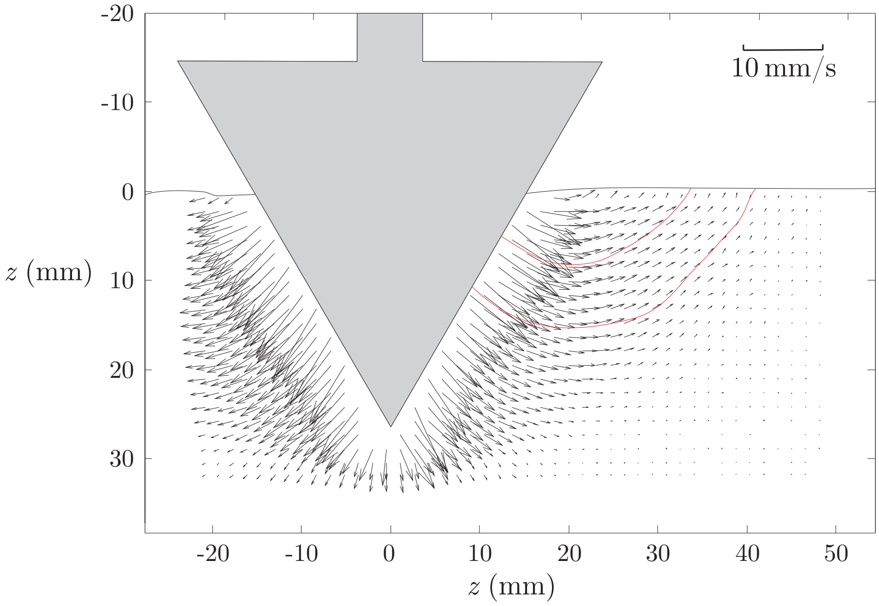

(a) PIV

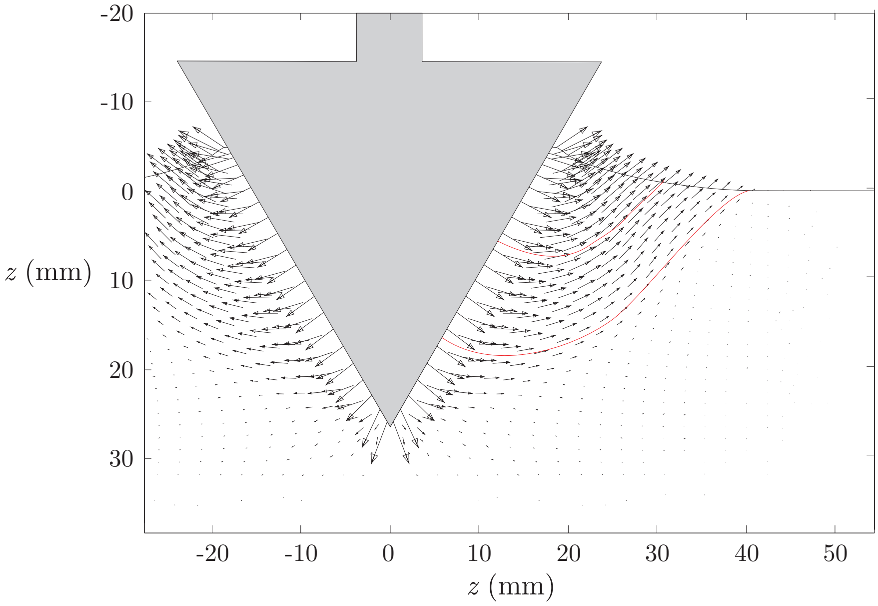

(b) Abaqus FEA with adhesion factor $\alpha = 1$

Figure 6.10: Displacement vector field around a 60° cone, with sketched streamlines (red)

while viewing a video of a complete set of test images. Despite being too labour-intensive to apply to a large number of points in each analysis, this method nevertheless provided confirmation that the grids obtained from PIV were reasonable. It was also possible to make some quantitative comparisons with the results of the Finite Element analyses. Figures 6.12a and 6.12b show an example where a distinctive patch of material close to the tip of a 30° cone was followed by eye to its deformed location. Direct measurement on the final image allowed the ratio of lengths L_1/L_2 to be calculated; L_1 and L_2 are defined in Figure 6.12c. The

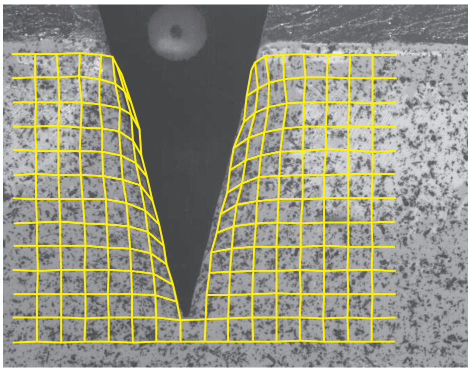

(a) 30° cone

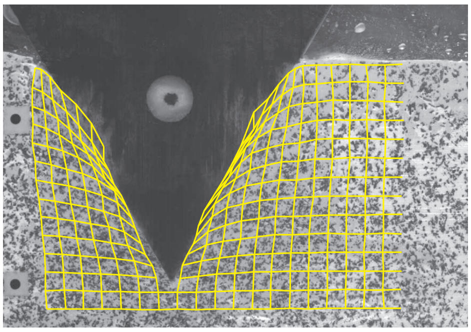

(b) 60° cone

Figure 6.11: Deformed grid of material points from PIV tracking

same ratio was also calculated from the ELFEN finite element results shown in Figure 3.17, using the values for rough cones (adhesion factor $\alpha = 1$). The results are shown in Table 6.1, together with those obtained with the 60° cone. The values agree closely. If however L_2 had been measured from the original surface level rather than from the deformed surface, the agreement between FE analysis and experiment would have been less good, due to the differences in the surface profiles around the cones.

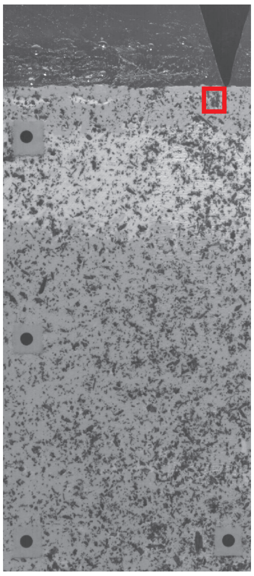

(a) Start of test

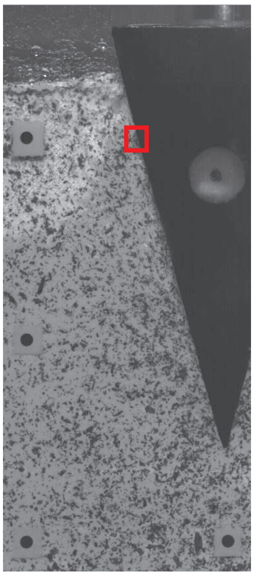

(b) End of test

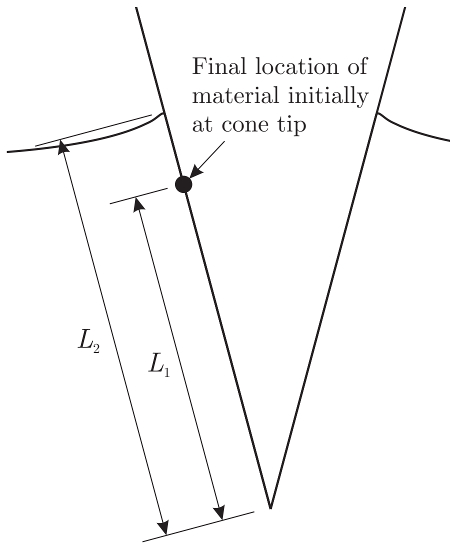

(c) Dimensions L_1 and L_2 for comparison of experimental and FE results

Figure 6.12: Example of visual tracking of a material under indentation with a 30° cone. Red box in (a) and (b) indicates a particular patch of modelling flock in its initial and final locations

Table 6.1: Comparison of final position of material point from ELFEN FE analysis and experimental observation

Cone angle	L_1/L_2	
β (°)	ELFEN FEA	Experiment
30	0.83	0.84
60	0.56	0.57

Chapter 7

Experimental investigation of fall cone rate effects

The aim of the laboratory experiments described in this chapter is to confirm whether the results of the rate-dependent finite element (FE) analyses described in Chapter 5 are representative of fall cone tests on a real clay.

The first set of tests, under displacement control, was intended to determine whether the kaolin used in the experiments exhibits rate-dependent undrained strength, and whether the form of rate dependence assumed in the FE analyses is similar to the actual rate effect. The simple model used in the FE had the following form (from Equation 5.2):

$$s_{\mathrm{u}} = s_{\mathrm{u0}} \left[1 + \mu \log_{10} \left(\frac{\max\left(\dot{\gamma}, \dot{\gamma}_{\mathrm{ref}}\right)}{\dot{\gamma}_{\mathrm{ref}}} \right) \right]. \tag{7.1}$$

It was hoped that, if the model fitted the real behaviour reasonably well, values of μ and $\dot{\gamma}_{\mathrm{ref}}$ could be inferred for the clay under test.

Having characterized the rate-dependent behaviour of the clay, a further series of tests was performed to compare slow displacement-controlled tests with full-speed freefall cone tests, allowing values of the parameter ζ to be determined. This quantity, which was introduced in Section 2.2.7, is the ratio of a clay's undrained strength at a reference strain rate to the dynamic strength exhibited in a fall-cone test, and will in general be less than one.

7.1 Laboratory equipment

The experimental setup is shown in Figures 7.1a and 7.1b. The main features required of the equipment are described in the following section. A more complete description of each aspect follows.

7.1.1 Overview of requirements

A key requirement of the equipment for these tests is that the same apparatus should allow tests of two types to be performed: slow tests in which cones are pushed into clay samples under displacement control, and fast freefall tests in which the same cones drop under their own weight creating indentations in the samples. In tests of both types, key results are the resisting force Q exerted on the cone by the clay, and the depth of indentation d (relative to the undisturbed clay surface) at which that force occurs.

In the displacement-controlled tests, the cone had to be pushed into the clay samples at a wide range of speeds (covering several orders of magnitude). In the freefall tests, the cone had to be accurately positioned above the sample, then allowed to fall freely into the sample under its own weight until it reached its final displacement.

The cone's displacement had to be measured throughout a freefall test at sufficiently high frequency to resolve the variation during a test lasting only a few hundredths of a second, without influencing the motion of the cone by, for example, applying external forces to it. Ideally, a non-contact measuring system would be used.

Similarly, the force between the cone and the deforming clay needed to be measured, also without influencing the motion of the cone.

7.1.2 Cones and sample cup

Figure 7.2 shows the cones, with angles 30° and 60°, which were used for these tests. They were machined from PMMA (Perspex), and their surfaces were polished to ensure that they were as smooth as possible. Each cone had a hollow, 10 mm-diameter shaft attached, which can be filled with lead shot to adjust the weight of the cone. The top of the shaft was threaded to allow the attachment of a steel end cap. At the base of this shaft, a 15 mm length was painted matt white, and a black circle approximately 2.5 mm in diameter was added with a marker pen (for reasons discussed further in Section 7.1.5). The masses of the 30° and 60° cones were 100 g and 60 g respectively, making them similar to cones supplied

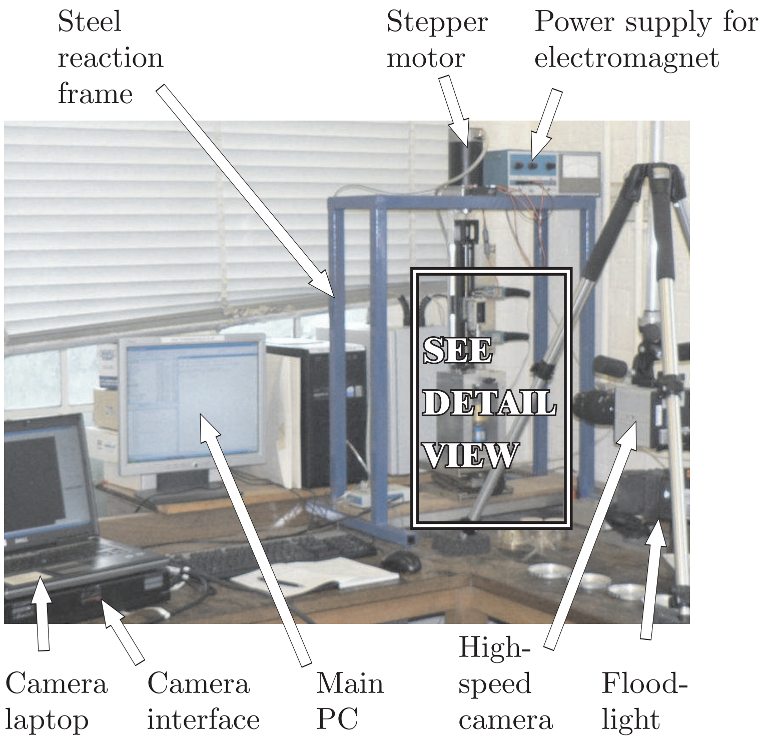

(a) Overall view

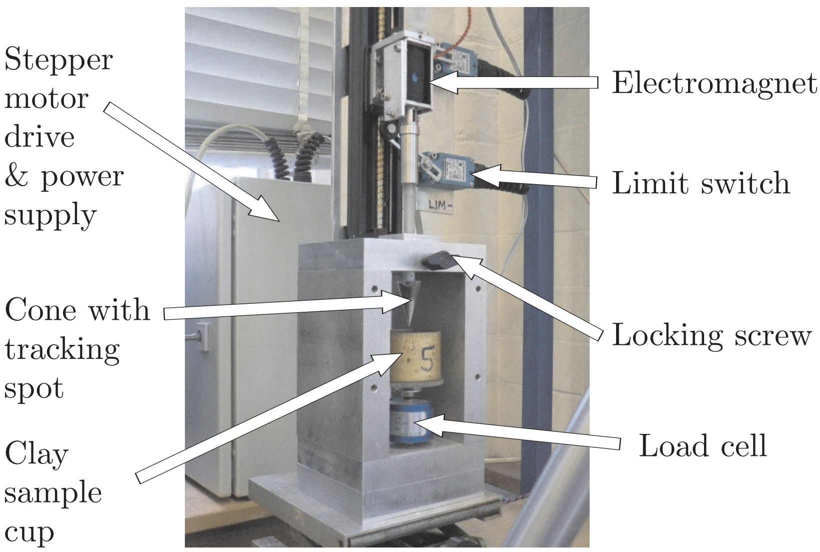

(b) Detail view

Figure 7.1: Views of laboratory equipment

by Geonor with their fall cone apparatus.

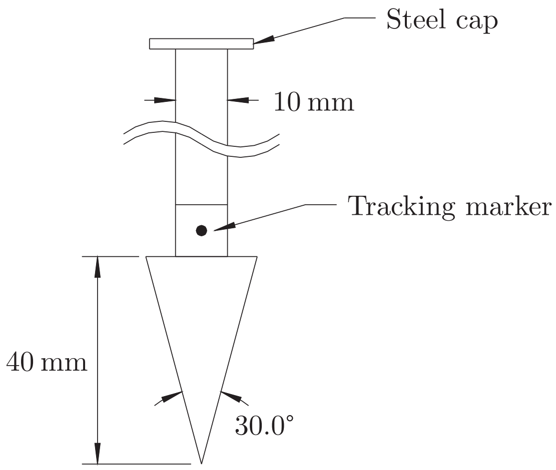

(a) 30°, 100 g cone

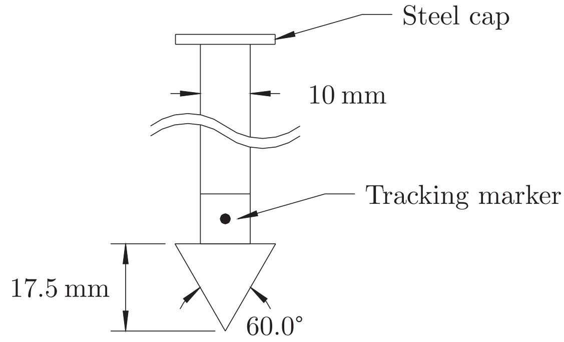

(b) $\beta = 60°$, 60 g cone

Figure 7.2: Cones used in this investigation

The clay samples to be indented were placed in smooth-sided cylindrical brass cups of diameter 55 mm and depth 40 mm, as specified by the British Standard fall cone test procedure (BSI, 1990). Finite element analyses in Section 4.4 indicated that the choice of this sample cup rather than the hemispherical type specified by Standard Norge (1988) would make little difference to the results, at least for penetrations up to $d = 20$ mm for a 30° cone or 16 mm for a 60° cone.

7.1.3 Actuator and cone release mechanism

To allow precise control of cone speed in the displacement-controlled tests, a computer-controlled linear actuator was used. The actuator carriage is mounted on a slide driven by a stepper motor through a ball screw. The actuator was manufactured by THK Co. Ltd., model number KR26, and has a 6 mm screw pitch and stroke 219 mm (more than sufficient for the tests described here).

The actuator was driven by an SY873 stepper motor supplied by Parker Hannifin Plc., combined with a Parker ViX500 microstepping drive unit capable of controlling the motor to a resolution of 50 000 steps per revolution. In combination with the 6 mm pitch of the ball screw, this gives a linear resolution of 120×10^{-9} m. The drive unit is controlled by uploading commands from a PC over an RS232 interface, either in real-time or by uploading a series of simple moves (defined by set values of acceleration, velocity, displacement and deceleration) to be executed on demand.

The KR26 actuator was mounted vertically as shown in Figure 7.1a, with the carriage attached to an electromagnet positioned above the steel end cap on the cone shaft. When activated, the electromagnet could be used to support the weight of the cone. From the electromagnet, the shaft passed down through a close-fitting clearance hole in a thick aluminium alloy plate to the cone below, as shown in Figure 7.1b. There will inevitably have been some contact between the shaft and the aluminium plate during a freefall test, but this was not expected to slow the cone significantly. A similar arrangement is used in commercially-produced fall cone equipment from Wykeham Farrance and Geonor. It is unlikely that a more elaborate linear bearing (as used for the PIV tests in Chapter 6) would have reduced resistance any further, and the additional inertia of the bearing elements would have further affected the motion of the cone.

Movement of the cone could be prevented by means of a locking screw in the aluminium plate. In all tests, the cone was initially supported by the electromagnet, and the cone tip was positioned at the sample surface by slowly advancing the actuator to the correct position. The cone could then either be moved by the actuator with the magnet still active (for a displacement-controlled test) or released to fall freely by switching the magnet off (for a freefall test).

7.1.4 Load measurement

The contact force between the cone and the clay was inferred from measurements of the reaction below the sample cup. Measurements were taken with a capacitive load cell supplied by RDP Electronics Ltd, model number MCL/50, with range $\pm 50\,\mathrm{N}$.

The capacitive measurement system operates by sensing the deflection of a load ring within the device, and is very tolerant of off-axis loading (RDP Electronics, 2007). The required signal conditioning electronics are integrated into the load cell, making a simple all-in-one package: the only additional equipment required was a $\pm 15\,\mathrm{V}$ DC electrical supply. The load cell gave a a full-scale output of $\pm 10\,\mathrm{V}$ DC. The resolution of the load cell–amplifier combination is specified as $\pm 0.01\%$ of full scale, limited by electrical noise (RDP Electronics, 2007).

The base of the load cell was mounted on a thick aluminium alloy plate using the male thread provided, while a platform to support a sample cup, machined from Perspex, was mounted on top. During a freefall test, it was anticipated that the maximum force would occur at the same instant as the peak deceleration of the cone. In rate-independent material, this deceleration would be $2g$ (see Figure 4.25c) requiring the net upward force on the cone to be twice its weight W and the force Q between the cone and clay to be $3W$. For the 100 g cone, the force on the load cell at this instant would be equal to Q plus the combined weights of the clay sample, brass cup and PMMA platform, making a total of approximately 5 N (in compression), corresponding to an output of -1 V from the load cell.

The load cell output lead was connected to a MicroDAQ-branded USB data acquisition (DAQ) device manufactured by Eagle Technology Ltd. The input range of the 12-bit analogue-to-digital converter was set to ± 1.25 V, giving a resolution of approximately 3×10^{-3} N in the converted values stored on the PC. The maximum data acquisition rate of the device is 49 kHz.

The load cell was calibrated at the beginning of the test program. Since only small loads were needed, calibration was achieved by placing small weights onto the load platform. Calibration was performed over a slightly larger range than was expected during the tests, 0–6 N. The cell was calibrated against a high-precision electronic scale (Avery Berkel model FB212), with resolution 0.01 g. The following expression was derived to convert the load cell's output V (in microvolts) to a force P (in Newtons):

$$P = -\left(5.663 \times 10^{-6}\right) V - (0.8341). \tag{7.2}$$

The negative slope ensured that values of P would be positive; the comparatively large offset results from the fact that the weight of the sample cup support was not included in the calibration force P.

7.1.5 Displacement measurement

During the freefall tests, it was necessary to obtain the variation of the displacement of the cone with time. To achieve this without influencing the motion of the cone, non-contact tracking was carried out using high-speed photography and subsequent PIV image analysis. The method is similar to that described in Chapter 6, but some details differ as described below.

High speed photography

The Photron FASTCAM high-speed camera described in Section 6.1.4 was used again, with the same 105 mm lens. Recall that the camera can record images at 1 kHz if the maximum 1024×1024 pixel resolution is required, but that it is also possible to combine lower resolutions with higher frame rates. Since the camera was being used to track vertical movement only, a narrow vertical strip of the field of view was selected as the region of interest. An area 128×672 pixels was selected, centred within the field of view. This allowed images to be recorded at 6 kHz.

The high frame-rate meant that additional lighting was again required. As before, care was taken to ensure the floodlight was activated only when completely necessary to avoid drying out the clay samples.

Image analysis

The image analysis needed to give values of cone displacement was performed using the software GeoPIV (White et al., 2003), described in Section 6.2. The method used here differs from that previously described primarily in how coordinates were converted from image to object space. The calibration routine provided by GeoPIV was not used here, partly because the distortions the software is designed to compensate for were not found to be a significant problem: the calibrations performed in Chapter 6 confirmed distortions with the camera and lens used here were not large. Additionally, one of the main sources of distortion in that work, the viewing window, is not present in this case.

A further reason for not using the calibration software was that it was difficult to provide the required reference location markers within the camera's field of view. Since the camera was already operating at its maximum data-transfer rate, widening the field of view would have required either the use of a lower resolution or a reduction in the frame-rate, neither of which was felt to be desirable.

Object-space measurements were instead obtained by the following simpler method. After each freefall test, the cone was locked in place by means of the locking screw shown in Figure 7.1b. The final displacement was then measured (to a precision of 0.02 mm) with a set of Vernier calipers. Having established the final displacement in both pixels (by PIV) and millimetres (by direct measurement), intermediate object-space displacements were obtained by interpolation, assuming a linear mapping from pixels to millimetres.

Performance of non-contact measurement system

The real-world accuracy of the photographic and image analysis techniques used here was assessed by moving the 30° cone through known distances and taking a series of photographs using the high-speed camera. Both cone and camera were placed in the positions they would occupy during the final experiments. In the first image, the cone was positioned close to the top of the image, and in each subsequent image it was lowered by 2.5 mm by manually turning the actuator ball-screw. The actual displacement of the cone was determined by means of a dial gauge attached to the actuator reaction frame, with 0.01 mm increments, while the PIV technique described above was used to give independent estimates of displacement from the images. As in the actual test procedure, PIV estimates were based on the measured final displacement.

Figure 7.3a shows the relationship between the displacement measurements obtained from the dial gauge and the image analysis technique, while Figure 7.3b shows the PIV measurements' apparent error relative to the dial gauge readings. The maximum error observed was 0.033 mm. Since the field of view of the camera was approximately 35 mm high, this represents a maximum error of less than 0.1% of the full scale reading, which compares favourably with the accuracy of commercially-available displacement transducers such as LVDTs, typically between 0.1% and 0.5% of full scale (RDP Electronics, 2008).

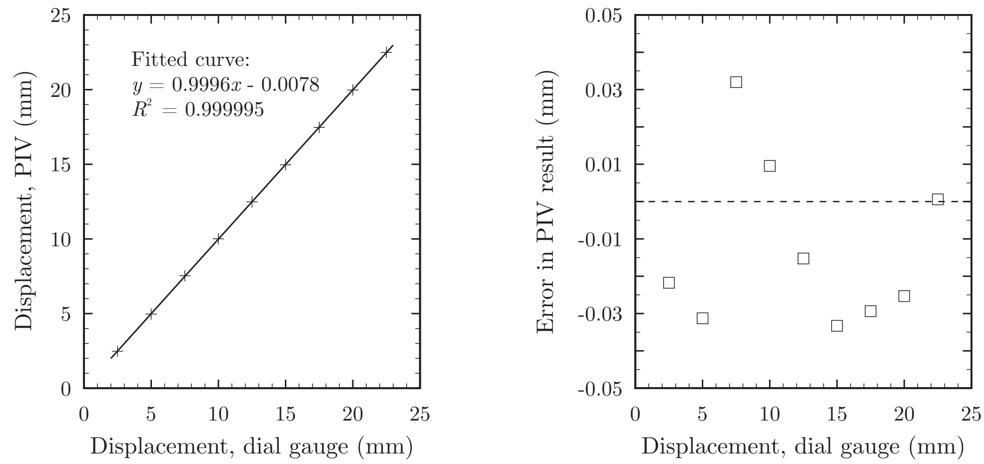

(a) Relationship between cone displacements from PIV and dial gauge

(b) Error in displacements obtained by PIV

Figure 7.3: Comparison of cone displacements from PIV and direct measurement

7.1.6 Clay sample preparation

Fall cone tests are most often performed on remoulded soil samples. This is the case in liquid limit tests (BSI, 1990), and in determining remoulded strength (Geonor, 2005b). Remoulded samples were used in these experiments to reproduce this aspect of engineering practice. Remoulding the samples thoroughly before testing ensured that strain softening would not be a factor in determining the results, thus isolating the rate dependence that was the principal object of this investigation. Using remoulded samples also provided a simple way to produce samples with a range of water contents (and therefore undrained strengths) to give a spread of results.

Blocks of kaolin clay were initially produced following the method described in Section 6.1.1, by consolidating from slurry with a high water content. After consolidation, the kaolin blocks were removed from the sample box, wrapped in clingfilm, and stored in a sealed plastic crate with a layer of water to ensure high humidity. These measures were taken to minimise drying of the samples.

Before each test, a suitable quantity of the kaolin was removed from storage and remoulded in the manner specified by the British Standard fall cone test procedure (BSI, 1990). The sample was placed on a glass plate on the laboratory bench and remoulded for 15 minutes using two palette knives, adding water gradually from a spray bottle to increase the water content if required. The remoulded soil was then pushed into the sample cups using a smaller palette knife, taking care to fill the bottom corners of the cup first and to avoid trapping pockets of air. Excess soil was struck off with the straight edge of the palette knife to leave a smooth surface, and the sample was covered with clingfilm until immediately before testing.

7.2 Tests with step-changed cone speed

The aim of these low-speed, displacement-controlled tests is to investigate the relationship between cone resistance and cone speed. The results are used to investigate the rate-dependence of the kaolin's strength, and the degree to which Equation 7.1 provides a satisfactory model for this.

Despite every care being taken to produce batches of identical soil samples, slight variation was inevitable. The measured values of cone resistance Q were expected to change by only 5 to 20% when tests were carried out at speeds that differed by an order of magnitude, so even small variations between samples could mask the differences the tests were intended to detect. Another possible source of variation between tests could be slight variations in the initial position of the cone tip relative to the sample surface. To avoid these problems, tests were carried out by pushing the cone at speed v_1 until it reached depth d_1, then suddenly changing to a different speed v_2 while monitoring the force under the cup. This allows comparisons to be made between results obtained while deforming the same material at different rates. The values of d_1, v_1 and v_2 in the various tests are given later.

There are precedents for changing the rate of a test on a soil sample to see what changes in behaviour result. Several authors have performed triaxial tests with step-changed strain rate to investigate rate-dependence (Graham et al., 1983; Oka et al., 2003). House et al. (2001) performed "twitch" tests in which the speed of a T-bar penetrometer was varied in several increments to investigate the transition between drained and undrained behaviour and thereby estimate the consolidation coefficient c_v. Randolph and Hope (2004) performed further twitch tests with a T-bar, and also investigated the use of a similar approach with the piezocone. The more common piezocone dissipation test, which allows the consolidation coefficient to be determined by stopping the cone and measuring the time needed for excess pore pressures to dissipate (Brouwer, 2008), could be regarded as an extreme example of a test with step-changed penetrometer speed.

7.2.1 Experimental method

Remoulded kaolin was prepared and placed into the brass sample containers as described in Section 7.1.6. Samples were produced in batches, each consisting of five cups of similar material.

Prior to each test, a single sample was placed on the platform above the load cell. Its weight W_cup was then measured, so that the force Q between the cone and clay could be calculated as $Q = P - W_\mathrm{cup}$ where P is the total compressive force measured by the load cell. To reduce the influence of electrical noise on the measurement, the weight was taken as the mean of 100 readings. Typically the mean of the 100 readings was around 1.7 N, and their standard deviation was not more than 0.018. The cone was positioned above the sample, supported by the electromagnet. With the locking screw released, the actuator was used to lower the cone slowly until its tip was level with the sample surface. Finally, the high-speed camera and its interface card were set up. The camera's field of view, aperture, shutter speed and focus were checked by viewing live images on the laptop computer attached to the camera interface. The frame rate was set to 1000 fps, and the controller instructed to await a triggering signal from the main PC two seconds prior to the change of cone speed before beginning to record images (it was not possible to record a stream of images from the start of the test because of the limited memory available on the camera controller). Since the displacement of the cone was controlled throughout the test, images from the camera were recorded only as a precaution, to ensure that the instant the cone speed changed could be accurately identified in the results.

To minimize human error, the actuator, load cell and camera were controlled automatically with no operator intervention during the tests. Once all preparations were completed, a script on the main PC caused the actuator to advance the cone at speed $v_1 = 1\,\mathrm{mm/s}$. The actuator's acceleration was set to $2000\,\mathrm{mm/s^2}$, so the time needed to reach full speed was only 0.0005 s, and was not taken into account in interpreting the results. 2 s before the time the cone tip was due to reach a depth d_1, the camera and DAQ were triggered to begin recording (both at 1 kHz). A pulse-train output from the camera controller was used as an external clock for the DAQ to ensure the camera images and load cell readings were synchronized.

Once the cone reached depth d_1, the actuator speed was changed to v_2 (again, the acceleration was $2000\,\mathrm{mm/s^2}$). The test then proceeded until either the cone reached a depth of 30 mm or an interval of 33 s had elapsed after the change of speed, whichever happened sooner. The limiting depth was chosen to ensure the cone did not hit the bottom of the cup, while the time limit corresponded to the capacity of the camera to store images.

The combinations of cone angle β, velocities v_1 and v_2 and the depth d_1 at which the speed change took place are shown in Table 7.1. A total of 44 tests were performed, of which 34 used the 30° cone and 10 the 60° cone. For the most part, the value of d_1 in the 30° cone tests was 20 mm; $d_1 = 10\,\mathrm{mm}$ was used in all the 60° cone tests and one batch of tests with the 30° cone. Nine tests were performed for each of $v_2/v_1 = 10$, 0.1, 0.01 and 0.001, and eight with $v_2/v_1 = 0.0001$ (the camera failed to operate in one early test). The values of v_2 therefore covered five orders of magnitude, from 10 mm/s to 0.1 µm/s. This is close to the maximum range achievable with the actuator used: decreasing the speed by a further factor of 10 would have resulted in intermittent motion, with several seconds between each

Table 7.1: Combinations of parameters used in displacement-controlled tests

Test	Angle β (°)	Initial speed v_1 (mm/s)	Final speed v_2 (mm/s)	Speed ratio v_2/v_1	Depth d_1 (mm)
1	30	1.0	0.001	0.001	10
2	30	1.0	0.01	0.01	10
3	30	1.0	0.1	0.1	10
4	30	1.0	10	10	10
5	30	1.0	0.001	0.001	20
6	30	1.0	0.1	0.1	20
7	30	1.0	10	10	20
8	30	1.0	0.01	0.01	20
9	30	1.0	0.001	0.001	20
10	30	1.0	0.01	0.01	20
11	30	1.0	0.1	0.1	20
12	30	1.0	10	10	20
13	30	1.0	0.001	0.001	20
14	30	1.0	0.001	0.001	20
15	30	1.0	0.01	0.01	20
16	30	1.0	0.1	0.1	20
17	30	1.0	10	10	20
18	30	1.0	0.01	0.01	20
19	30	1.0	0.001	0.001	20
20	30	1.0	0.01	0.01	20
21	30	1.0	0.1	0.1	20
22	30	1.0	10	10	20
23	30	1.0	0.1	0.1	20
24	30	1.0	0.001	0.001	20
25	30	1.0	0.01	0.01	20
26	30	1.0	0.1	0.1	20
27	30	1.0	10	10	20
28	30	1.0	10	10	20
29	30	1.0	0.0001	0.0001	20
30	30	1.0	0.0001	0.0001	20
31	30	1.0	0.0001	0.0001	20
32	30	1.0	0.0001	0.0001	20
33	30	1.0	0.0001	0.0001	20
34	30	1.0	0.0001	0.0001	20
35	60	1.0	0.001	0.001	10
36	60	1.0	0.01	0.01	10
37	60	1.0	0.1	0.1	10
38	60	1.0	10	10	10
39	60	1.0	0.001	0.001	10
40	60	1.0	0.01	0.01	10
41	60	1.0	0.1	0.1	10
42	60	1.0	10	10	10
43	60	1.0	0.0001	0.0001	10
44	60	1.0	0.0001	0.0001	10

step taken by the actuator, while increasing the speed was impossible because the distances required for acceleration and deceleration would have exceeded the depth of the sample.

Once each test had been completed, a small quantity of kaolin (approximately 15 g) from each sample was set aside to determine the water content w.

7.2.2 Results: 30° cone

The measured force Q was filtered by taking a 49-point centred moving average to remove most of the noise. Figure 7.4a shows example force–time curves from two typical tests with the 30° cone – these are the tests numbered 19 and 22 in Table 7.1 (with $v_2/v_1 = 0.001$ and 10 respectively). Before $t = 20\,\mathrm{s}$, the two curves are similar, with Q increasing as the cone was pushed further into the kaolin and contact area increased. In both cases, the cone speed was changed after 20 s, when the cone had reached $d = 20\,\mathrm{mm}$. In test 22, the speed was increased by a factor of 10. The slope of the force–time curve increased, but by viewing the force–time data directly it is difficult to see whether this was simply because the contact area was increasing more rapidly than before. The test was terminated at $t = 21\,\mathrm{s}$. In test 19, the speed was decreased by a factor of 1000. This led to a drop in resistance, which reached an approximately constant value after a transitional period lasting around 1 s.

The effect of rate of deformation on the strength of the kaolin is more apparent if values of Q/d^2 are plotted (see Figure 7.4b). Dividing the force by the square of a characteristic length of the deformation mechanism (in this case the cone displacement) gives a quantity with the dimensions of pressure. If the clay exhibited no rate-dependent behaviour (such that s_u had a constant value), Q/d^2 would be expected to remain constant throughout the test, as in the rate-independent FE analyses of Chapters 3 and 4. Instead, for $t < 20\,\mathrm{s}$ both curves have a slight downward trend. This is consistent with the rate-dependent FE results of Chapter 5. The cone speed ratio v/d decreased during this part of the test, leading to a gradual reduction in the average effective strain rate in the deforming region. After $t = 20\,\mathrm{s}$, the curves diverge. In test 22, the value of Q/d^2 increased suddenly, but then began to decrease again with a steeper slope than before the speed changed – as the speed was higher, v/d (and therefore the average strain rate) began to decrease more rapidly than before the change of cone speed. Towards the end of the test (approaching $t = 21\,\mathrm{s}$), the slope of the curve decreases once more and Q/d^2 becomes almost constant – with the speed v now constant (albeit at a new value v_2), the rate of change of v/d with time becomes more gradual as the depth of indentation increases.

Plotting Q/d^2 against t for test 19 shows a trend after $t = 20\,\mathrm{s}$ that is similar to the original plot of Q against t. After a transitional period a constant value is reached. This is not surprising: Q was essentially constant (Figure 7.4a) and has been divided by the square of d which is itself changing so slowly as to be imperceptible on the scale used.

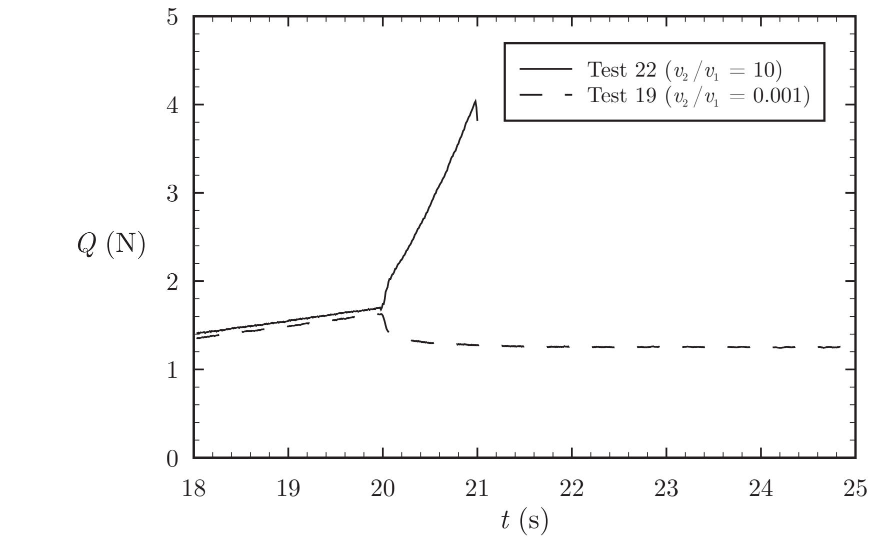

(a) Variation of Q with time

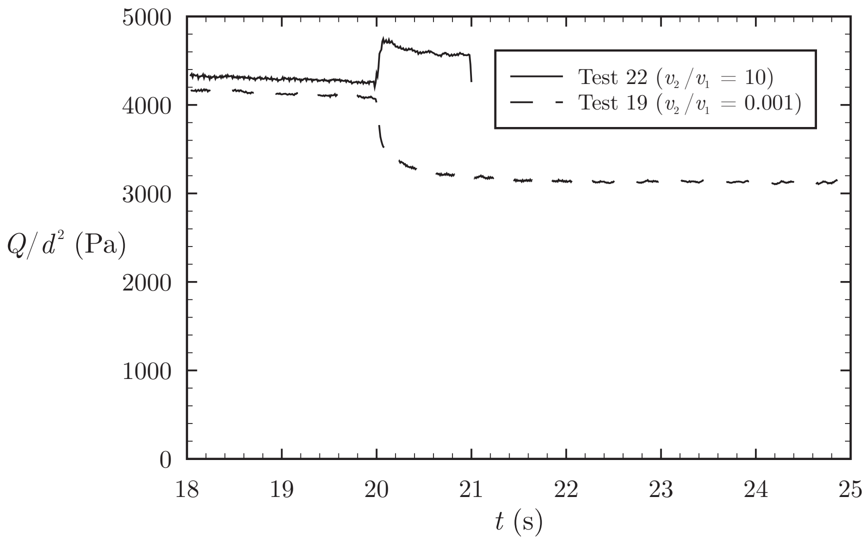

(b) Variation of Q/d^2 with time

Figure 7.4: Example results from displacement-controlled tests

From the results of each test, values of Q/d^2 were obtained immediately before and after the change in cone speed, allowing the ratio $(Q/d^2)_2/(Q/d^2)_1$ to be calculated. In cases with $v_2 < v_1$, for example test 19 (shown in Figure 7.4), the settled minimum value of $(Q/d^2)_2$ was used, after allowing the transitional period of approximately 1 s to complete. In cases with $v_2 > v_1$, such as test 22 (also shown in Figure 7.4), no such transitional period was allowed for – by the time any significant amount of time had passed the cone's displacement had changed substantially, and it was felt that this would influence the results more than any minor transitional effects would. The values of Q/d^2 used in these cases were therefore those immediately before and after the change in cone speed.

Figure 7.5 shows values of $(Q/d^2)_2/(Q/d^2)_1$ from all 34 of the 30° cone tests, plotted against $(v/d)_2/(v/d)_1$. Using values of v_2/v_1 would have made little difference, since the cone displacement d changed very little between the readings taken before and after the speed change. The data clearly confirm the existence of a link between cone resistance and normalised cone speed.

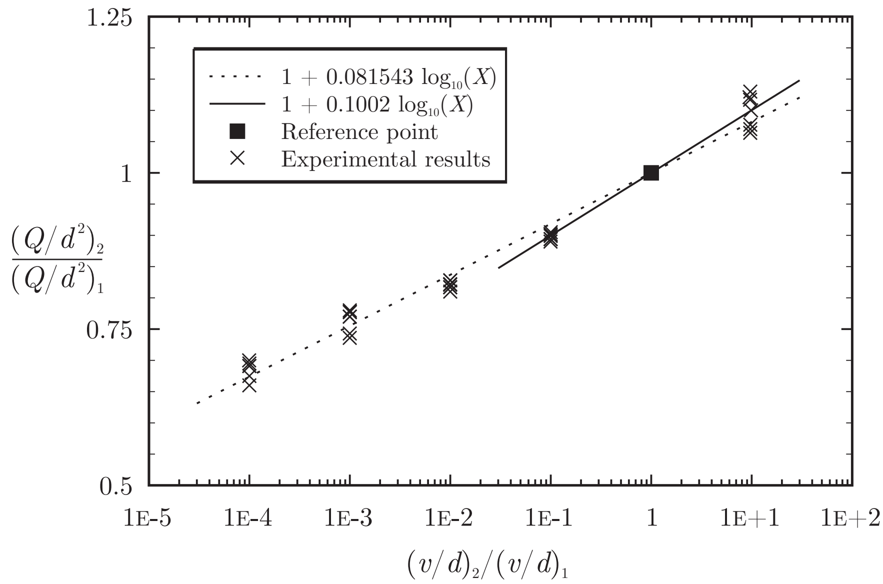

Figure 7.5: Influence of changing cone speed on normalised resistance for a 30° cone in remoulded kaolin

A value of the material rate dependence parameter μ was obtained by fitting a function to the experimental data. The form of the function used was

$$\frac{(Q/d^2)_2}{(Q/d^2)_1} = 1 + \mu \log_{10}\left[\frac{(v/d)_2}{(v/d)_1}\right] \tag{7.3}$$

Fitting all the available data gave $\mu \approx 0.08$. The resulting curve is shown by the dotted line in Figure 7.5. On inspection, it appears that the curve captures the overall trend well, but that the value of μ varies over the range of speeds covered by the tests.

This variation in μ became more apparent when separate estimates of μ were obtained from each individual test. Essentially, Equation 7.3 was fitted to each point on Figure 7.5 in turn. The resulting values of μ are plotted in Figure 7.6a. There is a definite increase in the values of μ derived from the experiments as $(v/d)_2/(v/d)_1$ increases from 1×10^{-4} to 1×10^{-1}. The final set of estimates (from tests with $v_2 = 10\,\text{mm/s}$) shows much more variation, probably because it was more difficult to read the value of $(Q/d^2)_2$ accurately in these cases – as shown in Figure 7.4b, the value varied rapidly during the period immediately following the change of cone speed, unlike in cases with small $v_2 < v_1$. Nevertheless, the mean estimate of μ (0.097) is approximately the same as that obtained with $v_2 = 0.1\,\text{mm/s}$ ($\mu = 0.102$). The second fitted curve in Figure 7.5 was obtained by fitting these fastest two sets of tests, and confirms that the apparent value of μ was close to 0.1. In the freefall cone tests to be presented in Section 7.3, v will typically be in excess of 100 mm/s; it therefore seems appropriate to use $\mu = 0.1$ in interpreting those results.

Figure 7.6b shows the same individual test estimates of μ as Figure 7.6a, but this time their variation with the samples' water content is shown. No clear trend is discernible.

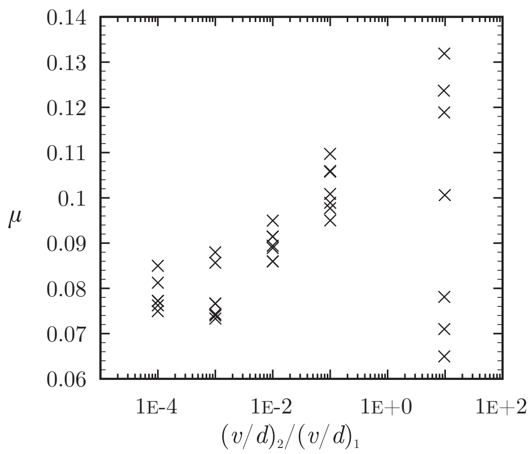

(a) μ by cone speed ratio

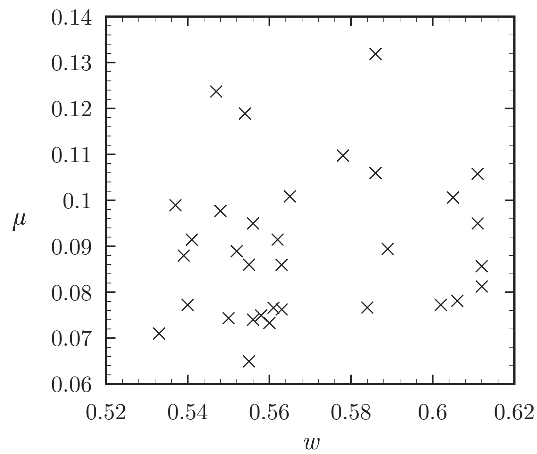

(b) μ by water content

Figure 7.6: Estimated values of μ from individual tests

7.2.3 Results: 60° cone

Values of force and displacement from the ten tests with the 60° cone were analysed as described above. The results are shown in Figure 7.7; the best-fit line that obeys Equation 7.3 is also shown. The value of the rate parameter μ is approximately 0.1, and the reduction in μ at lower cone speeds is less apparent than in the 30° cone results.

7.2.4 Drainage conditions in tests

Since the cone speed v_2 was as low as 0.1 µm/s in some of the tests reported here, the material response cannot be assumed to have been undrained. However, there was no sign

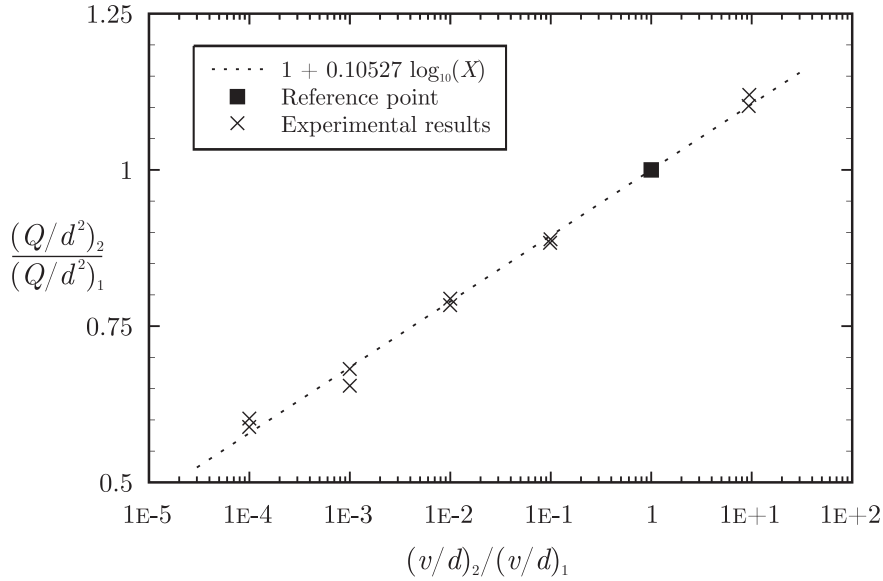

Figure 7.7: Influence of changing cone speed on normalised resistance for a 60° cone in remoulded kaolin

of the increase in resistance at reduced speed that would usually be expected with drained behaviour (see e.g. House et al., 2001; Randolph and Hope, 2004). Interpretation of the results of the tests with small v_2 is complicated by the fact that not all of the indentation took place at speed v_2 (which may well have been expected to give a drained response). Rather, all tests started at speed $v_1 = 1\,\text{mm/s}$. On the basis of FE analyses of coupled pore fluid flow–effective stress behaviour which are presented in Chapter 8, this was sufficiently fast to lead to a build-up of excess pore pressures around the cone. After the cone speed changed, a certain amount of time would have been required for the excess pore pressures to dissipate before the drained response could be seen.

The change in force observed approximately 1–2 seconds after the change in speed (as shown in Figure 7.4) was due to a combination of the viscous rate effect (characterised by μ) and pore pressure dissipation. Interpretation of the results requires consideration of the relative magnitudes of the changes in Q that result from these effects over the relevant time span. This issue is considered further in Section 8.4.

7.3 Freefall tests

The tests described in this section were carried out with the aim of establishing whether the finite element analyses of fall cone tests presented in Chapter 5 were able to provide useful predictions of the behaviour of real fall cones. Specifically, sets of four tests, each consisting of a pair of slow displacement-controlled tests and a pair of freefall indentation tests, were performed on samples of remoulded kaolin prepared as before. Each set of four tests was performed on a batch of similar clay samples prepared at the same time.

Taken together, the results of the displacement-controlled tests and freefall tests on each batch allowed experimental values of ζ to be obtained. The definition and significance of the parameter ζ are discussed in Section 2.2.7. Essentially, ζ is the ratio s_{u0}/s_{ud} of the static strength of a clay to its overall dynamic strength in a fall-cone test – the strength that, if it applied uniformly throughout the material during the entire test, would give the same final penetration h. The method by which values of ζ were obtained is given in Section 7.3.3.

Since the kaolin showed no sign of having a threshold strain rate below which there was no rate effect, there was no obvious preferred speed at which to perform the slow tests. 0.1 mm/s was selected as being much slower than the speeds the cones would reach in the freefall tests, while still being fast enough for experiments to be completed without the samples drying out significantly. However, the tests could just as well have been done more slowly or more quickly, and would have given different results. For this reason it was necessary to refer the results obtained in the displacement-controlled tests back to some baseline strain rate, even if the chosen rate had no special significance for the actual undrained behaviour of the kaolin. The value selected was $\dot{\gamma}_{\mathrm{ref}} = 3 \times 10^{-6}\,\mathrm{s}^{-1}$, as used in the Abaqus finite element analyses, as this made it easier to compare the experimental and FE results.

7.3.1 Experimental method

Kaolin was prepared by consolidating slurry from high water content as described in Section 7.1.6, then stored until needed. Batches of this material were then removed from storage and remoulded as before, adding water as required to give a range of strengths and therefore of fall cone penetration depths. Each batch of kaolin at a particular water content was large enough to fill four of the brass sample cups, which were covered with clingfilm until needed. A single test was performed on each of the four samples in each batch. Of the four tests, two were slow tests at constant speed 0.1 mm/s and two were freefall tests. The slow tests were performed first and last in each batch to detect whether there were significant changes in behaviour over the time taken for a test series.

The displacement-controlled tests were carried out in a similar fashion to the tests described in Section 7.2, with the exception that the cone speed was not changed during the analysis. Cones were pushed at constant speed $v = 0.1\,\mathrm{mm/s}$ to a depth of either 20 mm (for the 30° cone) or 15 mm (for the 60° cone). The force beneath the sample cup was measured throughout the test, at a sampling rate of 100 Hz, so that a total of 20 000 readings were taken in each 30° cone test and 15 000 for the 60° cone.

The procedure for the freefall tests was somewhat different. Once a cup of kaolin was placed on the load cell platform, the cone was lowered as before until its tip was at the surface of the clay sample, by controlling the actuator manually with the electromagnet activated to support the cone. Once the clay sample and cone were in position, a different script was used to automate the test. Because these tests were faster than those carried out under displacement control, the high-speed camera was primed to record images at the maximum available frame rate of 6 kHz. The DAQ was set to record measurements of the force under the sample cup synchronously with each image recorded by the camera, by using the "synch" output of the camera controller as an external clock source. The test was then started by simultaneously sending signals to the camera controller (which began recording images and also caused load data to be logged) and to a solid-state relay which controlled the electromagnet. Deactivating the magnet caused the cone to drop.

The cone fell under its own weight until coming to rest at displacement $d = h$. Values of Q and d throughout the test could be determined from the data recorded by the load cell and high-speed camera. Data were saved for 1 s, by which time the cones had always reached their final positions. Once all the data had been recorded, the locking screw was used to fix the cone carefully in position while its final displacement was measured (by using a Vernier caliper to measure from the lower face of the electromagnet to the cone shaft end cap).

7.3.2 Results: cone motion during a typical freefall test

The images recorded by the high-speed camera were processed as described in Section 7.1.5 to give the variation of the cone's displacement during the test. A typical example is shown in Figure 7.8a. The example shows the measured displacement–time profile for a 30° cone, using kaolin with $w = 0.57$. The cone reached its maximum displacement ($h = 19.5\,\mathrm{mm}$) after slightly less than 0.1 s. The PIV technique has captured the cone's displacement in sufficient detail to show the slight rebound of the cone after it reached its maximum penetration. This part of the displacement–time curve is shown in detail in Figure 7.8b. The oscillation of the cone about its final position came to an end after only a single cycle, indicating heavy damping. The cone rebounded by approximately 70 μm.

The possibility that the rebound observed in the freefall tests could be caused by changes in the axial deformation of the load cell was also considered. Based on the full-scale deflection specified by the manufacturer of the load cell (approximately 50 μm), the force in this freefall test (which is only 2 N) will cause a deflection of only 2 μm. The observed rebound of 70 μm cannot therefore be accounted for by the presence of the load cell.

Simple central difference numerical differentiation of the displacement data was used to estimate the cone's velocity. The results of this are shown in Figure 7.8c. The "noisy" appearance of the velocity–time curve is due to errors introduced by the use of numerical differentiation. The smoothed curve (shown in red) was obtained by calculating a 49-point centred moving average of the original velocity–time values.

Figure 7.8d shows estimates of the cone's acceleration, which were determined in two ways. The black curve was obtained by a second numerical differentiation of the velocity–time data, followed by moving-average smoothing as described above. The second, red curve was derived from the force data recorded by the load cell, as follows. The force P on the load cell was recorded throughout each test. A 49-point moving average of P was obtained to reduce noise in the data, and the reaction Q on the cone as it penetrated the kaolin was determined by subtracting the weight W_{cup} of the sample cup and its contents (obtained as the average of the first 49 load cell readings taken just before the cone began to penetrate the sample). The cone's acceleration was determined by subtracting the reaction Q from the cone's weight W, and dividing by its mass.

The two estimates of acceleration are similar throughout most of the period of the main cone penetration ($t < 0.1\,\text{s}$), except during the initial 0.025 s or so. At the start of the test, the acceleration obtained from the cone's measured displacement is substantially less than that calculated from the force acting on the cone. The most likely reason for this is that, in obtaining acceleration from the force data, it has been assumed that the only force on the cone at the start of the test was its own weight, giving it a 1–g acceleration as shown in the figure. Since the acceleration appears to have been less than this, the cone was held back in the earliest part of the test by some additional force, either friction between the cone shaft and the guide sleeve or residual attraction of the electromagnet. The difference between the two acceleration values rapidly decreases, however, suggesting the additional resistance quickly became insignificant.

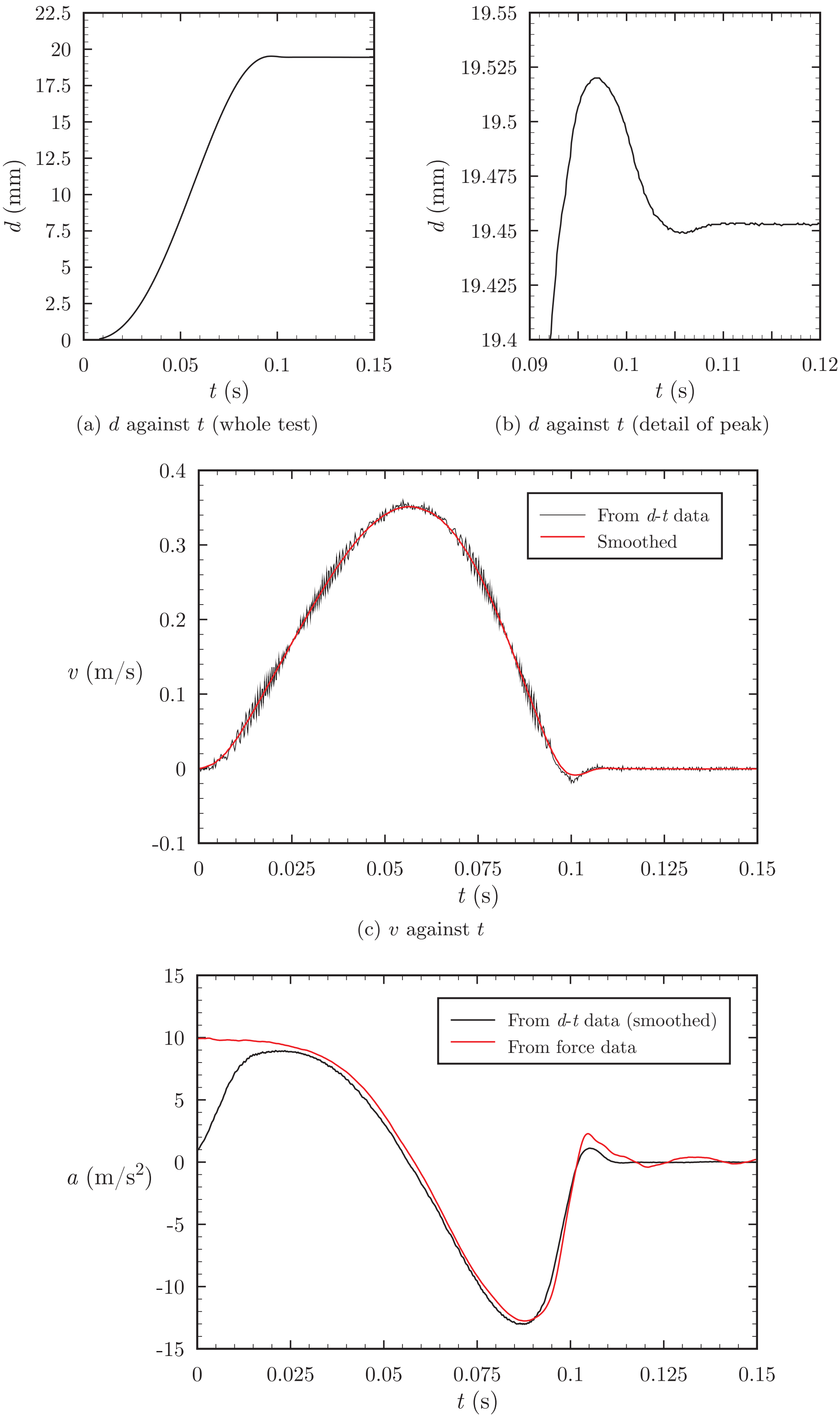

(a) d against t (whole test)

(b) d against t (detail of peak)

(c) v against t

(d) a against t

Figure 7.8: Example variation of speed, velocity and acceleration of a fall cone

Figure 7.9 shows the variation of Q with displacement d for the freefall test shown in Figure 7.8 and the other three tests from the same batch (one other freefall test and two at 0.1 mm/s). The existence of a rate effect cannot be mistaken, as the forces in the freefall tests are substantially higher than in the slower tests. For example, when $d = 15$ mm the average value of Q is 1.03 N for the two slow tests and 1.62 N in the freefall tests.

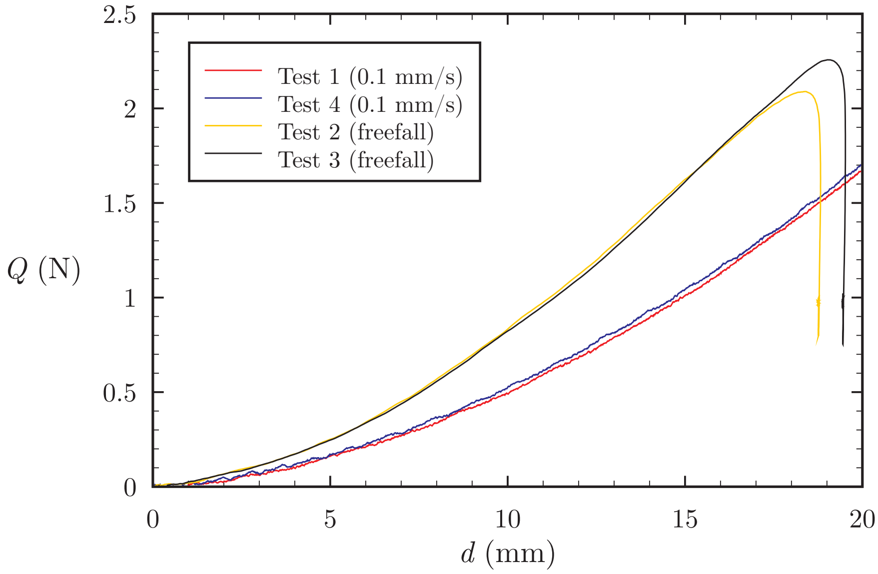

Figure 7.9: Force–displacement curves from two constant-speed and two freefall tests in similar kaolin samples

7.3.3 Results: comparison of displacement-controlled and freefall tests

In Chapter 5, values of the parameter ζ were obtained for various values of the rate parameter μ, using the results of Abaqus FE analyses. From Equation 5.11,

$$\zeta = h^2/(3h_\mathrm{s}^2) \tag{7.4}$$

where h is the maximum depth of penetration in a freefall test and h_s is the depth at which the resistance Q is equal to the cone weight W in a quasi-static test. For the purposes of the FE analyses, a quasi-static test could be considered to be one in which the velocity ratio v/d was less than or equal to $(v/d)_\mathrm{ref}$, so that the strength exhibited by the indented material was equal to s_{u0}. For the smooth 30° cone, $(v/d)_\mathrm{ref}$ was found to be $3.63 \times 10^{-6}\,\mathrm{s}^{-1}$, while the value for a smooth 60° cone was $1.75 \times 10^{-6}\,\mathrm{s}^{-1}$. For $\mu = 0.1$ (the value obtained experimentally for Speswhite kaolin), ζ was found to be 0.59.

A potential difficulty is that the slow tests were conducted with constant cone speed v.

The ratio v/d therefore varied throughout each test, and was always greater than $(v/d)_{\text{ref}}$. The values of Q obtained in the displacement-controlled laboratory tests were converted to Q_{ref} by extrapolating back to lower rates of strain, assuming that the undrained strength continued to vary linearly with the logarithm of strain rate. This was done using the following result (reported in Section 5.2) from the FE analyses:

$$\frac{Q}{Q_{\text{ref}}} = 1 + \mu \log_{10}\left[\frac{(v/d)}{(v/d)_{\text{ref}}}\right]. \tag{7.5}$$

With the values of $(v/d)_{\text{ref}}$ above, this equation allows Q_{ref} to be determined at any given instant during the displacement-controlled laboratory tests for which values of v, d and Q are available. Q_{ref} may be regarded as the force that would be measured in a test with v/d always equal to $(v/d)_{\text{ref}}$. Since Equation 7.5 was derived only from the results of FE analyses at speeds above that at which strain rates became significant, there is no implied assumption that the kaolin used in the laboratory exhibited a threshold strain rate below which there were no rate effects (as was the case in the FE material model).

Values of v/d in the displacement-controlled tests varied widely, being very large at the beginning of a test and decreasing in inverse proportion to the increasing penetration d. As a result, Q/Q_{ref} also varied throughout each test. By the time d reached 5 mm, v/d had decreased to $0.02\,\text{s}^{-1}$ and Q/Q_{ref} was around 1.37. By the end of the test, when d had increased to 20 mm, v/d was $0.005\,\text{s}^{-1}$ and Q/Q_{ref} had decreased to 1.31. Figure 7.10 shows the variation of Q and Q_{ref} together for comparison; the example shown is Test 1 in Figure 7.9.

From curves of Q_{ref} against d, the "static" cone penetration h_{s} was determined by finding the value of d for which Q_{ref} first exceeded the cone weight W. Each batch of four experiments gave two estimates of h_{s}, one from each displacement-controlled tests. The final penetration h from each freefall test was then used with Equation 7.4 to obtain an experimental value of ζ, taking h_{s} as being equal to $h_{\text{s,avg}}$, the mean of the values from the two displacement-controlled tests on samples from the same batch.

Table 7.2 shows the results obtained with the 30° cone, while those obtained with the 60° cone are given in Table 7.2. Estimates of ζ from individual tests ranged from 0.392 to 0.494, with a mean of 0.443. This differs significantly from the result obtained by finite element analysis with $\mu = 0.1$ which was 0.587. Referring to Figure 5.16, the experimentally-derived value of ζ corresponds to a higher value of the rate parameter μ than the value of

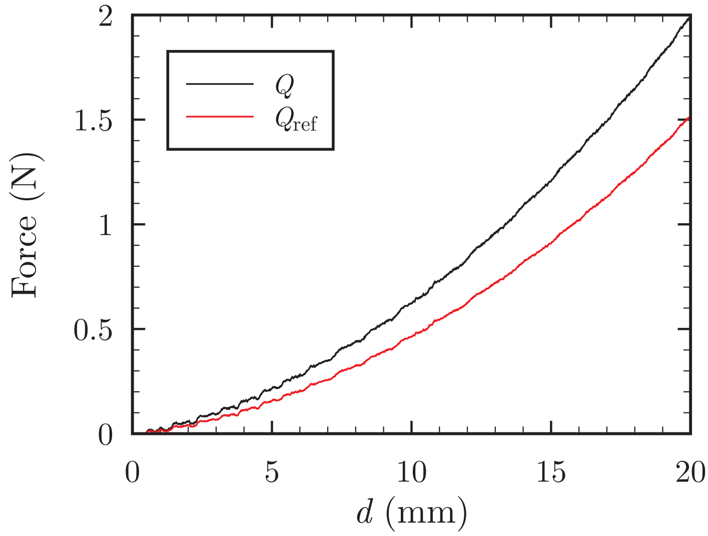

Figure 7.10: Comparison of Q and Q_{ref} in example displacement-controlled test

approximately 0.1 that was measured in the displacement-controlled tests with step-changed speed described in Section 7.2. This could be a continuation of the trend, suggested by Figure 7.6a, for rate effects to become increasingly significant at higher rates of strain, requiring the use of larger values of μ. This possibility is explored further in Section 7.3.4.

7.3.4 Results: Estimation of μ from freefall tests

The depths of indentation observed in the freefall tests were not as large as would have been expected from the low-speed force–displacement curves based on the value of μ (the increase in undrained strength s_{u} for a tenfold increase in strain rate) obtained in Section 7.2. However, these values of μ were derived from displacement-controlled tests in which the clay was subjected to lower strain rates than applied in the freefall tests. The possibility that μ changes significantly with strain rate will now be investigated, making use of the results of the freefall cone tests, in the hope of detecting this variation (which may be regarded as a second-order rate effect).

The analysis which follows is similar in many respects to that used in analysing the results of the displacement-controlled tests with step-changed cone speed that were presented in Section 7.2. Here, however, comparisons are drawn between measurements of cone resistance made in separate (but similar) clay samples.

To illustrate the method of analysis, consider the set of four tests for which force–displacement curves are shown in Figure 7.9. First, a specific value of the cone displacement d was selected, for example 10 mm. Values of cone resistance Q and speed v corresponding

Table 7.2: Values of ζ from experiments with a 30° cone

Batch no.	Test no.	Test type	h_s (mm)	$h_{s,avg}$ (mm)	h (mm)	$h/h_{s,avg}$	ζ
1	1	Slow	14.8	14.7	N/A	N/A	N/A
	2	Freefall	N/A		16.2	1.10	0.405
	3	Freefall	N/A		16.8	1.14	0.435
	4	Slow	14.5		N/A	N/A	N/A
2	1	Slow	15.6	15.8	N/A	N/A	N/A
	2	Freefall	N/A		17.9	1.13	0.426
	3	Freefall	N/A		17.2	1.08	0.392
	4	Slow	16.1		N/A	N/A	N/A
3	1	Slow	17.3	17.2	N/A	N/A	N/A
	2	Freefall	N/A		18.8	1.10	0.401
	3	Freefall	N/A		19.5	1.14	0.431
	4	Slow	17.1		N/A	N/A	N/A
4	1	Slow	17.4	17.5	N/A	N/A	N/A
	2	Freefall	N/A		19.7	1.13	0.424
	3	Freefall	N/A		20.9	1.19	0.473
	4	Slow	17.6		N/A	N/A	N/A
5	1	Slow	20.0	19.9	N/A	N/A	N/A
	2	Freefall	N/A		23.3	1.17	0.453
	3	Freefall	N/A		23.2	1.17	0.453
	4	Slow	19.9		N/A	N/A	N/A

Table 7.3: Values of ζ from experiments with a 60° cone

Batch no.	Test no.	Test type	h_s (mm)	$h_{s,avg}$ (mm)	h (mm)	$h/h_{s,avg}$	ζ
1	1	Slow	6.89	6.89	N/A	N/A	N/A
	2	Freefall	N/A		8.14	1.18	0.465
	3	Freefall	N/A		8.20	1.19	0.472
	4	Slow	6.90		N/A	N/A	N/A
2	1	Slow	6.92	6.97	N/A	N/A	N/A
	2	Freefall	N/A		8.30	1.19	0.473
	3	Freefall	N/A		8.48	1.22	0.494
	4	Slow	7.02		N/A	N/A	N/A
3	1	Slow	8.05	7.95	N/A	N/A	N/A
	2	Freefall	N/A		9.08	1.14	0.435
	3	Freefall	N/A		9.02	1.13	0.429
	4	Slow	7.85		N/A	N/A	N/A
4	1	Slow	8.53	8.52	N/A	N/A	N/A
	2	Freefall	N/A		9.58	1.13	0.422
	3	Freefall	N/A		10.3	1.21	0.490
	4	Slow	8.52		N/A	N/A	N/A

to $d = 10\,\text{mm}$ were obtained for all four tests. The mean of the two low-speed resistances was calculated, and is denoted Q_1. For each of the two freefall tests, the cone resistance at $d = 10\,\text{mm}$ was also obtained, and is denoted by Q_2. Similarly, v_1 is the cone speed in the slow tests (identical in all cases, and equal to 0.1 mm/s, while the instantaneous cone speed in each freefall test is denoted by v_2. Since all results in each batch of four tests are chosen to have identical values of d, there is no difference between the ratio of cone resistances Q_2/Q_1 and the ratio of normalized values $(Q/d^2)_2/(Q/d^2)_1$. Likewise, v_2/v_1 is no different from $(v/d)_2/(v/d)_1$.

Results were obtained in this way from the sets of force–displacement data (equivalent to Figure 7.9) for all tests with 30° and 60° cones. Sets of results were obtained from the 30° cone tests at $d = 10\,\text{mm}$, 12.5 mm, 15 mm and (where the freefall cone penetration was sufficient for data to be available) 17.5 mm. Since the 60° cones did not penetrate so deeply, results were obtained for $d = 5\,\text{mm}$ and 7.5 mm.

Figure 7.11 shows all the results. Since the values have been normalized with respect to the displacement-controlled test results within each group of results (corresponding to a particular batch of samples and value of d), all the slow test results correspond to the point $(1, 1)$. The results of the freefall tests are clustered towards the right-hand side of the plot, at values of v_2/v_1 of between 1400 and 4400. If the effect of strain rate on the undrained strength of the kaolin had followed the trend of increasing by a factor of $\mu \approx 0.1$ for a tenfold increase in strain rate, the values of Q_2/Q_1 for the freefall tests would be expected to lie between 1.3 and 1.4. In fact, the values are substantially higher, suggesting the value of μ varies significantly with strain rate.

The straight line in Figure 7.11 can be represented by

$$\frac{Q_2}{Q_1} = 1 + \mu \log_{10}\left(\frac{v_2}{v_1}\right). \tag{7.6}$$

The value of μ was selected to give the best fit in a least-squares sense to the data points, resulting in $\mu = 0.155$.

By linear interpolation between the values given in Table 5.2, the value of ζ from the finite element analyses that corresponds to $\mu = 0.155$ is found to be $\zeta \approx 0.48$. Re-analysing the experimental results with the higher value of μ gives $\zeta = 0.40$. Taking the value of μ as 0.155 therefore gives better agreement between numerical and experimental results, though the discrepancy is still around 17%. A partial explanation for the difference could be that the

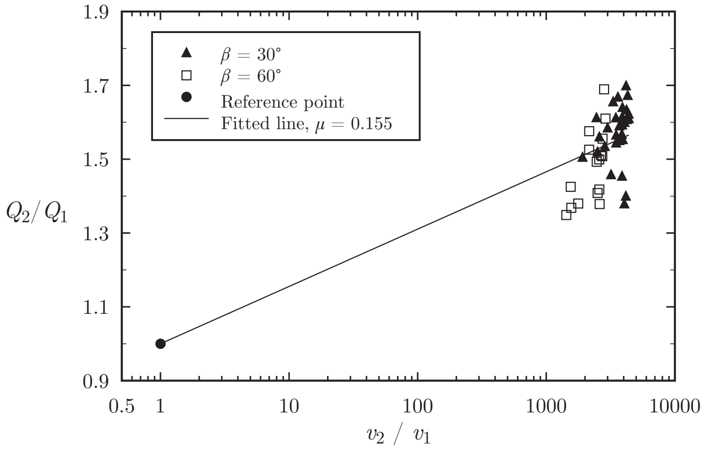

Figure 7.11: Determining μ by comparing freefall and displacement-controlled test results

motion of the cone in the laboratory freefall tests was influenced by forces other than only its weight and the resistance from the clay, such as friction with the aluminium plate through which the cone shaft passed, and any slight attraction from the electromagnet that remained after the current was switched off. Either of these effects would have slowed the cone's acceleration and reduced the final penetration h, and could therefore help in accounting for the low value of ζ $(= h^2/(3h_\mathrm{s}^2))$ obtained from the results of the experiments.

Chapter 8

Effective stress analysis with Abaqus/Standard

Although the explicit finite element method was felt to offer advantages for the purposes of this investigation, the implicit version of Abaqus (Abaqus/Standard) offers one important advantage in modelling problems with geomaterials: the possibility of performing coupled analyses accounting for the variation of pore pressure (and flow of pore fluid) within a deforming material whose constitutive behaviour is modelled in terms of effective stress. This allows the drainage conditions in the tests described in Chapter 7 to be investigated further.

First, the correct functioning of the Abaqus implementation of the Cam clay model was verified by re-analysing a published benchmark analysis. Carter (1982) carried out a series of finite element analyses of triaxial tests on clay, focusing particularly on the non-homogeneous nature of the variation of stress, pore pressure and void ratio within a sample. Carter published contour plots showing this non-homogeneity for a sample tested at a particular rate. These contour plots, together with a curve showing the transition between undrained and drained behaviour (in terms of the apparent deviatoric stress at failure in tests at different rates) have been reproduced satisfactorily with Abaqus.

The second series of analyses was intended to simulate displacement-controlled cone indentation tests at different constant speeds in kaolin samples similar to those used in Chapter 7. The particular intention was to explore the range of speeds over which the transition from undrained to drained behaviour takes place. The limiting values of cone speed (in dimensionless form) are compared with those reported by other authors.

Finally, results are presented for an analysis in which the cone speed v was suddenly decreased from $v_1 = 1\,\mathrm{mm/s}$ to $v_2 = 0.01\,\mathrm{mm/s}$, simulating one of the laboratory tests for which results were given in Section 7.2. The aim of this analysis is to obtain a better understanding of the drainage conditions in such a test.

8.1 Validation of Abaqus Cam clay model

The critical state clay plasticity model provided with Abaqus/Standard is in most respects an implementation of the modified Cam clay model (often called simply the Cam clay model) as described by (for example) Atkinson and Bransby (1978). The Cam clay model is based on laboratory results from conventional triaxial tests in which the intermediate principal stress must be equal to either the major or minor principal stress. A generalization of the model to non-triaxial stress states must involve some assumption regarding the shape of the yield surface in the deviatoric plane. The earliest of these generalizations was proposed by Roscoe and Burland (1968) and involves yield surfaces and plastic potentials that are circular in the deviatoric plane. This assumption is used here, though alternatives are available in Abaqus (Simulia, 2007).

The correct functioning of the Abaqus model was verified by carrying out a benchmark analysis based on the work of Carter (1982). Carter carried out finite element analysis to investigate the non-homogeneous behaviour of clay in the triaxial apparatus (a description of the analysis is also given by Muir Wood, 1990, pp. 377–382). The series of analyses reproduced here represent triaxial compression of a cylindrical sample of Weald clay with free drainage on all faces.

The dimensions of the sample are not given by Carter (1982), but the standard triaxial sample dimensions have been assumed (38.1 mm diameter, 76.2 mm height). Symmetry was exploited by modelling only the upper half of the sample, and performing a two-dimensional axisymmetric analysis. The lower edge of the model was therefore constrained from moving vertically, while the left edge (representing the centreline of the cylindrical triaxial sample) was constrained from moving horizontally and the outer edge of the sample was free to move in any direction. Vertical displacements were applied to the top of the sample so as to induce a final axial strain of 0.25, but this face was free to move horizontally (representing the presence of a smooth end platen). The total stress on the curved face of the sample was maintained at 207 kPa throughout the analysis. The model was given a mesh of 200

8-noded quadrilateral elements (type CAX8RP) with bi-quadratic functions representing displacements and bi-linear functions representing the variation of pore pressure within the element.

The following soil parameters were adopted for the Weald clay: $\lambda = 0.088$, $\kappa = 0.031$, $M = 0.882$, $G = 3\,\text{MPa}$ and $\Gamma = 2.0575$ (Γ is equal to $N-(\lambda-\kappa)\ln 2$). Since all analyses commenced after fully drained isotropic consolidation to $p' = 207\,\text{kPa}$, the initial void ratio was taken as $e = v - 1 = N - \lambda \ln p' = 0.624$. The permeability was taken to be $1.27 \times 10^{-12}\,\text{m/s}$.

Following Carter (1982), the transition between drained and undrained behaviour is illustrated in Figure 8.1, where deviatoric stress q at failure (taken to mean the value at 25% axial strain) is plotted against the axial strain rate $\dot{\varepsilon}_1$. The overall pattern shown by the results is similar to that given by Carter, however the new analyses suggest that fully drained behaviour is attained only at strain rates lower than those considered in the five analyses performed by Carter (which correspond to the shaded markers in Figure 8.1a). Carter's results indicate that drained failure will occur for an axial strain rate of $2.5 \times 10^{-5}\,\text{min}^{-1}$, while the Abaqus results suggest that behaviour cannot be considered fully drained with a strain rate greater than $2.5 \times 10^{-6}\,\text{min}^{-1}$. Since the mesh used by Carter (which consisted of 36 six-noded triangles) was rather coarse by comparison with that used in Abaqus, it seems reasonable to suggest the present results may be more accurate.

For copyright reasons, this figure cannot be made freely available on ORA. The content can be viewed either by looking up the reference in the caption or by viewing the printed version of the thesis.

(a) Results of Carter (1982)

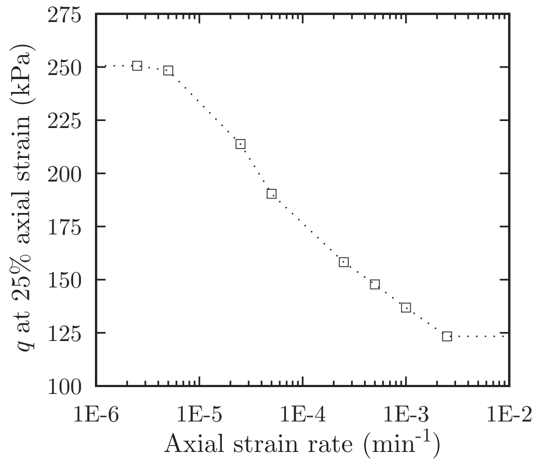

(b) Abaqus results (drainage from all faces)

Figure 8.1: Variation of strength of Weald clay in triaxial compression with axial strain rate

Carter (1982) also gave contour plots of the distribution of p', q, e and u within a sample after axial strain of $\varepsilon_1 = 5\%$ had been applied at $\dot{\varepsilon}_1 = 5 \times 10^{-4}\,\text{min}^{-1}$. The contour plot given by Carter, together with results obtained with Abaqus for the same case, are shown in Figure 8.2. Agreement between the two sets of results is generally good, and suggests that the Abaqus Cam clay model is functioning correctly.

8.2 Finite element model of cone indentation

8.2.1 Material properties

The Cam clay parameters used in the analyses were chosen to represent Speswhite kaolin, as this was the material used in the laboratory experiments described in Chapters 6 and 7. The properties of this material are widely available in the literature, though there is some variation between values given by different researchers. Martin (1994) gives a summary of some reported values.

The Cam clay parameters selected here are largely based on those reported by Martins (1983). The elastic parameter κ was taken as 0.04, and the slope M of the critical state line as 0.9. Martins reported λ to be a function of mean effective stress p', giving a value of $\lambda = 0.25$ at $p' = 5\,\text{kPa}$ decreasing to $\lambda = 0.18$ at $p' = 350\,\text{kPa}$. This variation was not allowed for in the Abaqus implementation of the critical state model, so a single representative value of $\lambda = 0.2$ was used. The model allows materials to have either constant shear modulus or constant Poisson's ratio. In the analyses described here, a constant Poisson's ratio of $\nu = 0.3$ was specified.

The coefficient of permeability was based on the work of Al-Tabbaa and Wood (1987), who performed falling-head permeability tests on normally-consolidated and overconsolidated samples of Speswhite kaolin with a range of void ratios. The samples were prepared in an oedometer modified to allow either horizontal or vertical permeability to be determined. A least-squares fit to the permeability–void ratio data for normally-consolidated kaolin gave the following approximate expressions for vertical permeability k_v and horizontal permeability k_h in terms of void ratio e:

$$k_\text{v} = 0.53e^{3.16} \times 10^{-9}\,\text{m/s} \tag{8.1}$$

$$k_\text{h} = 1.49e^{2.03} \times 10^{-9}\,\text{m/s}. \tag{8.2}$$

The resulting values of k_v and k_h for various void ratio are shown in Figure 8.3. At high water content, the curves converge such that permeability is essentially isotropic, a fact the

(a) Results of Carter (1982)

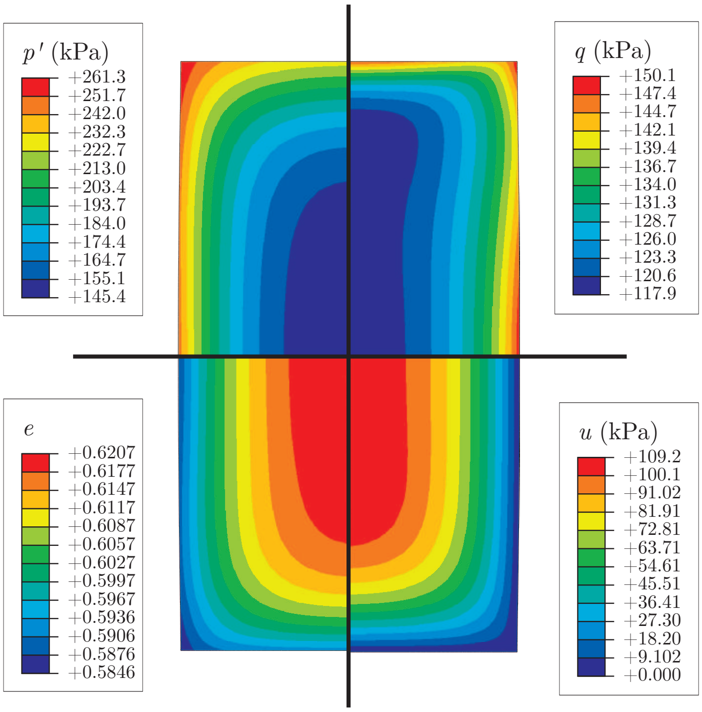

(b) Abaqus results

Figure 8.2: Contours of p', q, e and u in a triaxial sample of Weald clay at $\varepsilon_1 = 5\%$

authors attribute to the essentially random structure of clays with high void ratios. The same expressions were also found to provide a reasonable fit to data for overconsolidated kaolin, suggesting permeability is primarily related to void ratio and is independent of over-consolidation ratio (Al-Tabbaa and Wood, 1987).

Since the intention here is to model the behaviour of remoulded clays, there is no reason to expect that different vertical and horizontal permeability coefficients should apply. In the absence of results obtained specifically for remoulded kaolin, the average of the vertical and horizontal values from Al-Tabbaa and Wood (1987) was used. The variation of the mean permeability k_{ave} with void ratio is shown in Figure 8.3. For a void ratio of 1.0, $k_{\text{ave}} \approx 1 \times 10^{-9}$ m/s.

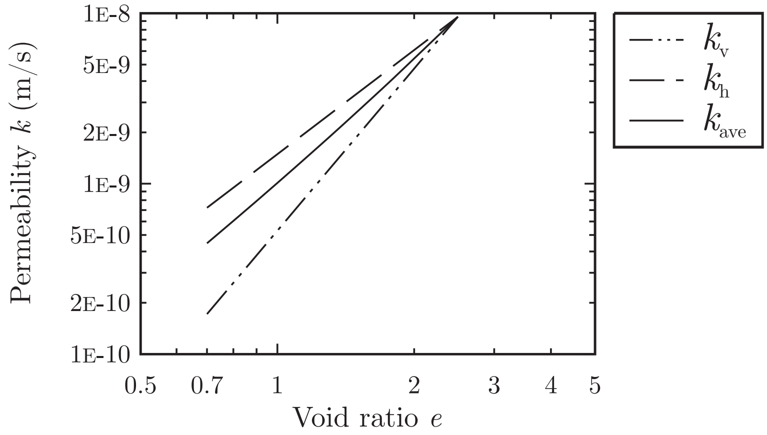

Figure 8.3: Variation of vertical and horizontal permeability with void ratio for Speswhite kaolin, from the expressions given by given by Al-Tabbaa and Wood (1987). The mean value adopted here is also shown

8.2.2 Initial conditions

The initial total stresses in the sample were taken as zero in all directions, and the initial pore pressure u as -22.22 kPa. The stresses in p'–q space therefore lay at the point $p' = 22.22$ kPa, $q = 0$, marked B in Figure 8.4. The initial size of the yield surface (p'_0 in Figure 8.4) was taken as 44.44 kPa.

The reasoning behind the choice of initial stress state is that soil samples are usually remoulded immediately before performing fall-cone tests. Remoulding, involving continuous undrained shearing for an extended period, places the soil at critical state (stress state A in Figure 8.4). Immediately after remoulding ceases, the total stress on the sample is reduced to zero. This undrained unloading causes a purely elastic response in the material, which

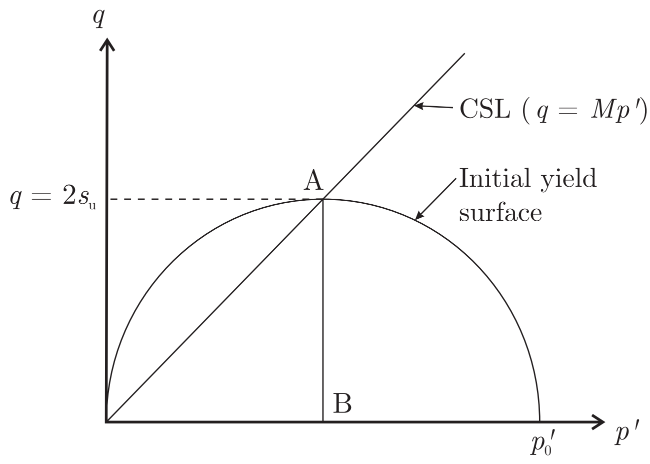

Figure 8.4: Stress state in q–p' space at start of analysis (point B)

will be governed by

$$\begin{bmatrix} \delta\varepsilon_{\mathrm{p}} \\ \delta\varepsilon_{\mathrm{q}} \end{bmatrix} = \begin{bmatrix} 1/K' & 0 \\ 0 & 1/3G' \end{bmatrix} \begin{bmatrix} \delta p' \\ \delta q \end{bmatrix} \tag{8.3}$$

where K' and G' are respectively the bulk and shear moduli of the soil skeleton, $\delta\varepsilon_{\mathrm{p}}$ is the volumetric strain, and $\delta\varepsilon_{\mathrm{q}}$ the triaxial shear strain. The off-diagonal zeros reflect the lack of coupling between volumetric and distortional strains in isotropic elasticity. In the absence of plastic strains, $\delta\varepsilon_{\mathrm{p}}$ and $\delta\varepsilon_{\mathrm{q}}$ are both the elastic and the total strain increments. From Equation 8.3 and the condition of constant volume (implied by the rapid and therefore undrained nature of the unloading), $\delta p'/K' = 0$, implying either that K' is infinite or that $\delta p'$ is zero. Since there is no reason for the soil skeleton to have infinite bulk modulus, the only reasonable solution is $\delta p' = 0$, which implies that unloading the material gives a stress path that is vertical in p'–q space (Muir Wood, 1990), so that the stress state in the material immediately prior to testing may be represented by the point B in Figure 8.4. The choice of $p'_0 = 44.44\,\mathrm{kPa}$ gives rise to an undrained strength $s_{\mathrm{u}} = Mp'_0/4$, equal to $10\,\mathrm{kPa}$.

8.2.3 Boundary conditions

As in the Abaqus/Explicit analyses with a rate-dependent Tresca material (described in Section 5.2), mechanical boundary conditions were chosen to represent a rough cylindrical cup of the British Standard size (diameter 55 mm and depth 40 mm; BSI, 1990). The radial and vertical displacements of nodes on the base and sides of the cup were specified to be zero.

In addition to the displacement boundary conditions, boundary conditions specifying the conditions for pore fluid flow on all boundaries had to be specified. No flow was permitted across the base and outer edge of the sample cup. A "drainage only" boundary condition was specified for the upper surface of the kaolin, meaning that pore water could flow across the boundary only when pore pressures in the material at the surface were positive. So, water could flow out of the clay, but no additional water could be drawn in. In fact it transpired that, since pore pressures on the free surface remained negative (representing suctions) throughout all the analyses, this boundary condition had the same effect as the zero-flow conditions imposed on other boundaries.

8.2.4 Type of element and structure of mesh

Abaqus/Standard does not provide the ALE adaptivity function that was used for the Abaqus/Explicit analyses previously described. The analyses described here were therefore performed without adaptive meshing, with the result that elements close to the face of the cone underwent larger distortions than would ideally have been tolerated. Only indentations with smooth cones ($\alpha = 0$) and the sharpest cone angle ($\beta = 30°$) could be analysed, as increasing either α or β resulted in elements being distorted so severely that the solver was unable to complete the analysis. Although the substantial element distortions would ideally have been avoided, experience in Chapter 4 suggested that a mesh with some highly distorted elements could nevertheless give results comparable with reference solutions obtained by other methods.

Abaqus analyses that involve coupled pore fluid flow and effective stress–strain behaviour must use one of the specialised element types provided. For the analyses described here, eight-noded axisymmetric quadrilateral elements with reduced integration were selected (specifically, Abaqus element type CAX8RP). The variation of displacement within each element is represented by quadratic functions, while pore pressure variation is linear.

The structure of the finite element meshes was similar to that already described, with smaller element sizes in the region of the model closest to the cone. In the first analyses the 12.5 mm-square region closest to the point of indentation was given a regular mesh of square elements, each of length 0.3125 mm. Further from the cone, the mesh density decreased as shown in Figure 8.5. Key dimensions are shown, including the final cone penetration $h = 10$ mm.

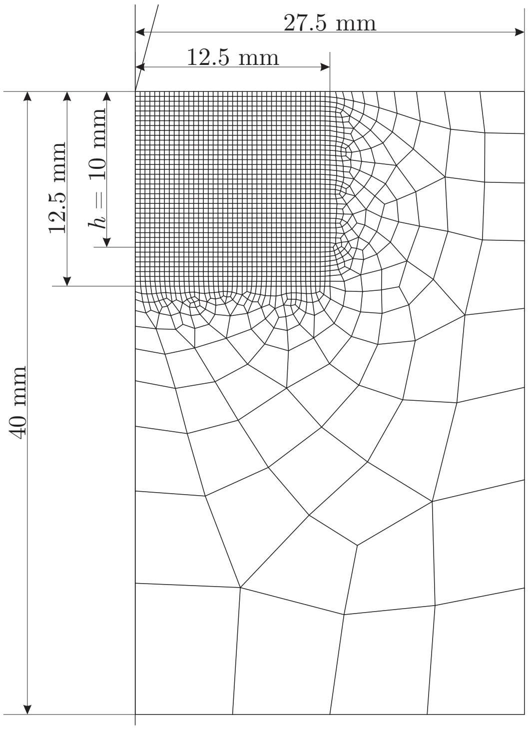

Figure 8.5: Dimensions of FE model, shown with coarse mesh in undeformed state

8.3 Analyses with constant cone speed

8.3.1 Cases considered

All analyses involved a 30° cone with a smooth surface (adhesion factor $\alpha = 0$), and were performed by pushing the cone downwards at constant speed until it had penetrated to a depth $d = 10$ mm. In the first analysis, the cone speed v was 1 m/s, which gave an undrained response. The speed v was then reduced by a factor of ten for each subsequent run. The cone resistance Q at a given depth d increased as the material's behaviour became first partially drained, then fully drained. Once Q ceased increasing significantly, the sequence of tests was stopped. In total, nine analyses were performed with v ranging from 1 m/s to 1×10^{-8} m/s, giving a "backbone" curve showing the variation of cone resistance with rate of indentation.

To verify that the mesh used was sufficiently refined, the initial series of tests was repeated with a finer mesh. This second mesh was identical to that shown in Figure 8.5 except that the nodal spacing in the finely-meshed region close to the cone was halved. There were therefore four times as many elements in this region of the model.

8.3.2 Results

Undrained response

In the fastest analysis, with $v = 1\,\mathrm{m/s}$, the final cone resistance Q (corresponding to $d = 10\,\mathrm{mm}$) was found to be equal to 1.10 N. Based on Equation 1.2 with an undrained strength $s_\mathrm{u} = 10\,\mathrm{kPa}$ and the value of N_ch in Table 3.4 (from analysis of a Tresca material using ELFEN), the predicted cone resistance is

$$Q = N_\mathrm{ch} s_\mathrm{u} \pi \tan^2\left(\frac{\beta}{2}\right) d^2 = 1.14\,\mathrm{N}, \tag{8.4}$$

which agrees fairly well with the force obtained here (the values differ by around 3.3%). Closer agreement could not be expected, since the Abaqus Cam clay model uses a yield surface that is circular in the deviatoric plane (rather than hexagonal as for a Tresca material).

The deformed mesh at the end of the analysis is shown in Figure 8.6, together with a dashed line showing the position of the free surface in the equivalent analysis with a Tresca material. The height of the lip immediately adjacent to the cone is similar in the Tresca and Cam clay analyses, but the deformed surface in the Cam clay analysis then curves downwards more rapidly so that it lies below the Tresca prediction. The two surfaces then cross over, and further from the cone the Cam clay surface lies marginally above the dotted line indicating the Tresca surface level; the height difference is imperceptible on the scale of Figure 8.6.

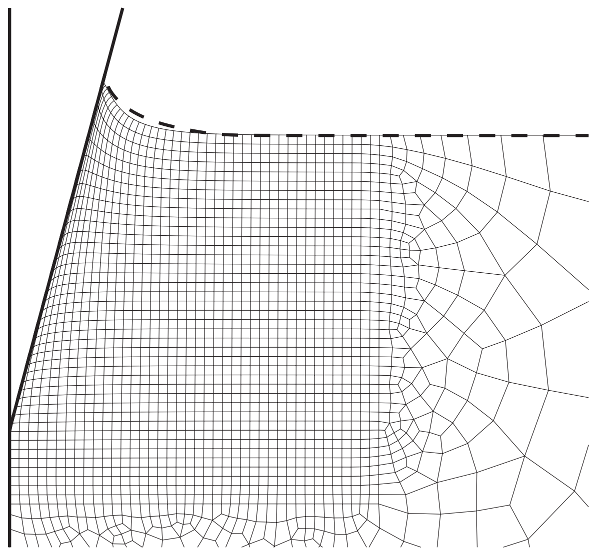

Figure 8.6: Deformed mesh at end of Cam clay analysis with $v = 1\,\mathrm{m/s}$. Dotted line indicates surface profile obtained with rate-independent Tresca material

Comparison of drained and undrained analyses

Figure 8.7 shows the variation of cone resistance Q with penetration depth d in the fastest and slowest cases (those with cone speed $v = 1\,\mathrm{m/s}$ and $v = 1 \times 10^{-8}\,\mathrm{m/s}$). In the slowest case, the value of Q at any given depth was approximately 33% higher than in the fastest.

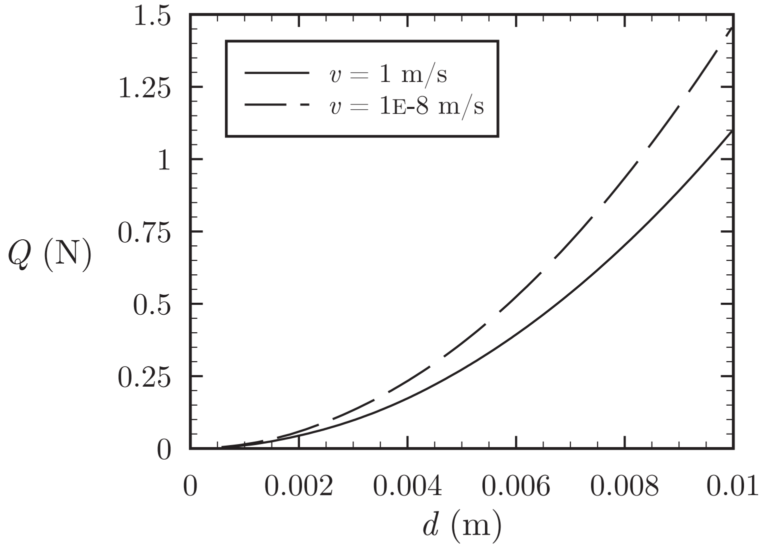

Figure 8.7: Force–displacement curves from undrained and drained analyses

The pore pressure distribution in the region of the model close to the cone at the end of the fastest analysis is shown in Figure 8.8. Far from the cone, the pore pressure is approximately equal to the initial value of $u = -22.22\,\mathrm{kPa}$. Close to the face of the cone, the pore water is no longer in suction but sees a positive pressure of of the same order of magnitude as the initial (negative) pore pressure. In the "lip" of material at the free surface adjacent to the cone, the pore pressure has decreased from the initial value, becoming more negative. The suction is not sufficient for the soil to become unsaturated, however: Khalili et al. (2004) state the air-entry suction for kaolin to be approximately 85 kPa.

In the slowest analysis, the pore pressures were approximately uniform throughout the model, ranging only between $-22.080\,\mathrm{kPa}$ adjacent to the face of the cone and $-22.081\,\mathrm{kPa}$ far away from the cone. The uniform tensile back pressure confirms that v was small enough for the material to respond in a fully drained fashion.

Stress paths in indented material

Stress paths at two locations within the deforming material were obtained for the fastest and slowest FE analyses (those with $v = 1\,\mathrm{m/s}$ and $1 \times 10^{-8}\,\mathrm{m/s}$ respectively). The locations of

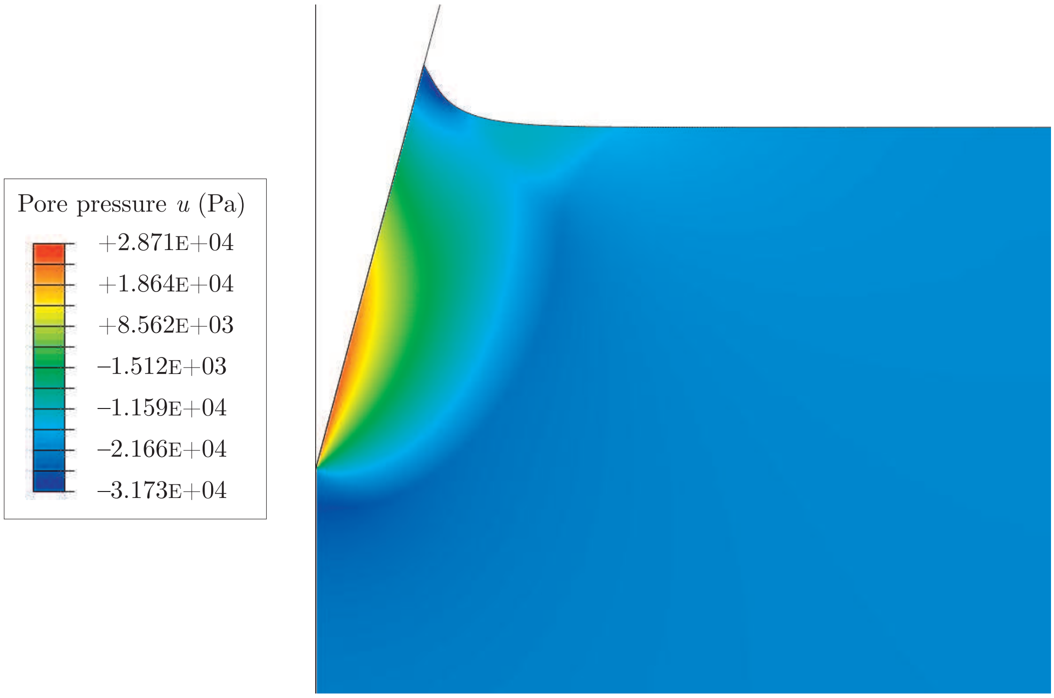

Figure 8.8: Distribution of pore pressure around cone. $d = 10\,\text{mm}$ and $v = 1\,\text{m/s}$

the two points are shown in Figure 8.9a. Point A was initially close to the centreline of the model, and was close to the face of the cone at the end of the analysis, while point B started close to the material surface and finished in the lip of displaced material. Points within elements immediately adjacent to the centreline were not selected, as the stresses could have been unreliable due to large element distortions. Stresses at the two points A and B were saved at 100 equal time intervals during the penetration of the cone, and are shown in Figure 8.9b (for point A) and Figure 8.9c (for point B).

In the analyses with $v = 1\,\text{m/s}$, similar stress paths were obtained at both points A and B. During the early part of each analysis the stresses at the relevant points lay inside the initial yield surface, and the material was elastic. As discussed in Section 8.2.2, undrained elastic behaviour gives rise to no changes in p' and so the stress paths are vertical on a plot of q against p'. The point where the stress paths meet the yield surface corresponds to the critical state. No hardening occurs and the material continues to deform with both q and p' constant.

In the slowest analyses, with $v = 1 \times 10^{-8}\,\text{m/s}$, the stress path at point A indicates that (before the soil yielded) the mean compressive effective stress on the sample decreased slightly. This suggests that the stresses induced in material ahead of the cone are dominated by tensile stretching rather than by compression. As the material yields, the stress path

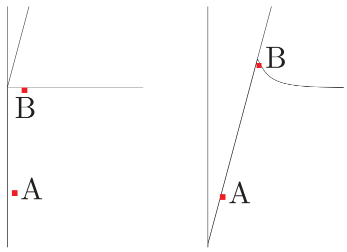

(a) Initial (left) and final (right) positions of points A and B

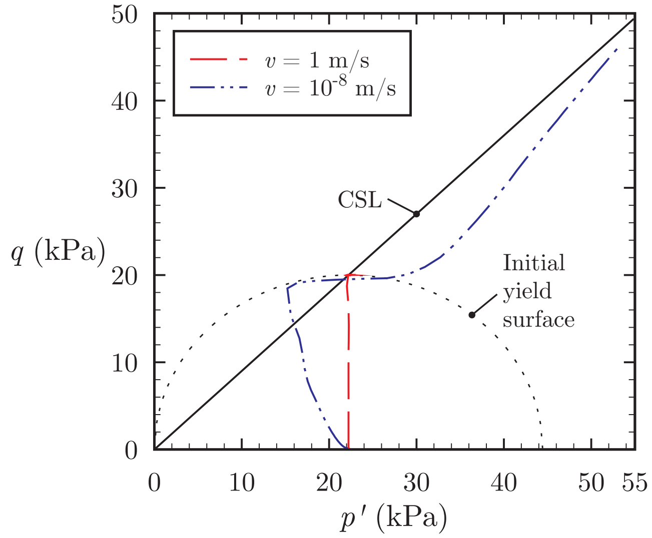

(b) Stress path at point A

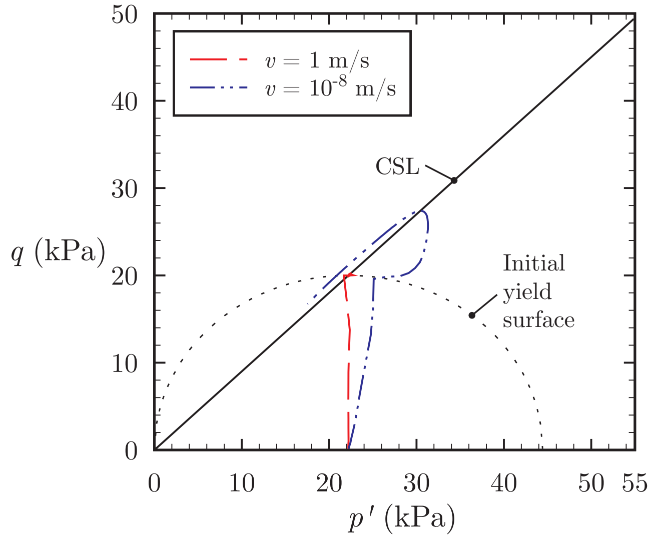

(c) Stress path at point B

Figure 8.9: Stress paths in p'–q space at two points within deforming material

tracks around the yield surface before moving toward higher stress states and approaching the critical state line. The stress path is outside the initial yield surface, indicating that substantial hardening has occurred. The stress path at point B is very unlike those observed in conventional triaxial tests, as the direction of the stress path changes as the material moves closer to the cone, into the region where tensile hoop stresses were observed with the Tresca material model (see Section 3.3.3). Although both q and p' initially increase, the stress path turns around and tracks down the critical state line as the analysis continues. By the end of the test, the material has undergone strain softening so that the final yield envelope lies inside the initial surface shown in Figure 8.9.

Transition from undrained to drained response

Having confirmed that the force–displacement response of the FE model in the fastest (undrained) analysis was similar to that with a Tresca material, and that the slowest analysis was sufficiently slow to give a drained response with no development of excess pore pressures, the transition between the two behaviours was studied.

The variation of resistance Q with cone speed v from the initial batch of nine analyses is shown in Figure 8.10. The forces shown are those at the end of the analysis, when $d = 10\,\mathrm{mm}$. As v decreases from the original value of $1\,\mathrm{m/s}$, the resistance Q remains fairly constant as v is reduced. After the speed has been reduced by a factor of 1000 (to $1 \times 10^{-3}\,\mathrm{m/s}$), the response is still basically undrained, and Q has increased by only around 2%. Most of the increase in resistance occurs as v reduces over the next three orders of magnitude, between $v = 1 \times 10^{-3}\,\mathrm{m/s}$ and $v = 1 \times 10^{-6}\,\mathrm{m/s}$, when Q is 31% larger than in the undrained analysis. When v is reduced by a further factor of 100, Q increases only slightly more, reaching a value 32.7% larger than in the undrained case.

If values of cone resistance Q are normalised by the Q_u, where the subscript "u" denotes the force obtained in the fastest (undrained) analysis, the transition between undrained and drained behaviour at different penetration depths may be compared. Figure 8.11a shows the variation of Q/Q_u with v for values of cone resistance at $d = 5\,\mathrm{mm}$ and $d = 10\,\mathrm{mm}$. The transition from undrained to drained behaviour takes place at higher speed when d is smaller.

From dimensional considerations it has been widely recognised (see e.g Finnie and Randolph, 1994; House et al., 2001; Randolph and Hope, 2004) that the degree of consolidation

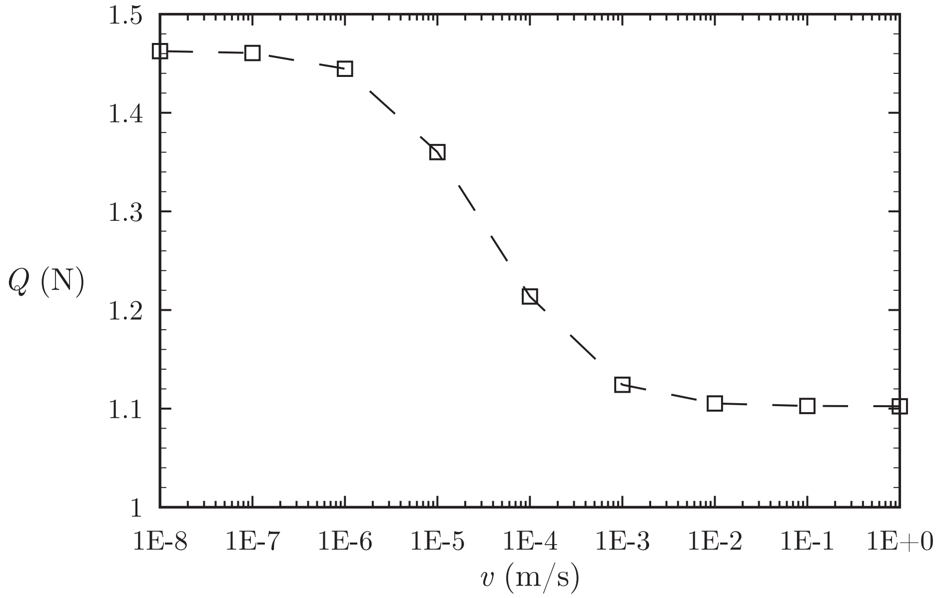

Figure 8.10: Variation of Q with v for $d = 10\,\mathrm{mm}$

during penetration can be assessed by reference to the dimensionless group

$$V = \frac{vD}{c_\mathrm{v}}, \tag{8.5}$$

where v is the speed of the cone, D its diameter and c_v the coefficient of consolidation. In general, the value of c_v is not constant but depends on stress state. Since a single value is required to make use of the dimensionless group in Equation 8.5, the value applicable to the material at the start of the analysis has been used. According to Muir Wood (1990), c_v for an overconsolidated material may be determined from

$$c_\mathrm{v} = \frac{kv\sigma'_\mathrm{v}}{\kappa\gamma_\mathrm{w}} \tag{8.6}$$

where v is the specific volume (equal to $1 + e$ where e is the void ratio), σ'_v is the vertical effective stress (here equal to the mean effective stress p' since the initial stress state is isotropic), γ_w is the unit weight of water and other symbols are as previously defined. The value of c_v which is applicable here is found to be $1.13 \times 10^{-7}\,\mathrm{m}^2/\mathrm{s}$ or $3.27\,\mathrm{m}^2/\mathrm{year}$.

If the data from Figure 8.11a are replotted using the dimensionless group V in place of the speed v, Figure 8.11b is obtained. In calculating V, the diameter D of the cone was calculated at the original soil surface, so that $D = 2d\tan\frac{\beta}{2}$.

Various suggestions have been made regarding the limiting values of V for drained and undrained behaviour. Finnie and Randolph (1994) performed tests on circular foundations, and suggested drained and undrained limits of $V = 0.01$ and 30 respectively. These limits are marked in Figure 8.11b and can be seen to agree well with the results of the present finite element analyses.

Experiments with a cylindrical T-bar penetrometer by House et al. (2001) suggested tighter limits of 0.1 and 10, which were confirmed by Randolph and Hope (2004). Randolph and Hope also reported limiting values for a piezocone (0.3 and 30). The limits reported by Finnie and Randolph (1994) agree more closely with those in the present analyses, suggesting that partially-drained behaviour occurs over a smaller range of values of V in tests performed at depth, while wider limits apply when a free surface is present.

Mesh refinement

When the analyses were repeated with a finer mesh, there was essentially no change in the results. The maximum change in the value of Q at $d = 10\,\mathrm{mm}$ was less than 0.07%, and occurred when the cone speed v was $1 \times 10^{-5}\,\mathrm{m/s}$. If results with the finer mesh are plotted on the same axes as those obtained with the coarser mesh, the curves are indistinguishable from one another.

8.4 Simulation of laboratory tests with step-changed cone speed

The laboratory tests reported in Section 7.2 involved pushing cones into samples at a constant speed $v_1 = 1 \times 10^{-3}\,\mathrm{m/s}$, then suddenly changing the speed to a new value v_2. Since the second stage of the test was sometimes performed at very low speed (as little as $1 \times 10^{-7}\,\mathrm{m/s}$), it is necessary to consider whether the behaviour of the clay was undrained or (partially or completely) drained.

The degree of drainage in these tests may be assessed by calculating values of the dimensionless group V (see Equation 8.5), and comparing them to the suggested limits of $V = 0.03$ for drained behaviour and $V = 100$ for undrained behaviour. The diameter D, speed v and consolidation coefficient c_v are required. D is similar for the 30° cone at depth $d = 20\,\mathrm{mm}$ and the 60° cone at $d = 10\,\mathrm{mm}$; the two cases give $D = 10.7\,\mathrm{mm}$ and $D = 11.5\,\mathrm{mm}$ respectively. The value of c_v may be taken as approximately $8 \times 10^{-8}\,\mathrm{m^2/s}$, as in Section

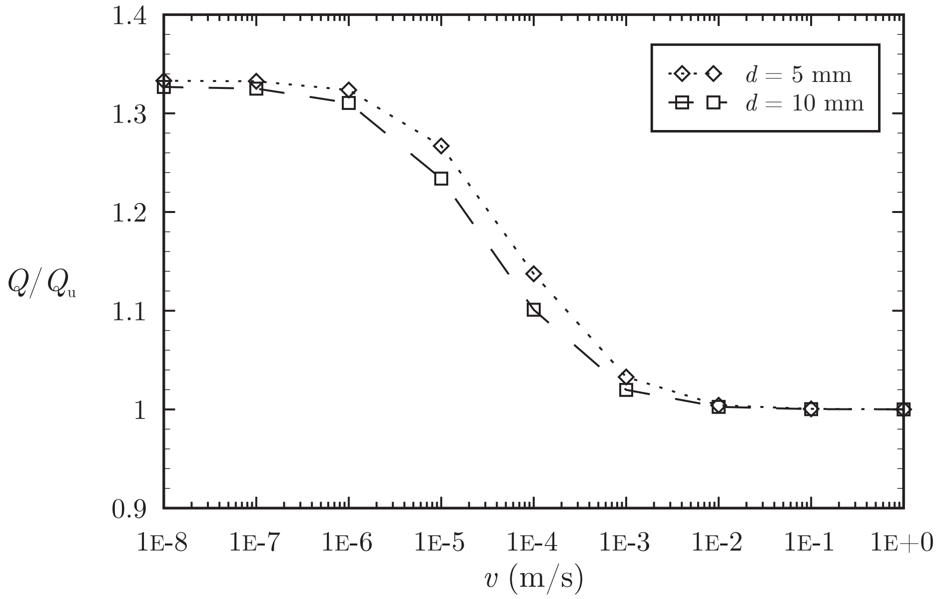

(a) Variation of Q/Q_u with cone speed v

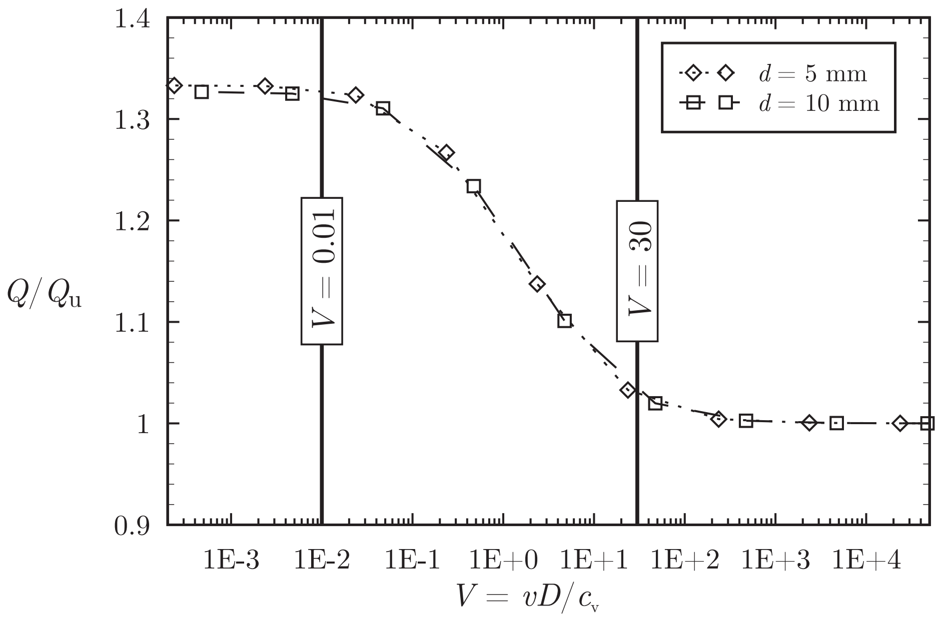

(b) Variation of Q/Q_u with V, showing limiting values proposed by Finnie and Randolph (1994) for drained and undrained behaviour

Figure 8.11: Transition from drained to undrained behaviour

8.3.2.

With the values of D and c_v given above, Equation 8.5 gives the V immediately before the change in cone speed as approximately 130. This suggests that the tests were undrained immediately before the change in speed. After the change in speed, V is approximately 0.013 with $v_2 = 1 \times 10^{-7}$ m/s, implying a drained response. In the fastest tests conditions were clearly undrained – with $v_2 = 1 \times 10^{-2}$ m/s, V is around 1300.

On the basis of the finite element results, therefore, the results presented in Figures 7.5 and 7.7 would be expected to span the transition from drained to undrained behaviour. However, there was no indication of an increase in resistance Q in the slowest tests, in contrast with the results reported by House et al. (2001) and Randolph and Hope (2004), and in the FE results presented here.

To better understand the response of a material when subjected to a sudden decrease in the dimensionless rate of testing V, such as was imposed in the tests reported here, a further finite element analysis was performed. The test modelled is similar to those reported Section 7.2. A smooth 30° cone was pushed to a depth $d = 10$ mm at constant speed 1×10^{-3} m/s into a Cam clay material with parameters chosen to represent Speswhite kaolin. However, the new analysis was not terminated at this stage but continued for a further 100 s at lower speed ($v = 1 \times 10^{-5}$ m/s).

8.4.1 Results

The variation of force Q with time t in the analysis is shown in Figure 8.12a. The speed of the cone changed from $v_1 = 1$ mm/s to $v_2 = 0.01$ mm/s at $t = 10$ s, when the indentation depth was 10 mm. From Figure 8.11a, this change in speed would be expected to give rise to an increase in Q of around 20%. However, because a finite period of time is required for dissipation of pore pressures, this transition occured gradually. After the change of speed, the force on the cone initially *decreased* slightly, reaching a minimum between two and three seconds later and then beginning to increase again.

In Figure 8.12b, Q/d^2 is plotted against d, where d is the displacement of the cone. Before the change in speed, Q/d^2 is approximately constant, as was observed to be the case in earlier analyses with a Tresca material.

The steep upward slope of the Q–t curve for $t < 10$ s is largely due to the increasing size of the indentation during that period, whereas the variation afterwards is largely due to time-

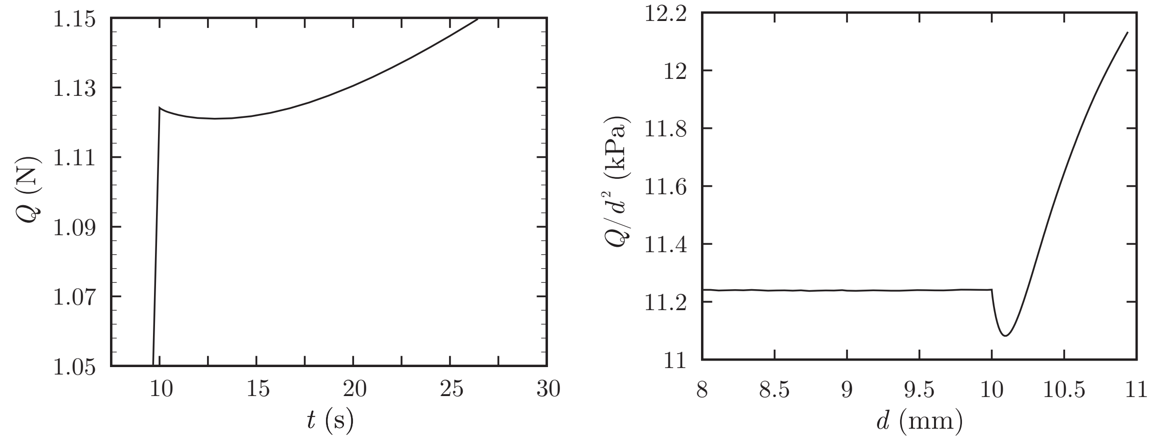

(a) Variation of Q with time

(b) Variation of Q/d^2 with displacement

Figure 8.12: Response of cone resistance to a sudden drop in speed at $t = 10\,\mathrm{s}$

dependent changes in the distribution of pore pressures around the cone. The distributions of pore pressure around the cone 0 s, 10 s and 20 s after the change in speed are shown in Figure 8.13. When the change in speed takes place, the maximum pore pressure adjacent to the cone is positive, and remains so for at least another 10 s.

In the laboratory tests of Section 7.2, values of Q/d^2 after the change in speed were always calculated from values measured in the 5 s period after the speed change. During this time, the pore pressure response predicted by the finite element analysis resulted in changes in Q/d^2 of only about 1%, or 0.5% for every tenfold change in the cone speed. Since this is only a small fraction of the changes measured in the laboratory, it seems reasonable to conclude that the changes were due to the viscous rate effect characterized by the rate parameter μ, which was not accounted for by the Cam clay material model used for the present FE analysis.

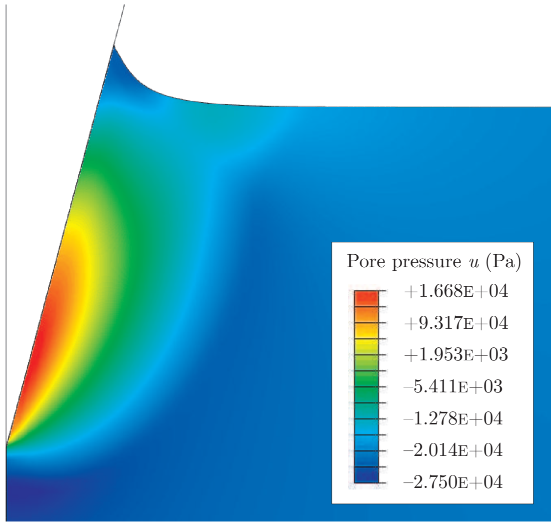

(a) t=10 s

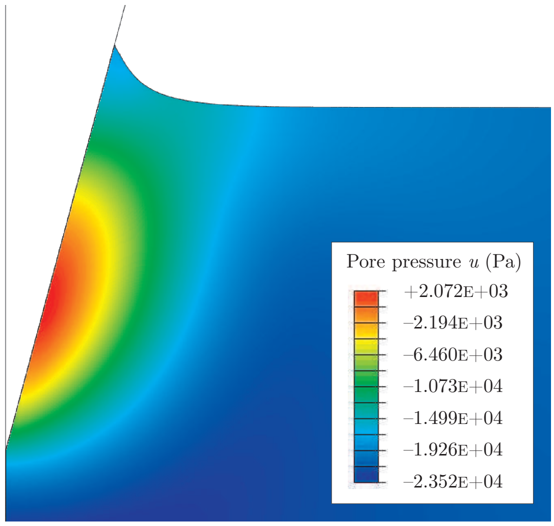

(b) t=20 s

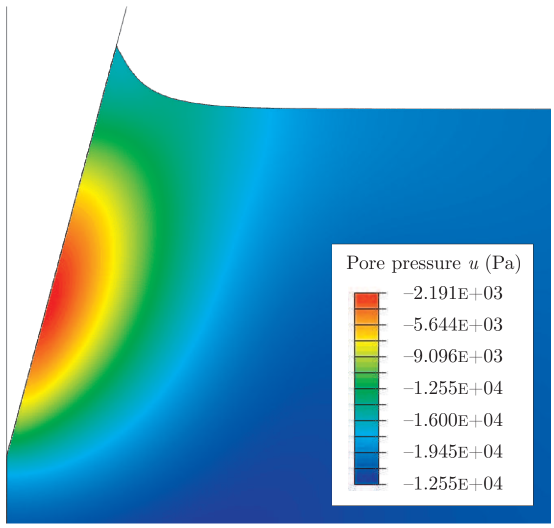

(c) t=30 s

Figure 8.13: Distribution of pore pressure around cone following reduction in cone speed at $t = 10\,\mathrm{s}$

Chapter 9

Concluding remarks

A substantial section of this thesis has been concerned with numerical modelling of the fall-cone test by the finite element method. An extensive series of quasi-static analyses has been performed, taking account of the effects of large displacements. In these analyses, the entire process of the penetration of an approximately rigid–plastic solid by a rigid conical indenter has been modelled, so that for the first time it has been possible to make an accurate assessment of the resistance due to displaced material building up around the cone. In addition, analyses have been performed with a rate-dependent material model. By a combination of analyses in which the rate of penetration was controlled and analyses in which the cone was allowed to drop freely (as in a fall-cone test) it has been possible to make a more accurate assessment of the strains and strain rates in the soil around a conical indenter, and to assess the influence that rate-dependent strength has on the results of a fall-cone test. Finally, experimental work has been undertaken to assess the extent to which the theoretical analyses give a true picture of the physical processes involved in the fall-cone test.

In this final chapter, the main findings of the research are summarized, and some proposals are made regarding the possible direction of future research in this area.

9.1 Main findings

9.1.1 Quasi-static analyses with rate-independent material

Analyses with ELFEN

An extensive series of finite element analyses of quasi-static cone indentation was conducted using the commercial finite element software ELFEN (Rockfield Software, 2005), as described in Chapter 3. The analyses involved adopting the use of an explicit dynamics approach, which differs fundamentally from the implicit time-domain integration rule which is more widely used in FE analyses for civil and geotechnical engineering. The method adopted proved to be a powerful means of analysing the problems considered in this thesis, which involved complex highly non-linear behaviour with contact between a rigid indenter and a deformable elastoplastic solid.

Thirty-eight separate combinations of cone angle β and adhesion factor α were considered in the analyses. The results of the ELFEN analyses were found to agree closely with existing solutions provided by Lockett (1963) for indentation with smooth cones with $\beta \geq 105°$. The maximum discrepancy between the new results and those of Lockett was found to be close to 1%. The area of contact predicted by the ELFEN analyses was also found to agree closely with the results given by Lockett. The numerical method adopted here was also able to provide solutions for cases with $\beta < 105°$, for which the method adopted by Lockett failed.

The vital importance of taking proper account of the displaced material around the cone was confirmed, since the bearing capacity factor N_{ch} taking account of heave around the cone was found to differ by up to 60% from the value N_{c} that would be obtained if heave were ignored (see Figure 3.21a). The influence of displaced material was greatest for large β, but the displaced material was still found to make a significant contribution to the total force on the cone in cases of interest in the fall-cone test ($\beta = 30°$ or $60°$), particularly when there was substantial adhesion between the cone and the clay – for a fully rough 30° cone, the adhesion between the displaced lip of material and the cone was found to contribute around 10% of the total force. Bearing capacity factors for cones with various angles and adhesion factors are summarised in Table 3.4.

In addition to their intended results, the ELFEN (and later Abaqus) finite element analyses offered insights into the difficulties various researchers have encountered in obtaining solutions to the cone indentation problem using the method of characteristics. For cones with $\beta < 105°$, the FE results predict that the stress state in the indented material close to the free surface, in the lip of material displaced by the penetrating cone, is not in accordance with the Haar–von Kármán hypothesis that is invariably assumed to hold when analysing indentation problems using the method of characteristics.

Analyses with Abaqus

The ELFEN results were shown to agree closely with those obtained from independent analyses with Abaqus/Explicit (Simulia, 2007). The Abaqus analyses made use of a VUMAT user material subroutine in which stress returns were performed in principal stress space, resulting in a remarkably simple and elegant algorithm described in Chapter 4 and Appendix A. In addition to successfully re-creating the ELFEN cone indentation results, the VUMAT was further validated by analysing the problem of continuous indentation with a smooth wedge, for which a theoretical solution is available that is believed to be exact (Hill et al., 1947).

The influence of boundary conditions was investigated, to determine whether the sample containers recommended by the British and Scandinavian test methods (BSI, 1990; Standard Norge, 1988) are sufficiently large to accommodate the failure mechanisms around 30° and 60° fall-cones. No problems were found to arise when the sample containers were assumed to be rough, however the smooth hemispherical cup was found to be potentially problematic for large depths of indentation. For this reason, it is important that the maximum depths of indentation recommended by Geonor (2005a) should not be exceeded. In addition, further analyses should be performed to determine whether the maximum penetration with a 60°, 10 g cone should be reduced from 20 mm to the 15 mm limit that is given for the 60 g cone.

The results of fall-cone tests on unconfined samples should not be accepted if the depth of the indentation exceeds approximately one sixth of the diameter of the sample.

9.1.2 FE analyses with rate-dependent material

Further Abaqus finite element analyses were performed in which the VUMAT material model was modified so the undrained strength s_u of the indented material depended on the maximum shear strain rate $\dot{\gamma}$. The form of variation assumed was

$$s_u = s_{u0}\left[1 + \mu \log_{10}\left(\frac{\max(\dot{\gamma}, \dot{\gamma}_{ref})}{\dot{\gamma}_{ref}}\right)\right], \tag{9.1}$$

so that two additional material parameters are required to define rate-dependent behaviour: a reference strain rate $\dot{\gamma}_{\mathrm{ref}}$, below which the material strength is equal to the "static" strength s_{u0}, and μ,the fractional increase in s_{u} that occurs for every tenfold increase in strain rate above the reference value.

Extensive analyses of displacement-controlled indentation of rate-dependent material were performed, consisting of a total of 80 analyses (40 cases were each analysed with two levels of mesh refinement). When the cones were pushed at high enough speeds for rate effects to be significant, the resistance Q encountered by the cones was found to vary linearly with the logarithm of the speed of the cone (for a given depth of indentation). This provides evidence that the deformation mechanism does not adapt significantly to compensate for the rate of penetration, as is predicted to occur in some other tests of undrained strength such as the shear vane (Einav and Randolph, 2006). This opens up the possibility that fall-cones and displacement-controlled indenters of similar geometry may be of value in allowing rapid and economical measurement of the effect of strain rate on undrained shear strength for a particular soil.

By back-analysis of the force–displacement curves for analyses with different cone speeds, it was possible to determine the speed at which rate effects began to be significant for each type of cone and therefore (since the value of the reference strain rate $\dot{\gamma}_{\mathrm{ref}}$ was known) the approximate relationship between cone speed, depth of indentation and the operative average strain rate in the plastically deforming material during a fall-cone or similar displacement-controlled test. The results are summarized in Table 5.1.

Finally, dynamic analyses of freefall cone tests in material with rate-dependent undrained shear strength were performed. The results are presented in Table 5.2, as values of the parameter $\zeta = s_{\mathrm{u0}}/s_{\mathrm{ud}}$ (introduced by Koumoto and Houlsby, 2001), which relates the static strength s_{u0} of a material to the "dynamic strength" s_{ud} it exhibits in a fall-cone test. As noted by Koumoto and Houlsby, the value of ζ can be combined with the bearing capacity factor N_{ch} to give a value for the cone factor K that was first defined by Hansbo (1957; see Equation 1.1). These K values in turn allow s_{u0} (more often simply called s_{u}) to be deduced from the fall-cone indentation depth h in a more rational and rigorous manner than has previously been possible. Example cone factors derived from the results of the FE analyses presented in this thesis can be found in Section 9.1.5.

9.1.3 Observation of cone indentation mechanisms

The experimental work described in Chapter 6 was intended to determine the patterns of plastic flow around cones indenting a real clay (Speswhite kaolin), and the results represent a partial success in achieving this goal. Some images were analysed and revealed deformation mechanisms with many similarities to those obtained from the FE analyses already described. However, the tests with 30° cones were somewhat marred by the tendency of the clay to pull away from the viewing window as a result of the tensile hoop stresses, meaning that the process being viewed could not be said to represent the desired axisymmetric situation. In addition, several tests (with both 30° and 60° cones) did not work well due to clay squeezing between the half-cone and the viewing window. An improved system for positioning the cone against the window would have helped with this aspect of the work. Some of the planned analysis of the results – for example, obtaining values of strain rate in the deforming material – proved impossible as the resolution of the images captured by the high-speed camera was insufficient to allow a sufficient number of test patches to be defined in the original image.

Despite the flaws mentioned above, the results that were presented in Chapter 6 are still believed to give some valuable insights into the areas in which the finite element analyses fall short of describing the actual behaviour of clay. In particular, the lack of a pronounced lip of displaced material around the cone in the half-cone experiments was consistent with qualitative observations in the experiments with a full fall-cone in Chapter 7. A photograph of a similar test by Hansbo (1957) seems to show a similar pattern, though the image is of very low resolution. All the finite element analyses, whatever the values selected for the adhesion factor α, showed the formation of a raised area of displaced material around the cone.

According to Larsson (2001), whether or not a lip forms is primarily a function of the rigidity of the material, as discussed in Section 2.1.3. However, although the rigidity index of the indented material was made unrealistically large in some of the Tresca FE analyses, a lip of similar size was predicted by the analysis with a Cam clay material model (with realistic material parameters) reported in Chapter 8. Also, it is difficult to see how the absence of a displaced lip around the cone can be compatible with the requirement that volume be conserved unless either the clay contains compressible air pockets or the introduced volume of the cone is accommodated by a more general distortion and upward movement of an extensive area of the indented clay. In any case, the lack of agreement between the experimental and numerically predicted failure mechanisms is a cause of concern.

9.1.4 Investigation of rate effects with a fall-cone

The experiments described in Chapter 7 provided several interesting insights into the rate dependence of the undrained strength of the Speswhite kaolin used in the laboratory, and also demonstrated some ways in which fall-cones, and displacement-controlled penetrometers of similar geometry to fall-cones, may be useful in future investigations of rate-dependent strength.

Experiments in which 30° and 60° cones were pushed into remoulded kaolin under displacement control with a sudden step-change in cone speed were carried out and proved to constitute a straightforward but effective way of investigating the response of the material to changes in strain rate. Tests were performed covering five orders of magnitude, as the cone speed v ranged from 10 mm/s to 0.1 μm/s. On the basis of the FE results shown in Table 5.1, the average shear strain rates $\dot{\gamma}_{\mathrm{ave}}$ corresponding to these values of v and the relevant depth of indentation d are of order $1 \times 10^{-5}\,\mathrm{s}^{-1}$ to $1\,\mathrm{s}^{-1}$. These are only approximate estimates as the values in Table 5.1 are dependent on the roughness of the cone. The results of these tests showed that Equation 9.1 represented the rate dependence of the kaolin well over this range of strain rates, with the factor μ generally being close to 0.1.

When values of the dynamic strength ratio parameter $\zeta = s_{\mathrm{u0}}/s_{\mathrm{ud}}$ were determined experimentally from comparisons of displacement-controlled and freefall cone tests on similar clay samples (in Section 7.3), the results were found to differ substantially from the FE prediction corresponding to $\mu = 0.1$. Instead, a lower value of ζ was obtained, suggesting that the value of μ from the displacement-controlled tests was not appropriate to represent the behaviour of the kaolin in the faster freefall tests, and that the correct value of μ was somewhat larger than 0.1.

The value of μ in the freefall tests was assessed by comparing the resistance Q in freefall and displacement-controlled tests at the same depth of indentation in similar samples of kaolin. This indicated that the correct value of μ was indeed greater than 0.1, being closer to 0.155. This result was surprising, since it had seemed reasonable to expect that the pattern of a 10% increase in strength per decade increase in strain rate, that had been found to apply over five orders of magnitude of strain rate, would continue to apply at the cone speeds in the freefall tests (in which the values of v were generally between one and two orders of magnitude greater than the maximum speed used in the displacement-controlled tests with step-changed cone speed). It therefore appears that the slope of the curve of s_u against the logarithm of strain rate does not remain constant at very high rates of strain, but (at least for the material used in these tests) increases quite markedly over the range of strain rates between $\dot{\gamma}_{\max} \approx 1\,\mathrm{s}^{-1}$ and $\dot{\gamma}_{\max} \approx 100\,\mathrm{s}^{-1}$. In this respect, the behaviour may be regarded as somewhat similar to that of a metal, as shown in Figure 2.15 for the example case of mild steel.

9.1.5 Cone factors

The indentation depth h obtained in a fall-cone test may be used to deduce the undrained shear strength s_u of the indented material, using the formula (from Equation 1.1)

$$s_u = \frac{KW}{h^2} \tag{9.2}$$

where W is the weight of the cone and K is the cone factor, as proposed by Hansbo (1957).

According to Koumoto and Houlsby (2001), the correct value of K (accounting for both surface heave and rate-dependent strength) can be obtained from Equation 1.5:

$$K = \frac{s_{u0}h^2}{W} = \frac{3\zeta}{F} = \frac{3\zeta}{\pi N_{ch}\tan^2(\beta/2)}. \tag{9.3}$$

The FE analyses reported in this thesis have given accurate numerical values of N_{ch} and ζ, and using these in the above equation allows K to be determined for a given cone angle, adhesion factor and value of μ. The value of N_{ch}, which can be obtained from Table 3.4, is dependent on the cone angle β and adhesion factor α. The value of ζ, which can be found in Table 5.2, depends on the rate dependence parameter μ of the indented material.

Values of K obtained from the numerical results in this thesis are shown in Figures 9.1a (for smooth cones) and 9.1b (for rough cones). The various curves illustrate the cone factors that would be appropriate for materials with different values of μ. Although the values of K are lower for rough cones than for smooth, the degree of uncertainty that is caused by an unknown value of μ is similar for all values of α and β. As an example, values of K for $\mu = 0$ are approximately 2.4 times greater than those for $\mu = 0.2$, across the full range of α and β.

It is interesting to examine the practical significance of this finding with reference to a specific example. If the depth of indentation in a fall-cone test with a 30°, 100 g cone was found to be 10 mm, and the adhesion factor α was taken to be equal to 0.5, then using Equation 9.2 with the numerically-derived K-value for a rate-independent material would give $s_u = 16.4$ kPa. If in fact the material was strongly rate-dependent, with $\mu = 0.2$, the correct interpretation of the test result, using the cone factor given by Equation 1.5 with the appropriate numerical values of N_{ch} and ζ, would give $s_u = 6.9$ kPa. Use of the rate-independent cone factor would have given a non-conservative error of 138%. The above example represents a worst-case scenario, as in reality most materials appear to exhibit rate-dependent strength with $\mu \approx 0.1$.

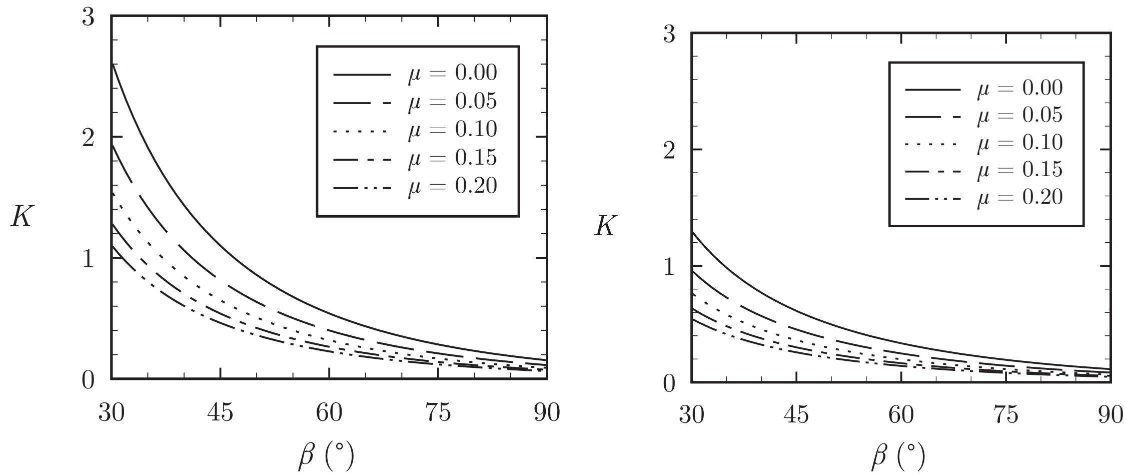

(a) Smooth cones ($\alpha = 0.0$)

(b) Rough cones ($\alpha = 1.0$)

Figure 9.1: Values of the cone factor K derived from the numerical results in this thesis

Various researchers have published experimentally-derived value of the cone factor K. The original tests by Hansbo (1957), which were discussed in Section 1.1.2, gave values of K for a 30° cone of either 0.8 or 1.0 for (nominally) undisturbed samples, with the choice of value depending on the type of sampler used (and therefore the degree of sample disturbance). For 60° cones, values between 0.2 and 0.25 were given for undisturbed samples, and a value for remoulded samples was also given (0.3). Later experiments by Karlsson (1961) obtained values of K that varied between 0.7 and 0.86 for the 30° cone and between 0.25 and 0.35 for the 60° cone.[1] Further experiments by Wood (1985) gave $K = 0.85$ for the 30° cone and $K = 0.29$ for the 60° cone. He also investigated the use of 45° and 75° cones, for which he obtained values of $K = 0.45$ and 0.19 respectively.

Previous attempts to derive theoretical values for K have generally given values that are

[1] It is generally accepted that the results of Karlsson (1961) were reported as too low by a factor of 10 in the original paper (Koumoto and Houlsby, 2001). Corrected values have been used here.

in excess of those obtained experimentally – see, for example, Koumoto and Houlsby (2001). The values of K given by the present numerical analyses (for the case $\mu = 0.1$) are compared with the experimental results of earlier researchers in Figure 9.2.

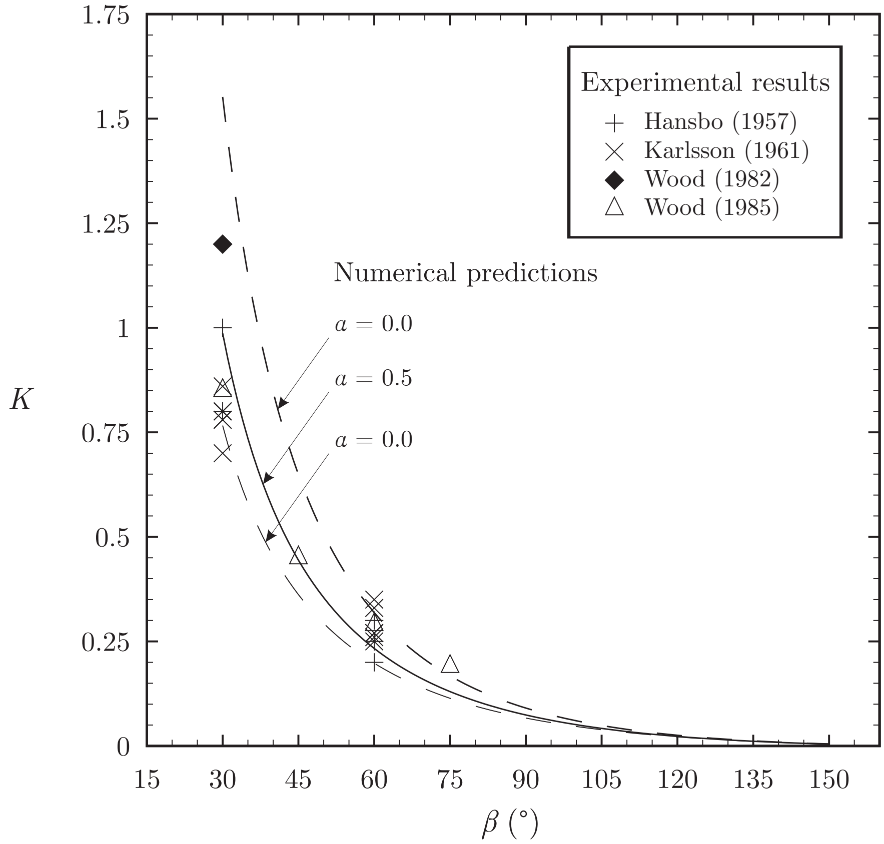

Figure 9.2: Variation of cone factor K with cone angle β: experimental results and numerical analyses with $\mu = 0.1$

In general, there is good agreement between the numerical and experimental results. In particular, the experimental cone factors for 30° cones generally lie in the range given by the numerical analyses for adhesion factors between 0.0 and 0.5. Koumoto and Houlsby (2001) found that their theoretical results did not agree particularly well with experiments for the 30° cone, and the numerical analyses reported here suggest that this lack of agreement was largely due to an underestimation of the role played by rate-dependence.

It is thought that at least two of the experimental K values shown in Figure 9.2 may be higher than they should be due to failing to take adequate account of the effect of strain rate on s_u. In describing his experiments on remoulded clay, Hansbo (1957) states that he found it necessary to rotate the shear vane "considerably more quickly" than usual. This would have resulted in vane readings that were excessively high due to rate effects (which may be considerable in vane tests, see Einav and Randolph, 2006). The value reported by

Wood (1982) was derived by extrapolating from Hansbo's result for a 60° cone in remoulded material, so its accuracy must also be in doubt.

9.2 Suggested future research

A long-standing barrier to the use of the method of characteristics to obtain plasticity solutions for conical indenters with $\beta < 105°$ has been uncertainty as to the form that the mesh of characteristics should take. The quasi-static analyses reported in Chapter 3 have provided clues that may allow the development of solutions in these cases, if a suitable analytical strategy can be developed for dealing with the part of the deforming region in which the Haar–von Kármán hypothesis is not applicable. It is hoped that this is one area in which the work reported here may be of value to future researchers.

The numerical and experimental results presented here strongly suggest that the geometry of the deformation mechanism around a conical indenter is influenced very little, if at all, by the speed at which the cone is pushed into the indented material. This was seen to be the case even when the strength of the indented material was strongly rate-dependent ($\mu = 0.2$). This finding implies that the relationship between the resistance encountered by the cone and its speed has the same form as the relationship between the material strength and the rate of strain, and means that Q–v curves from indentation experiments can be readily interpreted to give information about the fundamental rate-dependent shear strength behaviour of a material. The fall-cone, or a similar displacement-controlled device, may therefore offer the basis for a convenient method of further investigating the phenomenon of rate-dependent strength. The tests reported in Chapter 7 offer examples of how such tests might be carried out.

The experiments to observe deformation mechanisms around cones, which were reported in Chapter 6, were felt to be not entirely satisfactory. Undertaking tests of this type with clays (rather than coarse-grained sands) requires that very careful thought be given to the means by which the cone is positioned against the viewing window during the test. It is felt that a more satisfactory system might be found if the cone could be held against the window by a slight horizontal preload, and allowed to rotate in the plane perpendicular to the glass such that the mounting arrangement would be made self-aligning. This could allow the layer of rubber used in these tests (or the 'O'-ring used by Hossain et al., 2005) to be dispensed with, with the potential to give a more realistic representation of plastic flow in clay close to the metal surface of a cone, model foundation, or similar object. The problem of tensile hoop stresses causing clay to pull away from the viewing window would be more difficult to overcome.

One factor that is believed to influence the results of fall-cone tests was not considered in this thesis: the influence of strain-softening behaviour. Although this is not a factor in tests on remoulded clay, fall-cone tests are occasionally performed on undisturbed samples recovered from boreholes (though today in-situ tests using the piezocone are more common). There is scope for further numerical analyses to be carried out using a material model that is capable of accounting for this factor as well as rate effects. As demonstrated by Zhou and Randolph (2007), this can be done successfully by a further extension of the simple Tresca model for undrained material behaviour.

The implementation of a constitutive model that integrates viscoplastic rate effects with the effect of pore water flow, using the effective stress concept, would be of great value in advancing the work begun in Chapter 8. This would allow all the effects that are believed to influence indentation tests in clays to be integrated in a single numerical model, and would also allow the drainage conditions in displacement-controlled tests with step-changed cone speeds to be explored more fully than has been possible thus far.

Appendices

Appendix A

Stress returns in Tresca VUMAT

This appendix gives further details of the stress return algorithm used in the VUMAT material behaviour subroutine described in Chapter 4, which was used with the FE software Abaqus in carrying out the analyses described in this thesis.

As described in Chapter 5, the code was later modified so that the strength s_u of the material could be made to be dependent on the effective strain rate $\dot{\bar{\varepsilon}}$. This adaptation will also be described here.

The source code of the VUMAT is given in Appendix B.

Return algorithm

The VUMAT must determine the updated stress $\boldsymbol{\sigma}^\mathrm{C}$ at the end of the current increment, given the stress at the start of the increment $\boldsymbol{\sigma}^\mathrm{A}$ and the strain increment $\Delta\boldsymbol{\varepsilon}$ to be applied.

Before the main stress return calculation, rate dependent strength is implemented if required. The shear strain increment $\Delta\gamma$ is calculated from the components of the strain tensor $\Delta\boldsymbol{\varepsilon}$, then divided by the time interval Δt to give the effective shear strain rate $\dot{\gamma}$. This value is then used to obtain the shear strength at the current strain rate, using the relationship

$$s_\mathrm{u} = s_\mathrm{u0}\left[1 + \mu \log_{10}\left(\frac{\max\left(\dot{\gamma}, \dot{\gamma}_0\right)}{\dot{\gamma}_0}\right)\right], \tag{A.1}$$

where $\dot{\gamma}_0$ is a reference strain rate, s_u0 is the strength at the reference strain rate and μ is the relative increase in strength that accompanies a tenfold increase in strain rate. If a rate-independent analysis is being performed, this stage is omitted as a constant value of $s_\mathrm{u} = s_\mathrm{u0}$ is used.

To perform the stress return itself, an elastic trial stress $\boldsymbol{\sigma}^\mathrm{B}$ is first obtained, from $\boldsymbol{\sigma}^\mathrm{B} =$

$\boldsymbol{\sigma}^{\mathrm{A}} + \mathbf{D}\Delta\boldsymbol{\varepsilon}$ where $\mathbf{D}$ is the elastic constitutive matrix. If $\boldsymbol{\sigma}^{\mathrm{B}}$ lies outside the yield surface a plastic corrector $-\Delta\boldsymbol{\sigma}^{\mathrm{p}}$ must be found so that $\boldsymbol{\sigma}^{\mathrm{C}} = \boldsymbol{\sigma}^{\mathrm{B}} - \Delta\boldsymbol{\sigma}^{\mathrm{p}}$ lies on the yield surface.

The algorithm used to achieve this is shown in Table A.1. Note that $\boldsymbol{\sigma}'^{\mathrm{A}}$, $\boldsymbol{\sigma}'^{\mathrm{B}}$ and $\boldsymbol{\sigma}'^{\mathrm{C}}$ are stresses in the original coordinate system, while $\boldsymbol{\sigma}^{\mathrm{A}}$, $\boldsymbol{\sigma}^{\mathrm{B}}$ and $\boldsymbol{\sigma}^{\mathrm{C}}$ are in principal stress space. In general, the transformation may be described by a matrix $\mathbf{R}$ so that $\boldsymbol{\sigma}^{\mathrm{A}} = \mathbf{R}\boldsymbol{\sigma}'^{\mathrm{A}}$, for example.

In those cases where the elastic trial stress $\boldsymbol{\sigma}^{\mathrm{B}}$ is outside the yield surface, the stress return required is determined based on the values of the yield function, as described in Section 4.1.5. In cases 1 to 3 (as defined in Table A.1), stresses are returned to one of the planes that make up the yield surface (S_1, S_4 or S_6 in Figure 4.3). In these cases, the plastic corrector $\Delta\boldsymbol{\sigma}^{\mathrm{p}}$ is determined by multiplying a 3×1 vector $\mathbf{A}_i$ by the value of the relevant yield function. In cases 4 to 7, stresses are returned to one of the corners of the yield surface (L_{45}, L_{14}, L_{61} or L_{36} in Figure 4.3), and the values of $\Delta\boldsymbol{\sigma}^{\mathrm{p}}$ are given by the product of a 3×2 matrix $\mathbf{A}_{ij}$ with a vector containing the values of the two yield functions active at the corner. The value of the multiplier needed to obtain the corrector increment from the yield function(s) in each case is given in Table A.2.

Transformation of stresses

To implement the return algorithm described above, the stresses received as inputs to the material subroutine must be transformed to principal stress space, and eventually restored to the original coordinate system. If the analysis is plane strain or axisymmetric, the out-of-plane stress will be one of the principal stresses. The other two principal stresses will depend on the in-plane stresses.

The Mohr's circle in Figure A.1 represents the in-plane stress state. The direct stresses in the original coordinate system (as supplied to the VUMAT by Abaqus) are σ_x and σ_y (direct stresses) and $\tau_{yx} = -\tau_{xy}$ (the clockwise shear stresses). Note that it is not possible to say that σ_x is horizontal and σ_y vertical (for example) because stresses are passed to the VUMAT in coordinates whose basis system rotates with the material. The principal stresses are

$$\sigma_1 = s + R \tag{A.2}$$

$$\sigma_2 = s - R \tag{A.3}$$

Table A.1: Algorithm for stress return in Tresca VUMAT

Tresca VUMAT Algorithm

Input: $\boldsymbol{\sigma}'^{\mathrm{A}}$, $\Delta\boldsymbol{\varepsilon}$, Δt, $\mathbf{D}$, s_{u0} (and, for rate-dependent analyses, μ and $\dot{\bar{\varepsilon}}_0$)
Output: $\boldsymbol{\sigma}'^{\mathrm{C}}$

$\boldsymbol{\sigma}'^{\mathrm{B}} \leftarrow \boldsymbol{\sigma}'^{\mathrm{A}} + \mathbf{D}\Delta\boldsymbol{\varepsilon}$
$\boldsymbol{\sigma}^{\mathrm{B}} \leftarrow \mathbf{R}\boldsymbol{\sigma}'^{\mathrm{B}}$ {Transform to principal stress space}
if rate-dependence requested **then**
  $s_{\mathrm{u}} = s_{\mathrm{u0}}\left[1 + \mu \log_{10}\left(\frac{\max(\dot{\bar{\varepsilon}}, \dot{\bar{\varepsilon}}_0)}{\dot{\bar{\varepsilon}}_0}\right)\right]$
else
  $s_{\mathrm{u}} = s_{\mathrm{u0}}$
end if
$f_1 \leftarrow \sigma_1^{\mathrm{B}} - \sigma_2^{\mathrm{B}} - 2s_{\mathrm{u}}$
$f_2 \leftarrow \sigma_2^{\mathrm{B}} - \sigma_1^{\mathrm{B}} - 2s_{\mathrm{u}}$
$f_3 \leftarrow \sigma_2^{\mathrm{B}} - \sigma_3^{\mathrm{B}} - 2s_{\mathrm{u}}$
$f_4 \leftarrow \sigma_3^{\mathrm{B}} - \sigma_2^{\mathrm{B}} - 2s_{\mathrm{u}}$
$f_5 \leftarrow \sigma_3^{\mathrm{B}} - \sigma_1^{\mathrm{B}} - 2s_{\mathrm{u}}$
$f_6 \leftarrow \sigma_1^{\mathrm{B}} - \sigma_3^{\mathrm{B}} - 2s_{\mathrm{u}}$
if $\max(f_1, f_2, f_3, f_4, f_5, f_6) < 0$ **then** {Case 0: elastic, no stress return}
  $\boldsymbol{\sigma}^{\mathrm{C}} \leftarrow \boldsymbol{\sigma}^{\mathrm{B}}$
else if $f_1 \geq 2f_4$ **and** $f_1 \geq 2f_6$ **then** {Case 1: stress return to plane S_1}
  $\boldsymbol{\sigma}^{\mathrm{C}} \leftarrow \boldsymbol{\sigma}^{\mathrm{B}} - \mathbf{A}_1 f_1$
else if $f_4 \geq 2f_1$ **and** $f_4 \geq 2f_5$ **then** {Case 2: stress return to plane S_4}
  $\boldsymbol{\sigma}^{\mathrm{C}} \leftarrow \boldsymbol{\sigma}^{\mathrm{B}} - \mathbf{A}_4 f_4$
else if $f_6 \geq 2f_1$ **and** $f_6 \geq 2f_3$ **then** {Case 3: stress return to plane S_6}
  $\boldsymbol{\sigma}^{\mathrm{C}} \leftarrow \boldsymbol{\sigma}^{\mathrm{B}} - \mathbf{A}_6 f_6$
else if $f_6 < 2f_3$ **then** {Case 4: stress return to line L_{36}}
  $\boldsymbol{\sigma}^{\mathrm{C}} \leftarrow \boldsymbol{\sigma}^{\mathrm{B}} - \mathbf{A}_{36}\,[f_3\ f_6]^{\mathrm{T}}$
else if $f_1 < 2f_6$ **and** $f_6 < 2f_1$ **then** {Case 5: stress return to line L_{61}}
  $\boldsymbol{\sigma}^{\mathrm{C}} \leftarrow \boldsymbol{\sigma}^{\mathrm{B}} - \mathbf{A}_{16}\,[f_1,\ f_6]^{\mathrm{T}}$
else if $f_1 < 2f_4$ **and** $f_4 < 2f_1$ **then** {Case 6: stress return to line L_{14}}
  $\boldsymbol{\sigma}^{\mathrm{C}} \leftarrow \boldsymbol{\sigma}^{\mathrm{B}} - \mathbf{A}_{14}\,[f_1,\ f_4]^{\mathrm{T}}$
else if $f_4 < 2f_5$ **then** {Case 7: stress return to line L_{45}}
  $\boldsymbol{\sigma}^{\mathrm{C}} \leftarrow \boldsymbol{\sigma}^{\mathrm{B}} - \mathbf{A}_{45}\,[f_4,\ f_5]^{\mathrm{T}}$
end if
$\boldsymbol{\sigma}'^{\mathrm{C}} \leftarrow \mathbf{R}^{-1}\boldsymbol{\sigma}^{\mathrm{C}}$ {Transform back to original coordinates}
return $\boldsymbol{\sigma}'^{\mathrm{C}}$

Table A.2: Values of the multiplier **A** used to obtain $\Delta\boldsymbol{\sigma}^{\mathrm{p}}$ from yield function values for each of the cases in the algorithm of Table A.1

Case	Return to...	**A**
(0)	(N/A)	(0)
1	S_1	$\begin{bmatrix} \frac{1}{2} \\ -\frac{1}{2} \\ 0 \end{bmatrix}$
2	S_4	$\begin{bmatrix} 0 \\ -\frac{1}{2} \\ \frac{1}{2} \end{bmatrix}$
3	S_6	$\begin{bmatrix} \frac{1}{2} \\ 0 \\ -\frac{1}{2} \end{bmatrix}$
4	L_{36}	$\begin{bmatrix} -\frac{1}{3} & \frac{2}{3} \\ \frac{2}{3} & -\frac{1}{3} \\ -\frac{1}{3} & -\frac{1}{3} \end{bmatrix}$
5	L_{61}	$\begin{bmatrix} \frac{1}{3} & \frac{1}{3} \\ -\frac{2}{3} & \frac{1}{3} \\ \frac{1}{3} & -\frac{2}{3} \end{bmatrix}$
6	L_{14}	$\begin{bmatrix} \frac{2}{3} & -\frac{1}{3} \\ -\frac{1}{3} & -\frac{1}{3} \\ -\frac{1}{3} & \frac{2}{3} \end{bmatrix}$
7	L_{45}	$\begin{bmatrix} \frac{1}{3} & -\frac{2}{3} \\ -\frac{2}{3} & \frac{1}{3} \\ \frac{1}{3} & \frac{1}{3} \end{bmatrix}$

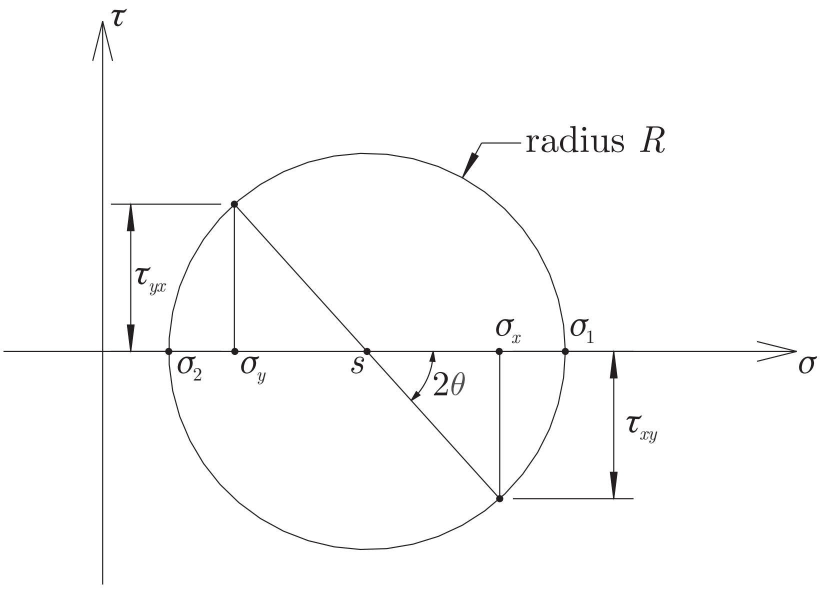

Figure A.1: Mohr circle for obtaining in-plane principal stresses

where $s = \frac{1}{2}\left(\sigma_x + \sigma_y\right)$ is the mean in-plane stress and R is the radius of the Mohr circle, given by

$$R = \sqrt{\frac{1}{4}\left(\sigma_x - \sigma_y\right)^2 + \left(\tau_{yx}\right)^2}. \tag{A.4}$$

The last principal stress is simply $\sigma_3 = \sigma_z$, which in axisymmetry is the hoop stress. The angle 2θ, which is needed to return the stresses to the original coordinates, can be found as

$$2\theta = \arctan\left(\frac{\tau_{yx}}{\frac{1}{2}\left(\sigma_x - \sigma_y\right)}\right), \quad 0 < \theta < \frac{\pi}{4}. \tag{A.5}$$

Once the principal stresses at the end of the increment have been determined using the algorithm of Table A.1, stresses can be restored to the original coordinate system as follows:

$$\sigma_x = \frac{1}{2}\left(\sigma_1 + \sigma_2\right) + \frac{1}{2}\left(\sigma_1 - \sigma_2\right)\cos\left(2\theta\right) \tag{A.6}$$

$$\sigma_y = \frac{1}{2}\left(\sigma_1 + \sigma_2\right) - \frac{1}{2}\left(\sigma_1 - \sigma_2\right)\cos\left(2\theta\right) \tag{A.7}$$

$$\sigma_z = \sigma_3 \tag{A.8}$$

$$\tau_{xy} = -\frac{1}{2}\left(\sigma_2 - \sigma_1\right)\sin\left(2\theta\right). \tag{A.9}$$

Appendix B

Tresca VUMAT source code

The Fortran 95 source code for the Abaqus user material subroutine described in Chapter 4 and Appendix A is included below.

```
!DEC$ FREEFORM
!
! NOTE: vaba_param.inc
! Inclusion of 'vaba_param.inc' is required for all VUMATs. It necessitates the
! use of implicit variable typing i.e. all variables with names starting with
! letters i to n inclusive are integers. In addition (and more usefully) floats
! are double or single precision as appropriate for the analysis.
!
! NOTE: Subroutine names
! Names of additional subroutines begin with the letter 'k' to avoid conflicts
! (as advised in ABAQUS documentation).
!
subroutine vumat(                                                          &
! ************************* ABAQUS VARIABLES ************************
! ** Read only (unmodifiable) variables **
  nblock, ndir, nshr, nstatev, nfieldv, nprops, lanneal,                   &
  stepTime, totalTime, dt, cmname, coordMp, charLength,                    &
  props, density, strainInc, relSpinInc,                                   &
  tempOld, stretchOld, defgradOld, fieldOld,                               &
  stressOld, stateOld, enerInternOld, enerInelasOld,                       &
  tempNew, stretchNew, defgradNew, fieldNew,                               &
! ** Write only (modifiable) variables **
  stressNew, stateNew, enerInternNew, enerInelasNew )
!
include 'vaba_param.inc'
!
dimension props(nprops), density(nblock), coordMp(nblock,*),               &
  charLength(nblock), strainInc(nblock,ndir+nshr),                         &
  relSpinInc(nblock,nshr), tempOld(nblock),                                &
  stretchOld(nblock,ndir+nshr),                                            &
  defgradOld(nblock,ndir+nshr+nshr),                                       &
  fieldOld(nblock,nfieldv), stressOld(nblock,ndir+nshr),                   &
  stateOld(nblock,nstatev), enerInternOld(nblock),                         &
  enerInelasOld(nblock), tempNew(nblock),                                  &
  stretchNew(nblock,ndir+nshr),                                            &
  defgradNew(nblock,ndir+nshr+nshr),                                       &
  fieldNew(nblock,nfieldv),                                                &
  stressNew(nblock,ndir+nshr), stateNew(nblock,nstatev),                   &
  enerInternNew(nblock), enerInelasNew(nblock)
!
character*80 cmname
!
! ************************* MY VARIABLES ************************
!
integer :: block_count
```

```
!
dimension DElas(4,4),       &
     stressNewInt(4,1),     &
     strainIncInt(4,1),     &
     strPr(3,1),            &
     a1(3,1), a2(3,2),      &
     dStressPlas(3,1)
! *****************************************************************
!
! ** Check ndir and nshr are consistent with 2D or axisymmetry.
!    Should have ndir=3 and nshr=1.
!
if ((ndir .ne. 3) .or. (nshr .ne. 1)) then
  call xplb_abqerr(-2,'VUMAT␣for␣use␣with␣2D␣models␣only.',0,0.0,'␣')
  call xplb_exit
end if
!
! ** Construct elastic stiffness matrix
!
E = props(1)
v = props(2)
!
tempOne = 1.0D0 - v
tempTwo = 1.0D0 - 2.0D0*v
!
DElas(1,1:4) = (/  tempOne,        v,         v,          0.0D0 /)
DElas(2,1:4) = (/        v,  tempOne,         v,          0.0D0 /)
DElas(3,1:4) = (/        v,        v,   tempOne,          0.0D0 /)
DElas(4,1:4) = (/    0.0D0,    0.0D0,     0.0D0, 0.5D0*tempTwo /)
!
DElas = ( E/((1.0D0+v)*(tempTwo)) ) * DElas
!
!************Begin main loop************
!
do 100 block_count = 1,nblock
  !
  ! Use engineering shear strain
  strainIncInt( 1:4, 1 ) = 2.0D0 * strainInc( block_count, 1:4 )
  !
  ! Adjust strength to account for strain rate, depending on flag props(6).
  call k_setStrength(c,props(3),props(5),props(4),props(6),effStrainRate,   &
    effStrainInc,strainIncInt,dt)
  !
  ! Elastic predictor stress
  stressNewInt = stressOld( block_count, 1:4 ) + matmul(DElas,strainIncInt)
  !
  ! Principal values of elastic trial stress
  stressMean = 0.5D0 * ( stressNewInt(1,1) + stressNewInt(2,1) )
  RMohr = sqrt((0.5D0*(stressNewInt(1,1) - stressNewInt(2,1)))**2         &
           + (stressNewInt(4,1))**2)
  !
  strPr(1,1) = stressMean + RMohr
  strPr(2,1) = stressMean - RMohr
  strPr(3,1) = stressNewInt(3,1)
  twoTheta = atan2( stressNewInt(4,1), 0.5D0*(stressNewInt(1,1)            &
             - stressNewInt(2,1)) )
  !
  ! Evaluate yield functions
  tempOne = 2.0D0 * c
  f1 = strPr(1,1) - strPr(2,1) - tempOne
  f2 = strPr(2,1) - strPr(1,1) - tempOne
  f3 = strPr(2,1) - strPr(3,1) - tempOne
  f4 = strPr(3,1) - strPr(2,1) - tempOne
  f5 = strPr(3,1) - strPr(1,1) - tempOne
  f6 = strPr(1,1) - strPr(3,1) - tempOne
  !
  ! Now act depending on yield function values...
  if ( (max(f1,f2,f3,f4,f5,f6) <= 0.0D0) .OR. (totalTime == 0.0D0)) then
    ! ** ELASTIC
    ! NB: must be elastic when called for data check, to give initial elastic
    ! wave speed.
    ! No action needs to be taken -- strPr is already correct!
    !
  else if ( (f1 >= 2.0D0*f4) .AND. (f1 >= 2.0D0*f6) ) then
```

```
    ! ** Return to single surface (1)
    a1(1:3,1) = (/ -0.5D0, 0.5D0, 0.0D0 /)
    strPr = strPr + a1*f1
    !
  else if ( (f4 >= 2.0D0*f1) .AND. (f4 >= 2.0D0*f5) ) then
    ! ** Return to single surface (4)
    a1(1:3,1) = (/ 0.0D0, 0.5D0, -0.5D0 /)
    strPr = strPr + a1*f4
    !
  else if ( (f6 >= 2.0D0*f1) .AND. (f6 >= 2.0D0*f3) ) then
    ! ** Return to single surface (6)
    a1(1:3,1) = (/ -0.5D0, 0.0D0, 0.5D0 /)
    strPr = strPr + a1*f6
    !
  else if (f6 < 2.0D0*f3) then
    ! ** Return to line (6/3)
    a2(1:3,1) = (/  1.0D0/3.0D0, -2.0D0/3.0D0, 1.0D0/3.0D0 /)
    a2(1:3,2) = (/ -2.0D0/3.0D0,  1.0D0/3.0D0, 1.0D0/3.0D0 /)
    strPr = strPr + matmul( a2, reshape( (/ f3, f6 /),(/ 2, 1 /) ) )
    !
  else if ( (f1 < 2.0D0*f6) .AND. (f6 < 2.0D0*f1) ) then
    ! ** Return to line (1/6)
    a2(1:3,1) = (/ -1.0D0/3.0D0,  2.0D0/3.0D0, -1.0D0/3.0D0 /)
    a2(1:3,2) = (/ -1.0D0/3.0D0, -1.0D0/3.0D0,  2.0D0/3.0D0 /)
    strPr = strPr + matmul( a2, reshape( (/ f1, f6 /),(/ 2, 1 /) ) )
    !
  else if ( (f1 < 2.0D0*f4) .AND. (f4 < 2.0D0*f1) ) then
    ! **  Return to line (4/1)
    a2(1:3,1) = (/ -2.0D0/3.0D0,  1.0D0/3.0D0,  1.0D0/3.0D0 /)
    a2(1:3,2) = (/  1.0D0/3.0D0,  1.0D0/3.0D0, -2.0D0/3.0D0 /)
    strPr = strPr + matmul( a2, reshape( (/ f1, f4 /),(/ 2, 1 /) ) )
    !
  else if (f4 < 2.0D0*f5) then
    ! **  Return to line (5/4)
    a2(1:3,1) = (/ -1.0D0/3.0D0,  2.0D0/3.0D0, -1.0D0/3.0D0 /)
    a2(1:3,2) = (/  2.0D0/3.0D0, -1.0D0/3.0D0, -1.0D0/3.0D0 /)
    strPr = strPr + matmul( a2, reshape( (/ f4, f5 /),(/ 2, 1 /) ) )
    !
  else
    ! ** ERROR - default case
    call xplb_abqerr(-2,'Default␣case␣reached␣in␣main␣"if"␣statement.',0,0.0,'␣')
    call xplb_exit
  end if
  !
  ! ** Transform principal stresses back to Cartesian
  twoTheta = -twoTheta
  stressMean = 0.5D0*(strPr(1,1) + strPr(2,1))
  offset  = 0.5D0*(strPr(1,1) - strPr(2,1)) * cos(twoTheta)
  stressNewInt(1,1) = stressMean + offset
  stressNewInt(2,1) = stressMean - offset
  stressNewInt(3,1) = strPr(3,1)
  stressNewInt(4,1) = 0.5D0*(strPr(2,1) - strPr(1,1)) * sin(twoTheta)
  !
  ! ** Prepare output
  stressNew( block_count , 1:4 ) = stressNewInt( 1:4, 1 )
  stateNew(  block_count , 1 ) = effStrainRate
  !
100 continue
!************End main loop************
!
end subroutine vumat
!
!*****************************************************************************************
!
subroutine k_setStrength(c,c0,r_mu,refStrainRate,rateSwitch,effStrainRate,  &
    effStrainInc,strainIncInt,dt)
!
! Subroutine to determine the effective strain rate and implement rate
! dependence if necessary.
! NB: Called even if rateSwitch=0 to get effStrainRate for output.
include 'vaba_param.inc'
dimension strainIncInt(4,1)
!
strainMean = 0.5D0*(strainIncInt(1,1) + strainIncInt(2,1))
```

```
RMohr = 0.5D0*sqrt( (strainIncInt(1,1) - strainIncInt(2,1))**2              &
        + (strainIncInt(4,1))**2 )
princStrainInc1 = strainMean + RMohr
princStrainInc2 = strainMean - RMohr
princStrainInc3 = strainIncInt(3,1)
!
! Find max shear strain as used by e.g. Randolph and Zhou
effStrainInc = 0.5D0*( abs(princStrainInc1 - princStrainInc2)               &
           + abs(princStrainInc2 - princStrainInc3)                         &
           + abs(princStrainInc3 - princStrainInc1) )
effStrainRate = effStrainInc / dt
if ( rateSwitch < 0.5) then
  c = c0
else
  ! log form
  c = c0*( 1.0D0 + r_mu*log10( ( max( effStrainRate, refStrainRate ) )     &
      / refStrainRate ) )
  ! arcsinh form
  ! NB: asinh(x) = log_n( x + sqrt(x**2 + 1.))
  !c = c0 * ( 1.0D0 + (r_mu/log(10.0D0))*log( (effStrainRate/refStrainRate)&
  !  + sqrt( (effStrainRate/refStrainRate)**2 + 1.0D0 ) ) )
end if
!
end subroutine k_setStrength
```

Appendix C

Calculation of strains from displacements

Parts of the work in this thesis involve processing data on the displacements at discrete points to give the rotations, strains etc. of the underlying material. The displacements may be from PIV analysis of experimental results, numerical integration of velocities from analytical plasticity solutions, or finite element analyses. The process for obtaining strains from displacements follows that described by White (2002).

In general, the displacements in two dimensions are represented as a grid of displacement vectors at each time step. This grid can be subdvided into triangular constant-strain elements with three nodes, as shown in Figure C.1. (X, Y) is the global coordinate system (non-rotating), and (x, y) is the local coordinate system in the frame of reference of the element (rotating). The displacements of the three markers forming the nodes of an element can be used to determine the displacement gradient matrix $\mathbf{L}$, using shape functions (e.g. Zienkiewicz, 1967, pp26–28), and hence the deformation gradient matrix can be found:

$$\mathbf{F} = \begin{bmatrix} \frac{\partial x}{\partial X} & \frac{\partial x}{\partial Y} \\ \frac{\partial y}{\partial X} & \frac{\partial y}{\partial Y} \end{bmatrix} = \mathbf{L} + \mathbf{I} = \begin{bmatrix} \frac{\partial u}{\partial X} & \frac{\partial u}{\partial Y} \\ \frac{\partial v}{\partial X} & \frac{\partial v}{\partial Y} \end{bmatrix} + \begin{bmatrix} 1 & 0 \\ 0 & 1 \end{bmatrix} \tag{C.1}$$

$\mathbf{F}$ represents the transformation of a vector from undeformed coordinates x, y to deformed coordinates x', y', as $[x', y']^{\mathrm{T}} = \mathbf{F}\,[x, y]^{\mathrm{T}}$. Where a series of displacements are applied incrementally, the deformation gradient $\mathbf{F}^n$ at increment n can be obtained by multiplying together the matrices for previous increments. So, after n increments $\mathbf{F}^n = (\mathbf{L}^n + \mathbf{I})\mathbf{F}^{n-1}$.

The deformation can be separated into strain and rotation by polar decomposition, as de-

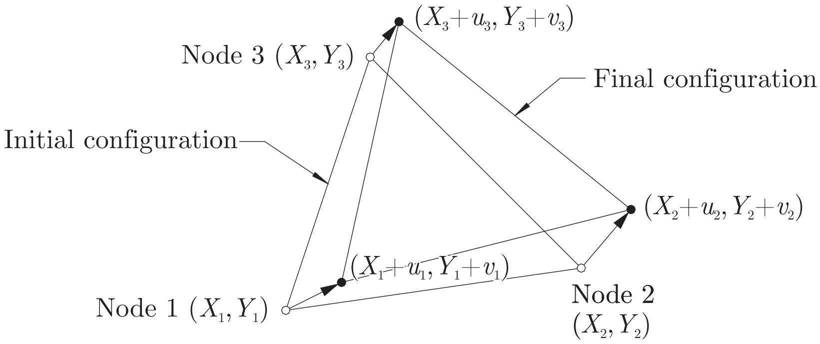

Figure C.1: Triangular element in original and deformed configurations

scribed in standard texts on continuum mechanics (e.g. Mase, 1970). The symmetric stretch matrix $\mathbf{U}$ represents strains, and the anti-symmetric matrix $\mathbf{R}$ gives rotations; $\mathbf{F} = \mathbf{RU}$. Since $\mathbf{R}^{\mathrm{T}}\mathbf{R} = \mathbf{I}$, the decomposition can be performed as follows:

$$\mathbf{U} = \left(\mathbf{F}^{\mathrm{T}}\mathbf{F}\right)^{1/2} \tag{C.2}$$

$$\mathbf{R} = \mathbf{F}\mathbf{U}^{-1} \tag{C.3}$$

The first element of $\mathbf{R}$ is equal to $\cos(\theta)$, allowing the rotation at a point to be determined. Familiar strain quantities can easily be recovered from the stretch matrix. For example, the in-plane engineering shear strain γ_{xy} is the sum of the off-diagonal elements. Volumetric strains were calculated directly from the nodal coordinates.

Bibliography

Abbo, A. J. and Sloan, S. W. (1995). A smooth hyperbolic approximation to the Mohr–Coulomb yield criterion. *Computers and Structures*, 54(3):427–441.

Al-Tabbaa, A. and Wood, D. M. (1987). Some measurements of the permeability of kaolin. *Géotechnique*, 37(4):499–503.

Astley, R. J. (1992). *Finite elements in solids and structures: an introduction*. Chapman and Hall, London.

Atkinson, J. H. and Bransby, P. L. (1978). *The Mechanics of Soils*. McGraw–Hill, London.

Bauwens-Crowet, C., Bauwens, J. C., and Homes, G. (1969). Tensile yield-stress behavior of glassy polymers. *Journal of Polymer Science Part A-2: Polymer Physics*, 7(4):735–742.

Berre, T. and Bjerrum, L. (1973). Shear strength of normally consolidated clays. In *Proc. 8th International Conference on Soil Mechanics and Foundation Engineering*, volume 1, pages 39–49, Moscow.

Bhattacharya, A. K. and Nix, W. D. (1988). Finite element simulation of indentation experiments. *International Journal of Solids and Structures*, 24(9):881–891.

Bhattacharya, A. K. and Nix, W. D. (1991). Finite element analysis of cone indentation. *International Journal of Solids and Structures*, 27(8):1047–1058.

Bingham, E. C. (1922). *Fluidity and Plasticity*. McGraw–Hill, New York.

Blatt, F. J. (1992). *Modern Physics*. McGraw–Hill, New York.

Bowden, R. K. (1988). *Compression behaviour and shear strength characteristics of a natural silty clay sedimented in the laboratory*. DPhil thesis, University of Oxford.

Brooke Ocean Technology Ltd. (2004). Free fall cone penetrometer. Brochure FFCPT–0404, ODIM Brooke Ocean, Dartmouth, Nova Scotia.

Brouwer, J.-J. M. (2008). *In-Situ Soil Testing*. Lankelma, Iden, East Sussex. Retrieved September 2008, `http://www.conepenetration.com/online-book/piezocone/dissipation-test`.

BSI (1990). Methods of test for soils for civil engineering purposes. classification tests. BS 1377–2:1990, BSI British Standards, London.

Carroll, W. F. (1988). A fast triaxial shear device. *Geotechnical Testing Journal*, 11(4):276–280.

Carroll, W. F. (1989). A nonlinear one-dimensional wave analysis of a triaxial soil specimen. *Geotechnical Testing Journal*, 12(1):45–49.

Carter, J. P. (1982). Predictions of the non-homogeneous behaviour of clay in the triaxial test. *Géotechnique*, 32(1):55–58.

Casagrande, A. and Wilson, S. D. (1951). Effect of rate of loading on the strength of clays and shales at constant water content. *Géotechnique*, 2(3):251–263.

Chen, B. S. and Mayne, P. W. (1994). Profiling the overconsolidation ratio of clays by piezocone tests. Technical Report GIT-CEEGEO-94-1, School of Civil and Environmental Engineering, Georgia Institute of Technology.

Cheng, R. Y. K. (1976). The effect of shearing strain-rate on the ultimate shearing resistance of clay. Technical Report CR–2634, NASA Langley Research Centre.

Cheng, R. Y. K. (1981). Effect of shearing strain-rate on the undrained strength of clay. In Yong, R. N. and Townsend, F. C., editors, *Laboratory shear strength of soil: a symposium. ASTM STP 740*, pages 243–253. ASTM.

Cheuk, C. Y., White, D. J., and Bolton, M. D. (2008). Uplift mechanisms of pipes buried in sand. *Journal of Geotechnical and Geoenvironmental Engineering*, 134(2):154–163.

Chung, W. J., Cho, J. W., and Belytschko, T. (1998). On the dynamic effects of explicit FEM in sheet metal forming analysis. *Engineering Computations*, 15(6):750–776.

Clausen, J., Damkilde, L., and Andersen, L. (2006). Efficient return algorithms for associated plasticity with multiple yield planes. *International Journal for Numerical Methods in Engineering*, 66(6):1036–1059.

Courant, R., Friedrichs, K., and Lewy, H. (1967). On the partial differential equations of mathematical physics. *IBM Journal of Research and Development*, 11(2):215–234. Trans. Phyllis Fox. First published in *Mathematische Annalen* 100:32-74 (1928).

Cowper, G. R. and Symonds, P. S. (1957). Strain hardening and strain-rate effects in the impact loading of cantilever beams. Technical Report 28, Brown University, Division of Applied Mathematics.

Crisfield, M. A. (1997). *Non-linear finite element analysis of solids and structures. Volume 2: advanced topics.* John Wiley & Sons, Chichester, England.

Dunne, F. and Petrinic, N. (2005). *Introduction to computational plasticity.* Oxford University Press.

Einav, I. and Randolph, M. F. (2005). Combining upper bound and strain path methods for evaluating penetration resistance. *International Journal for Numerical Methods in Engineering*, 63(14):1991–2016.

Einav, I. and Randolph, M. F. (2006). Effect of strain rate on mobilised strength and thickness of curved shear bands. *Géotechnique*, 56(7):501–504.

Eyring, H. (1936). Viscosity, plasticity, and diffusion as examples of absolute reaction rates. *Journal of Chemical Physics*, 4(4):283–291.

Fall, D. A. (2000). A numerical model for rapid determination of plasticity in fine-grained soils. *Ground Engineering*, 33(9):43–45.

Finnie, I. M. S. and Randolph, M. F. (1994). Punch-through and liquefaction induced failure of shallow foundations on calcareous sediments. In *Proc. International Conference on Behaviour of Offshore Structures (BOSS '94)*, pages 217–230, Boston.

Flanagan, D. P. and Belytschko, T. (1981). A uniform strain hexahedron and quadrilateral with orthogonal hourglass control. *International Journal for Numerical Methods in Engineering*, 17:679–706.

geoforum.com (2005). *Brief history of Swedish Soil Mechanics*. Webforum Europe AB. `http://www.geoforum.com/info/pileinfo/swedsoilmech.asp`.

Geonor (2005a). *Test equipment and field instrumentation catalogue*. Geonor A/S, Oslo, Norway. 26th August 2005.

Geonor (2005b). Instructions for use: Fall cone apparatus. Part no. 200000, Geonor A/S, Oslo.

Glasstone, S., Laidler, K., and Eyring, H. (1941). *The Theory of Rate Processes*. McGraw-Hill, New York.

Graham, J., Crooks, J. H. A., and Bell, A. L. (1983). Time effects on the stress-strain behaviour of natural soft clays. *Géotechnique*, 33(3):327–340.

Grunzweig, J., Longman, I. M., and Petch, N. J. (1954). Calculations and measurements on wedge-indentation. *Journal of the Mechanics and Physics of Solids*, 2(2):81–86.

Gue, S. S. (1984). *Ground heave around driven piles in clay*. DPhil thesis, University of Oxford.

Haar, A. and von Kármán, T. (1909). Zur theorie der spannungszustände in plastischen und sandartigen medien. *Nachrichten von der Gesellschaft der Wissenschaften zu Göttingen, Mathematisch-Physikalische Klasse*, pages 204–218.

Hansbo, S. (1957). A new approach to the determination of the shear strength of clay by the fall-cone test. *Proc. Royal Swedish Geotechnical Institute*, 14:7–47.

Harewood, F. J. and McHugh, P. E. (2007). Comparison of the implicit and explicit finite element methods using crystal plasticity. *Computational Materials Science*, 39(2):481–494.

Harison, J. A. (1988). Using the bs cone penetrometer for the determination of the plastic limit of soils. *Géotechnique*, 38(3):433–438.

Hill, R. (1950). *The Mathematical Theory of Plasticity*. Oxford University Press.

Hill, R., Lee, E. H., and Tupper, S. J. (1947). The theory of wedge indentation of ductile materials. *Proceedings of the Royal Society of London Series A – Mathematical and Physical Sciences*, 188(1013):273–290.

Hossain, M. S., Hu, Y., Randolph, M. F., and White, D. J. (2005). Limiting cavity depth for spudcan foundations penetrating clay. *Géotechnique*, 55(9):679–690.

Houlsby, G. T. (1982). Theoretical analysis of the fall cone test. *Géotechnique*, 32(2):111–118.

Houlsby, G. T. and Puzrin, A. M. (2002). Rate-dependent plasticity models derived from potential functions. *Journal of Rheology*, 46(1):113–126.

Houlsby, G. T. and Puzrin, A. M. (2006). *Principles of Hyperplasticity*. Springer.

Houlsby, G. T. and Wroth, C. P. (1982). Direct solution of plasticity problems in soils by the method of characteristics. In *Proc. 4th International Conference on Numerical Methods in Geomechanics*, volume 3, pages 1059–1071, Edmonton, Canada.

House, A. R., Oliveira, J. R. M. S., and Randolph, M. F. (2001). Evaluating the coefficient of consolidation using penetration tests. *International Journal of Physical Modelling in Geotechnics*, 1(3):17–25.

Iskander, M. G., Liu, J. Y., and Sadek, S. (2002). Transparent amorphous silica to model clay. *Journal of Geotechnical and Geoenvironmental Engineering*, 128(3):262–273.

Jirásek, M. and Bažant, Z. P. (2001). *Inelastic Analysis of Structures*. Wiley.

Johnson, G. R. and Cook, W. H. (1983). A constitutive model and data for metals subjected to large strains, high strain rates, and high temperatures. In *Proc. 7th International Symposium on Ballistics*, The Hague, Netherlands.

Johnson, K. L. (1970). The correlation of indentation experiments. *Journal of the Mechanics and Physics of Solids*, 18(2):115–126.

Jones, N. (1997). *Structural Impact*. Cambridge University Press.

Jung, D. W. and Yang, D. Y. (1998). Step-wise combined implicit-explicit finite-element simulation of autobody stamping processes. *Journal of Materials Processing Technology*, 83(1-3):245–260.

Karlsson, R. (1961). Suggested improvements in the liquid limit test, with reference to flow properties of remoulded clays. In *Proc. 5th International Conference on Soil Mechanics and Foundation Engineering*, volume 1, pages 171–184, Paris.

Khalili, N., Geiser, F., and Blight, G. E. (2004). Effective stress in unsaturated soils: review with new evidence. *International Journal of Geomechanics*, 4(2):115–126.

Kim, J., Kang, Y. H., Choi, H. H., Hwang, S. M., and Kang, B. S. (2002). Comparison of implicit and explicit finite-element methods for the hydroforming process of an automobile lower arm. *International Journal of Advanced Manufacturing Technology*, 20(6):407–413.

Koiter, W. T. (1953). Stress-strain relations, uniqueness and variational theorems for elasto-plastic materials with a singular yield surface. *Quarterly of Applied Mathematics*, 11(3):350–354.

Koumoto, T. and Houlsby, G. T. (2001). Theory and practice of the fall cone test. *Géotechnique*, 51(8):701–712.

Krieg, R. D. and Krieg, D. B. (1977). Accuracies of numerical solution methods for the elastic-perfectly plastic model. *Transactions of the ASME. Journal of Pressure Vessel Technology*, 99(4):510–515.

Kugener, S. (1995). Simulation of the crimping process by implicit and explicit finite element methods. *AMP Journal of Technology*, 4:8–15.

Kulhawy, F. H. and Mayne, P. W. (1990). Manual on estimating soil properties for foundation design. Technical Report EL-6800, Electric Power Research Institute.

Ladd, C. C. and Foott, R. (1974). New design procedures for stability of soft clays. *Journal of the Geotechnical Engineering Division, ASCE*, 100(7):763–786.

Larsson, P.-L. (2001). Investigation of sharp contact at rigid-plastic conditions. *International Journal of Mechanical Sciences*, 43:895–920.

Lefebvre, G. and LeBoeuf, D. (1987). Rate effects and cyclic loading of sensitive clays. *Journal of Geotechnical Engineering*, 113(5):476–489.

Lew, K. V. (1981). *Yielding criteria and limit state in a Winnipeg clay.* MSc thesis, University of Manitoba.

Lockett, F. J. (1963). Indentation of a rigid/plastic material by a conical indenter. *Journal of the Mechanics and Physics of Solids*, 11:345–355.

Low, III, S. and Fields, R. (1991). Multiaxial mechanical behaviour of 63Sn-37Pb solder. Technical Report FY2001, NIST Materials Science and Engineering Laboratory, Metallurgy Division.

Mackerle, J. (1999). Finite-element modelling of non-destructive material evaluation: a bibliography (1976-1997). *Modelling and Simulation in Materials Science and Engineering*, 7:107–145.

Maenchen, G. and Sack, S. (1964). The tensor code. In Alder, B., Fernbach, S., and Rotenberg, M., editors, *Methods in Computational Physics, Vol. 3, Fundamentals in Hydrodynamics*. Academic Press, New York.

Marsh, D. M. (1964). Plastic flow in glass. *Proceedings of the Royal Society of London Series A - Mathematical and Physical Sciences*, 279:420–435.

Martin, C. M. (1994). *Physical and numerical modelling of offshore foundations under combined loads.* DPhil thesis, University of Oxford.

Martin, C. M. (2004). User guide for ABC—Analysis of Bearing Capacity. Technical Report OUEL 2261/03, Department of Engineering Science, University of Oxford.

Martin, C. M. (2005). Exact bearing capacity calculations using the method of characteristics. In *Proc. 11th International Conference on Computer Methods and Advances in Geomechanics*, volume 4, pages 441–450, Turin, Italy.

Martins, J. P. (1983). *Shaft resistance of axially loaded piles in clay.* DPhil thesis, University of Oxford.

Mase, G. E. (1970). *Schaum's outline of theory and problems of continuum mechanics.* McGraw–Hill, New York.

MathWorks (2007). *MATLAB 7.4.0 (Release 2007a).* The MathWorks, Inc., Natick, Massachusetts.

May, R. E. (1987). *A study of the piezocone penetrometer in normally consolidated clay.* DPhil thesis, University of Oxford.

McCrum, N. G., Buckley, C. P., and Bucknall, C. B. (1997). *Principles of polymer engineering.* Oxford University Press, 2nd edition.

Mitchell, J. K. (1964). Shearing resistance of soils as a rate process. *Journal of the Soil Mechanics and Foundations Division, ASCE*, 90(SM 1):29–61.

Mitchell, J. K. (1993). *Fundamentals of soil behaviour (2nd edition).* John Wiley and Sons, New York.

Muir Wood, D. (1990). *Soil behaviour and critical state soil mechanics.* Cambridge University Press.

Murayama, S. and Shibata, T. (1958). On the rheological characters of clay, part 1. Technical report, Disaster Prevention Research Institute, University of Kyoto.

Nayak, G. C. and Zienkiewicz, O. C. (1972). Elasto-plastic stress analysis — a generalisation for various constitutive relations including strain softening. *International Journal for Numerical Methods in Engineering*, 5:113–135.

Oka, F., Kodaka, T., Kimoto, S., Ishigaki, S., and Tsuji, C. (2003). Step-changed strain rate effect on the stress-strain relations of clay and a constitutive modeling. *Soils and Foundations*, 43(4):189–202.

Ortiz, M. and Popov, E. P. (1985). Accuracy and stability of integration algorithms for elastoplastic constitutive relations. *International Journal for Numerical Methods in Engineering*, 21:1561–1576.

OSHA (1999). Excavations: hazard recognition in trenching and shoring. In *OSHA Technical Manual, 5th edition*. U.S. Department of Labor. Occupational Safety and Health Administration.

Perzyna, P. (1963). The constitutive equations for rate sensitive plastic materials. *The Quarterly Journal of Mechanics and Applied Mathematics*, 20:321–332.

Poeckert, R. H., Preston, J. M., Miller, T. M., Religa, R., and Eastgaard, A. (1997). A seabed penetrometer. Technical Memorandum 97/233, Defence Research Establishment Atlantic.

Randolph, M. F. (2004). Characterisation of soft sediments for offshore applications. In *Proc. 2nd International Conference on Site Investigation*, Porto.

Randolph, M. F. and Hope, S. (2004). Effect of cone velocity on cone resistance and excess pore pressures. In *Proc. International Symposium on Engineering Practice and Performance of Soft Deposits*, pages 147–152, Osaka.

Randolph, M. F., Steenfelt, J. S., and Wroth, C. P. (1979). The effect of pile type on design parameters for driven piles. In *Proc. 7th European Conference on Soil Mechanics and Foundation Engineering*, Brighton.

RDP Electronics (2007). *Technical Manual: Capacitive Load Cell Type MCL*. Document ref. CD1048J, RDP Electronics Ltd., Wolverhampton. `http://www.rdpe.com/cds/cd1048.pdf`.

RDP Electronics (2008). Online catalogue of displacement transducers. RDP Electronics Ltd., Wolverhampton. `http://www.rdpe.com/uk/men-disp.htm`.

Rockfield Software (1998). *ELFEN 2.8 – The Finite Element/Discrete Element System. Specification Overview*. Rockfield Software Ltd., Swansea, U.K.

Rockfield Software (2005). *ELFEN Explicit user manual, version 3.8*. Rockfield Software Ltd., Swansea, U.K.

Roscoe, K. H. and Burland, J. B. (1968). On the generalised stress-strain behaviour of "wet" clay. In Heyman, J. and Leckie, F. A., editors, *Engineering Plasticity: papers for a conference held in Cambridge, March 1968*, pages 535–609. Cambridge University Press.

Sadek, S., Iskander, M. G., and Liu, J. Y. (2003). Accuracy of digital image correlation for measuring deformations in transparent media. *Journal of Computing in Civil Engineering*, 17(2):88–96.

Sheahan, T. C., Ladd, C. C., and Germaine, J. T. (1996). Rate-dependent undrained shear behavior of saturated clay. *Journal of Geotechnical Engineering*, 122(2):9–108.

Shield, R. T. (1955). On the plastic flow of metals under conditions of axial symmetry. *Proceedings of the Royal Society of London Series A - Mathematical and Physical Sciences*, 233(1193):267–287.

Simulia (2007). *Abaqus online documentation, version 6.7.* Dassault Systèmes simulia corp., Suresnes, France.

Sloan, S. W. and Booker, J. R. (1986). Removal of singularities in Tresca and Mohr–Coulomb yield functions. *Communications in Applied Numerical Methods*, 2:173–179.

Smith, I. M. and Griffiths, D. V. (1998). *Programming the Finite Element Method (3rd edition).* John Wiley & Sons Ltd., Chichester, England.

Smith, M. G. (1993). *A laboratory study of the Marchetti dilatometer.* DPhil thesis, University of Oxford.

Standard Norge (1988). *Geotechnical testing, laboratory methods: determination of undrained shear strength by fall-cone testing.* NS 8015, Standard Norge, Lysaker, Norway.

Stone, K. J. L. and Phan, K. D. (1995). Cone penetration tests near the plastic limit. *Géotechnique*, 45(1):155–158.

Susila, E. and Hryciw, R. D. (2003). Large displacement fem modelling of the cone penetration test (cpt) in normally consolidated sand. *International Journal for Numerical and Analytical Methods in Geomechanics*, 27:585–602.

Swedish State Railways (1922). Statens Järnvägar Geotekniska Meddelanden 2. Geotechnical Commission of the Swedish State Railways, 1914–1922, final report.

Symonds, P. S. (1967). Survey of methods of analysis for plastic deformation of structures under dynamic loading. Technical Report BU/NSRDC/1-67, Brown University, Division of Engineering.

Tabor, D. (1951). *The hardness of metals.* Oxford University Press.

Taylor, L., Cao, J., Karafillis, A. P., and Boyce, M. C. (1995). Numerical simulations of sheet-metal forming. *Journal of Materials Processing Technology*, 50(1-4):168–179.

Vaid, Y. P. and Campanella, R. G. (1977). Time-dependent behavior of undisturbed clay. *Journal of the Geotechnical Engineering Division, ASCE*, 103(No. GT7):693–709.

van Leer, B. (1977). Towards the ultimate conservative finite difference scheme. IV. A new approach to numerical convection. *Journal of Computational Physics*, 23(3):276–299.

Vardoulakis, I. G. (2000). Catastrophic landslides due to frictional heating of the failure plane. *Mechanics of Cohesive-Frictional Materials*, 5:443–467.

Vardoulakis, I. G. and Graf, B. (1985). Calibration of constitutive models for granular materials using data from biaxial experiments. *Géotechnique*, 35(3):299–317.

Wahlberg, A. (1901). Brinell's method of determining hardness and other properties of iron and steel. *Journal of the Iron and Steel Institute*, 59(1):243.

Walker, J. and Yu, H. S. (2006). Adaptive finite element analysis of cone penetration in clay. *Acta Geotechnica*, 1:43–57.

White, D. J. (2002). *An investigation into the behaviour of pressed-in piles.* PhD thesis, University of Cambridge.

White, D. J. and Take, W. A. (2002). GeoPIV: Particle Image Velocimetry (PIV) software for use in geotechnical testing. Technical Report CUED/D-SOILS/TR322, University of Cambridge.

White, D. J., Take, W. A., and Bolton, M. D. (2003). Soil deformation measurement using particle image velocimetry (piv) and photogrammetry. *Géotechnique*, 53(7):619–631.

Whitlow, R. (2001). *Basic Soil Mechanics*. Pearson Education, Harlow, England, 4th edition.

Wilkins, M. (1964). Calculation of elastoplastic flows. In Alder, B., Fernbach, S., and Rotenberg, M., editors, *Methods in Computational Physics, Vol. 3, Fundamentals in Hydrodynamics*, pages 211–263. Academic Press, New York.

Wood, D. M. (1982). Cone penetrometer and liquid limit. *Géotechnique*, 32(1):152–157.

Wood, D. M. (1985). Some fall-cone tests. *Géotechnique*, 35(1):64–68.

Wood, D. M. and Wroth, C. P. (1978). The use of the cone penetrometer to determine the plastic limit of soils. *Ground Engineering*, 11(3):37.

Xu, G. (2008). Personal communication. Dr. Guangquan Xu, Fugro GeoConsulting Ltd., Wallingford, England.

Zhou, H. and Randolph, M. F. (2007). Computational techniques and shear band development for cylindrical and spherical penetrometers in strain-softening clay. *International Journal of Geomechanics*, 7(4):287–295.

Zhou, H. and Randolph, M. F. (2009). Resistance of full-flow penetrometers in rate-dependent strain-softening clay. *Géotechnique*, 59(2):79–86.

Zienkiewicz, O. C. (1967). *The finite element method in structural and continuum mechanics*. McGraw–Hill, London.